Morten Onsrud

Carbon Cones as Negative Electrode Material in Lithium-Ion Batteries

Thesis for the degree of Philosophiae Doctor

Trondheim, September 2012

Norwegian University of Science and Technology
Faculty of Natural Sciences and Technology
Department of Materials Science and Engineering

NTNU – Trondheim
Norwegian University of
Science and Technology

NTNU
Norwegian University of Science and Technology

Thesis for the degree of Philosophiae Doctor

Faculty of Natural Sciences and Technology
Department of Materials Science and Engineering

ISBN 978-82-471-3793-2 (printed ver.)
ISBN 978-82-471-3794-9 (electronic ver.)
ISSN 1503-8181

Doctoral theses at NTNU, 2012:244

Printed by NTNU-trykk

To Trygve Foosnæs, friend and mentor.

Preface

In April of 2006, I received an e-mail from Professor Trygve Foosnæs regarding a student project. Professor Foosnæs was looking for someone who could start studying a new material called carbon cones. I promptly replied to the e-mail to show my interest. At that time, I was an exchange student at RWTH Aachen University in Germany, but I agreed to meet with Professor Foosnæs back in Trondheim to discuss the project during the Easter holiday. I was introduced to Nils Myklebust and the three of us decided to start a collaboration together. I began working on the carbon cones material later that year. Initially, my focus was on characterization of the carbon cones. I continued this work for my master thesis study. However, Nils Myklebust, as a representative from the industry, was very eager to start manufacturing carbon cones. Till then, we had only worked on carbon cones produced at an earlier stage. Professor Foosnæs informed me about a newly established program (Nærings-PhD) at the Research Council of Norway (NFR) where the goal was to improve the collaboration between industry and universities. He suggested that I should apply for this program. Together with Nils Myklebust, we worked out an application and after some initial problems we got a positive response from NFR. I started on my ambitious goal of producing a new carbon material in September 2008. We were able to perform 29 reactor runs in all, where most of our attempts gave us a carbon product. Unfortunately, the product was not what we were trying produce. Instead we were making really expensive low quality carbon black. Approximately one year into my PhD., we were still not producing carbon cones. At the same time, the financial crisis hit Europe hard and as a consequence we ran out of money to do our costly experiments. Since we had no positive results to show for, the funding of the carbon cones production project stopped. On top of this, in late April 2009, my supervisor Professor Trygve Foosnæs passed away, only 58 years old. With both the knowledge and the money gone, I was not interested in carrying on with my current work. I could not imagine a rewarding doctoral degree without any practical experiments. Also, the main the reason why I started on a PhD was gone. My aim had all along been to produce a new carbon structure. However, I did not want to quit so I knew I had to make some changes. I was lucky enough to pick out a new supervisor. I naturally chose my favorite lecturer from my days as a master student which was at that time newly employed Associate Professor Fride Vullum-Bruer. I knew that she had a background in lithium-ion batteries among other things. I also knew that carbon materials were extensively used as anode material in lithium-ion batteries. I was figuratively sitting on kilos of a relatively new, unique, and untested material

suitable for this purpose. My new supervisor was positive to my idea. She told me that SINTEF was starting up a project on lithium-ion batteries and I saw the opportunity to join forces with my colleagues. As I started working towards employing carbon cones as negative electrode material in lithium-ion batteries, I also began a close collaboration with SINTEF. Together we solved many of the initial problems related to such a project. Today, I would say that we have successfully established a lithium-ion battery laboratory and research group at our department. It was not my initial intention to work with lithium-ion batteries or electrochemistry, but I have enjoyed working in this field and I appreciate the new knowledge I have obtained. To sum up some of my thoughts from these past years, I would say that I have had a blessing in disguise.

Acknowledgment

I would first and foremost like to thank my deceased supervisor Professor Trygve Foosnæs. His persuasive words convinced me to start working on a doctoral degree. His positive energy was a strong motivation for me to continue on my collaboration with him. Tragically, Trygve Foosnæs passed away after one year into my doctoral degree. I chose to continue my work and I picked out Associate Professor Fride Vullum-Bruer as my new supervisor. I'm grateful for this choice every day. Associate Professor Fride Vullum-Bruer deserves all the recognition she can get. The idea for this work originated during one of our first meeting Associate Professor Vullum-Bruer has been extremely helpful and she has been a great inspiration for me.

Another great source of inspiration has been my two industrial contacts Nils Myklebust and Dr. Jean Patrick Pinheiro. I owe them both many thanks for being willing to help me through difficult times. Nils Myklebust was my nearest colleague during the carbon cones production period. He taught me a lot about solving practical problems that occurred during production. I'm also very grateful for his contribution to the administrative problems we have encountered. The collaboration between NTNU, The Research Council of Norway, Aker Solutions, and Scatec would not have been possible without his help. Dr. Jean Patrick Pinheiros knowledge on carbon materials has been vital for my understanding of carbon cones. We have had many fruitful discussions and this have resulted in great ideas. Dr. Pinheiro has also contributed with FEGSEM images of the newest carbon material. I have enjoyed my regular visits to his laboratory.

I would like to show my gratitude to my friends in Japan. Professor Masahiro Tatsumisago was kind to let me join his research group at Osaka Prefecture University. I also have to thank Associate Professor Kiyoharu Tadanaga for helping me with all the practical arrangements during my stay and Assistant Professor Akitoshi Hayashi for his knowledge in questions regarding all solid state lithium-ion batteries. I also appreciate the friendship I obtained with the PhD.-students and master students I met in Osaka. They really made my stay memorable.

I'm grateful for the support I got from Professor Tor Grande after Professor Foosnæs passed away and the help I got from Professor Mari-Ann Einarsrud to arrange my research stay in Japan.

Many thanks are also sent to my friends and colleagues in the battery research group. PhD-students Carl Erik Lie Foss, Haitao Zhou and Conor Mc-

Carthy deserve acknowledgment. I feel that our co-operation have been very rewarding. I'm grateful for the help I have received from master students Marius Uv Nagell, Phung Hieu Dinh Tran, Alf Petter Syvertsen, and Øystein Gullbrekken. Their contributions have been very useful for me.

Our colleagues from SINTEF have also been of great help. I'm very thankful for being given the opportunity to cooperate so closely. I have to especially thank Dr. Edel Sheridan for introducing me to the world of batteries and for her enthusiastic support during the initial and final stage of my battery research. Within the SINTEF institution, I want to acknowledge Steinar Prytz and Ingeborg Solheim for their work on the carbon production. On the battery side, other SINTEF people I would like to thank are Dr. Anita Fossdal, Jannicke Kvello, and Dr. Ann-Mari Svensson. Calin Daniel Marioare deserves recognition for the TEM images he provided of the conical carbon stacks.

My most sincere thanks goes also to Annette Linda Vestlund, Lise Våland Sund, and Ingeborg Guldal at the Research Council of Norway. Thanks for the industrial-PhD funding.

I would also like to express my gratitude to the people of Scatec AS and Aker Solutions AS who made this work feasible. I'm thankful for the materials given to our research group. We have been given commercial graphite from TIMCAL Graphite & Carbon, while we received copper current collectors from Circuit Foil. Arkema provided us with electrode binder material.

Finally, I would like to acknowledge my family and friends for their good spirits, never-ending encouragement, and support.

Abstract

New and improved lithium-ion batteries can be developed by increasing their capacity. One way of achieving this is to find better anode alternatives to replace the conventional graphite anode. Carbon cones is a type of carbon material that is not very well known and might possess interesting properties for this purpose. The material consists of three types of carbon; cones, disks, and carbon black. The most unique structure is the cone and hence the name carbon cones. The easiest way to imagine these conical carbon structures is to look at them as graphene sheets rolled up into a cone. During production in a hot plasma furnace, several graphene layers are formed on top of one another into a multilayered cone. Five different conical structures have been observed, each of which has a different apex angle, giving a very pointed or a more flat conical structure. Instead of having the normal hexagonal packing of carbon atoms like a regular graphene sheet, the cones contain between 1 and 5 pentagons at its apex. The pentagons induce a curvature in the structure. Carbon disks do not contain any pentagons in their structure and are therefore flat.

Carbon cones have been investigated with different methods as a potential new anode material in lithium-ion batteries. The performance of the carbon cones has been compared to commercially available graphite. The conical carbon structures produced in earlier experiments have also been investigated and characterized with electron microscopy, X-ray diffraction and Raman spectroscopy. The crystallinity of the carbon cones has been modified by applying various heat treatments. The cones have also undergone chemical and microwave irradiation treatments in an attempt to alter their performance in lithium-ion batteries.

The investigations indicate that the carbon cones might be an alternative material for lithium-ion battery applications. However, there are still many challenges which need to be dealt with. The largest of them, is the problem of reproducing the carbon cones material.

Battery is here to stay

J. A. Hetfield

Contents

Chapter 1

Introduction

This section is divided into two parts, referring to the carbon cones project and the lithium-ion batteries part separately. The initial part will give a brief introduction to the carbon cones material and its production attempts. The second part will introduce the reader to lithium-ion batteries (LIB) and will explain the reason for the ever increasing popularity of this technology.

1.1 Carbon Cones

The unique structures of carbon cones were first produced in 1995 at a carbon black pilot plant in Hofors, Sweden [1]. The initial goal of the experiments was to develop a new method of producing carbon black. Surprisingly, the researcher discovered conical structures along with flat disks of carbon. At first, the carbon cones material was discarded, but the material got renewed interest after further development in the carbon technology field. New carbon materials such as carbon nanotubes and Buckminsterfullerenes emerged and they lead to an enormous interest in carbon materials. The discovery of these new materials and their development contributed to growth in many other areas. As a part of this development, it was decided that the production of carbon cones was to be restarted. The ultimate goal was to include carbon cones in the so-called carbon technology renaissance. 29 trial runs were performed in total. Most of the trial runs succeeded in producing carbon powder. However, only on a few occasions, the conical shape characteristic of the carbon cones was observed. Production of carbon materials of similar size, shape and quality as the original carbon

cones was not achieved. Due to unfortunate circumstances, the carbon cones production project was terminated after only one year. In this study, several aspects of the carbon structure are addressed. The main contribution has been the study of its performance in lithium-ion batteries.

1.2 Lithium-Ion Batteries

Portable energy sources and especially batteries have an ever greater impact on our everyday life. Batteries are therefore getting increasingly more important for us. Electronic devices are constantly demanding more and more energy as laptops, cellular phones, cameras etc. are becoming more advanced. Lighter and more energy dense solutions are necessary for a future world. Advances in battery technology and concerns regarding climate-change have accelerated the research focus on the electrification of vehicles. Effective batteries will be needed as the society transforms towards more green and environmentally sound technology. Many renewable energy sources such as wind and solar can only produce electricity periodically when the conditions allow it. Batteries can be used to optimize the energy distribution of renewable energy.

Even thought batteries have been around for at least 200 years, there is still no ultimate solution for our hunger for more power. There might not be such a thing as the perfect battery. However, researchers are still working persistently to improve current batteries. They are partially succeeding, but there has not been a battery revolution similar to the one in electronic circuitry, where the number of transistors have typically doubled every second year. The general public is demanding similar progress, but the effect of miniaturization does not apply for batteries in the same manner as for electronic circuitry. The periodic table of elements contains a limited amount of elements and only a fraction of them can be used in practical battery systems. Nevertheless, researchers are still vigorously testing new compositions, searching for the perfect battery with high energy density, light construction, good safety and the ability to undergo thousands of cycles without losing capacity. Nonetheless, different applications have different criteria and demands. An ideal battery for a cellular phone might be a poor choice for electric vehicles.

The world market for lithium-ion battery is constantly growing due to an insatiable appetite for more power and energy capacity. Today, the power source of choice for portable applications is the lithium-ion battery because of its high energy density and high electromotive force and it will continue to be dominating for the indistinguishable future.

Today, almost all battery technology uses carbon in one form or another. The morphology and purity are the most important factors in the carbons used in practical cells. In lithium-ion batteries, carbon has two main purposes as active anode material and conductive diluent. Both factors are immensely important to the battery's performance.

Many types of carbon are industrially available for lithium-ion battery purposes. The structure influences the electrochemical properties. In the case of lithium-ion batteries, the carbon anode has a great impact on the cell performance parameters such as cycle life and rate capability. Hard carbons offer high capacity, but also high irreversible capacity. On the other hand, more expensive mesocarbon microbeads (MCMB) have a good capacity and low irreversible capacity. Lower priced graphite with a capacity close to the theoretical capacity (372 mAh/g) has a larger capacity loss. The chemistry of the carbon anode surface and the morphology have a great impact on the formation of the solid electrolyte interphase formation, and on the overall electrochemical anode behavior.

This work presents recent developments in the field of lithium-ion batteries, where a new carbon material has been utilized. The main target of this study has evolved into the testing and implementation of the carbon cones for battery applications. The initial idea/anticipation was that carbon cones would combine the high specific charge of disordered carbon and the charge/discharge potential characteristics of graphite materials.

Chapter 2

Background

2.1 A Brief History of Carbon Materials

The word carbon comes from the Latin word for charcoal, carbo. From the early days of mankind, carbon has been used as either firewood or drawing materials [1]. Early recollections tell how carbon black was used as a pigment and for printing. As mankind evolved, microporous charcoal was used in gunpowder and as an anti-acid agent. The most significant carbon manufacturing technology may have been the development of the electrical resistance furnace to manufacture synthetic graphite. The petroleum, aluminum and iron-making industry have all contributed to the further development of carbon technology [2].

At the end of the eighteenth century, it was known that graphite and diamond were two different forms of the same element. For a long time these allotropes were believed to be the only two structures of crystalline carbon [3]. The third major form was observed as late as 1985 when Kroto *et al.* [4] discovered the Buckminsterfullerene. The existence of the fourth type of carbon, the carbon nanotubes became known to the scientific community in 1991 [5]. The discovery of carbon nanotubes is a contentious topic. It is believed that Iijima's work is particularly important because it brought the carbon nanotube issue into awareness for scientists around the world. In 1994, Ge *et al.* [6] observed fullerene cones. These cones can be regarded as a hybrid material between open fullerene structures and graphene. Large quantities of similar carbon cones were

[1] The word "graphite" comes from Greek "graph(ein)" meaning to draw or write.

discovered in the silos of a hot plasma reactor that was designed to produce carbon black in 1995 [7]. It is the material from this reactor which has been studied in this work. In 2010, Andre K. Geim and Konstantin S. Novoselov got the Nobel prize in physics for their groundbreaking work on graphene. Today, carbon can be found in many different fields, ranging from the ancient techniques of producing lamp black (early form of carbon black) to high tech applications, for instance lithium-ion batteries.

2.2 Carbon Cones as a Novel Carbon Material

When the carbon cones were first produced, it was discarded as merely a by-product. The original goal had been to produce carbon black by utilizing a hot plasma furnace and the pyrolysis of hydrocarbons. As the engineers studied the material with electron microscopy, they did not find carbon black as expected, but instead conical structures of different sizes and apex angles. The carbon cones were not produced during the subsequent runs and the idea of producing carbon cones was discarded since the main goal of the manufacture all along had been to produce carbon black[2].

The initial aim of this doctoral degree was to reproduce the reactor conditions in order to produce more carbon cones material. If this succeeded, the next step would be to produce specific cone structures with a fixed size and apex angle. Eventually, the ultimate goal would be to produce specially designed carbon materials. The underlying process was from the beginning continuous and potentially large quantities of carbon could be produced. If the carbon cones process had been successful, the cost of, for instance carbon nanotubes would have decreased dramatically.

The achieved results were not as successful as originally anticipated. The main product in the silos of the reactor was carbon black. Efforts were made to improve the process. The outcome were stacks of carbon with a conical tip, see Fig. 5.15, much like the carbon material published by Ohtani *et al.* [8].

However, due to the lack of positive results and the financial situation in Europe at that time, the funding for further experiments was canceled. The focus was changed to characterization and possible applications of carbon cones in lithium-ion batteries.

[2] There is a limited supply of carbon cones due to the small amount produced

2.3 A Brief History of Batteries

The history of electrochemical batteries dates back several thousand years. This is confirmed by the findings of ancient jars which had been gold plated by electrochemical means. There is evidence that primitive batteries (Baghdad battery) were used in Iraq and Egypt for electroplating and precious metal gilding. However, this technology was lost and forgotten for many centuries [9].

Before the battery was reinvented, electrostatic machines were the only sources of electrical current for a long time. It was Benjamin Franklin, who first used the term "battery" in 1749 after experimenting with capacitors coupled together to form a "battery" [10].[3]

Between 1780 and 1786, Luigi Galvani demonstrated that dead frogs twitched when they came in contact with two different metals. He claimed the existence of "animal electricity" [11], but he was later proven wrong by Alessandro Volta. Volta believed the electricity originated from the different metals and not from the frog [12]. He developed the first practical method in generating electricity with the first proven battery as he invented the Voltaic Pile [13]. German scientist Johan Wilhelm Ritter was able to make the first rechargeable battery (Ritterian-Pile) in 1802 [14]. However, the "Piles"' could not deliver electric current for a long period of time. This limitation was solved by John Frederic Daniell as he invented the Daniell cell in 1836 [15]. The Daniell cell utilized two electrolytes (copper sulfate and zinc sulfate) yielding a potential of 1.1 V. As time went on, several inventors created improved batteries. One of the most successful cells was the Grove cell from William Robert Grove in 1844. It had almost twice the voltage of the Daniell cell, but it gave off poisonous fumes during operation along with several other disadvantages. In 1859, a successful rechargeable battery was developed by French scientist, Gaston Planté. His battery was the lead-acid battery, still used in vehicles today [16]. Georges Leclanché patented the carbon-zinc wet cell battery (Leclanché cell) in 1866 [17]. In 1886 Carl Gassner, made a modified version of the Leclanché cell with no liquid electrolyte, known as the dry cell [18]. Up to this time all cells were assembled in a vessel with large amounts of liquid electrolytes. Due to the risk of spilling, the batteries were limited to stationary applications. The applications for the early batteries were telegraphy, signaling, telephones and electrical lighting. With the dry cell no maintenance was required, nor did it spill. It could also be used in any orientation. With these properties the battery became transportable and

[3] One definition of the word battery is: An array of similar devices intended for simultaneous use

as a consequence, the flashlight was invented a few years later. The Swedish inventor Waldmar Junger made the first nickel-cadmium rechargeable battery in 1899 [19]. It had a considerably better energy density then the lead-acid battery, but it was also much more expensive. Thomas Alva Edison developed the nickel-cadmium cell technology further, but with iron instead of cadmium which he patented in 1903 [20]. In 1957, Lewis Urry created the Alkaline-Manganese Battery [21]. Its battery life lasted five to eight times longer than the preceding primary carbon-zinc battery. In the early 1970s, nickel hydrogen batteries entered the market. The hydrogen was kept in pressurized cells [22]. In the late 1980s a variation of the nickel hydrogen battery was created. It was the secondary nickel-metal hydride battery which used a hydrogen-absorbing alloy for the negative electrode [23]. In the 1970s, the first primary lithium cells were commercialized [24]. In 1980, John B. Goodenough's group created a rechargeable cell using lithium cobalt oxide as the positive electrode [25]. This is regarded as the pivotal moment for the realization of lithium-ion batteries. In 1991, stable secondary lithium-ion batteries were marketed by Sony [26]. Five years later the lithium-ion polymer battery was released. The electrolyte was a solid polymer composite. They have the advantage of being more flexible and can be shaped into a confined space. Since then, there has been a continuous improvement of lithium-ion battery technology by modifications of electrodes and electrolyte.

2.4 Lithium-Ion Batteries

Lithium-ion battery technology is superior to many other battery technologies because of its high energy density and high potential. Fig. 2.1 compares different secondary battery technologies.

Chemistry, performance, cost, and safety varies with the different lithium-ion battery technologies, but of all the rechargeable batteries, lithium-ion batteries can store more energy per weight/volume then any other commercial successful technology. It is also superior regarding resilience because lithium-ion batteries can retain its charge/discharge capacity over many cycles. The self discharge is negligible. Many battery scientists now agree that the batteries for portable devices are adequate for their purpose. Many batteries today, out-live their respective electrical device. For instance, very few people keep their cell phone for more than three years, while the batteries can be operational for longer. However, if a battery is going to be used in a car, the life-time has to be increased even further. Luckily, many researchers are working on this. Environmental

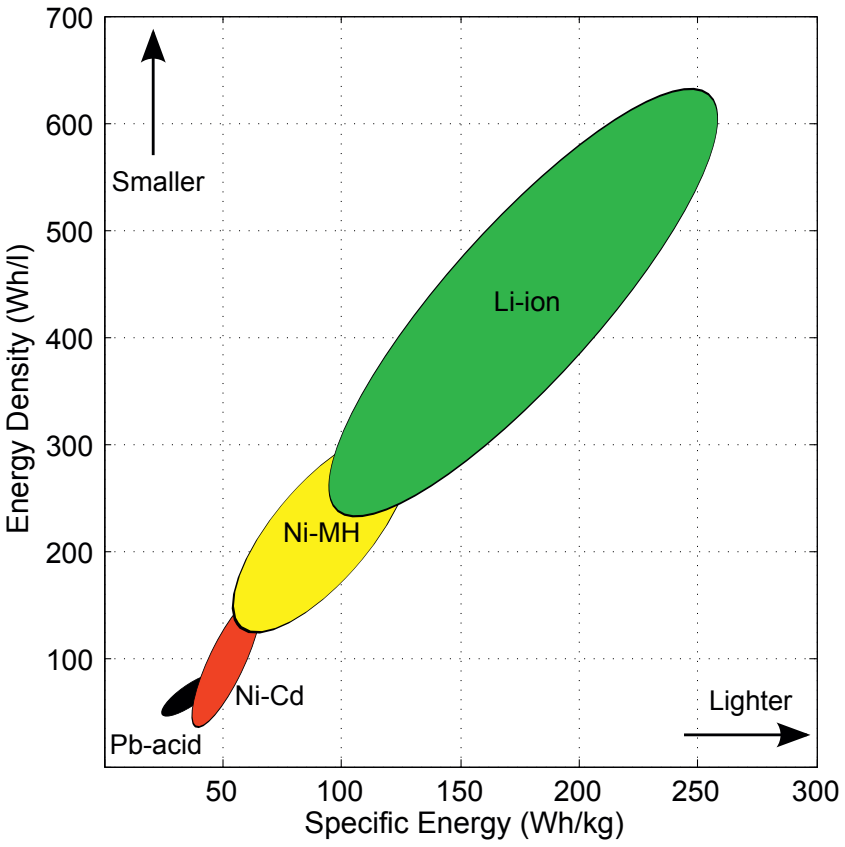

Figure 2.1: Comparison of common secondary battery technologies [27]

concerns will continue to drive the development for more advanced batteries. The use of non-aqueous electrolytes allow for cells with a wide temperature operation range. Due to the high voltage cells of lithium-ion technology, fewer cells are needed to produce the equivalent voltage. The lithium-ion cell has no memory effect, and only demonstrates a slow loss of charge when inactive. Durability, cost, and intrinsic safety are important factors which are likely to be improved in the near future.

Chapter 3

Theory

The theoretical part is a short independent and self-supported text. The text will enable the reader to understand the basic principles of the various topics related to carbon and lithium-ion batteries. As with other parts in the thesis, this section is divided into a section regarding carbon related topics, while the another section handles the issues of lithium-ion batteries.

In some parts of this text, the term "carbon cones" is referred to as individual structures. Other times, carbon cones apply to the material produced in the pyrolytic Kværner carbon black and hydrogen process. It is essential to be aware of the difference. The carbon cones material consists of several types of carbon, where the carbon disks are the predominant component in the material. Nevertheless, the material is named carbon cones due to the uniqueness of the cone morphology. Even though most of the carbon cones material bulk properties derives from the carbon disks, the name carbon cones has been incorporated into this work for a long time and is therefore kept in order to avoid confusion.

3.1 Carbon Materials

This section covers the basics of carbon materials. There is a vast collection of carbon materials available, of which the most fundamental types are discussed below.

Carbon is the sixth element in the periodic table of elements. As with the 92 naturally occurring elements, it has a unique set of properties unlike any

Table 3.1: Average bond enthalpies between carbon atoms at 25 °C. C=C bond is calculated from benzene

Bond	Strength (kJ/mol)
C−C	346
C=C	614
C≡C	839
C=C	507

other element. Due to its four valence electrons, carbon can bond to form long chains, large lattices or bond with a wide variety of different atoms, and the carbon-carbon bond is exceptionally strong. The carbon atom is small, hence the shared electrons are close to the nucleus which makes the electron-nucleus attraction strong. The average bond enthalpies are given in Table 3.1

As an element, carbon is very intriguing as it can be put together in many ways, forming a vast range of different types of carbons [28, 29]. As two single bonds are stronger than one double bond and three single bonds are stronger than one triple bond, carbon prefers to form chains or lattices with single or conjugated double bonds. In fact, the nearest neighbor C=C bonding in graphite is significantly stronger than the C−C bonding in diamond [30].

Besides diamond, graphite is perhaps the most well known of the carbon allotropes[1]. Pure carbon can also exist as fullerenes or carbon nanotubes. Carbon cones can be considered as a relatively new morphology. The properties of these materials vary immensely due to the different structures. It is expected that the single cone has properties that are similar to the Buckminsterfullerene and the carbon nanotubes [31], while the carbon cones materials studied here will have characteristic resembling graphite and disordered carbon.

3.1.1 Orbital Hybridization

It is important to understand the bonding interactions between the carbon atoms in order to obtain a good knowledge of the properties of carbon materials. A carbon atom has six electrons. Two of these electrons fill the 1s orbital. The other four electrons, the valence electrons, are responsible for bonding to other atoms. The electron configuration for carbon is $1s^2\ 2s^2\ 2p^2$. There is a small energy difference between the filled 2s shell and the 2p shell. The atoms

[1] A humorous presentation of the carbon family can be seen on page 218.

achieve their lowest energy state by promoting the 2s electrons into a hybridization with the 2p electrons. The hybridization sp^2 corresponds to the periodic lattice of graphite and the hybridization sp^3 corresponds to the periodic lattice of diamond [3], see Fig. 3.1. The sp^2 structure has the lowest energy state and graphite is therefore more abundant in nature. The sp^3 hybridization found in diamond is actually thermodynamically unstable, see Eq. 3.1 [32].

$$\mathrm{C_{diamond}} \longrightarrow \mathrm{C_{graphite}} \qquad \Delta H = -4.1\mathrm{kJ/mol} \tag{3.1}$$

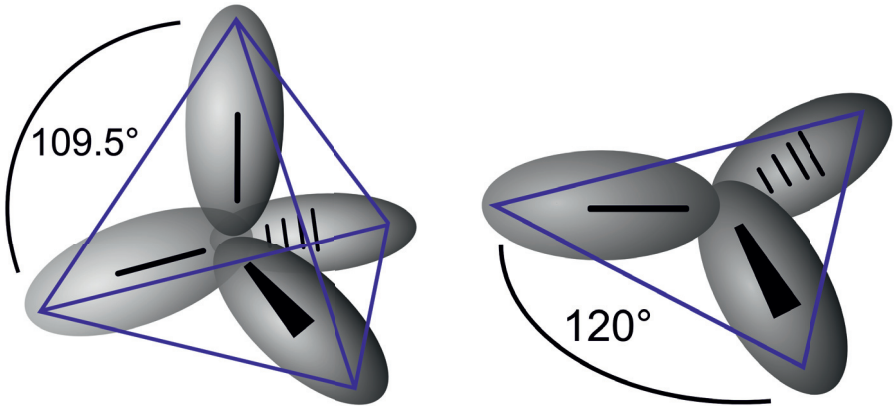

(a) (b)

Figure 3.1: a) The sp^3 hybrid orbital of diamond and b) the sp^2 hybrid orbital of graphite. [3]

Hybridization of s- and p-orbitals take place by promotion of one 2s-electron into an empty p-orbital, see Eq. 3.2 and 3.3.

For diamond:

$$1\,\mathrm{s^2 2s^2 2p_x^1 2p_y^1} \xrightarrow{\text{promotion}} 1s^2 2s^1 2p_x^1 2p_y^1 2p_z^1 \xrightarrow{\text{hybridization}} 1s^2 (sp^3)^4 \tag{3.2}$$

For graphite:

$$1\,\mathrm{s^2 2s^2 2p_x^1 2p_y^1} \xrightarrow{\text{promotion}} 1s^2 2s^1 2p_x^1 2p_y^1 2p_z^1 \xrightarrow{\text{hybridization}} 1s^2 (sp^2)^3 2p_z^1 \tag{3.3}$$

The equivalent atomic orbitals (sp) are established when the atoms are involved in bonding with other atoms. For the diamond structure, a regular tetrahedron of four sp^3 σ-bonds is created. For graphite, carbon atoms are bound to

three other carbon atoms by overlapping three sp^2 hybrid σ-bonds. The carbon atoms in graphite creates conjugated π-bonds with the last $2p_z$ orbital.

3.1.2 Graphite and Graphene

Graphite is characterized by a three-dimensional structure of flat layers of carbon arranged in a systematic stacking sequence along the c-axis . In each layer (graphene), carbon atoms are assembled by occupying the corners in a regular hexagon. The hexagons all share one edge with six other hexagons forming a honeycomb structure. The distance between the in-plane carbon atoms are 1.41 Å, while the inter-layer distance is 3.35 Å for the ideal graphite [33].

Some carbons can be described as structural units or building blocks constructed together to form the carbon material. The parameter L_a describes the diameter of a structural unit. The layers tend to arrange parallel and the term L_c describes the stacking height. The d_{002} term is the spacing between the layers (meaning interlayer spacing) [3]. These three parameters can be used to describe carbon structures. Graphite is an example of a material constructed of structural units or basic building blocks, where L_a and L_c are relatively large.

For graphite, three valence electrons occupy the planar sp^2 hybrid orbital. Together they will form three σ-bonds with an angle of 120° between each other. Trigonal carbon atoms will therefore prefer a planar orientation. The three in-plane σ-bonds are responsible for the planar honeycomb structure, see Fig. 3.2.

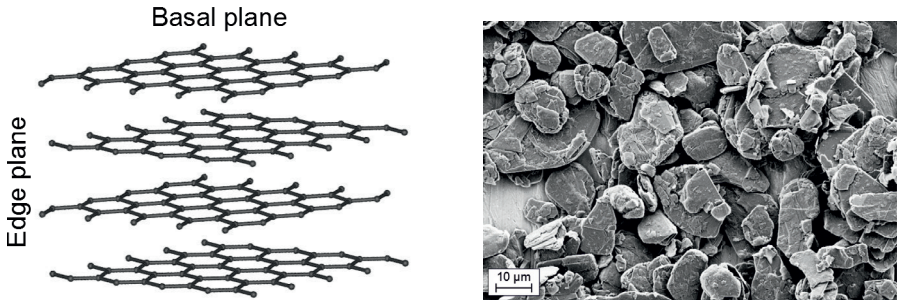

(a) (b)

Figure 3.2: a) A schematic presentation of the graphite structure [34] b) and FEGSEM picture of commercially available graphite from Timcal.

Carbons with both σ-bonds and π-bonds create layered structures of a highly

anisotropic nature. The sp^2 hybridization of graphite involves two of the three p-orbitals. The last p-orbital is oriented perpendicularly to the hexagonal network. This orbital is occupied by a fourth electron. The last valence electron will fill an out-of-plane p_z-orbital. This orthogonal orbital is only half-filled and it can therefore create covalent π-bonds. The out-of-plane π-electrons are responsible for graphite's thermal and electrical conductivity along the plane. Graphite is black because the π-electrons absorb light in the visible spectrum.

Graphite consists of layers of hexagonally arranged carbon atoms. The layers are stacked in a three-dimensional crystalline long range order. Two different stacking orders yield polymorphs, hexagonal(ABAB) and rhombohedral(ABCABC). The weak interplanar bonding of metallic nature has a strength comparable to Van der Waals bonding.

One single sheet of the honeycomb structure is called graphene. It can be regarded as a polycyclic aromatic hydrocarbon of quasi infinite size. Long range π-conjugation of the graphene structure yields exceptional mechanical, thermal and electrical properties. For instance, the in-plane thermal conductivity of graphene is higher than in diamond [35].

The relatively weak bonds between the graphene sheets make graphite soft and useful as a lubricant [36]. Some typical bulk properties of graphite are given below [3]:

- Semi-metal (Band gap 0.04 eV)
- Electrical conductivity similar to iron
- Soft and deformable
- Density 2.26 g/cm^3

Carbon of a graphitic nature has principally two different surfaces, namely the edge (prismatic) plane and basal plane, see Fig. 3.2a. Perfect basal planes are homogeneous as the surface only consists of carbon atoms. Defects and contamination can occur in the non-ideal case. The heterogeneous edge plane is rougher and contains different surface groups [37]. The two planes exhibit different chemical and physical behavior especially in lithium-ion batteries [38].

3.1.3 Diamond

The structure and thus the properties of diamond are completely different compared to graphite. The four valence electrons are located in a sp^3 hybrid orbital.

This orbital hybridization creates a tetrahedral structure to bond with four other carbon atoms, as shown in Fig. 3.3. All the valence electrons in diamond are in covalent σ-bonds and not in delocalized π-bonds. Pure undoped diamond is thus electrically insulating.

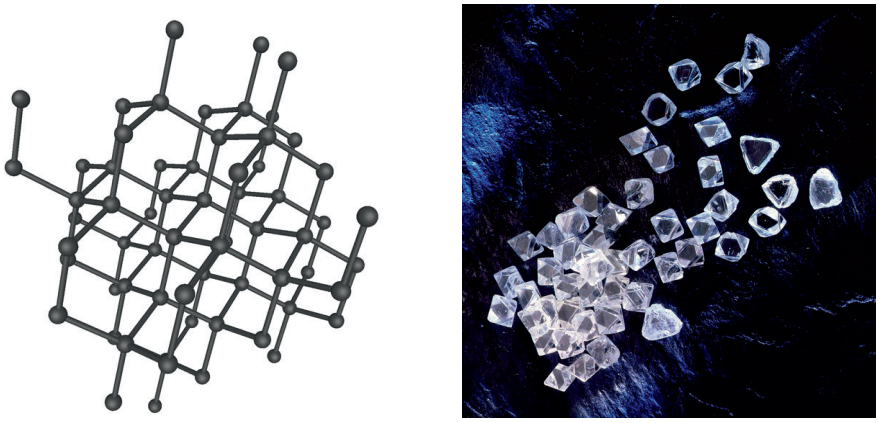

(a) (b)

Figure 3.3: a) A schematic presentation of the diamond structure [34] b) and a picture of unpolished diamonds showing the characteristic cubic structure. The clear color indicates pure diamonds.

Diamond is an allotropic form of carbon with a cubic structure. It is thermodynamically metastable at room temperature and atmospheric pressure. Carbon solids with pure σ-bonds create a rigid and isotropic three-dimensional diamond. A diamond that is not contaminated with other elements is transparent and clear to the human eye. The electrons only absorb light in the ultraviolet spectral region. Diamonds have high index of refraction and a high thermal conductivity [39]. Some typical bulk properties of diamond are given below:

- Extremely hard, least deformable
- Extremely high thermal conductivity
- Electric insulator (Band gap 5.5 eV)
- Density 3.51 g/c^{3}m

Lonsdaleite or hexagonal diamond is another rare allotrope of carbon. This polymorph is sometimes found in meteors.

3.1.4 Carbon Nanotubes

A carbon nanotube (CNT) can be regarded as a graphene sheet rolled into a small hollow tube. The tubes can be single-walled (SWNT) or concentrically multi-walled (MWNT). A single-walled carbon nanotube is presented in Fig. 3.4. The main bonding is by sp^2 hybrid orbitals. The graphene sheets are curved and therefore the sp^2 bonds are σ-π rehybridized. The three σ-bonds are slightly out of plane and the π-orbital is more delocalized on the outside than on the inside of the tube. This special σ-π rehybridization makes CNT stronger, thermally and electrically more conductive, and more chemically active than graphite [40]. CNTs allow for defects in its honeycomb network, which can be for instance pentagons or heptagons of carbon or other elements that dopes the structure. These types of defects will change the diameter or the orientation of the tubes. The angle at which the graphene sheet is rolled up into a SWNT dramatically changes the electrical transport properties [41]. Tubes with a helical twist along its length in the structure lattice (chiral) have semiconducting properties. The zigzag and the armchair structured (achiral) tubes have a metallic nature.

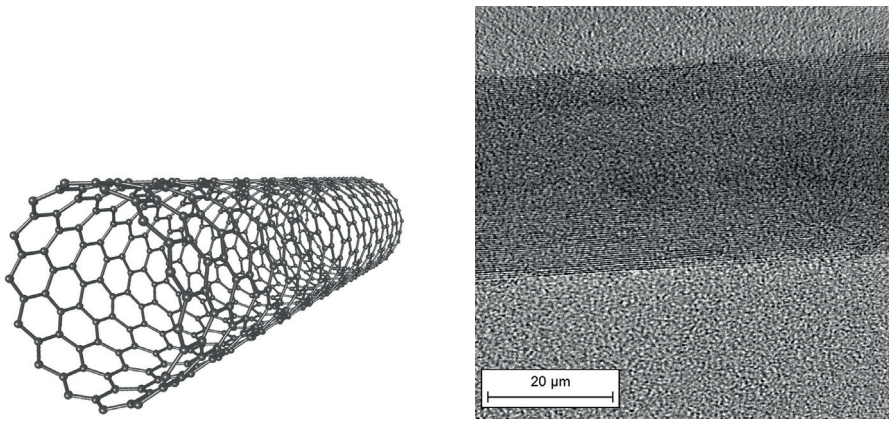

(a) (b)

Figure 3.4: a) A schematic presentation of the single walled carbon nanotube [34] b) and a TEM image of a multi-walled carbon nanotube from N-tec.

3.1.5 Buckminsterfullerene

The Buckminsterfullerene (or football molecule) is a distinct carbon structure named after the architect Richard Buckminster Fuller. All the carbon atoms are located at the surface of a hollow sphere. The structure of a fullerene is shown in Fig. 3.5. Such hollow spheres can exist in a wide range of sizes, but the most stable and therefore the most abundant structure is C_{60} [4]. The C_{60} is perfectly symmetric and the 60 carbon atoms are arranged in hexagonal or pentagonal arrays with 20 hexagons and 12 pentagons [2]. This type of structure opens up for a wide range of potential applications within nanodevices and catalysis [42]. In addition to the single sphere, buckminsterfullerenes can also exist as spheres within spheres like the layers of an onion.

A rehybridization occurs because of the curvature of the graphitic bonds in the structure of fullerenes. The sp^2 and sp^3 form an intermediate hybridization, $sp^{2+\epsilon}$ where ϵ is a factor between 0 and 1 which depends on the degree of curvature [43].

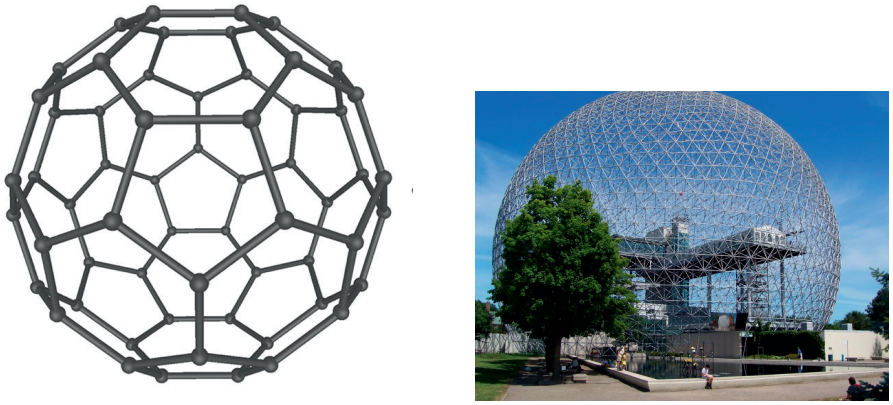

(a) (b)

Figure 3.5: a) A schematic presentation of the C_{60} fullerene [34] b) and a picture of the Montreal Biosphère designed by architect Richard Buckminster Fuller.

Fullerenes are formed in a condensing carbon vapor environment [3], where carbon chains are linked together to form graphene layers. These free floating small graphene sheets have a large ratio of dangling bonds compared to the atoms in the large graphene layers. The dangling bonds have a physical tendency of reaching the lowest energy level possible. By eliminating its dangling bonds,

the lowest level is reached as the sheets curl up into spheres. The curvature is effectuated by changing some of the six-membered carbon rings into pentagons [2]. The growing edge can overrun the opposite side, causing the growth of an onion-like structure. The curvature induces large strains in the spheroidal structures which makes the larger graphite structures more stable than the fullerenes, but the reason for its existence is due to the kinetics of the formation.

3.1.6 Carbon Black

Carbon black are nanometric spheres or spherical fused agglomerates of low range ordered carbon. Carbon black can be obtained from incomplete combustion or pyrolysis. The particle size can range from 10 nm to 500 nm (see Fig. 3.6a), while agglomerates are typically 1 µm [44]. The structure is composed of small crystallite graphitic short-range order areas in a turbostratic order. Turbostratic is a type of crystalline structure where the fundamental graphene planes have slipped sideways relative to each other, causing the spacing between planes to be larger than ideal. In carbon black, the graphitic basal layers are oriented towards the particle surface. Carbon black has a high surface to volume ratio and can be used as an additive in rubber, paint, toners, and in the metallurgical industry. Carbon black is used as an additive to improve the electrical conductivity between active materials in lithium-ion batteries [45]. Carbon black increases the particle-particle contact and particle contact to current collector. Amorphous carbon, which must not be mistaken with carbon black, does not have the long-range crystalline order of the graphitic materials. Amorphous carbons have large variations in the interatomic distance and interbonding angles [28, 39].

There are several proposed mechanisms for carbon black formation [47]. However, there is some sort of scientific consensus on the carbon black formation. The process involves three stages.

1. Nucleation of precursors as the transformation from a molecular system to a particulate system occurs.
2. Aggregation of colliding particles produced by the nucleation to form larger spherical particles.
3. Agglomeration of spherical particles into chains or clusters.

[2] Heptagons can also create curvature in the hexagonal lattice

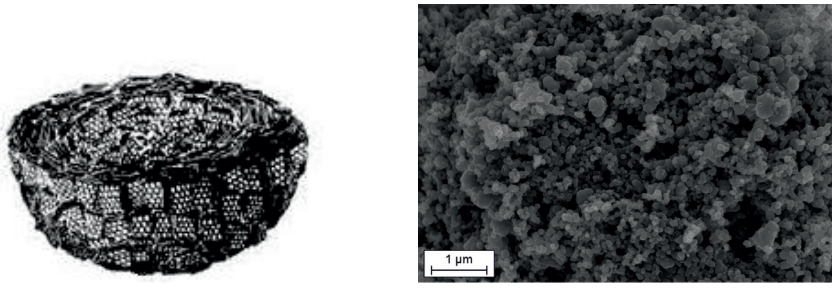

(a) (b)

Figure 3.6: a) A schematic cross section of a primary carbon black particle [46] b) and a FEGSEM picture of structured aggregates of fused primary carbon black particles produced in this project.

The first step is the least understood and of primary interest in this thesis as carbon cones are single particles. More information regarding the nucleation can be found elsewhere [47].

3.1.7 Carbon Cones

Carbon cones (CC) can be regarded as a distinct and unique type of carbon structure. It can be conceptualized by rolling a graphene layer into a conical shape, much like an ice-cream cone or conical Asian hat, see Fig. 3.7. The theoretical cone apex has a similar structure to a segment of a fullerene. The tip consists of one or several carbon pentagon rings in the hexagonal pattern. The cone wall is similar to the graphene layer, but it is in this case bent. The rehybridization will be stronger close to the apex as the cone radius decreases and the bending increases.

The concept of a cone structure made out of carbon has been known for quite some time. One of the first papers to discuss alternative planar or three-dimensional networks of carbon was published by Balaban *et al.* in 1968 [48]. The first visual observation came many years later, when Ge *et al.* [6] discovered carbon cones with an apex angle of $19° \pm 0.5°$. Three years later, in 1997, Krishnan *et al.* reported five distinct types of cones with different apex angles [7]. The very same carbon cones are studied in this work.

The cones have a hollow interior and a symmetry that is different from other carbon structures. The observed cones are piles of conical graphene sheets

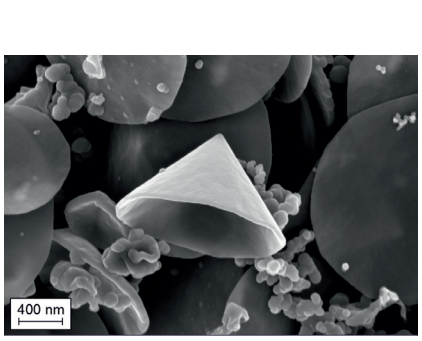

(a)

(b)

Figure 3.7: a) A FEGSEM image of a carbon cone provided by N-tec b) and a picture of the author wearing a traditional Asian conical hat.

stacked on top of each other.

It is possible to imagine a cone constructed by removing 60° sectors from a flat graphene sheet and joining the loose ends together. Since it is only possible to remove five sectors(60°, 120°, 180°, 240°, and 300°) it is possible to produce five different cones, see Fig. 3.8.

To solve the atomic arrangement problem that will naturally occur at the apex when the sheet is connected, the carbon atoms will form pentagons in the honeycomb network. This will result in σ-π rehybridization of the sp^2 bonds like in fullerenes. If one 60° sector is removed, the carbon structure will have one pentagon at the apex. If two 60° sectors are removed, the carbon structure will have two pentagons at the apex and so on. It is possible to see the different cone configurations in Fig. 3.9a and 3.9b.

The pentagon is regarded as a defect or fault in a flat hexagonal network. It is not possible to create a curved structure such as C_{60} from a pure hexagonal network without including pentagon rings. There is a mathematical relationship between the apex angle and the number of sectors left in the cone [49, 50]. See Fig. 3.10 and Eq. 3.4 - 3.7 for details. The apex angle α is given by equation 3.4.

$$\sin\left(\frac{\alpha}{2}\right) = \frac{r}{R}, \tag{3.4}$$

where r is the radius of the cone base and R is the slant height of the cone. The circumference (c) of the cone can be calculated from the following equation:

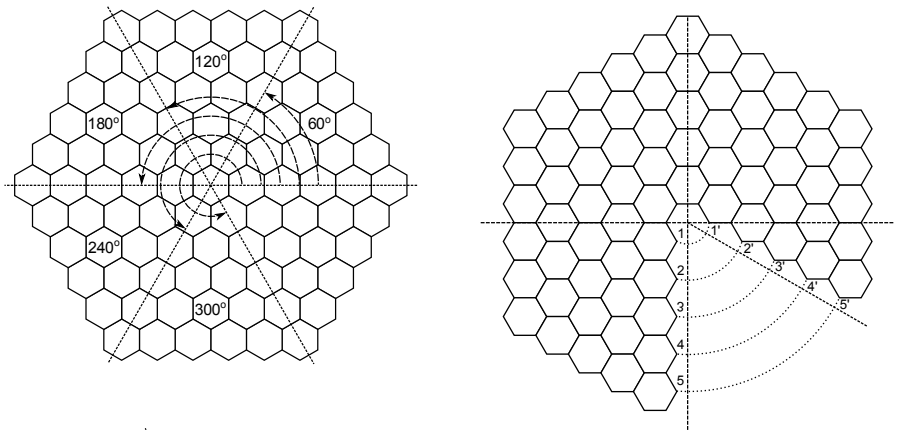

(a) (b)

Figure 3.8: a) Sections of the hexagonal pattern and b) imagined cone formation

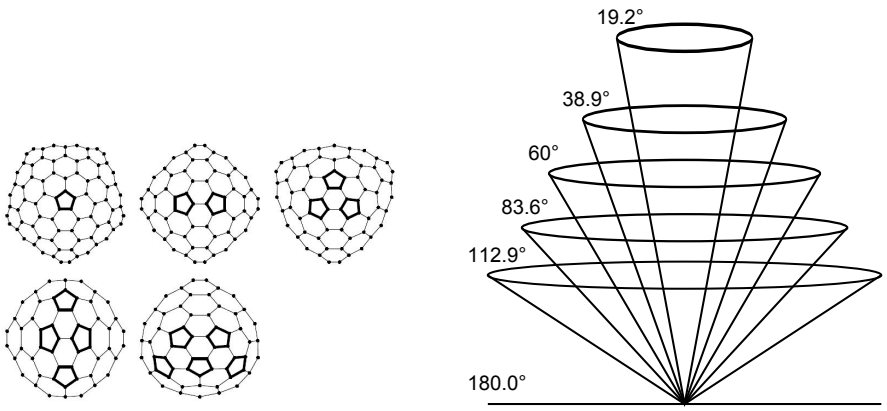

(a) (b)

Figure 3.9: a) The five different tip topologies of the most stable cones [49] b) and a schematic presentation of the different carbon cone apex angles [6].

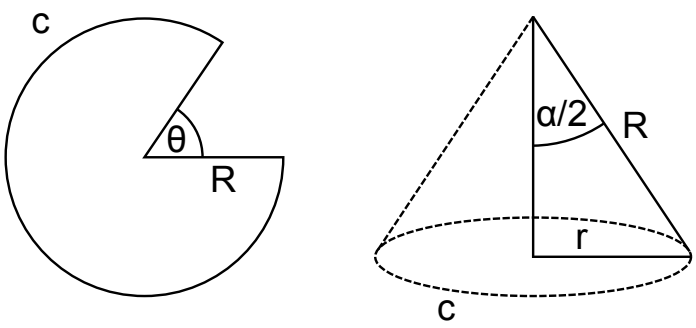

Figure 3.10: A schematic aid for the reader to understand the mathematical relationship of the cone parameters.

$$c = 2\pi r = 2\pi \left(1 - \frac{N_5}{6}\right) R, \tag{3.5}$$

where N_5 is the number of 60° sectors (θ) left in the graphene sheet or the number of pentagons in the cone structure. The radius of the cone base (r) is given by Eq. 3.6. By substituting this for r in Eq. 3.4, the angle α can be expressed merely in terms of N_5, as seen in Eq. 3.7.

$$r = \left(1 - \frac{N_5}{6}\right) R, \tag{3.6}$$

$$\sin\left(\frac{\alpha}{2}\right) = 1 - \frac{N_5}{6}. \tag{3.7}$$

Table 3.2 shows the apex angles and the disclination of the graphene sheet.

Table 3.2: Table of apex angles (α) and other geometrical parameters.

60° sectors	**Pentagons**	**Apex angle**	**Wedge**
1	1	19.2°	300°
2	2	38.9°	240°
3	3	60.0°	180°
4	4	83.6°	120°
5	5	112.9°	60°

The apex angle is the only theoretical angle possible with the introduction of pentagons in the graphite structure. This fact can be derived from Euler's Theorem [49]. The theorem states that the convex polyhedron with f faces, n vertices, e edges satisfies equation 3.8

$$f + n - e = 2 \tag{3.8}$$

By considering the symmetry of a graphene sheet and Euler's theorem, it can be shown that only five types of cones can be produced from a continuous sheet of graphene.

Some cones are observed with a different apex angle [7]. This can be explained with easy reasoning. The lose end of a graphene sector can be overlapped with the other part of the sheet.

There are several theories for the formation of fullerenes which can be adopted to the carbon cones. One of them are the so-called "pentagon-road" [51]. The "pentagon-road" model states that the dangling bonds energy at the edges of a flat graphene sheet is high. The dangling bonds can be regarded as open bonds of terminal carbon atoms. If the temperature is high enough and time is allowed for annealing, the structure will try to eliminate the dangling bonds and to reduce the circumference of the sheet by incorporating pentagons in the structure.

Another theory is the "ring-stacking" model. It is based on selective assembly of monocyclic carbon rings, where seeds or nuclei of pentagons or hexagons are connected [7].

The mechanism for the formation of the cones is not fully understood. However, it is possible to combine information from the recent articles and findings, to get a reasonably evident picture of the growth mechanism [52]. The cones that are produced by the pyrolytic Kværner carbon black and hydrogen process are believed to consist of stacked graphene cones with identical topologies. These carbon cones have a large amount of disordered carbon on the surface of the cone structure. It is reasonable to assume that the cones have a highly ordered core and a disordered outer shell.

3.1.8 Carbon Disks

The batch from the Kværner carbon black and hydrogen process also contains small disks of graphite. These are considered to be planar cones with an apex angle of 180° and therefore no pentagons are included in the structure. If the

graphene sheet has a pentagon in its structure, it is automatically a cone. It is also possible to find heptagons as a defect in carbon structures. The heptagon has the opposite effect of a pentagon. The heptagon will "open up" the structure. Other types of polygons have never been observed in graphene sheets [52].

Carbon disks are believed to be the most important constituent in the carbon cones material, as it is the most abundant. The disks can be regarded as flat cones without any pentagon carbon rings to make the essential defect for the cone structure. The disks size is somewhat bigger than for the cones. The disk thickness ranges from 5-6 nm to 60-70 nm. The diameter ranges from 0.5 µm to 4 µm [53]. The disks display six pairs of similar facets at the rim. Two interfacial angles ($\theta_1 = (22 \pm 1)^\circ$ and $\theta_2 = (60^\circ - \theta_1)$) are associated with the facets and the Miller indices of (100) and (210). The facets indicate a long range periodic structure [54].

3.1.9 Carbon Production in Hot Torch Plasma Reactor

The plasma reactor operates on principles similar to arc welding, where an electrical arc is struck between two electrodes. High energy arcs induce high temperatures through large resistive heating, which partly ionize the surrounding gas and thereby creating plasma gas. For the Kværner carbon black and hydrogen process, the gas is injected in between two concentric electrodes. The plasma gas is enclosed in the reactor chamber and controlled with magnetic coils due to its charged particles [55].

There is little knowledge on the mechanisms involved in the carbon cones production. The discussion (Section 6.1) in this study tries to shed some new light on the processes occurring during formation. Some of the important parameters are elucidated in the following section.

During reproduction trials, the oil derivate and the atomizing gas are preheated to achieve a better atomization of the oil through the nozzle. An efficient atomization is important as the starting material for these carbon structures are carbon atoms or small carbon-based compounds [47]. A large fraction of the energy used for heating, evaporating and converting the oil derivate comes from the plasma gas. If the oil derivate is preheated first, the required energy from the plasma gas is reduced and the process can therefore achieve a higher temperature inside the reactor chamber which is favorable for carbon production.

It is believed that the cones were only produced during a limited time. As the oil derivate was sprayed through the nozzle, some material deposited as coke on the inner reactor walls. The coke build-up filled certain sections and

lead to blocked pathways for the gas/particle flow. The product during these production conditions had a high content of carbon cones. Subsequently, the trial run was repeated with the same parameters, but the coke deposit was removed prior to the start-up. With these conditions, no carbon cones were produced. This fact shows the importance of finding the correct temperature profile and holding times.

A possible cone initiation could occur when the evaporated oil, diluted in hydrogen, flows into the reactor chamber and blends with large amounts of hot plasma gas before the mixture flows into the cooler and the filters. When the oil derivate aerosol reaches a hot zone, it decomposes before the carbon recombines into solid particles while the residual hydrogen forms hydrogen gas. The solid carbon is recycled if the particle size it to small for the filters. As the particle reenters the reactor, further carbon growth can take place [56].

Another idea for producing cones could be to insert a seed material into the reactor. The seed will act as a starting material for further cone growth. This can be achieved by heating up for instance anthracene or thiophene to its boiling point and leading the vapor into the reactor. The compounds can also be mixed directly with the oil derivate. Anthracene is a polycyclic aromatic hydrocarbon of three fused benzene rings, while Thiophene is a heterocyclic compound consisting of a flat five membered ring with one sulfur atom, see Fig. 3.11. A sulfur compound was chosen because sulfur is known to initiate structural defects in the hexagonal lattice of carbon [57]. Introduction of seeds can also be achieved by recycling the exhaust gases going out of the reactor, as mentioned above. The exhaust gas contains among other things several types of polyaromatic hydrocarbons [58].

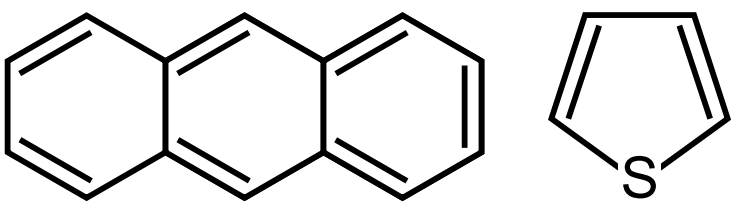

(a) (b)

Figure 3.11: a) Formula of anthracene and b) thiophene

3.1.10 The Pyrolysis Process

Pyrolysis is the process of thermally degrading hydrocarbons (organic compounds) to carbonaceous materials in the absence of air/oxygen [59]. It involves irreversible changes in both physical state and chemical composition, simultaneously.

For a pyrolysis process in a plasma reactor, the reaction is promoted by an external energy source (the plasma generator) rather than by the hydrocarbon combustion itself. Although the carbon formation mechanism is to some extent still a subject of dispute among researchers, it is possible to simplify the thermal decomposition of hydrocarbons down to two phases, namely cracking and synthesis [60], see Eq. 3.9 and 3.10, respectively.

$$\mathrm{C_nH_{2n+x}} + \text{Electrical Energy} \longrightarrow \mathrm{C_nH_a} + \frac{1}{2}(2\,\mathrm{n} + \mathrm{x} - \mathrm{a})\mathrm{H_2} \tag{3.9}$$

where $\mathrm{n} > \mathrm{a}$

$$\mathrm{C_nH_a} + \text{Electrical Energy} \longrightarrow \mathrm{nC} + \frac{\mathrm{a}}{2}\mathrm{H_2} \tag{3.10}$$

For carbon black, an important theory states that acetylene is an intermediate building block for carbon black formation. The formation can also arise from the formation of $\mathrm{C_nH_a}$ ions or radicals. This will lead to a polyaromatization and a dehydrogenation. Extremely small carbon particles will agglomerate to form larger carbon particles. All the familiar carbon black formation theories involve at least two main steps of initial formation and agglomeration. A combination of several theories might be necessary to achieve a more complete understanding [47].

It is natural to presume that the pyrolysis process of carbon cones is similar to that of carbon black, since the intention was originally to produce carbon black. However, larger graphitized particles of the cones indicate much higher temperature. In the case of the carbon cones production, the oil derivate was also decomposed through an intermediate of polyaromatic hydrocarbons [61].

3.1.11 Heat Treatment, Carbonization, and Graphitization

Heat treatment in an inert atmosphere decomposes organic compounds into carbonaceous residues (carbonization). The product depends on the original

texture of the starting material. For some materials, the carbonization process proceeds through an intermediate liquid phase or mesophase. Most of these materials become highly graphitic at heat treatment temperatures, typically between 1000 °C and 3000 °C. These carbons are often called "soft" carbons. They have highly anisotropic properties combined with low surface area and low porosity. Organic materials, which remains entirely in a solid phase during carbonization do not develop a significant degree of crystallization or graphite structure even at temperatures up to 3400 °C [62]. These non-graphitizing carbons are described as "hard" carbons. The hard carbons have isotropic properties, a significant surface area and high pore volume. The graphitization resistance is due to the tangled arrangement of the small crystallites. In short, the structure of the initial carbon material normally determines the properties of the graphitized material because of the thermally activated kinetic process of graphitization [44].

The solid state transformation process of changing thermodynamically unstable carbon into graphitic carbon by heat is called graphitization. Parameters such as surface area, surface heterogeneity, crystallite size and lattice spacing are all effected by graphitization. The process involves displacement and rearrangement of the carbon sheets to form a larger three-dimensional ordering. Graphitization is done by heat treatment, which is the controlled heating and cooling of a material to change its physical and mechanical properties. During the thermal process it is possible to remove defects such as heteroatoms, vacancies (Schottsky defects), and interstitial carbon atoms (Frenkel defect) by annealing [3].

An increase in the degree of crystallinity of a carbon material occurs when it is heat treated to a certain temperature. The process increases the ordering of carbon atoms in the carbon structure. The same phenomenon will occur for the original carbon cones samples and thereby radically change the fundamental morphology. It is possible to study these changes with Raman spectroscopy, electron microscopy, and X-ray diffraction techniques, to name a few. Heat treatment of carbon materials conducted at temperatures just over 1100 °C in an inert atmosphere has an effect on morphology [63]. Raising the temperature to 2700 °C or even higher has a powerful effect on the order of graphitic layers. In the presence of oxygen, some carbons start to gasify at temperatures as low as 400 °C [3].

In this study, heat treatment is utilized to relate the graphitization with battery performance. The thermal process is performed in a graphite induction furnace where residence time, desired temperature and argon atmosphere are kept constant.

3.2 Lithium-Ion Batteries

3.2.1 A Short Battery Introduction

A cell is the smallest electrochemical unit. The battery is a device consisting of one or several cells connected in parallel or in series. A complete battery also consists of a casing and contact terminals. Each cell can convert chemical energy to electrical energy. In a secondary cell this process can be reversed to convert electrical energy into chemical energy [27]. The conversion consists of a reduction-oxidation (redox) reaction which involves a transfer of electrons from one electrode to the other through an external circuit, which can be exploited as work. An electrode reaction involves a transfer of charge between the electrode and species in the electrolyte. The electrode reaction includes several steps; mass transport of reactants towards electrode/electrolyte interphase, electrons transfer between the electrode and reactant and product moving away from the electrode to permit new reactants to react with the electrode. The electrodes in a cell are the negative anode and the positive cathode.

Anode

The anode, or the negative electrode, gives up electrons as it is oxidized. A good anode should act as an efficient reducing agent. It should have a high coulombic output and good conductivity. It should also be easy and cheap to manufacture. The most used anodes for lithium-ion batteries are carbon-based materials. The ideal carbon material for lithium-ion batteries would have large specific capacity and low irreversible capacity. Irreversible capacity can be related to the specific surface area of the carbon material in addition to chemical reactions occurring between the anode surface and the electrolyte [64].

Cathode

The cathode or the positive electrode absorbs electrons as it is reduced. A good cathode should possess chemical stability towards the electrolyte. It should be an efficient oxidizing agent. The cathode should have a high voltage against the anode material. The most used and practical cathodes in lithium-ion batteries are lithium transition metal oxides.

Battery Components

Other major components in a cell are the electrolyte and the external cell casing (container and terminals). In many cell setups, there is also the need for separators, gaskets and spacers. Large battery packs and normally lithium-ion batteries also need internal circuitry to control the battery. The electrolyte is an ionic conductor which act as an ion transport medium between the electrodes. As an ionic conductor, the electrolyte has to be electronically insulating to prevent short circuiting of the cell. The electrolyte is usually an organic solvent with a dissolved salt. It can also be a solid, molten salt or polymer. The electrolyte should not react with the electrode materials nor change properties in the intended temperature range. A separator's main task is to physically separate the electrodes to prevent internal short circuiting, while allowing lithium ions to migrate through. The separator is typically made of a microporous polymer membrane.

Battery Requirements

A good battery should consists of an anode and a cathode material with a high potential difference. The battery should be light weight and have a high current capacity. For chemical and practical reasons lithium ion batteries are one of the most promising technologies. Lithium metal has a strong reduction potential. This means that only anhydrous materials can be used in the cell. Existing water will be reduced and create hydrogen gas. The electrolytes are therefore typically organic compounds with salt added to yield ionic conductivity.

Lithium ion batteries are classified as secondary (rechargeable) batteries in opposition to primary (non-rechargeable) lithium metal batteries. A secondary battery can be charged after discharge by sending current through the battery in the opposite direction to the discharge current. The energy density is typically lower for secondary batteries than for primary batteries, but secondary batteries have usually high power density, high discharge rate, flat discharge curves, and of course the ability to be recharged several times. Other important requirements are good cycle life, hence total energy throughput to end of life. The calender life which is the total time elapsed to end of life is also crucial.

Bucket/Water Analogy and Battery Conventions

It is possible to use a bucket and water analogy to understand different concepts of the working principles of a battery. The water can be thought of as electrons.

To explain the water/electrons, the current or flow of electrons can be regarded as the flow of water. The buckets will represent the battery or more specifically the electrodes. If a filled bucket, which is located above the an empty bucket, is poured into the one below, it is possible to extract work from this process. If the buckets are connected with a tube, the water pressure will be equivalent to the voltage. If the height difference is increased, the water pressure will increase. The application of voltage is the driving force for an electrode reaction. Voltage can be regarded as the energy required to move charge, see Eq. 3.11

$$V = Joule/Coulomb \tag{3.11}$$

The amount of work that is possible to extract depends on the size of the buckets and the difference of height. The amount of water or bucket size is equivalent to battery capacity. The amount of power which is possible to extract depends on the diameter of the tube. A wider diameter will let more water through the tube. This is equivalent to the rate of discharge for the battery or the speed at which energy can be extracted. Like the buckets can store water, the electrodes in a battery can store energy, see Fig. 3.12.

A common convention for the charging and discharging of batteries, is the term "C-rate" or "hourly rate". It is used as an alternative for current while referring to time or hours. The rate is often normalized with respect to the cell's full capacity and a desired time period. For example, the current to charge a 1 Ah cell from zero to full charge in 5 h is the C/5 rate or in this case a current of 0.2 A. The term is also applied to the discharge rate. C-rates are useful for comparing cells directly as it is not effected by the minor variations in the electrodes. Other essential battery conventions are given in Table 3.3. Some parameters are omitted or described elsewhere in the text.

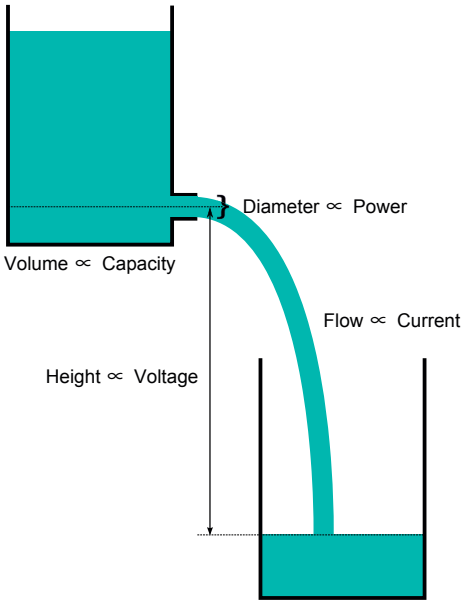

Figure 3.12: The bucket and water analogy

Table 3.3: Terminology and battery parameters

Parameter	**Explanation**	**Units**
Capacity	Amount of electrical charge	Ah
Current	Flow of electric charge	A
Voltage	Electrical potential difference	V
Power	Product of current and voltage	W
Energy	Work of a system over time	Wh
Energy Density	Energy/volume	Wh/l
Specific Energy	Energy/mass	Wh/kg
Coulombic Efficiency	Ratio between charge out and charge in	%
Cycle	A single charge and discharge	
Cycle life	Cycling time before the cell is unusable	
Open-Circuit Voltage	No load voltage	V

3.2.2 Operation Principles - Lithium-Ion Batteries

Both the anode and the cathode serve as a host for lithium ions. The lithium ions are incorporated as part of the positive and negative electrodes. The lithium ion sites in the host materials are at a different chemical potential. Energy can be extracted as the electrons move to a lower electrical potential while maintaining charge neutrality in the cell. The electrode materials are not consumed during the electron/ion exchange.

To clarify the role of the electrodes, it is important to mention that on discharge, the negative electrode is called the anode and the positive electrode is called the cathode. However, during charging the negative electrode is now referred to as the cathode, while the positive electrode is called the anode. The negative electrode is always labeled as the negative terminal and the positive electrode is always at the positive terminal. To ease the explanation below, a $LiCoO_2$/graphite cell is considered.

Charging

In the charging process, current is forced through the external circuit by a power supply in opposite direction compared to that of the discharge process. The voltage source must be higher than the equilibrium potentials of the two half cells. Oxidation takes place at the positive electrode and reduction takes place at the negative electrode. The charging is defined as an increase in voltage across the cell. Typical lithium-ion batteries with a carbon based anode and a lithium containing cathode are assembled in a discharged state. When a $LiCoO_2$/graphite cell is charged, lithium ions are transported from the $LiCoO_2$ electrode to the graphite electrode in an intercalation process. Intercalation will be treated in Section 3.2.6. In the case of carbon/lithium half-cells such as those used in this work, the cell is in a charged state when assembled, meaning that the charging is a delithiation process of the carbon.

Discharging

Discharge is defined as the process where there is a decrease in voltage. If the cell is connected to an external load, electrons will flow spontaneously from the anode (oxidation) and be accepted at the cathode (reduction). The charge neutrality is kept by the flow of lithium ions between the electrodes where lithium ions deintercalate from the graphite and intercalate into the $LiCoO_2$ structure. The discharge is a spontaneous process, which is controlled by diffusion and

driven by the thermodynamics of the cell (chemical potential). The shift observed between the discharge and charge voltage is due to the internal resistance of the cell, see for instance Fig. 5.38. For the carbon/lithium half-cells, the lithiation of carbon is a discharging process.

Cell Setup

It is important to notice that the cell studied in this work is a lithium/carbon half-cell, and not a complete cell consisting of for example $LiCoO_2$ and graphite. In other words, the carbon material has been cycled repeatedly against lithium metal. The focus has been on carbon materials and by testing half-cells, the experimental work has been simplified by eliminating several parameters. The charging and discharging principle for a lithium carbon half-cell is shown in Fig. 3.13. Notice that the lithium cations travel towards the carbon during discharge. In complete lithium-ion batteries the lithium cation travels towards the carbon during charge.

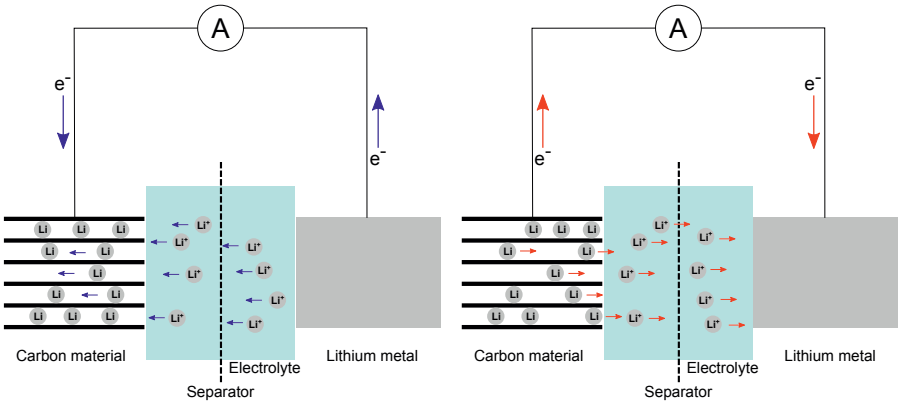

(a) Discharging (b) Charging

Figure 3.13: Carbon/lithium half-cell working principle.

3.2.3 Thermodynamic and Kinetic Considerations

To describe a battery system and its cell reaction, it is important to understand the fundamental parameters of thermodynamics and kinetics. As for many other systems, a battery can be in two different states. At equilibrium no current

flows around in the system and all reactions are balanced. The thermodynamic parameters describing this state will represent the maximum theoretical values of the cell. The kinetic parameters will appear when the cell reaction begins and the cell is no longer in equilibrium. The kinetics will interfere with the values given by the thermodynamic data. Mass transport of ions by diffusion or migration to the electrode surface and voltage drop caused by the current flow is included in the kinetics [65].

Thermodynamics of an Electrochemical Cell

The thermodynamic parameter entropy (S) is a measure of energy spread (disorder) in a chemical system. It can be defined in terms of heat and temperature, see Eq. 3.12.

$$\Delta S = \frac{\Delta Q}{T} \tag{3.12}$$

where ΔS is entropy change, ΔQ is the amount of energy and T is temperature.

The second law of thermodynamics states (Eq. 3.13) that the total entropy ($\Delta S_{universe}$) must increase for all real processes.

$$\Delta S_{\text{universe}} > 0 \tag{3.13}$$

The entropy of the universe can be divided into the entropy of a system and its surroundings, see Eq. 3.14

$$\Delta S_{\text{universe}} = \Delta S_{\text{system}} + \Delta S_{\text{surroundings}} \tag{3.14}$$

From Eq. 3.12, it is possible to derive Eq. 3.15.

$$\Delta S_{\text{surroundings}} = \frac{\text{Heat change of surroundings}}{T} \tag{3.15}$$

The heat change of the surroundings is the enthalpy change ($-\Delta H$) of the reaction at constant pressure. Enthalpy change is the release or absorbed heat. The total entropy is then:

$$\Delta S_{\text{universe}} = \Delta S_{\text{system}} - \frac{\Delta H}{T} \tag{3.16}$$

Eq. 3.16 can be regarded as the total spreading of energy as a result of a reaction at constant temperature and pressure. By multiplying Eq. 3.16 with $-T$, the following reaction is obtained, see Eq. 3.17.

$$-T\Delta S_{\text{universe}} = -T\Delta S_{\text{system}} + \Delta H \tag{3.17}$$

The first term $-T\Delta S_{universe}$ is the free energy change of the reaction. This expression is also called ΔG or Gibbs free energy, see Eq. 3.18.

$$\Delta G = \Delta H - T\Delta S_{\text{system}} \tag{3.18}$$

where T is temperature in K. A spontaneous reaction has a positive ΔS. This means that ΔG is negative if the enthalpy change is small. ΔG or Gibbs free energy can be regarded as the net amount of energy that can be used as work when the energy is spread out or as the maximum amount of work which can be extracted from a reaction.

When regarding an electrochemical system, the electrons in a cell have a lower potential energy at the cathode than at the anode. They lose energy over a potential difference. This change in energy can be extracted as work. The energy drop per charge is the voltage or electric potential (ΔE). To find the energy change, voltage is multiplied with the charge transferred.

$$\text{energy} = \text{voltage} \times \text{charge} \tag{3.19}$$

If one volt moves one mole of electrons the energy drop is 96485 J. This value can be used as a conversion factor, 96485 J/Vmol and is called Faraday's constant (F) [66]. If a voltage (ΔE) moves n moles of electrons, the expression above (Eq. 3.19) becomes:

$$\text{energy drop} = nF\Delta E \tag{3.20}$$

The energy drop represents the maximum amount of work a cell can do. The maximum amount of work for a reaction is given by $-\Delta G$ and since an electrochemical cell is in fact a redox reaction, the following relationship is obtained.

$$\Delta G = -nF\Delta E \tag{3.21}$$

where n is the number electrons involved in the stoichiometric cell reaction. A redox reaction with a positive ΔE is spontaneous. ΔE becomes a direct measurement of ΔG. The free energy (ΔG) can be harnessed as the push of electrons

through a wire. ΔG describes the maximum amount of chemical energy which can be converted to electrical energy. Therefore, a direct measurement of a cell's potential is a direct measurement of Gibbs free energy. The maximum amount of electrical energy delivered from an electrochemical cell that is stored or supplied by the electrodes depends on the change in free energy ΔG in the electrochemical reaction. The change in free energy ΔG of a cell is the driving force which enables the battery to deliver electrons to an external circuit.

The other thermodynamic parameters for an electrochemical cell in equilibrium are:

- Enthalpy of reaction ΔH
- Entropy of reaction ΔS

ΔH represents the amount of energy released or absorbed. It is the maximum heat generation if all the electrochemical energy is converted to heat. ΔS is the reversible energy loss/gain connected with the electrochemical reaction. The product of the temperature and the entropy is the reversible amount of heat consumed or released during the reaction. The relation between these parameter are described in Eq. 3.18.

The changes in entropy can also be expressed in terms of pressure, and entropy obeys the following equation,

$$\Delta S = R \ln \frac{P_0}{P} \tag{3.22}$$

By combining Eq. 3.22, 3.18, and 3.21, it is possible to derive the Nernst equation, see Eq. 3.23.

$$E = E^0 - \frac{RT}{nF} \ln \frac{\prod (a_i)^j_{react}}{\prod (a_i)^j_{prod}} \tag{3.23}$$

where a_i is the activity of component i, j is the number of equivalents of component i in the reaction, R is the molar gas constant for an ideal gas (8.314472 J/Kmol [66]), E is the measured voltage, E^0 is the voltage at standard conditions, and *react* and *prod* are abbreviations for reactants and products [65]. With the Nernst equation it is possible to determine the voltage effect of changing concentrations, pressure and temperature. Concentrations and pressure can be substituted with the activities given in Eq. 3.23.

The derived voltage from the thermodynamic calculations are based on the voltage difference between two electrodes. The absolute potential between an electrode and the electrolyte is not possible to measure because the electrolyte is not an electronic conductor. The use of a reference electrode is therefore necessary. To achieve a basis for the electrode potential for various electrode materials in lithium-ion batteries, lithium metal is used as a reference electrode.

Chemical Potential in Lithium Carbon Half-Cells

Chemical potential (μ) can be regarded as a force causing changes in chemical systems. It is refereed to as partial molar Gibbs energy and it is measured in energy per particle or (J/mol). Under ideal conditions, laboratory experiments are often performed under constant temperature and pressure. The chemical potential can therefore be given as the partial derivative of Gibbs energy.

$$\mu_i = \left(\frac{\partial G}{\partial N_i}\right)_{T,p,N_{j\neq i}} \tag{3.24}$$

In general, species (or here electrons) move from a higher chemical potential to a lower chemical potential. The composition of lithium is set, and therefore its chemical potential is constant [67]. All changes in the cell's voltage is therefore due to changes in the carbon as long as the temperature and pressure are fixed. These changes may be reduction of surface groups, exfoliation, formation of SEI, and intercalation. However, both temperature and pressure might change during charge/discharge, which makes the potential difficult to predict. A slow drift in the open circuit voltage (OCV) might be due to small side reactions and solid state diffusion of lithium ions in the intercalation host material as the equilibrium has not been reached [68]. OCV for a half-cell of graphitic Li_xC_6 against lithium metal is a direct measurement of the difference in chemical potential for a lithium atom in the metal and in the graphite. The chemical potential of lithium atoms depends on the local chemical environment at the atomic scale. The cell voltage is a function of the difference in chemical potential between the electrodes. Equilibrium OCV (E) is the difference in chemical potential of lithium ions in the anode and in the cathode.

$$E = \frac{\mu_{Li(C)} - \mu_{Li(A)}}{F} \tag{3.25}$$

The chemical potentials of lithium in coexisting graphite intercalation compound (GIC) phases are equal. The coexisting phases will therefore create

plateaus in the voltage versus capacity plots. Lithium ions remain in the graphite when the cell is fully charged because it is energetically favorable for Li ions to stay inside a host material rather than on the surface deposited as lithium metal.

In electrochemistry, the term electrochemical potential is also used. It characterizes all the influences on a charge species motion including electric potential [69].

Kinetics of an Electrochemical Cell

As soon as the current starts to flow in a cell, the situation changes [65]. The cell reaction has to occur at a corresponding rate given by Faradays law, see Eq. 3.26, which states that

$$m = \frac{Q}{F}\frac{M}{z} \tag{3.26}$$

where m is the mass of the altered electrode in grams, Q is the total electric charge passed through the electrode, F is the Faraday constant, M is the molar mass of the electrode, and z is the electrons transferred per ion.

The electron transfer occurs in one direction and the mass transport needs to move the reacting substances to and from the electrode surfaces. To obtain this current flow, extra energy is needed, which results in a difference between the voltage at equilibrium and the voltage at a current flow. The change in voltage incorporates several factors, including overvoltage which is caused by electrochemical reactions and concentration changes due to transport phenomena. At the same time, the ohmic voltage drops caused by the electronic and ionic current in the electronically conducting part of the cell and the electrolyte, respectively. The sum of these factors are called polarization. In an electrochemical reaction, the reaction path normally consists of several reaction steps, also including the charge transfer. The slowest reaction step will be decisive for the total reaction. Overvoltages and limiting reaction rates are caused by the slowest reaction step. Migration and diffusion of lithium cations are important kinetic parameters in lithium-ion batteries and these are often slow processes compared to electron transfer.

3.2.4 Lithium-Ion Battery Technology Compared to Other Secondary Batteries

Rechargeable batteries are used in a wide range of applications such as consumer electronic devices (tools, PCs, toys, mobile telephones, cameras, camcorders, MP3-players, GPS devices, etc.) and electric vehicles. The different battery technologies are almost as plentiful as its applications. However, there are a few technologies which have been more popular due to desired properties.

In a rechargeable battery, the transformation of the chemical energy to electrical energy and back again should proceed reversibly, as well as being energy effective and cause little physical change in the electrodes. Unwanted side reactions should be minimal. The chemical environment inside a cell can cause deterioration of its components, loss of life and loss of capacity. Low internal resistance and good performance over a wide temperature range is also desired. With these requirements, only a limited number of materials are suitable to be employed in rechargeable batteries.

Lithium-ion batteries now possess over half of the worlds market in secondary batteries. Commercial lithium-ion cells have high specific energy (150 Wh/kg) and high energy density (400 Wh/l) [27]. These high values make this technology very attractive for products that are sensitive to volume and weight. Lithium-ion batteries have a very low self-discharge rate of typically 2 % - 8 % per month depending on the technology. The cycle life exceeds that of many other types of batteries and can easily last over 1000 cycles. A relative broad temperature range of operation is also one of the features for this type of battery, however this depends heavily on the specific lithium-ion technology. A single cell usually operate between 2.5 V to 4.2 V. This is three times the voltage of competitive technologies such as NiCd and NiMH, this means that fewer cells are needed in order to power the same application. The rate capability is also particularly high, allowing continuous discharge rates at 5C and pulse discharge rates at 25C [27].

Several designs are available, such as spiral wound cylindrical, wound prismatic, flat plate prismatic, and coin cells, the latter, which are used in this work. Commercial cells can range from small 0.1 Ah cells to large 160 Ah cells [27] .

Table 3.4 summarizes the advantages and the disadvantages of lithium-ion batteries relative to other existing technologies.

A limiting feature of the lithium-ion batteries, is that they degrade if they are discharged below 2 V. The cells might also vent when being overcharged as they do not have a chemical mechanism to avoid overcharging. Therefore, the bat-

Table 3.4: Advantages and disadvantages of lithium-ion batteries

Advantages	**Disadvantages**
High specific energy (Wh/g)	Moderate, but decreasing cost
High energy density (Wh/l)	Unstable at high temperatures
Wide temperature range	Battery management circuits
Long shelf life	Thermal runaway if misused
Low discharge rate	Capacity loss if overcharged
Rapid charge capability	Possible gas formation
High rate capability	
High power discharge capability	
Low maintenance (Sealed cells)	
High coulombic and energy efficiency	
Long cycle life	
No memory effect	

teries need external circuitry to manage these problems. Battery management circuits are necessary to control the cell and avoid overcharge/overdischarge. The battery management circuits can also provide information regarding state of charge and safety precautions.

Lithium-ion batteries can also degrade and permanently lose capacity at elevated temperatures (65 °C) due to the chemically instable $LiPF_6$-salt and lithium metal oxide cathodes. Low temperatures can deteriorate cell performance by retardation of the lithium ion transport within the cells [70].

3.2.5 Negative Electrodes

Initially lithium metal was used as the negative electrode material due to its high specific capacity and highly negative reduction potential. However, during cycling dendrites may grow on the lithium surface and lead to short circuiting in the cell. These cells therefore had a very short life time and constituted a potential danger such as thermal runaway [3]. Intercalation compounds of carbon (see Section 3.2.6) became interesting for researchers as these materials are close to the lithium potential and do not involve the same dangers for the end users. The intercalation compound is less exposed to dendrite formation, compared to metallic lithium, as lithium is entrapped in between the carbon atoms, hence making it safer.

[3] Thermal runaway is explained in Section 3.2.12

Carbon

Carbon is the most used material for negative electrodes. The theoretical capacity of carbon (LiC_6) is 372 mAh/g. Although this is an order of magnitude lower than lithium metal (3860 mAh/g), carbon has the ability to be cycled efficiently. A wide variety of carbons are today utilized as anode material for lithium-ion batteries. In the beginning, petroleum coke was used, and coke-based materials had a capacity of 180 mAh/g [27]. Later on, graphitic spheres such as Mesocarbon Microbeads (MCMB) were employed into lithium-ion batteries. MCMBs have a specific capacity of 300 mAh/g. MCMBs also offer a low irreversible capacity loss due to low specific surface area. Other carbons used in lithium-ion batteries are low cost natural graphite and high capacity hard carbon materials. As explained in section 3.1, there is a large variety of carbon materials. For lithium-ion battery purposes, they can be divided into two main categories, as shown in Table 3.5

Table 3.5: Different carbon materials for the lithium-ion battery.

Graphitic Carbons	**Non-Graphitic Carbons**
Natural graphite	Activated carbons
Synthetic graphite	Glassy carbon
Flakes	Amorphous carbons
Microbeads	Cokes
Fibers	Carbon blacks
Whiskers	

Types of carbon materials specifically used in lithium-ion batteries [71]:

1. Highly Oriented Pyrolytic Graphite (HOPG)
2. Natural graphite
3. Synthetic graphite
4. Hard carbon
5. Mesophase low temperature fibers and mesocarbon microbead (MCMB) carbons

The structure of carbon dictates the electrochemical properties such as potential and capacity. The basic building blocks of graphite consists of planar sheets (graphene) in a hexagonal pattern stacked on top of each other, as mentioned in section 3.1.2. In hexagonal graphite, the layers are stacked in ABAB

order, see Fig. 3.14b. The less common rhombohedral graphite is stacked in an ABCABC order. Rhombohedral graphite shows a higher specific capacity than hexagonal graphite. It is believed that the rhombohedral graphite prevents exfoliation of the carbon layers. A combination of both graphite structures also produces more defects at the grain boundaries where lithium can be stored [72, 73]. Graphites may contain random stacking and a mix of these structures. The layers do not have to be parallel, but they can be rotated or shifted (turbostatic structure). The morphologies can be very diverse, ranging from flat plates, to fibers or spheres. Graphite in general is discussed more closely in Section 3.1.2.

Silicon

Silicon has in recent years been heavily studied as an anode material for lithium-ion batteries. Silicon can store large amounts of lithium as it forms a Li-Si alloy [74]. The capacity is ten times higher than for carbon. However, there are several issues that need to be resolved before it can be successfully commercialized. Silicon has a relatively low voltage compared to carbon. During the alloy formation, silicon undergoes a volume increase leading to an enormous strain which again leads to decrepitation. The latter problem can be solved by producing nanoparticles or nanowires as they do not undergo decrepitation and cracking. Nevertheless, if the anode capacity is successfully increased by tenfold, the total capacity (mAh/g) of a complete cell will only increase by 35 %. For a complete battery with casing, terminals, and circuitry, the capacity increase will be even lower. This is attributed to the fact that the cell is cathode-limited. The practical capacity of $LiCoO_2$ is typically 140 mAh/g [75], while the completely lithiated state of silicon ($Li_{21}Si_5$) has a theoretical capacity of 4010 mAh/g [76].

Table 3.6 shows the advantages and disadvantages of different anode materials.

Table 3.6: Type of anode materials

Type	**Example**	**Advantage**	**Disadvantage**
Intercalation	Graphite, carbon	Small volume and structural changes	Small capacity
Li-Alloy	Al, Si, Sn	Large capacity	Large volume and structural changes
Displacement Reaction	CoO, CuO	Large capacity	Large volume and structural changes

3.2.6 Intercalation

Intercalation[4] is the reversible process of introducing atoms, ions, or molecules in between the structural layers of a highly anisotropic host material [77–79]. Typically, layered solids can intercalate various guest species (intercalant). The intercalants can be both Lewis bases (electron donors) or Lewis acids (electron acceptors). The electronic properties of the host material changes drastically as an effect of the intercalant interaction with the host material. Intercalated compounds are rarely stable in air.

Carbon materials such as graphite are ideal host materials because of the repetitive graphene sheet structure. Graphite intercalation compounds (GIC) are complex structures with the general formula YC_x where Y is the element inserted into the carbon material and x represents the number of carbon (C) atoms. Many GICs have a high electrical conductivity, which allows for fast charge transfer during electrochemical reactions [33]. This can be employed in electrochemical cells.

In lithium-ion batteries, lithium ions act as the guest species. Intercalation occurs at both electrodes and the insertion and removal of lithium ions are not detrimental to the host material's structure. Since the process is reversible, the lithium ion batteries can be charged and discharged many times as the ions move in and out of the electrodes [80]. For the graphite anodes, the lithium carbon intercalation reaction is given below where x is a factor between 0 and 1:

$$6\,\mathrm{C} + \mathrm{xLi}^+ + \mathrm{xe}^- \rightleftharpoons \mathrm{Li_xC_6} \tag{3.27}$$

When the carbon material is electrochemically reduced, lithium ions from the electrolyte approach the carbon surface where there is a charge transfer. The intercalation proceeds at the edge plane on the armchair or zigzag faces of the carbon material. Intercalation through the basal plane is not possible unless there are defect sites available. The lithium enters between the planes and intercalates parallel to the basal plane. The lithium atoms settle in the center of the hexagonal carbon rings. At atmospheric pressure, the intercalation occurs till there is one lithium atom to six carbon atoms, see Fig. 3.14a. In graphite, there is a small volume change (10.7 % along the c-axis) as the electrode reaches its fully intercalated state [80].

[4] The author tries to distinguish between intercalation and insertion. Intercalation is explained on this page, while insertion is mainly used for the formation of the lithium-rich disordered carbon. Lithiation is a collective term for both processes. The same distinctions are given for deintercalation, deinsertion, and delithiation.

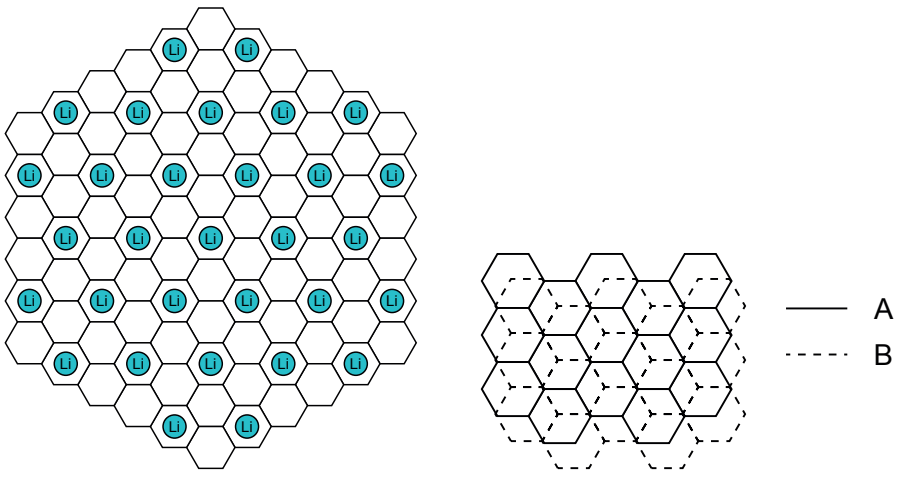

Figure 3.14: a) The basal plane of the LiC_6 and b) the ABAB stacking sequence of hexagonal graphite.

During the lithium intercalation into carbon, carbon transforms from ABAB (hexagonal) or ABCABC (rhombohedral) stacking sequence to AAAA stacking sequence [81]. This is a process which requires some energy and contributes to an energy conversion efficiency of below 100 %. The lithium atoms will have an $\alpha\alpha$ stacking order in the intercalation compound and a Li-C_6-Li-C_6-chain along the c-axis is created.

A characteristic feature of the GIC is the staging phenomenon by a periodic ordering of intercalant layers between the graphene/graphite layers [33]. The stage-1 compound has a layer of lithium between every graphene sheet and has a stoichiometric formula of LiC_6. In general, stage-n has lithium layers between every n graphene sheet, see Fig. 3.15a. The figure shows that the lithium atoms agglomerate between the carbon layers rather than distribute evenly. The stepwise process is a staging phenomena which can be observed in XRD and in galvanostatic measurements [82]. The Daumas-Herold model explains the transformation between the different stages, see Fig. 3.15b [83]. The stoichiometric relationship between the different stages are given below [80].

$$2\,\mathrm{LiC_6} \overset{\text{Stage}-1}{\rightleftharpoons} \mathrm{Li} + \mathrm{LiC_{12}}$$

$$3\,\mathrm{LiC_{12}} \overset{\text{Stage}-2}{\rightleftharpoons} \mathrm{Li} + 2\,\mathrm{LiC_{18}}$$

$$3\,\mathrm{LiC_{18}} \overset{\text{Stage}-3}{\rightleftharpoons} \mathrm{Li} + 2\,\mathrm{LiC_{27}}$$

$$4\,\mathrm{LiC_{27}} \overset{\text{Stage}-4}{\rightleftharpoons} \mathrm{Li} + 3\,\mathrm{LiC_{36}}$$

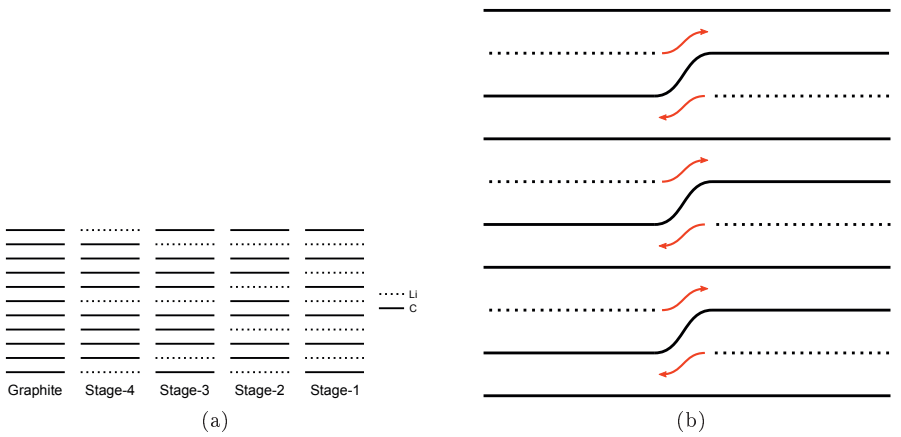

Figure 3.15: a)A simplified representation of the intercalation stages in graphite. The stage number represent the number of graphene layers between the lithium layers. b) The formation of a stage-1 GIC from a stage-2 GIC with the Daumas-Herold mechanism.

The existence of non-stoichiometric GIC has been shown [84, 85]. One of these non-stoichiometric GIC is the dilute stage-1 compound. Here, the lithium atom randomly occupies sites between the graphene layers. With non-stoichiometric GIC liquid-type stage-2 compounds there are no long range ordering between the lithium atoms, but the compound has the nominal composition of $\mathrm{LiC_{18}}$.

By utilizing galvanostatic measurements, the stepwise process can be observed as voltage plateaus as the transformation from one stage to another occurs, as shown in for instance Fig. 5.50. The plateaus show the coexistence

of two phases [80], where the most lithium rich stage is formed at low voltage. There are no plateaus for disordered carbon as there are no intercalation processes occurring [86]. Insertion of lithium ions into disordered carbon takes place as adsorption on both sides of the graphene layer and on their edges [87].

3.2.7 Positive Electrodes

The cathode material acts as a host for lithium ions. The positive electrode material in lithium-ion batteries consists mainly of a lithiated metal oxide as the active material. The materials used are normally layered metal oxides such as spinels or olivines. Common for all structures is that they allow for extraction and insertion of lithium ions. Requirements for positive electrode materials are summarized below.

- Can store large amount of lithium
- High potential relative to lithium
- Good reversibility of lithium ions in and out of structure
- Stability
- Good lithium ion diffusivity
- Good electronic conductivity
- Do not dissolve in electrolyte
- Inexpensive reagents
- Easy synthesis

One type of layered metal oxide has the general formula $LiMO_2$ where M is a transition metal. In the layered structure, the Li^+ and M^{3+} cations occupy every second plane(111) of the layered rock-salt structure. This yields a sequence of -O-Li-O-M-O- on the c-axis [75]. Since the commercialization of the lithium-ion batteries by Sony in 1991, the most common positive electrode material has been $LiCoO_2$ due to its high operation potential, good cycle life, and ease of synthesis [88]. An irreversible phase transition occurs at $x<0.5$ in Li_xCoO_2 limiting the capacity of $LiCoO_2$ to approximately 140 mAh/g. The Li_xCoO_2 structure becomes more unstable as the lithium ions are extracted [89]. The

structure can be seen in Fig. 3.16a. The electrode reaction for the $LiCoO_2$ is given in Eq. 3.28.

$$LiCoO_2 \rightleftharpoons Li_xCoO_2 + (1-x)Li^+ + (1-x)e^- \tag{3.28}$$

Oxides with the general formula LiM_2O_4 form the spinel crystal structure. The structure offers great stability as the lithium ions can be extracted without the collapse of the spinel framework. The crystal arrangement at the edges provides a good electrical conductivity compared to other cathode materials. Empty sites in the three-dimensional structure accommodate for a fairly good lithium ion conductivity. For economical and environmental reasons, $LiMn_2O_4$ is a good alternative to the layered oxides. However, spinel structures have slightly lower energy density compared to the layered structures, but the voltage is relatively high, 4.0 V vs. Li/Li^+. The $LiMn_2O_4$ crystal structure can be seen in Fig. 3.16b.

The olivine structure can act as a lithium extraction and insertion host combined with a carbon anode. The general formula is $LiMPO_4$ which can be seen in Fig. 3.16c for M = Fe. Olivines have approximately half the energy density compared to layered compounds. Nevertheless, the $LiFePO_4$ structure has been extensively studied due to the abundance of iron, low cost, and environmentally friendly properties [75]. The olivine $LiFePO_4$ has the advantage that it can not be overcharged and therefore show good safety characteristics. The major drawbacks are low operating voltage, low theoretical capacity, and low crystallographic density.

Some polyanion-containing frameworks can accept two lithium ions per transition metal atom. A class of silicates (Li_2MSiO_4) has this property and it can therefore achieve higher capacities and energy densities (Theoretical capacity of the approximately 330 mAh/g). Li_2FeSiO_4 has shown promising characteristics, especially for stable cycle life. However, these silicates suffer from poor electronic conductivity and slow reaction kinetics. The crystalline structure can be seen in Fig. 3.16d. Nanostructuring of the materials, for instance produced by the sol-gel route, may help overcome these problems. Coating with a highly conductive material such as carbon is another solution [90].

As well as for the anodes, the cathode needs various additives to perform well. The positive electrode consists of a binder and usually an electronic conducting material. The binder is typically polyvinylidene fluoride (PVDF) and the conducting material is carbon black.

In general, the challenges which must be overcome for alternative positive electrode materials are among others to reduce high material costs, avoid

exothermic decomposition (safety issues), reduce toxicity, and last but not least to improve capacity.

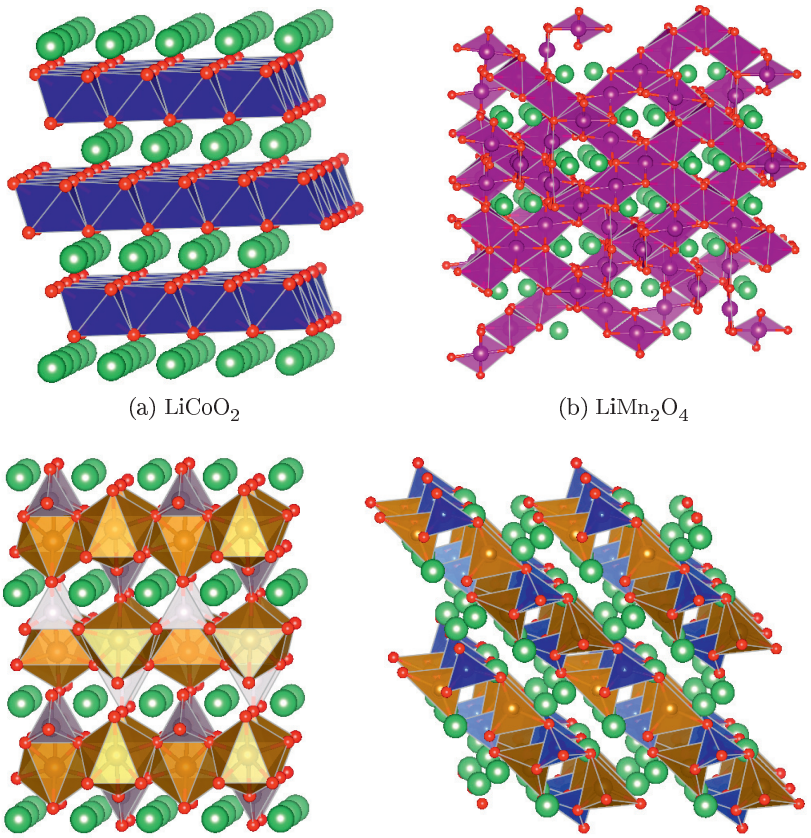

(a) $LiCoO_2$ (b) $LiMn_2O_4$

(c) $LiFePO_4$ (d) Li_2FeSiO_4

Figure 3.16: Crystal structures of typical positive materials for lithium-ion batteries [91].

The most common cathode materials are summarized in Table 3.7.

Table 3.7: Type of cathode materials

Type	Example	Insertion dimension
Layered Compounds	$LiCoO_2$, $LiNiO_2$, $LiTiS_2$	2D
Spinels	$LiMn_2O_4$, $LiTi_2S_4$	3D
Olivines	$LiFePO_4$	1D

3.2.8 Other Electrode Components

Binder

The binder is used to keep the structural integrity of the electrode and ensure proper adhesion to the current collector. By doing so, it also contributes in maintaining the capacity and cycleability of the cell. It has to form a network between the particles of the active material and the conductive additives. It also has to accommodate for electronic and ionic transport. The binder needs to be flexible in order to facilitate volume changes in the electrode material during charge and discharge. The binder also needs to be uniformly distributed in the finished electrode in order to prevent large agglomerates of binder that could hinder electron and ion diffusion [92]. In addition, thermal stability and consequently safety behavior of lithium-ion cells are influenced by the binder [93]. Polyvinylidene fluoride (PVDF) is the most common binder material for commercial lithium-ion batteries. PVDF polymer chains can be branched and have a broad molecular weight distribution. This polymer is soluble in 1-methyl-2-pyrrolidinone (NMP) [94] and is stable at high voltages. PVDF is also electrochemically stable in contact with the electrolyte mixtures used in lithium-ion batteries. A well-known drawback with fluorinated hydrocarbons like PVDF is its impact on the environment. Fluorinated hydrocarbons are known for the depletion of the ozone layer. PVDF is nondegradable in nature and alternatives are therefore desirable [45].

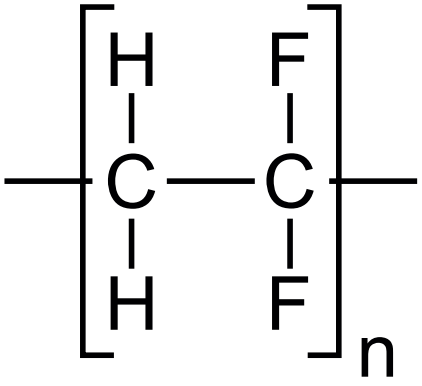

(a)

(b)

Figure 3.17: a) The -(CH2-CF2)- monomer of PVDF b) and as powder.

Conductive Additives

Conductive additives are necessary to ensure electronic conductivity between the active particles in the electrode. Carbon black is mostly used due to its low cost, low weight and good conductivity. Carbon fibers and nanotubes are used in high performance cells. For typical cathode materials, like lithium metal oxides, a large amount of conductive additives is needed as the cathode often is a poor electronic conductor. Carbon based anodes need less additives due to their intrinsic electronic conductivity. In combination with the binder and the active material, these components determine the porosity of the electrode and the electrolyte penetration depth. The conductive additives can also contribute to enhanced wetting of the electrode.

Current Collector

Current collectors, such as copper and aluminum, must be electrochemical inert in the potential window of operation for its corresponding electrode. Corrosion should be avoided as it results in a gradual increase in the internal cell resistance which again leads to capacity fade. Safety may also be affected as current collector corrosion can induce short-circuiting. The formation of a protective passive layer is important for ensuring a good overall battery performance. The current collectors should be as thin as practically possible to allow more active material in the cell and to reduce the cell weight [95].

3.2.9 Electrolyte

General considerations

In electrochemical cells, the electrolyte will conduct charge as free ions which are transported between the electrodes. A wide range electrolytes for lithium-ion batteries are available [70, 96]. They can be divided into the following categories [76]:

- Organic liquid electrolytes
- Ionic liquids
- Inorganic liquid electrolytes
- Solid polymer electrolytes
- Inorganic solid electrolytes
- Hybrid electrolyte systems

In general, electrolytes for lithium-ion batteries have a certain set of desired properties:

- High lithium ion conductivity
- Wide electrochemical window of stability
- Retention of electrode/electrolyte interphase
- Chemical stability
- Safety (nonflammable)

Organic Liquid Electrolytes

The most used electrolytes are an ion-conducting solution which is made up of a liquid organic solvent and a lithium-based salt [97]. These electrolytes can have a large liquid temperature range between -50 °C to above 300 °C. They also have a stable voltage window of more than 5 V. It is required that the electrolyte has a minimum conductivity of 10^{-3} mS/cm.

Different alkyl carbonates are often used as solvents as they have aprotic and polar properties. Ethylene carbonate (EC), diethyl carbonate (DEC), dimethyl carbonate (DMC), propylene carbonate (PC), and ethylmethyl carbonate (EMC) are among the most common. A high dielectric constant to

dissolve and dissociate the electrolyte salt is necessary [98]. The alkyl carbonates are reasonably good solvents for lithium salts and their low viscosity facilitates lithium ion diffusion. Several solvents can be used at the same time to increase the cell performance, often providing a higher conductivity and a broader temperature range. Ethylene carbonate (EC) promotes formation of the solid electrolyte interphase on the carbon surface, which will increase the kinetic stability [99]. Carbonates are stable in a wide potential window (1.3 V - 4.5 V vs. Li for 1 mol/L $LiPF_6$ in EC:DEC(1:1) [100,101]).

Many lithium salts have been investigated [70], but in many aspects $LiPF_6$ is the preferred salt. A commonly used electrolyte composition is $LiPF_6$ salt in a mixture of ethylene carbonate and diethyl carbonate. This mixture has a high ionic conductivity (above 10^{-3} S/cm) and high lithium ion transference number ($\approx$0.4) [102]. However, $LiPF_6$ is expensive and it yields hydrofluoric acid (HF) upon reaction with water.

The main drawbacks of the organic liquid electrolytes are their high cost, environmental issues and flammability. Also, their behavior at high and low temperature is not optimal. A wide temperature range effects the conductivity, wetting of the electrode, and viscosity. At elevated temperatures the electrode material can react with the electrolyte. During high current discharge the electrolyte should not contribute to resistive heating or voltage loss. The ideal electrolyte possesses many properties which cannot be fulfilled simultaneously, but good approximations can be achieved by using mixtures of different solvents and salts. Due to the liquid state, leakage can occur, leading to safety and performance concerns.

Electrolyte Additives

Different compounds can be added in small amounts to the electrolyte with the purpose of improving its properties [70]. The additives, such as vinylene carbonate (VC), do not alter the principal properties of the electrolyte. Additives can function as:

- overcharge protection
- wetting compound
- flame retardation
- trap for undesired components
- improvement of conductivity

- control of SEI formation

3.2.10 Separator

The separator does not actively participate in the electrochemical reaction, but it serves two primary functions in a battery. It physically separates the positive and negative electrode in order to prevent direct contact and short circuiting. The second function is to permit ionic current with minimal hindrance. As these requirements are conflicting, a compromise in the form of a porous nonconductor is needed. An ideal separator is electronically insulating and does not decrease the intrinsic ion mobility of the electrolyte. Other important properties for a good separator are listed below [103].

- Sufficient strength and stability to allow handling.
- Resistant to degradation in an electrochemical environment
- Prevent penetration of particles
- No shrinking or yielding
- Stable for many years and over a wide temperature range
- Easily wetted by electrolyte
- Uniformity
- Pore size less than 1 µm

To achieve these properties a porous polymer membrane is commonly used. It typically has a thickness of 25 µm, nano-sized pores below 100 nm, and a porosity of approximately 40 %. Some membranes have a three layered polypropylene/polyethylene/polypropylene structure. A clever feature of separators containing polyethylene (PE) is their low melting temperature. At 135 °C PE melts and loses its porosity. This prevents the cell from working and thereby works as a safety precausion inhibiting thermal runaways. Selection of the correct type of separator is important for high power cells.

3.2.11 Solid Electrolyte Interphase

The solid electrolyte interphase (SEI) is a passivation layer created mainly on the anode side of the lithium-ion battery as a result of electrolyte decomposing at the electrode surface, see Fig. 3.18. The formation occurs first and foremost

during the first few charge/discharge cycles. However, additional growth can occur dependent on both system chemistry and temperature [104]. The features of the SEI is crucial for many battery characteristics. These characteristics include irreversible capacity loss (C_{irr}), cyclability, exfoliation, safety, and overall battery performance.

Factors affecting the SEI is given below:

- Type of carbon
- Pretreatment of carbon
- Electrolyte composition
- Mode of cycling

As a lithium-ion cell is charged for the first time, the electrolyte is reduced at the negatively polarized carbon electrode. The SEI layer consists of organic and inorganic electrolyte decomposition products from the reduction reaction. In the ideal case, the protecting SEI layer prevents further electrolyte decomposition and development of fresh SEI. This is achieved by blocking electron transport through the interphase. Fortunately, the SEI allows for lithium ions to pass through during charge/discharge and this feature is a prerequisite for the lithium ion battery to function [105]. The SEI layer will also contribute to prevent rapid charge/discharge.

As the SEI is formed, it consumes lithium ions. The SEI formation reaction is irreversible and the consumed lithium ions can not participate in the reversible intercalation reactions. It is therefore electrochemically inactive in the cell and a result of this is loss in capacity. The loss is not desired as the cell "loses" lithium and the cell performance is lowered. It is important to minimize/stabilize the SEI formation in order to avoid charge loss. However, the presence of a SEI is very important as it prevents further capacity loss. It also prevents solvent molecule co-intercalation and exfoliation [106, 107]. A stable SEI will therefore contribute to good cyclability.

Graphite can exfoliate and fracture under external influences. If cracking is allowed to continue, fresh surface is exposed to the electrolyte which will lead to further SEI film formation and lithium ion losses. The stability of the SEI is essential, as a destruction and restoration of the layer will deplete the amount of electrolyte and finally leading to battery failure [108]. Additives can be used to ensure a rapid SEI development during fast charging of the battery [96].

Electrolytes based on alkyl carbonates are thermodynamically unstable at low or high potentials versus Li/Li^+. The electrolyte will therefore degrade upon

potential change. As the electrolyte degrades, both the solvent and the salt are reduced in competing and parallel processes resulting in a complex deposition layer. The ideal properties of the SEI are summarized below:

- minimum electronic conductivity
- maximum lithium ion conductivity
- Impenetrable for foreign species present in electrolyte
- Prohibit penetration of solvated lithium ions to prevent exfoliation
- Rapid SEI formation
- Uniform morphology
- Consist of stable and insoluble passivation compounds
- Flexibility
- Good adhesion to carbon

The SEI formation can be observed as a plateau in galvanostatic measurements [108]. The potential value of the plateau varies with system chemistry, but the most adopted value in literature is set around 0.8 V [109]. The plateau does often not occur in subsequent cycles, indicating the importance of the first cycle. However, it is believed that even for the best SEI layers, the formation continues for a few cycles. It is desirable that the SEI formation occurs before the start of the intercalation [110].

The thickness of the SEI layer varies immensely, from a few Å to tens of nm [109]. It is suggested that the SEI consists of a dense layer of inorganic compounds near the carbon followed by a porous organic layer close to the electrolyte [109, 110]. The SEI has a different character depending on whether if it is deposited on the basal plane or the edge plane [111, 112]. The oxidation mechanism on the two planes is different as the edge surface is rich in inorganic compounds and the basal plane has deposits mainly of organ compounds [38]. The difference is indicated by different colors in Fig. 3.18. A good overview of the different SEI compounds are given in a publication by Verma *et al.* [105].

Similar surface films can also form on the cathode material. It is believed that the cathode SEI contributes more to the overall cell resistance [70]. During film formation, the electrolyte is oxidized on the cathode surface. CO_2 and CO can be generated. The gas generation and the voltage where the gas generation occurs depend on:

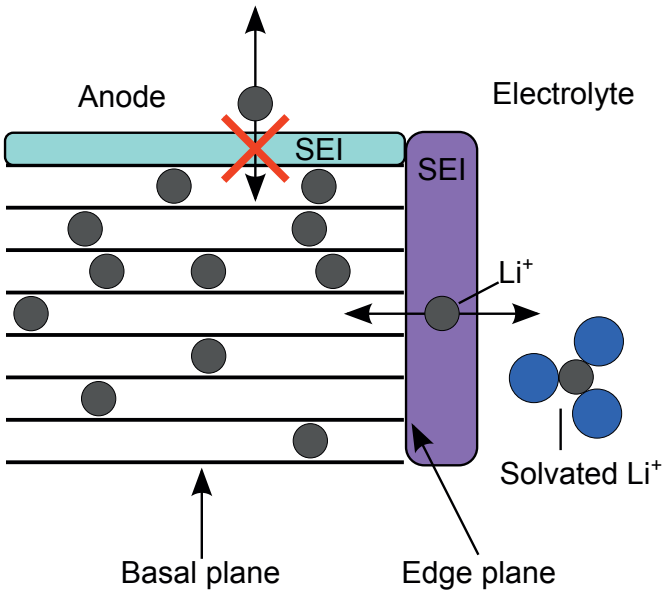

Figure 3.18: SEI formation on both basal plane and edge plane of the graphite crystal. The two different films have completely different functions. Edge plane SEI acts as a transport medium for cations, while basal plane SEI prevents further film formation [98].

- Surface chemistry of the cathode particles
- Electrolyte type
- Impurities of the electrolyte

Factors Which May Affect the Battery Performance Negatively

During charge/discharge, graphite will to some degree swell and shrink. The mechanical deformation can result in the electrode delaminating from the current collector. The volume changes may prevent the binder and the conductive carbon from working properly. These processes may result in further losses of active material which can not be used in the cell. Active material particle size distribution influences the effect of the volume changes as it alters the poros-

ity. Volume changes that are a few percent higher than the elastic limit of the material may dramatically change cycle life. Other factors that may affect the mechanical failure are the utilization of the cells capacity and the rate of the utilization. At a high rate, the utilization of the cell's capacity is localized to the outer particle surface.

Reactions which can negatively affect the cell characteristics includes:

- Continuous SEI growth.
- Oxidation of the electrolyte, which leads to consumption of electrolyte and salt.
- Traces of water may produce HF and damage the SEI.
- For complete cells, HF can damage the positive electrodes. Transition metals dissolution will damage the positive electrode and it can disturb the SEI greatly.
- Oxidation of separator.

This list is far from complete, but it provides an overview of the main parasitic reactions that consumes charge.

3.2.12 Safety Issues

Any device or substance which can store a certain amount of energy is a potential danger as for instance a pressure vessel or a barrel of oil. Batteries are no exception. Batteries convert chemical energy in a confined environment to direct electrical energy. If a battery malfunctions, the stored energy can be released as heat. In defective lithium-ion batteries temperatures can reach 600 °C. The gases created can reach even higher temperatures and are capable of melting steel. The cause of such thermal incidents are normally attributed to one of the following events:

- Internal short circuit
  - Foreign particles
  - Ripped separator
  - Physical abuse
  - Deposition of conductive material on separator

  - Dendrite growth

- External heat
- Overcharging

Thermal runaway can occur and be a potential threat in lithium-ion batteries. If the cell can dissipate the heat developed during charge/discharge, nothing abnormal will happen. However, if more heat is created than the cell can dissipate exothermic reactions may start. The process proceeds as the conditions go from isothermal to more adiabatic-like circumstances due to the insufficient heat transport. As the cell's temperature rises, the rate of the exothermic chemical reactions will increase further, without significantly increasing the desired galvanic reactions. This chain reaction of different mechanisms leads to thermal runaway [113]. Exothermic reactions in the cell include thermal decomposition of electrolyte, reduction and oxidation of the electrolyte at the anode and cathode, respectively, thermal decomposition of electrodes, and melting of separator leading to internal short circuiting.

Electrodeposited lithium may alter the morphology of the carbon surface and therefore the electrical behavior of the cell. It is desirable to prevent this from happening as it also may be a safety concern. However, to achieve high energy densities with good cycle performance, it is important to utilize all of the electrode material. This means that the cells should be charged and depleted fully, but still avoid overcharge and overdischarge [114].

The present system was developed to meet the criteria set by safety regulations. Since metallic lithium is not present in the complete cell, these cells are less chemically reactive and hence safer. The safety issue is very important for batteries in the consumer market.

A selection of safety evaluation methods, including heating test, nail penetration test, overcharge test, and crush test, are well described in Ref. [115].

3.3 Cell and Electrode Evaluation

Several techniques have been implemented to evaluate the cells and the electrode material. In the following sections some of these techniques will be described.

3.3.1 Charge/Discharge Measurements

The battery capacity or the amount of energy in a battery can be measured with charge/discharge measurements. It is relatively straightforward to measure the galvanostatic behavior. The discharge capacity can be obtained/calculated by discharging a two electrode cell with a constant current while measuring the time it takes to reach the end-of-discharge voltage. The charge capacity can be found in a similar fashion.

The current or C-rate is of great importance for galvanostatic charge/discharge measurements. Higher currents lead naturally to lower charge/discharge times. Moreover, the capacity also fades at high currents due to IR losses and the polarization effects such as slow lithium ion diffusion.

Capacity results are often used to conclude if the electrode is suitable for battery purposes. Nonetheless, charge/discharge measurements are usually not enough to make an accurate assessment of the electrode quality. Several other methods are therefore implemented.

3.3.2 Electrochemical Impedance Spectroscopy

Electrochemical impedance spectroscopy (EIS) is a powerful technique for obtaining information on reactions and transport processes within an electrochemical system. It is used for the investigation of a wide range of applications like batteries, fuel cells, capacitors, and corrosion cells [116]. It can also be used for other non-electrochemical applications like quality testing of motor oil and human skin samples to mention but a few. In battery research, EIS can be used along the whole development process starting from the study of half-cell reactions to quality control of complete battery modules.

Electrical resistance or impedance is the system's ability to resist the flow of electrical current. The unit of electrical resistance and impedance is measured in Ohm (Ω). Resistance (R) is defined as the ratio between voltage (E) and current (I) given by Ohm's law, see Eq. 3.29.

$$R = \frac{E}{I} \tag{3.29}$$

However, this is only valid for an ideal resistor. An ideal resistor fulfills certain requirements as listed below:

- The alternating current and the voltage response are in phase and vice versa.

- Resistance is independent of frequency.
- There is a linear relationship between current and voltage.

In real life, electrochemical systems are not ideal and instead they show a more complex behavior. By applying an alternating current or voltage to a cell, the requirements listed above are often not fulfilled. Moreover, some cell elements complicate things further by acting as charge storing capacitors. For this behavior, impedance can be used to describe the ability to resist electrical current.

A typical potentiostatic electrochemical impedance measurement is usually measured by applying a small ac sine wave potential to an electrochemical cell while the current through the cell is measured. If the alternating excitation signal is small, then the cell's response is said to be pseudo-linear. An actual electrochemical cell is not linear, but an approximation can be made, see Fig. 3.19a.

The current signal from the sinusoidal applied voltage through the electrochemical cell will be a sinusoid with the same frequency, but shifted in phase, see Fig. 3.19b. A delay or advance in the response compared to the stimulus is described with the phase shift. The current response has also a magnitude parameter. The ratio between the potential stimulus and current response with respect to the phase and magnitude gives the impedance, see Eq. 3.32

The voltage perturbation signal can be expressed by:

$$E_t = E_0 \sin(\omega t) \tag{3.30}$$

where E_t is the voltage at time t, E_0 is the amplitude and ω is the angular frequency ($\omega = 2\pi f$, where f is given in Hz). The pseudo-linear current response (I_t) will be

$$I_t = I_0 \sin(\omega t + \phi) \tag{3.31}$$

where I_0 is the current amplitude and ϕ is the phase shift. By combining Eq. 3.29, 3.30, and 3.31, the following equation for impedance is given:

$$Z = \frac{E_t}{I_t} = \frac{E_0 \sin(\omega t)}{I_0 \sin(\omega t + \phi)} = Z_0 \frac{\sin(\omega t)}{\sin(\omega t + \phi)} \tag{3.32}$$

where Z_0 is the magnitude of the impedance. If the voltage excitation signal and the current response are plotted on the x-axis and y-axis respectively, the resulting figure will be a Lissajous oval as shown in Fig. 3.19c.

By using the Taylor series of the exponential function and trigonometric functions, it is possible to derive Euler's formula, see Eq. 3.33. The formula establishes the relationship between the trigonometric functions and the complex exponential function. With this relationship it is possible to transform the voltage stimulus and current response to a complex exponential function which simplifies the calculations related to alternating oscillations.

$$\exp(jx) = \cos x + j \sin x \tag{3.33}$$

where j is the imaginary unit ($\sqrt{-1}$) and x equals to all real numbers. By using Euler's formula, it is possible to express the impedance as a complex function. The voltage perturbation can be expressed as a complex function:

$$E_t = E_0 \exp(j\omega t) \tag{3.34}$$

and the current response signal is then:

$$I_t = I_0 \exp(j\omega t - \phi) \tag{3.35}$$

The impedance is also given as a complex number:

$$Z = \frac{E_t}{I_t} = Z_0 \exp(j\phi) = Z_0(\cos\phi + j \sin\phi) \tag{3.36}$$

Z is a function of frequency and Eq. 3.36 can be plotted as a "Nyquist plot" by plotting the real part is on the x-axis and the imaginary part on the y-axis. The impedance for one particular frequency is represented as a point in the complex plane (Nyquist plot) with the magnitude (Z_0) and phase (ϕ), see Fig. 3.19d. The impedance is therefore given as a vector. An impedance spectrum is obtained by repeating the measurements over a series of different frequencies.

In the Nyquist plot, the low frequencies are located on the right side while the high frequencies are on the left. Due to the lack of frequency information, frequencies should be added at characteristic points in the plot. In this graphical presentation it is important to notice that the y-axis is negative.

Information about the kinetics in a electrochemical system can be derived from EIS. The idea is as follows: Different processes occurring partly simultaneously are characterized by different time constants. Some processes are slow, others are fast. For low perturbation frequencies, all processes can keep up with the applied stimulus. As the frequency is increased, some processes can not keep up. This will change the magnitude and phase shift and hence the measured

impedance. At some point, a process will withdraw as the applied frequency is increasing. The drop out is a direct measurement of the kinetics of the process. The kinetic behavior of the complete system can be mapped out.

As explain above, impedance spectroscopy allows for individual measurements of the different contribution to the cell impedance. It has the ability to distinguish electric and dielectric properties of individual components under investigation. For a typical electrochemical cell, the contributions are the electrical and ionic impedance of the electrolyte, surface film impedance and charge transfer. Interpret the impedance results can be a troublesome task. An equivalent circuit which will give a similar impedance response has to be established. For the equivalent circuit to be useful, the circuit elements should have a basis in the physical electrochemistry [117]. Circuit elements such as resistors, capacitors, and inductors together with some special elements are used. The resistor can be equivalent to the electrolyte resistance. The capacitors can describe the double layer capacitance on the electrodes. Induction can be explained by absorption at low frequencies and artifacts at high frequencies due to wire interaction. The special constant phase element can tell something about inhomogeneous surfaces and the distribution of physical processes.

For lithium-ion batteries, the characteristics of lithium insertion into graphitic anodes are greatly affected by the kinetics of intercalation [118]. A good understanding of the kinetics are important for improving high rate charge/discharge performance. Such information can be obtain by determining the diffusion coefficient of lithium ions in carbon with EIS. It is desirable with a large coefficient as it allows for high rate charging. A low lithium diffusion coefficient may lead to lithium metal deposition. The insertion of lithium ions involves a series of complex processes such as diffusion in the electrolyte, migration through the passivation film (SEI), charge transfer at the carbon surface, and the mentioned diffusion of lithium ions in the carbon host. Due to their different time constants, it is, at least in theory, possible to separate most of these phenomena.

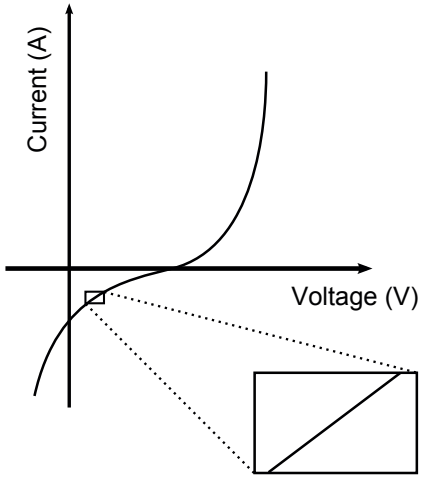

(a) Pseudo-linearity

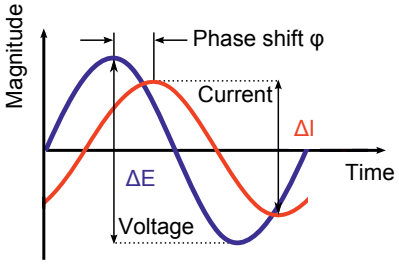

(b) The voltage perturbation and the current response

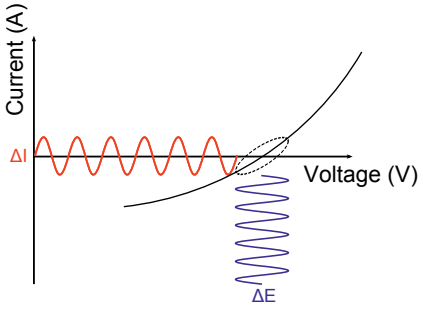

(c) Lissajous curve

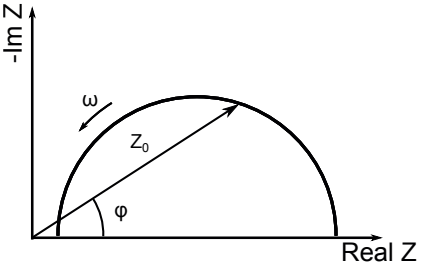

(d) Nyquist plot

Figure 3.19: A selection of plots showing relationships useful for electrochemical impedance spectroscopy.

3.3.3 Cyclic Voltammetry

Cyclic Voltammetry (CV) is a widely used potentiodynamic technique for investigating electrochemical reactions as it offers a fast location of the redox voltages for the electroactive species in the test setup.

A potentiostat with a three electrode system (working electrode, reference electrode, and counter electrode) is needed to perform cyclic voltammetry. In cyclic voltammetry, a fixed potential range is employed from a lower limit (V_1) to an upper limit (V_2) as shown in Fig. 3.20a. When the working electrode's potential reaches V_2, the scan is reversed and the voltage is swept back to V_1 [69,119]. The voltage can be swept multiple times between these limits at a fixed scan rate (V/s). The potential is applied between the working electrode and the reference electrode, while the current is measured between the working electrode and the counter electrode. The data is plotted as current versus potential in a cyclic voltammogram, see Fig. 3.20b. The forward scan produces a current peak as a reduction reaction of an electrolyte component occurs. The current will increase until it reaches the reduction potential of the component and then decrease as the concentration of the component is depleted at the electrode surface. When the applied potential is reversed, the potential will reoxidize the product if the redox reaction is reversible. A current peak of reversed polarity (from the forward scan) is produced during the oxidation. A hysteresis between the potential values of the current peaks may occur due to diffusion rates of the analyte and the activation barrier for electron transfer between the electrode and the electrolyte. Information about the reversibility of the system can be extracted from the data. The characteristics of cyclic voltammetry are given by the rate of the electron transfer reactions, the chemical reactivity of the electroactive species and the voltage scan rate [120].

For lithium-ion battery experiments, low scan rates and thin electrodes are essential to study the insertion and extraction of lithium ions in carbon materials. The intercalation process is slow and observation of distinct current peaks is not possible at high scan rates. With low scan rates it is possible to avoid heterogeneous charging/discharging of the electrode and to reduce the kinetic influence of lithium ion diffusion in carbon [87].

Oxidation peaks will occur when the lithium ions are inserted into the graphite. Similar reduction peaks will be observed during the reversible process of lithium ion extraction. The spikes will be located at different intercalation potentials depending on the stage formation of the graphite intercalated compound. The CV curves can therefore give information about the island model of the staging process [121].

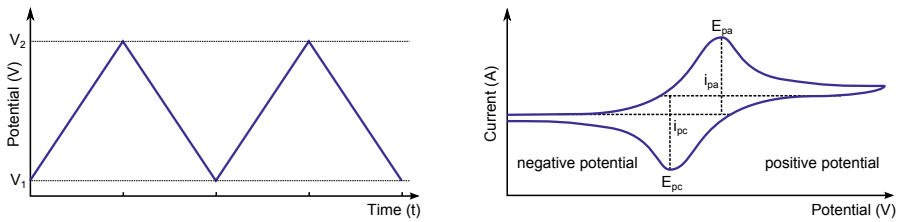

(a) (b)

Figure 3.20: a) The potential waveform describing the range of a CV scan. b) The current response of a typical CV measurement where pa and pc stands for peak anodic and peak cathodic, respectively.

3.4 Thermal studies

3.4.1 Differential Scanning Calorimetry

Calorimetry is the study of heat transfer during physical and/or chemical processes [122]. Additionally, differential scanning calorimetry (DSC) is a rapid and sensitive analytical technique for measuring thermal effects. DSC measures the heat in and out of a sample relative to a reference as the sample is heated or cooled with a linear temperature ramp. The heat difference is plotted as a function of temperature. In other words, an almost zero temperature difference is kept between a substance and an inert reference. The two chambers containing the sample and the reference are subjected to identical temperature regimes at a known rate [122–124]. Heat will flow to or from the sample when the sample is subjected to a physical transformation (e.g. phase transition or chemical reaction). The direction of the heat flow depends on whether the process is exothermic (heat flows out of the sample) or endothermic (heat flows into the sample). DSC measures the enthalpy change (ΔH) needed to keep the sample and the reference at the same temperature. DSC can also yield the heat capacity of the sample.

The DSC curves (also called thermograms) show the heat flow (W) as a function of time or temperature. Fig. 3.21b shows a typical DSC curve. A peak in the curve will occur as thermal reactions or transitions take place in the sample leading to heat being generated or consumed. The area under the peak is the total heat generated from the process. The reaction or transition temperature is of great importance when studying thermal properties. A background measurement should be taken before each experiment/sample measurement in order to

avoid artifacts from the sample holder and reference. The curves can be used to calculate the enthalpies of the transformations as the enthalpy is proportional to the area under the curve.

Power-Compensation Differential Scanning Calorimetry

The DSC apparatus used in this study is a power-compensation differential scanning calorimeter. It has separate sample and reference temperature sensors and heaters [122], see Fig. 3.21a. The DSC utilizes thermocouples to measure the temperature, The temperature is proportional to the difference in heat flow rates. The temperature difference between the sample and the reference is kept at zero by using the individual heaters.

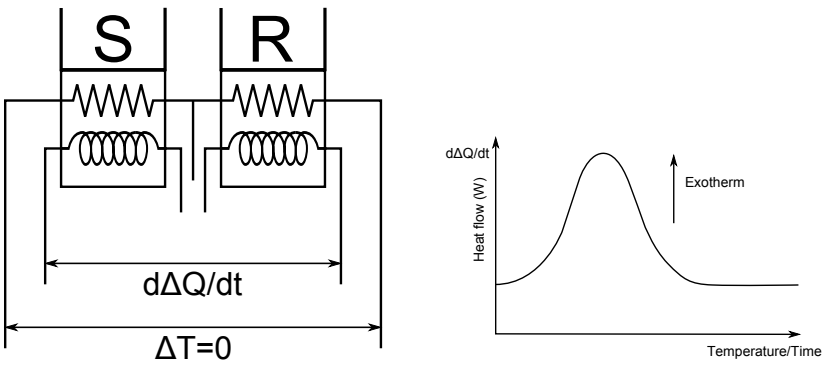

(a) (b)

Figure 3.21: a) A schematic of a power-compensation differential scanning calorimeter with individual sample and reference sensors and furnaces. S and R refers to the sample and reference respectively. b) A typical thermal analysis curve

Safety Screening of Lithium-Ion Batteries

DSC is an excellent tool for characterizing thermal safety issues occurring in lithium-ion batteries. Several studies have been performed to show the relevance between DSC and the safety of lithium-ion batteries [125,126]. The DSC measures the thermal stability of plain electrodes as well as the combination of the electrode and electrolyte. For carbon based anodes the thermal stability is influenced by the solid electrolyte interphase (SEI) and the lithiated state of

the electrode. Exothermic reactions at low temperatures are undesirable as this may lead to a series of other unwanted reactions.

Thermal instabilities can occur at elevated temperatures for lithium-ion batteries. A rise in temperature can be caused by abuse or a malfunctioning cell. If the heat generation surpasses the heat dissipation, thermal runaway might occur as exothermic reactions are allowed to proceed [115]. Thermal runaway results in safety problems such as fires and explosions. Large battery packs are more likely to suffer from thermal runaways than single cells. The heat in large packs is not easily dissipated. Moreover, cells connected in parallel or series can be in an overcharged state due to minor performance differences in each cell. This is particularly apparent for older cells where the state of charge can be different for the same voltage [127].

Positive lithium metal oxides are potentially the most hazardous material within a lithium-ion cell. An energetic heat evolution starting at temperatures around 200 °C is associated with the reaction between delithiated oxide and the electrolyte [128]. The exothermic effect for cycled carbon electrodes is much smaller and occurs at lower temperatures compared to the lithium metal oxides. However, the heat response of carbon anodes can act as a fuse for thermal runaway in lithium-ion cells. Heat signatures of different carbonaceous anodes are therefore of major interest for battery researchers [129].

3.4.2 Thermal Conductivity of Electrode Materials

Lithium-ion batteries can convert chemical energy to electric work with efficiencies of approximately 95 % [130]. The rest of the energy is transformed into heat. In fact, heat is generated in all electrochemical cells where chemical energy is converted into electrical energy and vice versa. Thermal considerations are therefore crucial for all electrochemical systems. In batteries, it is especially important to avoid detrimental incidents such as thermal runaway [93,115].

The generation of heat in a cell depends on many factors such as state of charge, cell chemistry, direction of current, temperature, and charge/discharge rate. There are several heat sources in a battery [131,132]. The cell reactions taking place inside a battery are either exothermic or endothermic depending on the current direction. Electrochemical reactions can act as both a heat source and heat sink. The electrochemical reaction takes place at both the anode/electrolyte interphase and cathode/electrolyte interphase. For lithium-ion cells, this heat generation can therefore be divided into lithium extraction heat and lithium intercalation heat.

Joule heating occurs due to ohmic potential drop across the cell. The most significant potential drop in a cell is within the electrolyte. Ion conduction resistance in the electrolyte will contribute to the heat formation. Joule heating is given by Joule's law, see Eq. 3.37

$$P = I^2 R \tag{3.37}$$

where P is the heat effect (W), I is the current (A) through the conductor and R is the resistance (Ω). Defects in both the cell design and electroactive components can increase resistance and therefore the Joule heating.

The third heat generation process is the active polarization heat. Energy is required for the lithium diffusion and the movement of atoms/ions in the cell reaction. The energies originate from either the extraction or intercalation of lithium ions. Degradation of the electrode surface results in increased polarization.

External thermal effects can be a problem if a cell is surrounded by other cells or electric devices. The cell can become thermally insulated and the generated heat will not dissipate. The temperature inside the battery effects factors like power, energy, safety and cycle loss to mention but a few. By dissipating the heat or regulating the temperature, optimum performance can be achieved. This is especially important within a single cell, but equally important within battery modules to reduce unbalanced cell capacity. The dissipation of heat depends on the chemistry, geometry, and the path to a potential heat sink.

The thermal conduction of electrodes plays an important role in the heat dissipation and therefore to problems related to heat generation. Heat conduction is one of three methods of heat transfer. Heat conduction is the spontaneous transfer of thermal energy from a hot object to a cold object when not considering radiation or convection. The process equalizes temperature differences. The thermal energy is transfered by the same coulombic forces that support the structure of matter, therefore heat conduction requires direct contact between hot and cold matter [133, 134].

Fourier's law is an empirical law which can explain thermal conductivity [135]. It deals with the relationship between the heat flow rate in a material and the temperature gradient in the direction of energy flow. In other words, heat flux is proportional to the magnitude of the temperature gradient, see Eq. 3.38.

$$q_x = -k\frac{\Delta T}{\Delta x} \tag{3.38}$$

where q_x ($\frac{W}{m^2}$) is the heat flow rate, and $\frac{\Delta T}{\Delta x}$ ($\frac{K}{m}$) is the thermal gradient in the direction of the heat flow. The minus sign shows that the heat flows from a hotter to a colder region. Thermal conductivity is denoted k ($\frac{W}{mK}$). It accounts for the fact that materials heat up or retain heat differently. The equation above is expressed in one dimensional form as the setup used in the experiments conducted in this project is designed to measure thermal conductivity in one direction.

The setup for these experiments are also designed for steady state conditions. Due to conservation of energy, the heat-transfer rate into a system is equal the heat-transfer rate out of a system if no heat is generated from within. For such a system, the temperature difference across the sample is proportional to the heat-transfer rate. The proportional factor is defined as the thermal resistance $R(\frac{Km^2}{W})$, see Eq 3.39. The relationship is equivalent to Ohm's law.

$$R \equiv \frac{\Delta T}{q_x} = \frac{\Delta x}{k} \tag{3.39}$$

By measuring q_x, ΔT, and Δx, where ΔT is the temperature difference of the sample and Δx is the sample thickness, it is possible to obtain the thermal conductivity k.

By applying Eq. 3.38 and Eq. 3.39 to the experimental setup in Fig. 3.22a, the following equations can be obtained.

$$q_{\text{upper}} = k_{\text{upper}} \frac{T_1 - T_3}{x_1 - x_3} \tag{3.40}$$

$$q_{\text{lower}} = k_{\text{lower}} \frac{T_6 - T_8}{x_6 - x_8} \tag{3.41}$$

$$q_{\text{sample}} = \frac{q_{\text{upper}} + q_{\text{lower}}}{2} \tag{3.42}$$

$$R_{\text{sample}} = \frac{T_4 - T_5}{q_{\text{sample}}} = \frac{\Delta x_{\text{sample}}}{k_{\text{sample}}} \tag{3.43}$$

where q_{upper} and q_{lower} refer to the heat flow rate through the plane of the upper and lower stainless steel cylinders, respectively. q_{sample} is the average value of q_{upper} and q_{lower}. All three values should be equal if the thermal conductors and sample is perfectly insulated. k_{upper} and k_{lower} are the thermal conductivity of the upper and lower stainless steel cylinders. These values are the same, as

both cylinders are made of the same stainless steel material. The subscripted numbers relate to the thermocouple number and its placement in Fig. 3.22a. T_i is measured temperature at thermocouple i, while $x_i - x_j$ are the distance between thermocouple i and j. Δx_{sample} is the sample thickness. R_{sample} and k_{sample} are the thermal resistance and thermal conductivity of the sample.

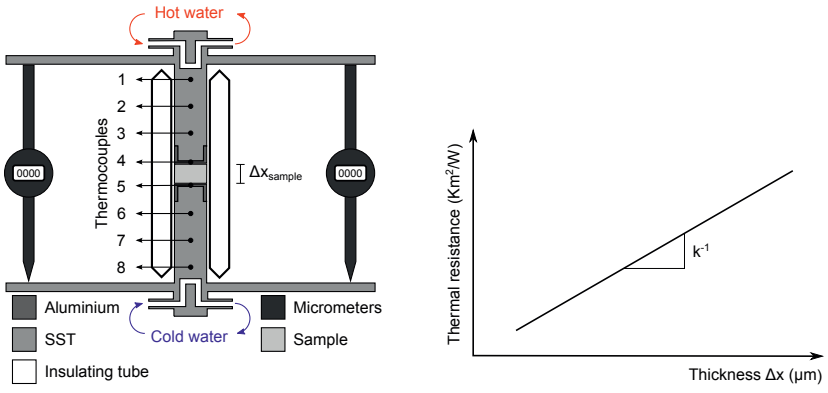

(a) (b)

Figure 3.22: a) A schematic representation of the apparatus used for thermal conduction measurements of electrode materials. SST is an abbreviation for stainless steel cylinders, which are used as both a heat flux meter and compactors of the investigated sample. b) A typical graph of the linear thermal resistance where the thermal conductivity(k) is the inverse of the slope.

Chapter 4

Experimental

4.1 Carbon Cones Production Attempt's at SINTEFs Locations

The original carbon cones materials were produced in a hot plasma reactor located in Hofors, Sweden. A smaller pilot reactor located at SINTEF, Trondheim was modified for the purpose of reproducing carbon cones by trying to replicate the conditions of the Hofors reactor. Details about the design and operation of the reactor are proprietary information of n-Tec AS and cannot be disclosed in this work. Therefore a simplified description is given here.

Before each trial run, both the gas and oil derivate supply was checked. The gas supply had to be sufficient, since the bottles could not be changed during operation. The oil derivate was preheated (70 °C) to reduce viscosity. At this point any additives were added and mixed properly into the oil derivate.

For the reactor start-up, the reactor was flushed with argon gas. The inner linings of the reactor consisted of graphite and the carbon would oxidize if any oxygen was present at high temperatures. When the flushing was complete, the heating of the reactor started along with the start up of the water cooling system. When the temperature reached a certain threshold, the current of the arc discharge was turned on. As the temperature was steadily increasing, the ongoing gas flow was gradually switched from argon to hydrogen. The hydrogen gas was led into the reactor and was allowed to flow between the electrodes in the plasma generator. An electric arc was controlled and stabilized by means of

magnetic coils and the hydrogen plasma gas flow. The plasma gas was heated up to high temperatures while it flowed between the electrodes and into the reactor chamber.

When the temperature was sufficiently high, the oil derivate, consisting of various hydrocarbons [1], was injected into the reactor and decomposed in a pyrolytic reaction. The oil derivate (hydrocarbon source) was pumped into the reactor through a nozzle. This mixture would pass through a zone near the electric arc in the reactor chamber where it would blend with the hot plasma gas. The oil derivate would then vaporize and go through a pyrolysis process in the reaction chamber. Hydrocarbons would decompose to elementary carbon, lighter hydrocarbons, some other chemical compounds and hydrogen gas. The produced carbon was taken out through filters and the pyrolytic hydrogen gas was recycled as plasma gas, while the reactor product and the exhaust gas were blown out through a filter. The discharge current was cut when the trial run was over. At the same time the hydrogen gas filling the reactor was diluted with argon gas until no hydrogen was left in the system. The reactor was cooled down over night before the gas and water cooling was terminated. At this point the reactor was opened and the electrodes were inspected for wear and tear. The electrodes were changed if necessary and prepared for the next trial run. Potential carbon residue on the inner linings was removed before the feeding lance was removed, and the nozzle was cleaned if necessary. The produced carbon material was collected from the filters before the results were analyzed with an electron microscope. The main operation of the reactor was done by Steinar Prytz, SINTEF. A rough overview of the different trial runs are given below. CC01 refer to the first production attempt. Details are again omitted due to proprietary issues.

- CC01-CC10: Checked the effect of flow pattern, oil/gas ratios, and residence times at temperatures below 2300 °C.
- CC11-CC21: The effect of recycling the product was tested. In addition, chemicals were added to the feed stock. The insulation was also improved to increase the reactor temperature.
- CC22-CC29: Minor geometry charges were performed and the investigation of higher temperature were prioritized (above 2300 °C).

A schematic representation of the reactor is shown in Fig. 4.1 while a simplified flow diagram of the total production is given in Fig. 4.2.

[1] The chemical composition of the oil derivate is omitted due to proprietary rights.

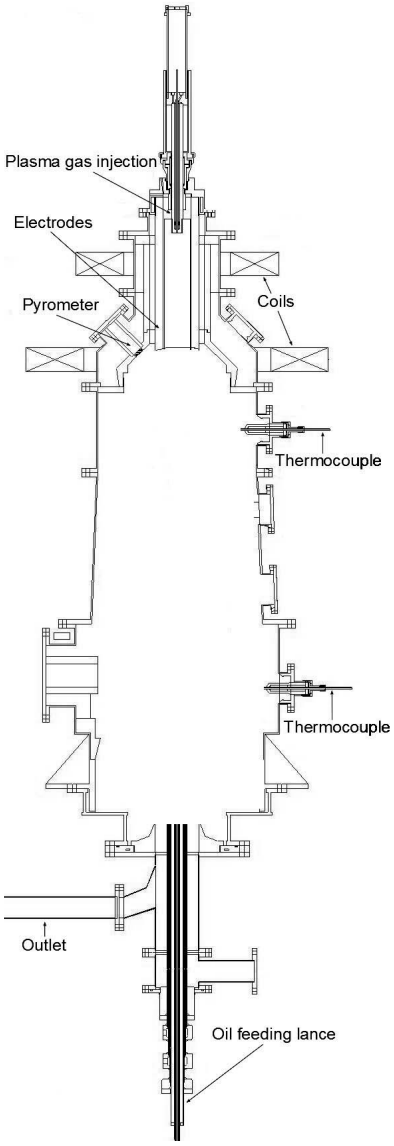

Figure 4.1: A simplified schematic of the SINTEF reactor. Details are omitted due to proprietary information.

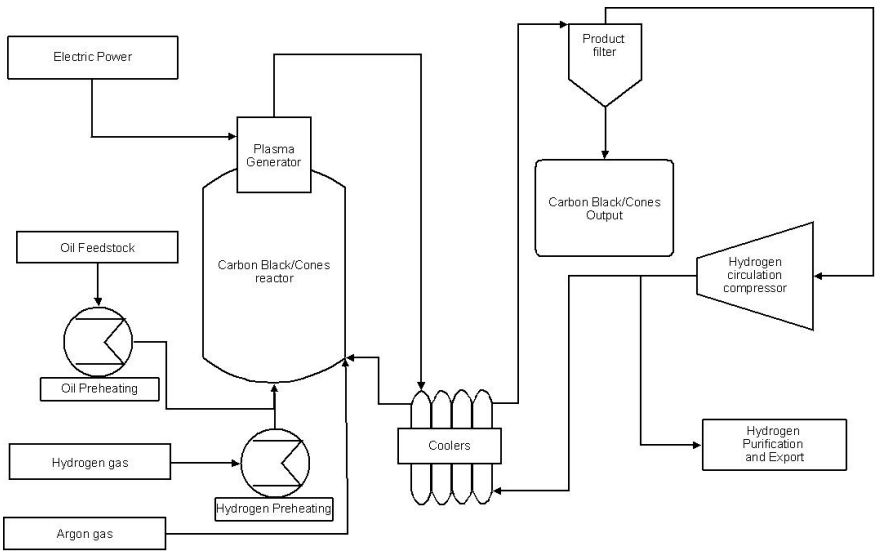

Figure 4.2: A simplified flow diagram of the carbon cones process.

4.1.1 Heat Treatment of Carbon Cones

The original carbon cones were heat treated to alter the overall structure of the carbon as it has a significant effect on the corresponding battery performance. This process was performed at different temperatures with a Xerion (XGRAPHIT) furnace, see Fig. 4.3a. The furnace has a graphite-based heating and insulation system. As-produced carbon cones (20 g) were filled and compressed in a graphite crucible. The crucible was transferred to the furnace chamber and the furnace chamber was lifted into a water-cooled double walled vessel. The furnace chamber was then evacuated and filled with argon gas functioning as a protective gas atmosphere, while the heating was performed at 20 °C/min from room temperature to 2000 °C. From 2000 °C to temperatures of 2700 °C, the heating rate was 10 °C/min. All heat treatments in this furnace were performed in flowing argon atmosphere. The samples were held at the desired heat treatment level for 3 h before the sample temperature was lowered to ambient temperatures by cooling of the argon flow. The sample was then hand crushed in a mortar and sieved in order to pulverize the material and break up any agglomerates.

(a)

(b)

Figure 4.3: a) The Xerion furnace used for heat treatment of carbon cones. b) Approximately 20 g of carbon cones were filled and pressed into graphite crucibles.

4.1.2 Oxidation of Carbon Cones

Carbon cones were oxidize to reduce the surface carbon atoms reactivity to the electrolyte. In addition, oxidation can drastically alter the material by burning large quantities of carbon. Three different methods were used to oxidize the carbon material. These will be described in more detail in the following sections.

Heat Treated in Air at 900 °C

Approximately 6 g of basic grade carbon cones were weighed out in an alumina crucible. The crucible was transferred to a tube furnace where the material was heated with a heating rate of 200 °C/h until the temperature reached 900 °C. The set temperature was held for 1 h while the furnace was purged with synthetic air. After heat treatment, the sample was cooled down to room temperature and reweighed.

All other heat treatments in air were performed with the same temperature

profile.

Hydrogen Peroxide (H_2O_2) Treatment

Hydrogen peroxide (200 mL, 30 % in a water solution) from Sigma Aldich and basic grade carbon cones (3 g) were mixed in an Erlenmeyer flask. The dispersion was stirred with a magnet for 4 h before it was filtered with a water jet vacuum pump system. The carbon was rinsed with distilled water untill the waste water was pH neutral. An oven was used for drying the carbon overnight at 150 °C.

Nitric Acid (HNO_3) Treatment

Basic grade carbon cones (3 g) were mixed with nitric acid (200 mL, 65 %, Merck) in an Erlenmeyer flask. The mixture was heated to its boiling point on a heating plate, while stirring with a magnet for 4 h. A water jet vacuum pump was used to filter the material. The carbon was rinsed with distilled water untill the waste water was pH neutral, before it was dryed overnight at 150 °C.

4.1.3 Functionalized Carbon Cones

The oxygen functionalized carbon cones were provided by n-Tec. The material contained between 12 wt% - 17 wt% oxygen. The oxygen content was measured with an oxygen analyzer (Leco TC-436DR) by Anne Støre, SINTEF.

4.1.4 Microwave Irradiation

Microwave treatment was used with the intention to alter the surface structure of the carbon cones. It is anticipated that small amounts of volatile compounds present in the raw carbon cones will evaporate by applying microwave energy to the material.

Basic grade carbon cones were irradiated with microwaves using a standard kitchen microwave oven (Matsui, Model No. MS-106WH) at full power (1150 W) for 20 s, 2450 MHz). The carbon cones powder was transfered to a sealed Teflon container (Savillex, 60 mL digestion vessel) prior to the irradiation. The container was assembled in an argon filled glove box to ensure argon atmosphere. Microwave irradiation with air was also tested.

4.2 Carbon Characterization

4.2.1 Electron Microscope

Microscope investigations of the pristine and modified carbon material have been performed with a Zeiss Ultra 55 Limited Edition field emission scanning electron microscope (FEGSEM). Images were taken of either carbon powder or tape casted electrodes. The carbon powder was dispersed in ethanol before a few drops of the mixture was transferred to the sample holder where the ethanol was allowed to evaporate. The tape casted electrode material was cut up in suitable pieces and attached to samples holders with conducting adhesive tape. The samples were placed into the electron microscope chamber and evacuated before the images were acquired. The FEGSEM was operated at different conditions, but an acceleration voltage of 0.5 kV and a working distance of 2 mm proved to give good images together with the in-lens detector. The FEGSEM was extensively used because of its sufficiently high resolution and its simple procedure for sample preparation. The quality of the FEGSEM images exceed that of a normal SEM.

A transmission electron microscope (TEM) was also employed for studying the carbon cones in more detail. The TEM used in this study was a JEOL JEM-2010. The samples were prepared by mixing ethanol and carbon cones in a small glass container. This container was then submerged into an ultrasound bath for a minute for the carbon particles to thoroughly disperse in the ethanol. A few droplets from the mixture was transfered to a holey carbon coated copper grid with a mesh size of approximately 0.5 µm - 2 µm. The sample holder was carefully loaded into the TEM before images were obtained.

All electron microscope images have been modified with the purpose of improving the scale bar visibility.

4.2.2 X-ray Diffraction

Powder X-ray diffraction (XRD) was used to measure the crystallinity of various carbon cones materials. The data was collected with a Bruker AXS D8 FOCUS X-ray diffractometer with a Lynxeye™detector. The X-ray source consisted of Cu $K_\alpha 1$ and $K_\alpha 2$ radiation. The measurements were recorded from 2θ values of 10° to 80°. The current and voltage for the X-ray tube were 40 V and 40 mA. Other experimental parameters were the scan steps of 0.04°, slit size of 0.6 mm and a 0.2 s counting time for each step.

The sample preparation was done by dispersing the carbon material in ethanol before a few drops were placed on a single silicon crystal sample holder. The sample holder was inserted onto the loading board of the diffractometer after the ethanol was evaporated.

4.2.3 Raman Spectroscopy

Raman Spectroscopy was used to observe the vibrational modes of the carbon material. The Raman spectroscopy was carried out at the Department of Chemical Engineering, NTNU. The instrument used was a Jobin Yvon Horiba Labram spectrometer. Fig. 4.4a shows the Raman spectrometer used in this work.

The Raman spectrometer had to be calibrated against a single crystal silicon reference, before it could be used to study the carbon samples. This type of single crystal has a very distinct peak at 521 cm^{-1}.

The studied samples were cut out of the electrode material used in the carbon/lithium half-cells, which in addition to the carbon also contained the polyvinylidene diflouride (PVDF) binder. The sample was mounted on a stage and the laser beam was focused on the sample by adjusting the sample height. A microscope with 50× objective was used to observe the relevant area. Fig. 4.4b shows a typical sample surface for the focused laser beam.

The measurements were performed between 100 cm^{-1} and 2000 cm^{-1} The acquisition time was set to 60 s and each scan was done five times, before the average signals were calculated. The signals were registered on a computer.

A continuous wave He-Ne laser (20 mW) with a wavelength of 632.8 nm and a beam diameter of 100 µm was used. As the laser diameter is larger than the carbon particles, one measurement is sufficient to obtain an average sample spectrum.

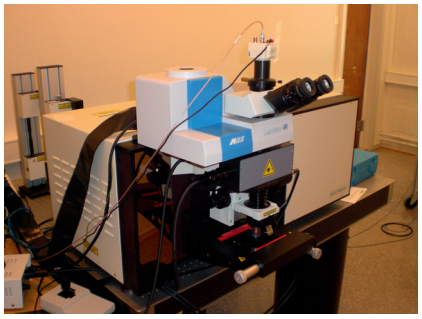

(a)

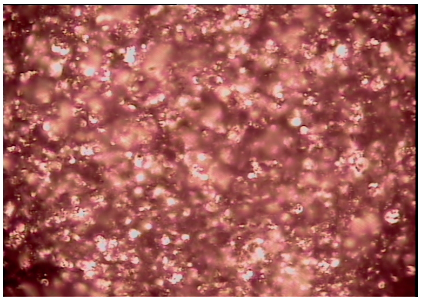

(b)

Figure 4.4: a) Raman spectrometer with a microscope for adjustment purposes. b) A picture of a studied sample surface with the focus within the plane

4.2.4 Nitrogen Adsorption Measurements (BET)

BET measurements were made using a Micromeritics Tristar 3000 to determine the specific surface area of the various carbon materials. All samples were dried and degassed in vacuum overnight at 250 °C. The adsorption isotherms were plotted from five different relative pressures

4.2.5 Density Measurements of Carbon Powder

The apparent bulk density of carbon powder is commonly measured with a Scott Volumeter (as described in standard ASTM B329-06.) A device similar to the Scott Volumeter was built to determinate the density, see Fig. 4.5.

The equipment was put together by cutting 45° slits in a PVC tube (length: 30 cm, diameter: 4 cm). Glass plates were inserted into the slits as baffle plates. A crucible with a known volume was placed under the tube. The fixed volume of the crucible was measured with a burette to 22.95 mL. Two funnels were used to lead the powder into the tube and crucible. When performing density measurements, the empty crucible was weighed out and placed under the baffled tube. Carbon powder was poured into a sieve, which was emptied over the top funnel until the crucible was full. The powder was carefully leveled with a spatula to ensure the complete filling of the crucible and avoid compressing the powder. The crucible was then weighed and the weight difference and density were calculated. This procedure was repeated for each relevant carbon material.

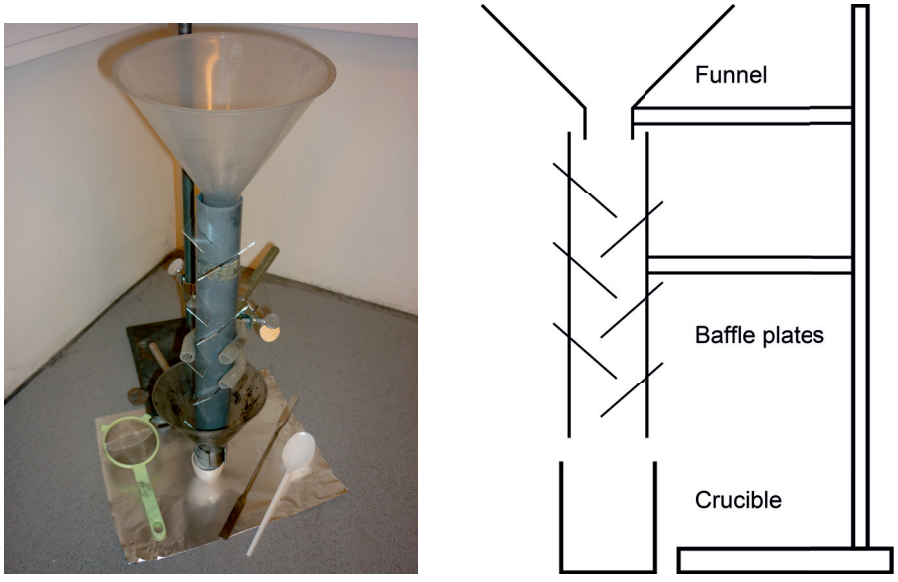

(a) (b)

Figure 4.5: a) An in-house modified scott volumeter and b) a simplified schematic of the cross section.

4.3 Manufacturing and Testing of Lithium-Ion Batteries

The preparation of lithium-ion cells consisted of several manufacturing steps, all which will be described in this section. In short, a carbon based slurry was tape casted onto a copper foil. This was the base material for the carbon electrodes which were assembled together with a counter electrode, separator and electrolyte into a cell.

4.3.1 Preparation of Slurry

The slurry was prepared by several different methods, all of which evolved from each other. Only the final method is described below as it was the method used for the tested cells.

The slurries were based on either carbon cones material or commercially

available graphite purchased from Timcal (Timrex). The slurries were prepared by mixing 95 wt% of dry powder with 5 wt% binder polyvinylidene flouride (PVDF, Kynar 761). For the graphite electrodes, 5 wt% of the 95 wt% was substituted with carbon black. No carbon black was added to the carbon cones due to the natural presence of carbon black in the material. All constituents were mixed together in a small steel vessel (15 mL) together with a suitable amount (3 - 10 g) of solvent 1-methyl-2-pyrrolidinone (NMP, Sigma-Aldrich). The solvent amount varied depending on the carbon material, where a larger amount of solvent was generally required for the cones compared to the Timcal graphite. Large surface area and spesific particle morphology of the carbon cones, as opposed to the graphite, are the reason for the differences in solvent amounts. The viscosity of the suspension was prioritized, rather than having the same mass ratios between the solid and liquid compounds. A small steel ball (15 mm) was added before the vessel was closed.

The vessel was inserted in a Retsch Mixer Mill 2000. The container shook for a least 3 minutes depending on the amount of solvent and slurry viscosity. The amplitude is set to 65 %. After this treatment the container was opened and the slurry was visually inspected. If the viscosity was too high for the slurry to be tape casted, more NMP was added. The container was then closed again and shaken for another 3 min. This process was continued until a suitable slurry was obtained. The total amount of solvent was already known if a slurry of the same carbon material was previously produced.

4.3.2 Tape Casting and Preparation of Electrodes

The tape casts were prepared in the following fashion on a K Control Coater from RK PrintCoat Instruments Ltd, see Fig. 4.6a. A piece of Mylar® plastic sheet was placed in the bed of the tape caster to prevent any contamination from the bed. The plastic sheet was cleaned with ethanol before the copper foil was placed on top. Copper foil was also cleaned with ethanol in order to prevent contamination of the finished cast. A doctor blade was adjusted according to the desired electrode thickness before it was assembled to the tape caster. A doctor blade gap of 150 µm was normally used. Previously prepared slurry from the steel container was transferred onto the copper foil. As the tape caster was switched on, the doctor blade spread the slurry out on the copper foil as a homogeneously thick film. Different tape casting speeds (between 1 cm/s - 8 cm/s) were used as the slurries showed shear thinning properties. Heating elements inside the bed were switched on at 60 °C and the slurry was left to

(a) Steel container used to prepare slurry.

(b) Retsch Mixer Mill 2000.

dry for 2 h.

The dry slurry, now called the tape cast, was additionally dried in a vacuum oven overnight at 120 °C. Finally, the tape cast was dried under vacuum at 80 °C in the antechamber furnace of the glove box as the tape cast was introduced to an inert argon atmosphere, (O_2<1 ppm, H_2O<1 ppm).

Electrodes (diameter: 16 mm) were cut out of the tape cast using a HSNG-EP Electrode Punch from Hohsen Corp., see Fig. 4.6b.

4.3.3 Electrolyte Mixing

The electrolyte mixture used in this study was a solution of 1M $LiPF_6$ in an equigravimetric mixture of ethyl- and diethyl-carbonate. Ethyl-carbonate (EC) was heated on a hot plate to approximately 45 °C in order to melt the solvent. 0.338 g of $LiPF_6$ (Sigma Aldrich, battery grade) was weighed in a small glass beaker. 1.25 g of diethyl-carbonate (DEC) was added to the salt together with 1.25 g of melted EC. The solution was stirred with a magnetic stirrer for 30 min before it was poured over into a small sealed bottle. The work was performed within the glove box.

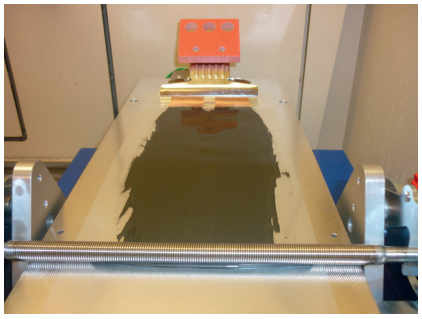

(a)

(b)

Figure 4.6: a) Tape casting of two parallel copper foils with a coating bar instead of the normally used doctor blade. b) Electrode punch tool.

4.3.4 Assembly of Coin Cells

Stainless steel CR2016 coin cells (diameter: 20 mm, height: 1.6 mm) from Hohsen Corp. were used as casings for the tested cells. Lithium foil from Sigma Aldrich (thickness: 0.75 mm) was cut out (diameter: 14 mm) with a punching tool as counter electrodes. The lithium electrodes were smaller compared to the carbon electrodes in order to ease the cell assembly. The ratio between the electrodes was taken into account when calculating the specific capacity and charge rates. A gasket was placed together with a precut carbon electrode in the bottom coin cell case. Between 30 - 60 µL electrolyte was added to the electrode. Usually, an amount of 50 µL was sufficient to ensure proper wetting of the electrode. A separator of trilayer microporous polypropylene/polyethylene/polypropylene (Celgard® 2325) was placed on the wet electrode. The lithium electrode was then stacked on top of the separator before a stainless steel spacer (thickness: 0.3 mm) was placed on top of the cell in order to achieve electrical contact within the cell. The coin cell cap was assembled before the cell was sealed with an automatic crimping machine from Hohsen Corp. Open-circuit potentials of the half-cells were measured as an initial check to see if the cell could hold a potential. Short circuited cells would be discarded. The cell assembly was performed in an argon filled glove box ($O_2 < 0.1$ ppm, $H_2O < 0.1$ ppm). For the capacity calculations, the electrode mass was determined by subtracting the weight of the current collector from the total electrode mass. Multiple cells were manufactured for each configuration/parallel to ensure reproducibility.

4.3.5 Assembly of Test Cell for Electrochemical Impedance Spectroscopy and Cyclic Voltammetry.

Electrochemical impedance spectroscopy and cyclic voltammetry were performed with a three electrode setup. The cells were assemble in a HS-3E Test Cell from Hohsen Corp., see Fig. 4.7. The same electrode material used in the coin cells were also used in the test cell. Metallic lithium foil was used as both reference (diameter: 5 mm) and counter electrodes (diameter: 14 mm). Two layers of microporous PP/PE/PP trilayer membranes (Celgard 2325, (diameter: 22 mm)) were used to avoid short circuiting between the three electrodes. Between 50 µL - 100 µL electrolyte was used to properly soak the separators and wet the electrodes. More electrolyte had to be used for the test cells compared to the coin cells due to the electrolyte absorption of two separators. The electrolyte used was the same as for the coin cells. The open-circuit potential was measured to confirm a correct assembly of the test cell.

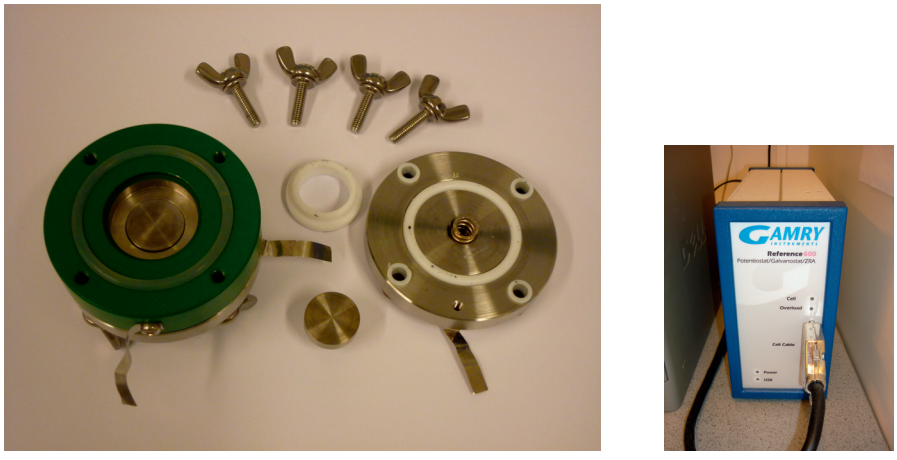

(a) (b)

Figure 4.7: a) A disassembled test cell from Hohsen Corp. used for cyclic voltammetry and electrochemical impedance spectroscopy. b) Gamry Reference 600 potentiostat™

4.3.6 Galvanostatic Measurements

The galvanostatic investigations were carried out using the assembled CR2016 coin cells in a Solartron Analytical 1480 Multistat. Several lithiation - delithiation cycles were performed at different rates. The cells were cycled between 1.5 V and 0.005 V. The end-of-discharge voltage was set to 0.005 V to avoid deposition of lithium metal. At least three parallels of the same electrode material were tested to obtain reproducibly data.

A typical charge pattern for the half cells involved initially slow rates and higher current rates for subsequent cycles as it was desirable to measure the capacity at various rates. The first cycle was set to 10 mA/g in order to allow formation of a complete solid electrolyte interphase. C-rates for subsequent cycles were C/20, C/10, C/5, C/2, and C corresponding to a theoretical capacity of 372 mAh/g in 20 h, 10 h, 5 h, 2 h, and 1 h, respectively. Each rate was cycled twice. All cycles were performed at room temperature.

Long-term cyclic performance was investigated on a selection of cells with a Maccor model 4200 Automated Test System. Each cell was cycled between 1.5 V and 0.005 V. The initial current was set at 10 mA/g before the cells were cycled 100 times at C/4.

4.3.7 Electrochemical Impedance Spectroscopy

The electrochemical impedance spectroscopy was carried out in using the assembled 3-electrode test cell and a Gamry Reference 600 potentiostat™. The impedance measurements for the carbon electrode were performed under open circuit voltage (OCV), 0.5 V, 0.2 V, and 0.005 V in a frequency range from 100000 Hz to 0.01 Hz at room temperature. The voltage perturbation was set to 5 mV and the measurements were collected with ten points per decade. All cells were monitored at OCV to stabilize electrolyte absorption and any potential film growth on the lithium counter electrode.

4.3.8 Cyclic Voltammetry

The experimental setup consisted of the same apparatus as described above in Section 4.3.7. Initially, the voltage was swept from open circuit voltage (OCV) to 0.4 V with a rate of 0.05 mV/s. At 0.4 V, the sweep rate was changed to 15 µV/s. The cell was cycled twice from from 0.4 V to 0.005 V. The measurements were performed at room temperature.

4.3.9 Differential Scanning Calorimetry

Differential scanning calorimetry (DSC) can be used to evaluate exothermic and endothermic reactions in a system. Lithiated and delithiated carbon electrodes were measured with DSC (PerkinElmer DSC 7). The electrodes were galvanostatically cycled with an initial charge and discharge of 10 mA/g (approximately C/37) and 5 subsequent cycles at C/4. The lithium carbon half-cells were disassembled inside an argon-filled glove box. 5 mm disks of both lithiated and delithiated carbon samples were punched out and weighed. The samples were sealed with gold plated copper seals into stainless steel capsules (PerkinElmer). The seal could withstand pressures of 150 atmospheres. Measurements were made from 30 °C to 400 °C with a heating rate of 2.5 °C/min. The capsules were weighed before and after analysis to detect potential leakage. An empty sealed capsule was used as a reference. Background scans (empty capsule) were taken prior to each sample. The background was subtracted from the corresponding sample analysis curve. The DSC equipment can be seen in Fig. 4.8.

(a) (b)

Figure 4.8: a) Photograph of DSC sample punching tool. b) DSC 7 for PerkinElmer with coolant system and a computer connected via TAC 7/DX Thermal Analysis Instrument Controller.

4.3.10 Thermal Conductivity Measurements

An in-house apparatus, see Fig. 4.9a, was used to measure thermal conductivity of different electrode materials. The apparatus is described in detail in Ref. [136]. The tested materials were three different carbon anodes and one $LiCoO_2$ cathode ($LiCoO_2$ on aluminum foil, MTI Corp.). The samples were

measured in both a dry and wet state with and without electrolyte. The wet electrodes were soaked with a mixture resembling an electrolyte used in lithium-ion batteries. To determine the thermal conductivities of the electrode material, a constant heat flux method was used. The apparatus is designed to record heat fluxes in only one dimension as it is thermally insulated in the radial direction.

Disks of electrode material were cut out with a diameter of 21 mm, see Fig. 4.9b. The apparatus was kept under pressure overnight to avoid expansion of the thermal collectors. The pressure was released before the apparatus was disassembled. Further on, electrodes were stacked together in pairs with the active material pressed together on the bottom steel cylinder. The stacking height was set by the desired number of pairs. Two micrometer gauges (Mitutoyo Digimatic Indicator ID-C Series 543) were used to measure the stack thickness. The solvent mixture was added in between the active material if the measurements were performed for soaked electrodes. The solvent was an equigravimetric mixture of ethyl- and diethyl-carbonate without the hygroscopic $LiPF_6$-salt. For each pair, the mixture was deposited on one electrode until the it was soaked before the other electrode was placed on top of the first one. The apparatus was put back together. In the soaked case, electrodes and steel cylinders were wrapped in parafilm® to avoid evaporation of the solvent. An outer thermal insulation tube was fitted in the end. A pressure of 9.3 bar was to applied to the stainless steel cylinders to ensure good thermal contact. The compression was set with a pneumatic piston. Thermal conductivity was measured within a certain time interval for the soaked electrodes to check if the system obtained a steady state. The dry electrode measurements were not time dependent. The temperature differences and heat fluxes were measured with eight thermocouples (type K) placed in the steel cylinders as indicated in Fig. 3.22a. The temperatures were recorded 30 times with a 30 s interval using an Agilent Acquisition Switch Unit 34970A. The last 20 recordings were used to calculate an average temperature and its standard deviation. These values were used for further calculations of thermal resistivity. The total heat flux was controlled by the water temperature at each end of the apparatus. The heating and cooling waters were set to 35 °C and 10 °C, respectively.

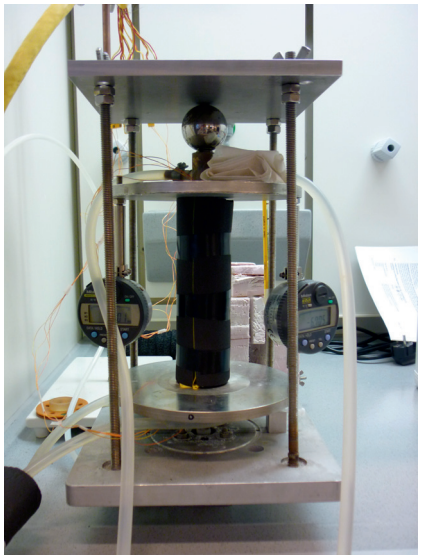

(a)

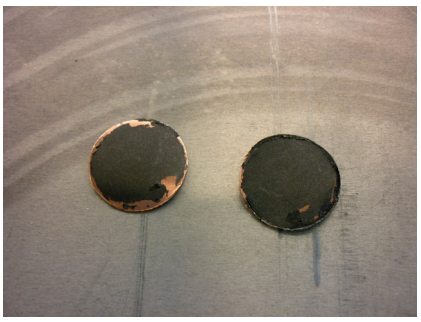

(b)

Figure 4.9: a) Experimental setup for thermal resistance measurements. A schematic representation of this setup is given in Fig. 3.22. b) A pair of typical samples used in this setup after testing.

Chapter 5

Results

5.1 Carbon Cones

5.1.1 Basic Grade Carbon Cones

From the original raw carbon cones production, a relatively large, but limited amount of carbon material was produced. In this material, carbon cones, carbon disks, and carbon black were observed. Several different batches of this mixture were produced with varying quality. The quality depended on the time of production, meaning that the material changed characteristics during fabrication. Two different batches were saved for future applications and analysis. Both samples have been utilized for the lithium-ion battery related experiments in this work. One batch which consists of mainly high quality carbon cones is referred to as "basic grade" carbon cones, while the second batch consisting of low quality material is called "low grade" carbon cones. In general, basic grade carbon cones have been utilized if nothing else is specified. The amount of carbon cones structures was approximately 20 % , while the amount of carbon disks and carbon black were around 70 % and 10 %, respectively in the highest quality basic grade batch [137]. This result was obtained by merely counting the various structures observed in SEM images. This particle distribution is somewhat uncertain due to the method used to acquire these results. It is believed that also the low grade material has the same cone/disc/carbon black ratio. The difference between the two materials is mainly the amount of disordered carbon covering the structures of which the low grade carbon cones are covered

with a thicker layer of disordered carbon compared to the basic grade. These observations are done with FEGSEM.

Fig. 5.1. shows a typical overview of the as-produced basic grade carbon cones material. The arrows indicate clearly the different components.

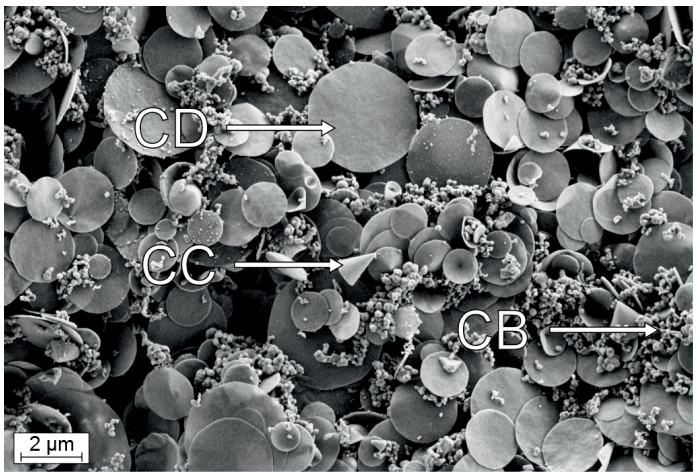

Figure 5.1: An overview FEGSEM image of untreated basic grade carbon cones from the Kværner carbon black and hydrogen process. CC indicates the position of the carbon cones, while CD and CB pinpoints the carbon disks and carbon black, respectively.

The carbon cones with different apex angles can be seen in Fig. 5.2 - 5.7. The five different cone structures correspond to the 60° disclinations of the honeycomb structure as predicted by theory, see Section 3.1.7. The circular disks can be regarded as planar cones.

The typical cone size varies between 500 nm to 2 µm in diameter at the base of the structure, while the height can vary from 500 nm to 5 µm, and the total wall thickness is measured to be 50 nm to 150 nm. Cone dimensions are highly dependent on the apex angle as it defines the shape. The carbon disks have a diameter of 500 nm to 4 µm and a wall thickness similar to that of the cones.

Both the cones and the disks consist of two parts, an inner core and an outer shell, where the core can be regarded as piles of stacked cones/disks. The outer shell consists of very disordered carbon, which can easily be graphitized upon heat treatment. For a cone core, it is predicted that the inter-spacing distance

between the layers is 3.4 Å [50]. Diffraction analysis indicate that 10 % to 20 % of the scattered intensity comes from the crystaline core [53]. The core can then be estimated by simple calculations to be between 15 to 85 graphene sheets thick.

Transmission Electron Microscope

Transmission electron microscope (TEM) images were taken of the original basic grade carbon cones batch. The TEM images show distinctly different types of cones and their apex angles, see Fig. 5.2 - 5.7. Fig. 5.7 is a close-up of the apex of Fig. 5.6 where it is possible to distinguish the different carbon layers from each other, as well as observing the curvature of the carbon layer within the area of the apex angle. The TEM images also show signs of carbon disks and carbon black. The carbon covered copper lattice of the perforated grid sample holder can be seen in the background.

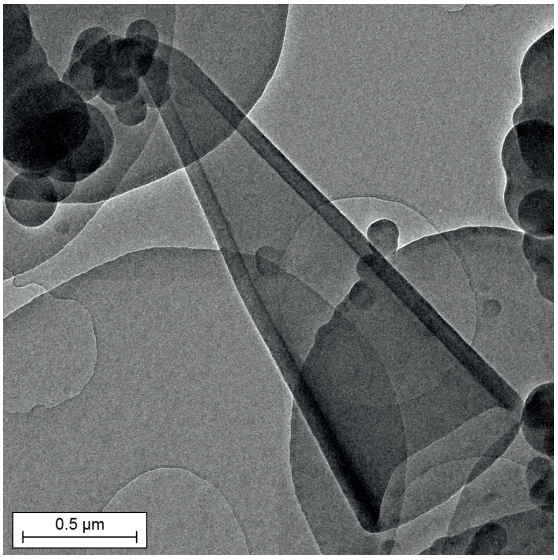

Figure 5.2: Transmission electron microscope image of a carbon cone with the theoretical apex angle of 19.2°.

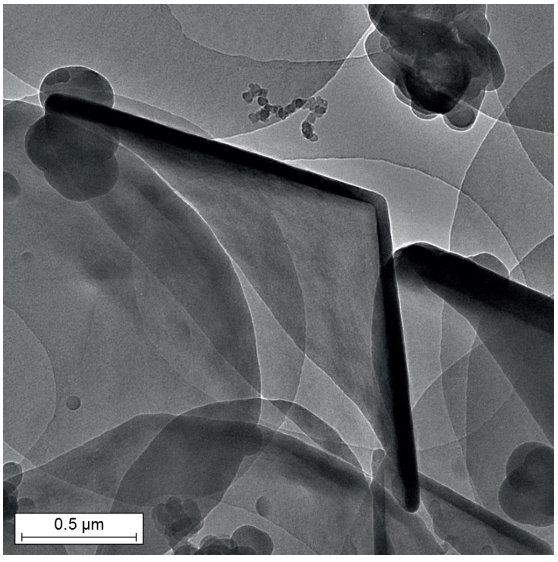

Figure 5.3: Transmission electron microscope image of a carbon cone with the theoretical apex angle of 112.9°.

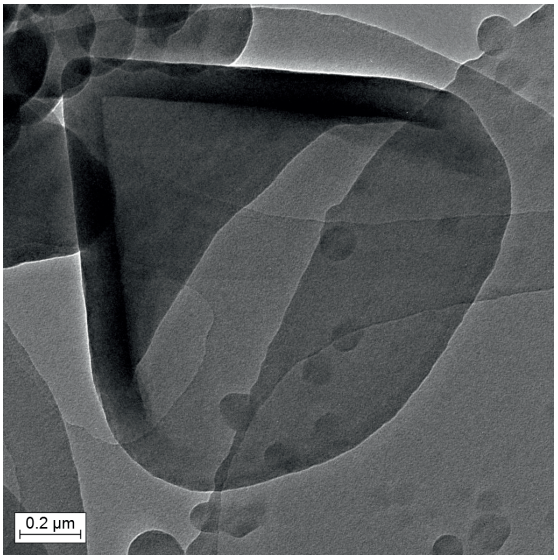

Figure 5.4: Transmission electron microscope image of a carbon cone with the theoretical apex angle of 60.0°.

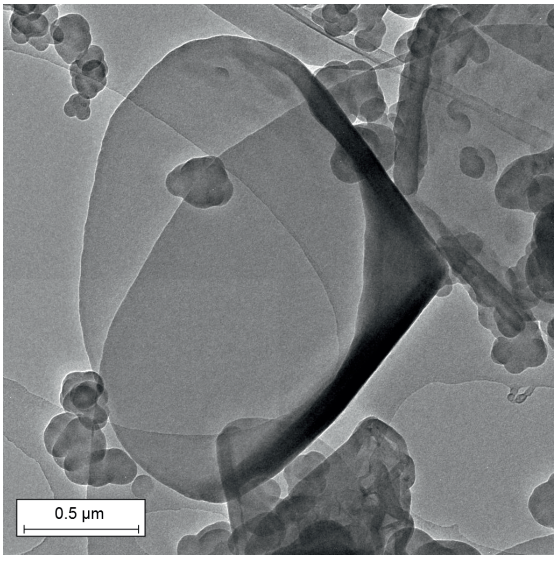

Figure 5.5: Transmission electron microscope image of a carbon cone with the theoretical apex angle of 83.6°.

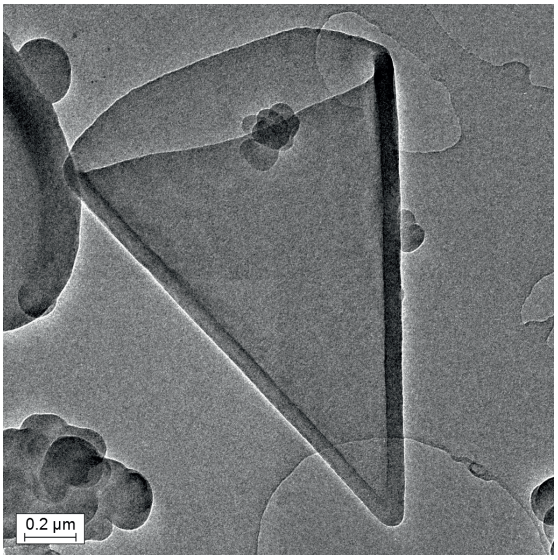

Figure 5.6: Transmission electron microscope image of a carbon cone with the theoretical apex angle of 38.9°.

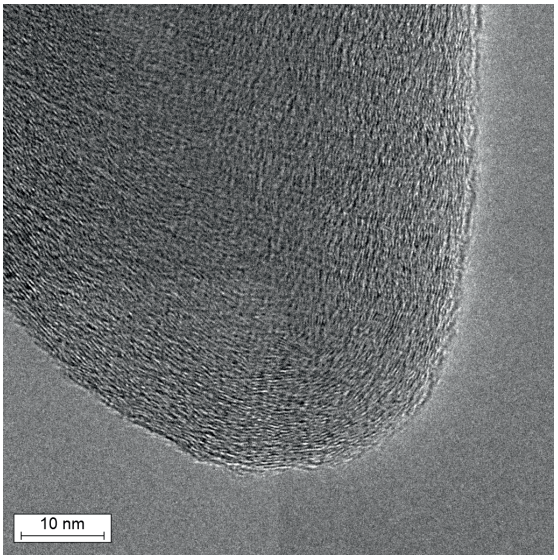

Figure 5.7: High resolution image of the apex of the cone shown in Fig. 5.6.

5.1.2 Low Grade Carbon Cones

Low grade carbon cones were produced at a later phase compared to the basic grade carbon cones. The low grade carbon cones are similar to the basic grade carbon cones in shape and size, but the components in the low grade carbon cones are thicker than those of the basic grade material. The distinctly different parts can be seen in Fig. 5.8. The typical size of the low grade carbon cones is of the same order of magnitude as for basic grade carbon cones. However, the wall thickness is measured with FEGSEM to be around 200 nm.

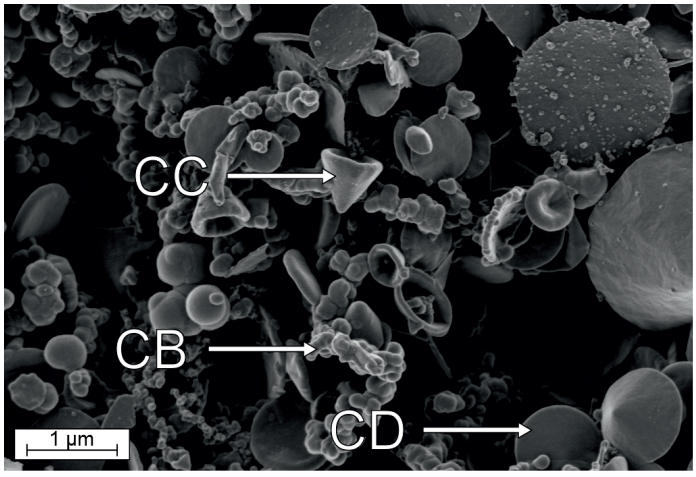

Figure 5.8: FEGSEM image of untreated low grade carbon cones from the Kværner carbon black and hydrogen process. The different components are covered with a thicker layer of disordered carbon compared to the basic grade carbon cones. CC, CD, and CB represent carbon cones, carbon disks and carbon black, respectively.

5.1.3 Abnormal Basic Grade Carbon Cones

Even though the majority of the carbon cones are perfectly symmetric and follow the theoretical predictions given in Section 3.1.7, there are a minute amount of anomalous cones present in the material, see Fig. 5.9 to Fig. 5.12. Non-symmetrical cones can provide important information on the initial cone formation process as discussed in Section 6.1.1. Fig. 5.9 shows what was initially a cone with an apex angle of 38.9°. However, an introduced pentagon

defect changes the structure to a cone with 19.2° apex angle. On the left side of Fig. 5.10, it is possible to see the same cone growth development where a 19.2°cone has been transformed into a tube by the introduction of an extra pentagon defect. Fig. 5.11 depicts a cone with 60° starting angle. As a pentagon defect is introduced, the cone closes into a 38.9°cone. Fig. 5.12 shows a 83.2°cone with two pentagon defects leading to a 19.2°cone.

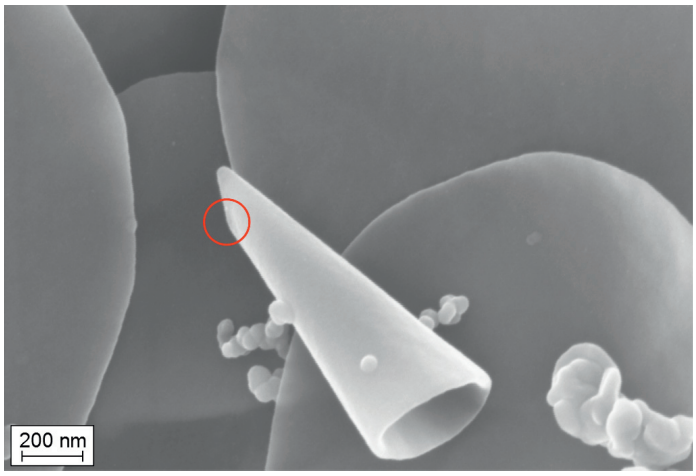

Figure 5.9: A FEGSEM image of a carbon cone with an extra encircled pentagon defect changing the cone structure.

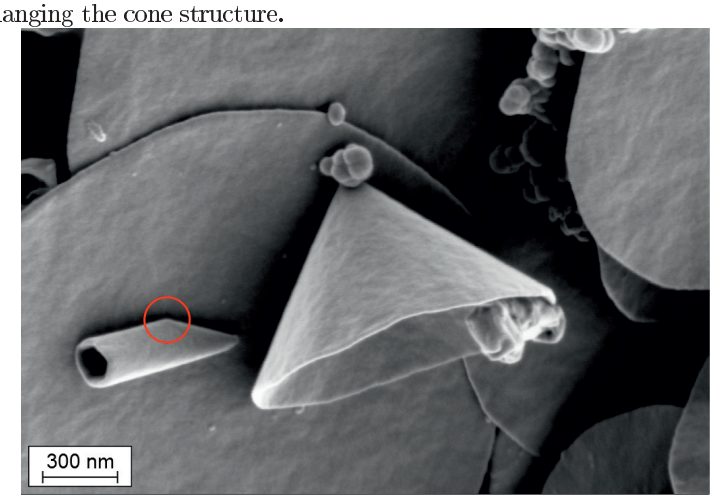

Figure 5.10: A FEGSEM image showing on the left side of the image, a carbon tube with an 19.2° apex angle closure. The transition is enabled with an encircled pentagon defect.

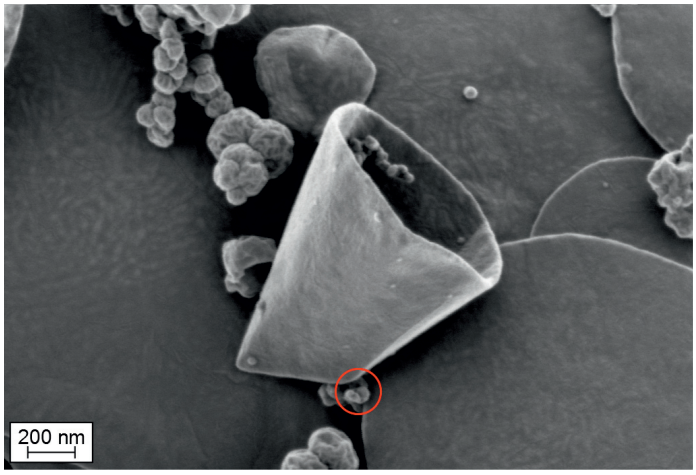

Figure 5.11: A FEGSEM image of a 60° carbon cone which is transformed into a 112.9° cone by a pentagon defect.

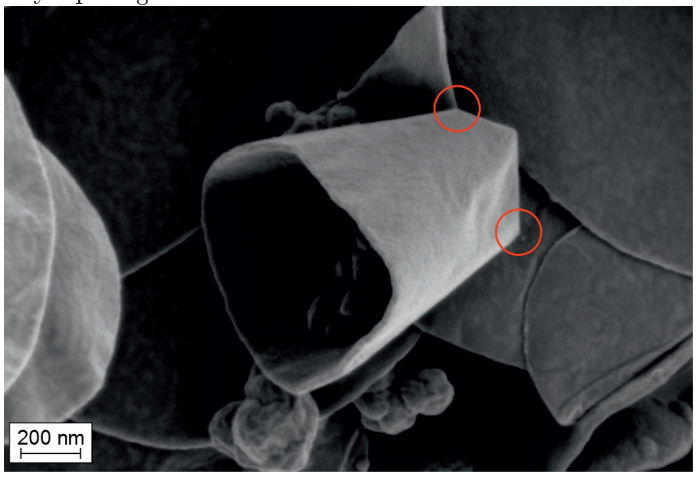

Figure 5.12: A FEGSEM image of two single pentagons defects which are responsible for the closure of a 83.2° cone.

5.2 New Carbon Cones Production Attempts

The initial goal of this work was to reproduce the original carbon cones material. 29 experimental attempts in total were carried out over the duration of approximately one year. The trial runs were performed in a hot plasma reactor by employing the plasma to a pyrolysis process of hydrocarbons. Selected images of the samples are shown in this section. The produced samples contained mostly various grades of carbon black as seen in Fig. 5.13. However, small quantities of carbon nanotubes were also found, see Fig. 5.24. No considerable amount of cones or disk were produced or observed in the new reactor batches. However, some conical-like structures were found on the inner reactor lining. The new structures are typically 50 µm long and 10 µm in diameter. They resemble a stack of several conical structures, much like a stack of pancakes or in the shape of a cigar. The stacks are similar to the carbon structures reported by Ohtani *et al.* [8].

The electron microscope images in the subsequent sections show several types of carbon structures, see Fig. 5.13 - 5.24. The field emission gun scanning electron microscope (FEGSEM) was extensively used because of its sufficiently high resolution and its simple procedure for sample preparation. Several FEGSEM recordings were taken after each reactor trial with the purpose of discovering fresh batches of cones. Unfortunately, no considerable amount of cones was found. The images below in the subsequent sections show various carbon products found in the bag filter and the inner parts of the reactor.

Some remaining oil derivates were also observed with the naked eye in the filters from the reactor outlet. These findings indicate that the test run did not succeed due to the incomplete pyrolysis of the oil derivate. Gas measurements obtained during the trail runs show that the hot torch plasma reactor also produces small amounts of other compounds such as light hydrocarbons, hydrogen sulfide, and naphthalene [58].

Further details regarding process parameters and reactor modifications can not be given due to proprietary issues.

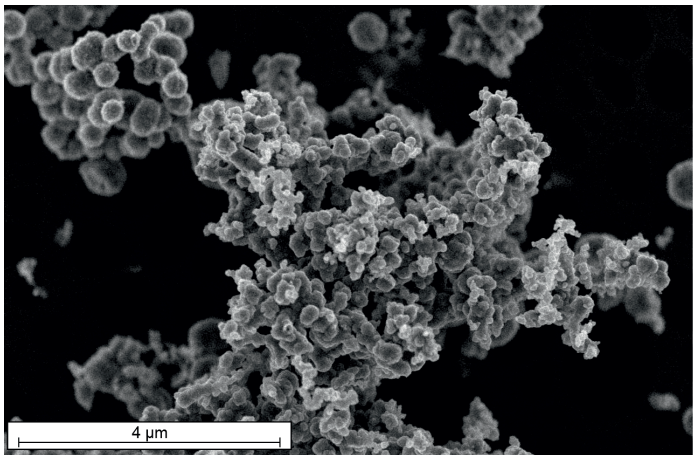

Figure 5.13: An overview FEGSEM image of a typical sample from trial run 21.

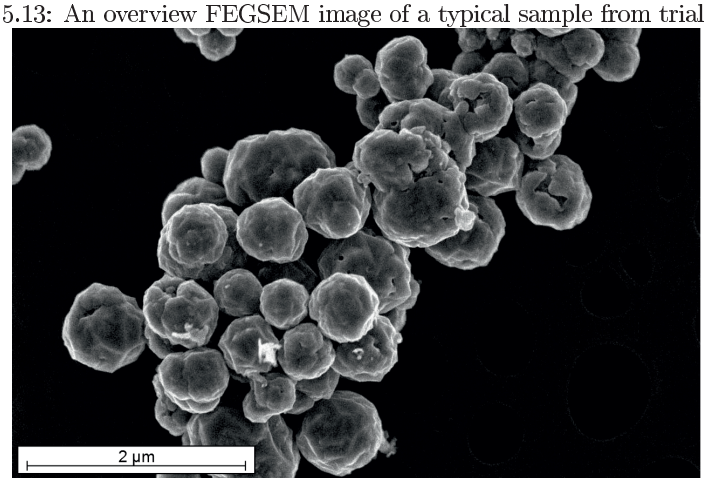

Figure 5.14: A close-up FEGSEM image of a typical sample from trial run 21.

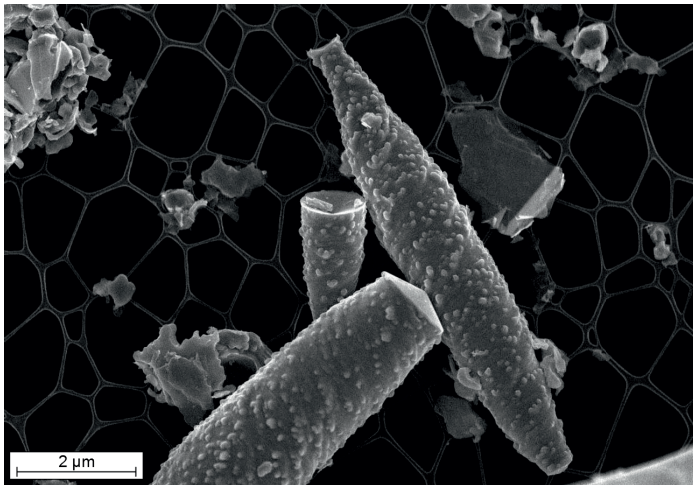

Figure 5.15: Stack of carbon with a high aspect ratio collected in the bottom tray of the reactor after trial run 24.

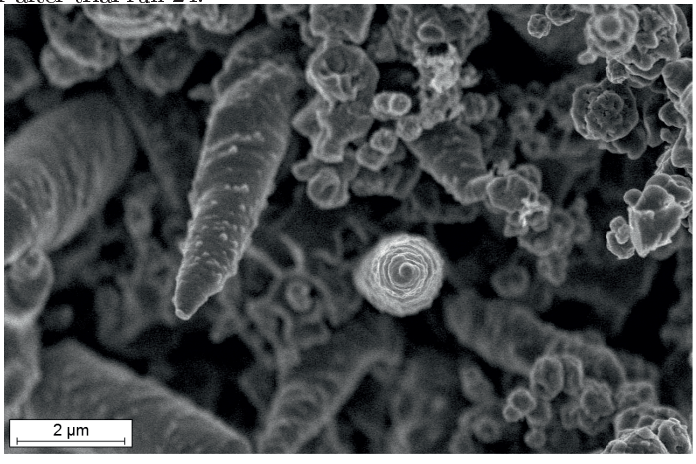

Figure 5.16: FEGSEM image of carbon scrolls found inside the reactor from trial run 21.

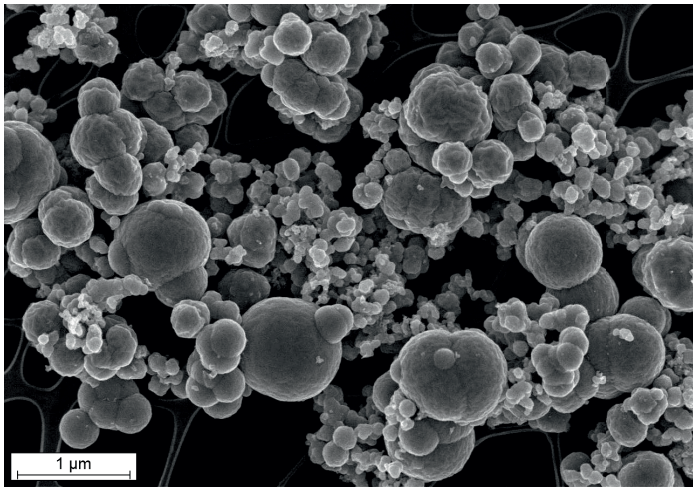

Figure 5.17: Typical reaction product of spherical particle of different sizes found in the bag filter from trial run 24.

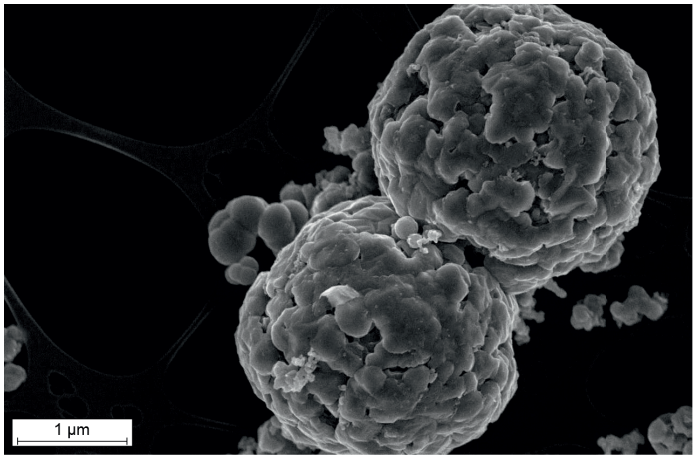

Figure 5.18: Spherical particles from trial run 23 where it seems that the particle growth is caused by patches of added carbon.

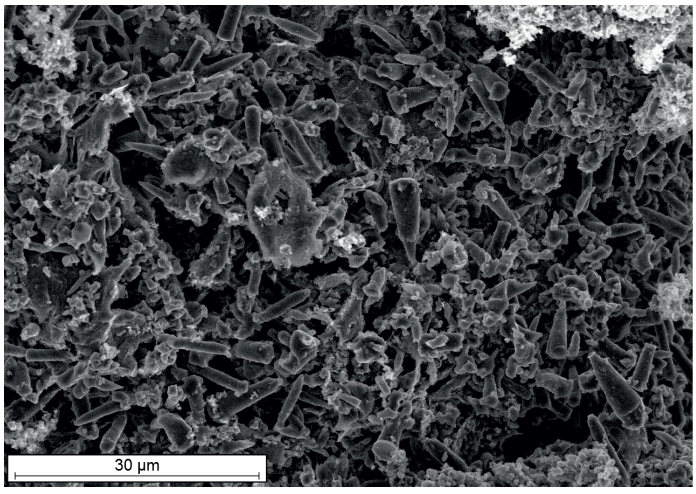

Figure 5.19: An area with high density of carbon stacks. The material was found in the reactors bottom flange after trial run 25.

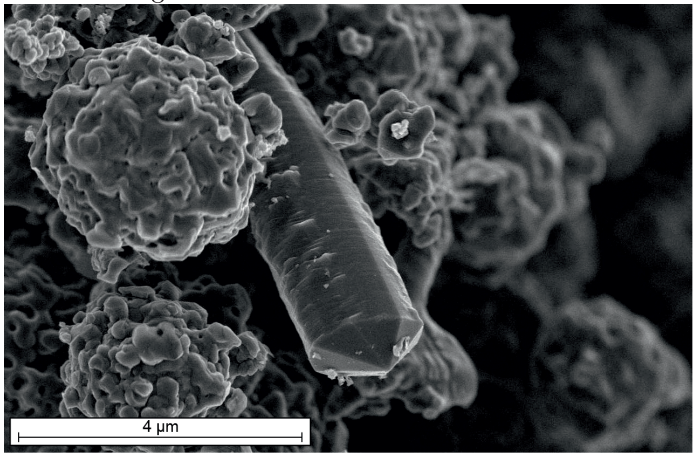

Figure 5.20: A close-up of a carbon stack from trial run 17. The material is collected from the inner lining of the reactor.

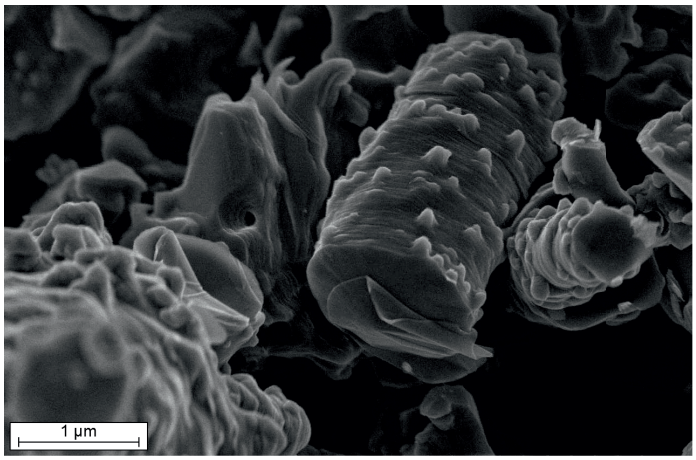

Figure 5.21: A stack of carbon where one layer has become separated from the rest.

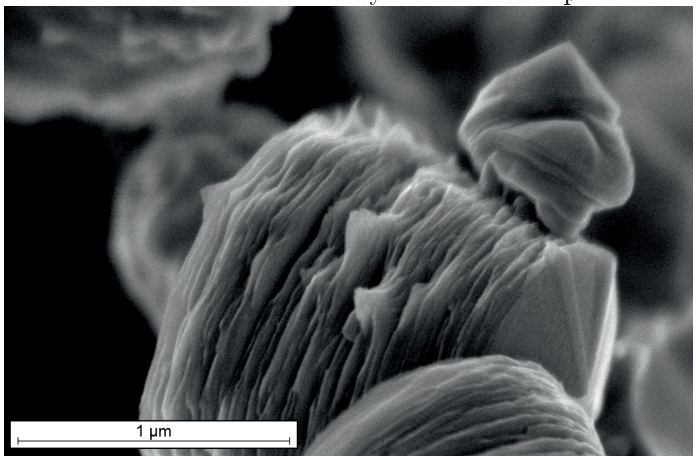

Figure 5.22: Another stack of carbon, which are similar to the layers of exfoliated graphite.

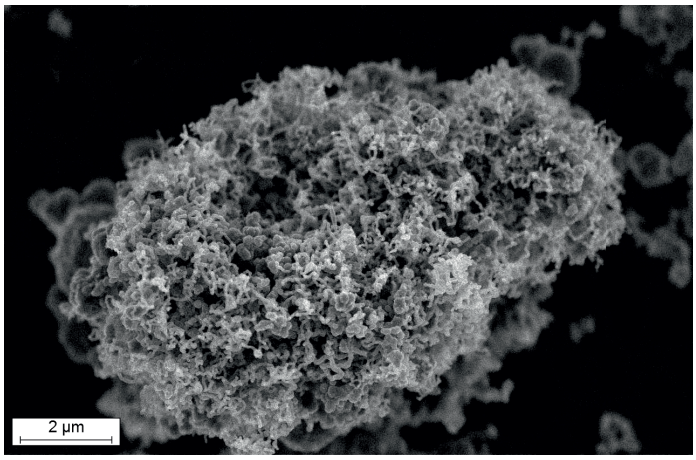

Figure 5.23: FEGSEM image of nanofibers found in the filters from trial run 21.

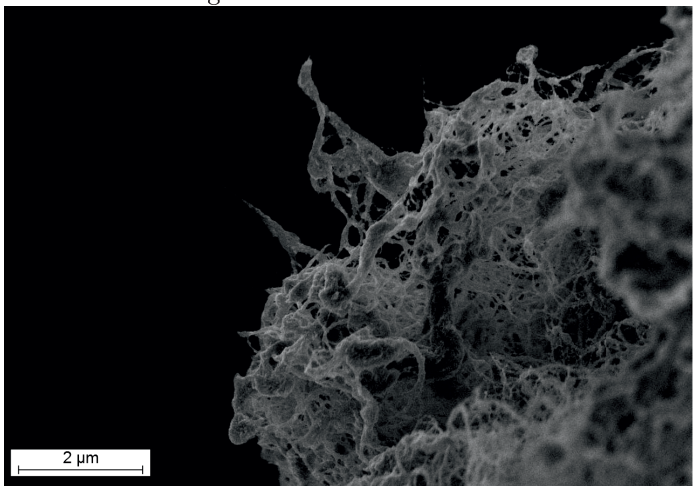

Figure 5.24: A net of carbon nanotubes found in the bag filter after trial run 26.

TEM Images of Carbon Material From the New Carbon Cones Production Attempts

Transmission electron microscope images were also captured of the newly formed materials. The typical free single particle carbon cones structures were not found. However, some conical shapes were observed, see Fig. 5.25 and 5.26. Fig. 5.25 shows the distinct structure of the 112.9°cone. Single layers of carbon can also be observed. These specific images are from trial run number 20 and the samples are collected from the inner wall of the reactor.

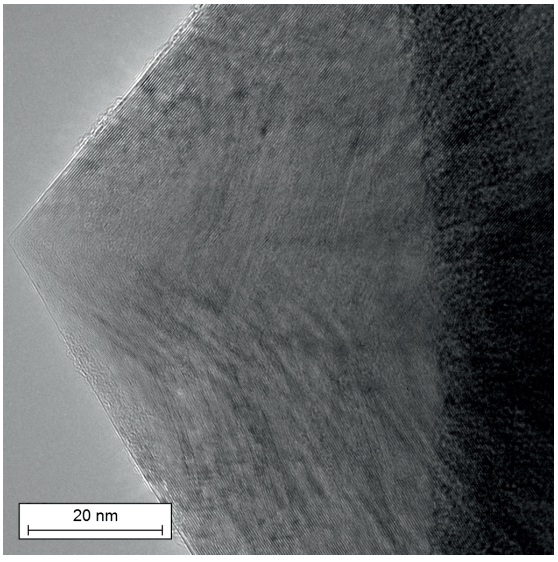

Figure 5.25: High resolution TEM images of a conical shape found inside the reactor. The apex angle indicates the presence of a single pentagon carbon ring structure.

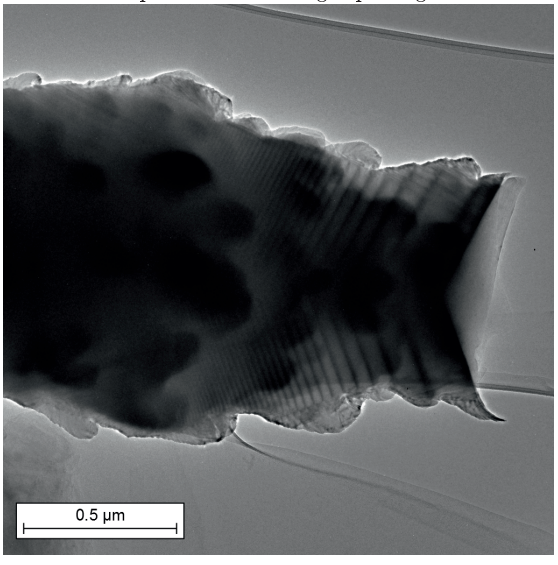

Figure 5.26: High resolution TEM images of structures similar to herringbone shaped carbon fiber [8].

5.3 Characterization and Modification of Carbon Cones

5.3.1 Post Treatment of Carbon Cones

The two carbon cones materials, namely basic grade and low grade, were treated in various ways to study the effect on the cell properties when used as anode material in lithium-ion batteries. A test tree diagram is devised to ease the understanding of the relations between the different samples, see Fig. 5.27. Both the basic grade carbon cones and low grade carbon cones have been modified in different manners, However, the emphasis has been on basic grade carbon cones. Each material has been given a specific short name as shown in Table 5.1. It is important to point out that none of the newly produced material, i.e. carbon stacks (from the SINTEF reactor) were tested as electrode material.

Table 5.1: Table of short names and corresponding sample treatment. The carbon materials have been heat treated in an argon atmosphere for 3 h if not otherwise specified.

Short name	**Description**
CCRAW	Untreated basic grade carbon cones.
CC950	Heat treated at 950 °C.
CC1800	Heat treated at 1800 °C.
CC2000	Heat treated at 2000 °C.
CC2200	Heat treated at 2200 °C.
CC2700	Heat treated at 2700 °C.
5050CCRAWCC2700	50 wt% of CCRAW and 50 wt% of CC2700.
CC900Air	CCRAW oxidized at 900 °C in air for 1 h.
CC900Ar-Air	CC900Air heat treated at 900 °C for 1 h.
CC900Air2700	CC2700 oxidized at 900 °C in air for 1 h.
CCH2O2	CCRAW treated in hydrogen peroxide.
CCHNO3	CCRAW treated in nitric acid.
CC-Func	CCRAW functionalized with oxygen.
CC900-Func	CC-Func heat treated at 900 °C for 1 h.
MWCCAr	CCRAW microwave treated in argon atmosphere.
MWCCAir	CCRAW microwave treated in air atmosphere.
LGCC	Untreated low grade carbon cones.
LGCC2700	Low grade carbon cones heat treated at 2700 °C.

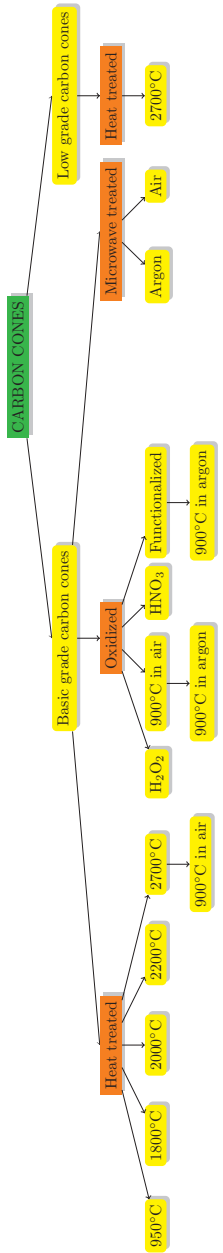

Figure 5.27: A tree diagram of the various carbon cones samples with the as-produced basic grade and low grade carbon cones as starting material. Yellow boxes refer to the tested material, while orange boxes represent the different treatment categories. A combination of untreated and heat treated basic grade carbon cones (5050CCRAWCC2700, see Table 5.1) has also been tested.

5.3.2 Heat Treatment of Carbon Cones

Some samples studied in this work were heat treated at high temperatures in flowing argon gas at atmospheric pressure in order to study the effect on the carbon structure and subsequent performance in lithium-ion batteries. Different temperatures at large intervals were chosen including 950 °C, 1800 °C, 2000 °C, 2200 °C, and 2700 °C. The samples were investigated by FEGSEM to investigate any morphological changes induced by the heat treatment. Images of basic grade carbon cones heat treated at 2700 °C are shown in Fig. 5.28 and 5.29. Facets can be seen which indicate a crystalline structure.

5.3.3 X-Ray Diffraction

X-ray powder diffraction (XRD) was performed on several different carbon samples in order to investigate structural changes. The X-ray diffractograms for all of the heat treated basic grade carbon cones samples are given in Fig. 5.30, along with the diffractogram of the untreated material. The untreated material (CCRAW) as well as the CC950 have a broad peak at 26°. As the heat treatment temperature increases, this peak becomes sharper and more intense. For the samples heat treated at higher temperatures (1800 °C and above), the diffractograms show small peaks at 42° and 54° in addition to the peak at 26°.

XRD data from the oxidized samples have also been obtained. The results are presented in Fig. 5.31. All the diffraction responses are identical to the untreated carbon cones with the main signal contribution at 26°. One exception might be the CC-Func sample which has a slightly broader 26° peak, and a small diffraction line at 42° can also be seen.

Fig. 5.32 represents the XRD results from the low grade carbon cones and the microwave treated carbon material. MWCCAr, MWCCAir, and LGCC are very similar to the untreated basic carbon cones with a weak diffraction line at 26°. The heat treated low grade carbon cones (LGCC2700) show a strong peak at 26° and two weaker peaks at 42° and 54°.

5.3.4 Raman Spectroscopy

Raman spectra have been obtained to characterize the surface structure of the different electrode materials used in the carbon/lithium half-cells.

The Raman spectra of the heat treated carbon cones are depicted in Fig. 5.33. Two peaks are present in all the measurements; the D-band at 1330 cm^{-1} and

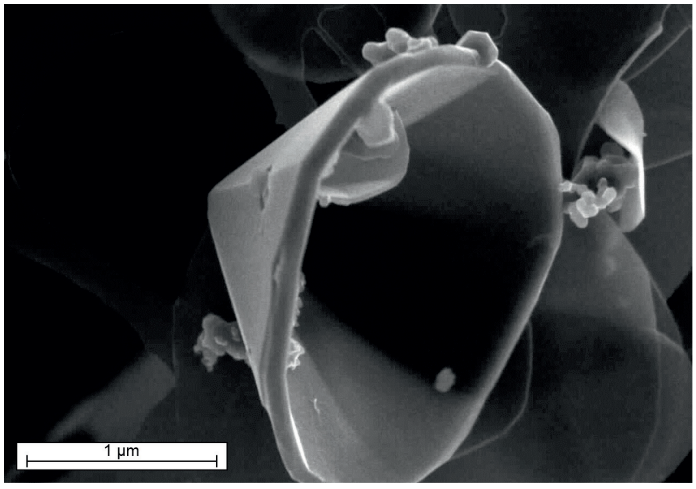

Figure 5.28: FEGSEM image of a single cone heat treated at 2700 °C in argon. Facets are clearly visible.

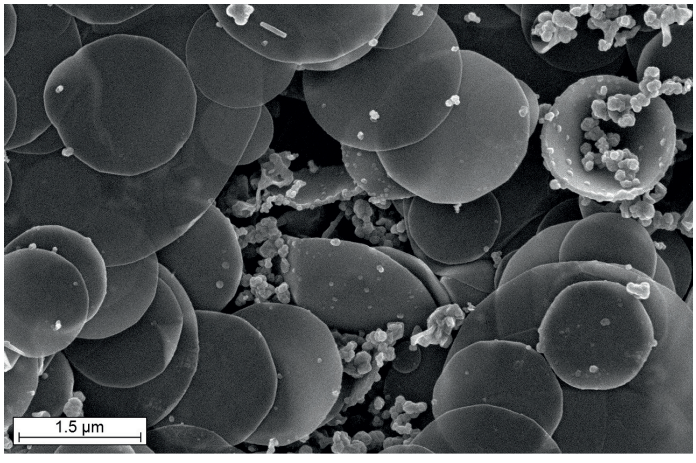

Figure 5.29: An overview FEGSEM image of mainly carbon disks annealed at 2700 °C in argon.

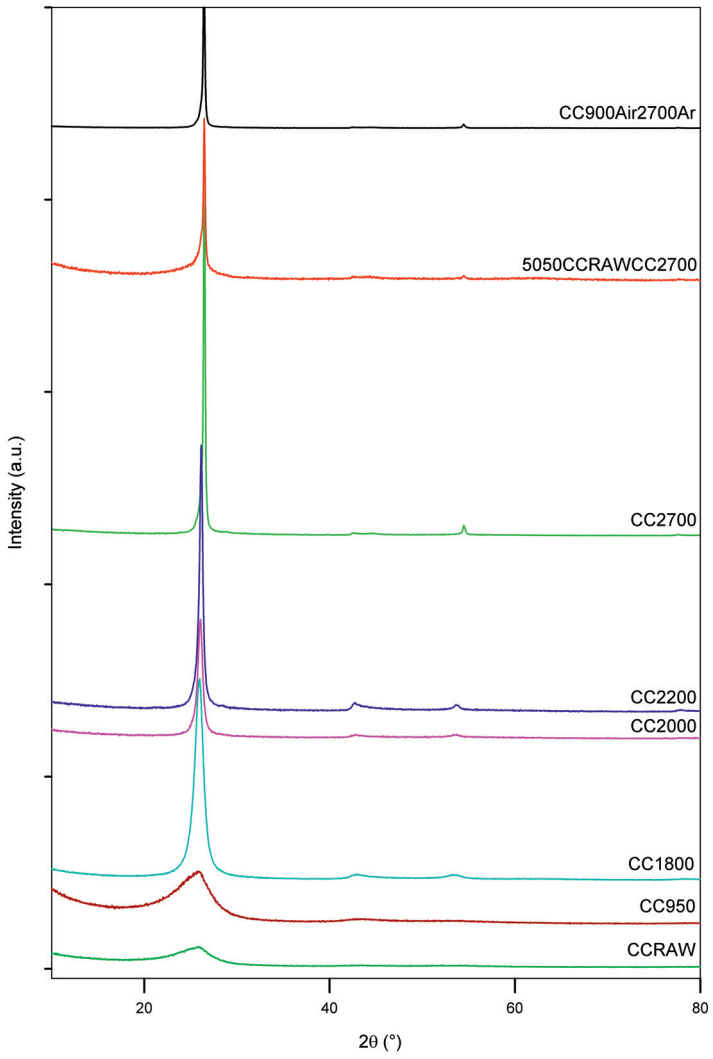

Figure 5.30: Powder X-ray diffractograms of the heat treated carbon cone samples and the air oxidized 2700 °C sample along with a reference diffractogram of the untreated sample (CCRAW).

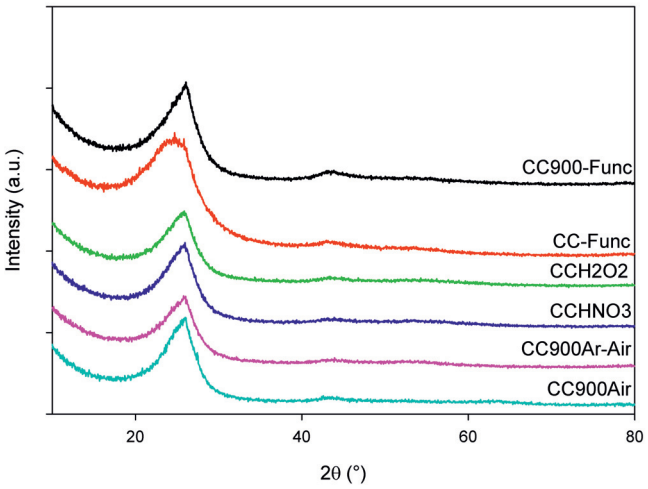

Figure 5.31: Powder X-ray diffractogram of the different oxidized carbon cones materials.

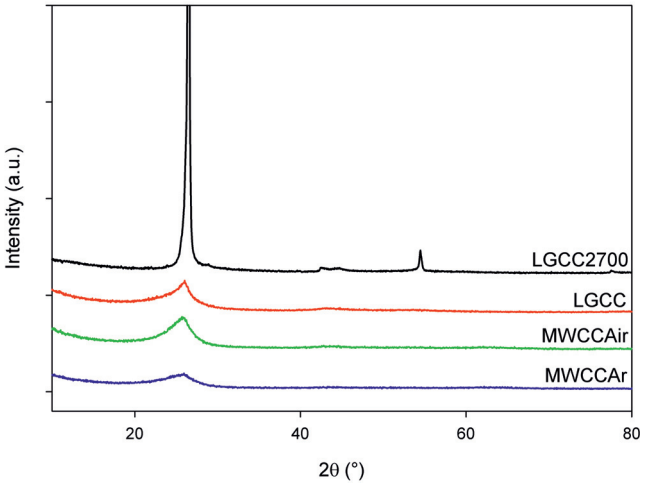

Figure 5.32: Powder X-ray diffractogram of the microwave treated and the low grade carbon cones materials.

the G-band at around 1580 cm^{-1}. Some spectra also contain the D'-band at 1620 cm^{-1}. The Raman intensities of the different samples vary greatly. However, there is a trend showing a stronger G-band peak compared to the D-band peak with increasing heat treatment temperature. This trend is best presented in Fig. 5.34 in which the intensity ratios are represented. The electrode containing 50 wt% untreated basic grade carbon cones and 50 wt% of basic grade carbon cones heat treated at 2700 °C (5050CCRAWCC2700), as shown in Fig. 5.33, shows features from each constituent. The large D-band of the basic grade carbon cones overshadows the D-band of the heat treated sample, while the G-band of the heat treated sample dominates the G-band signals. The oxidized and heat treated sample (CC900Air2700) does not show large differences compared to the material which is only heat treated (CC2700). In addition to the observed changes in intensity, the full width half maximum (FWHM) of the G-band deceases with heat treatment temperature. Also, many of the spectra show a shoulder peak on the G-band peak at around 1620 cm^{-1}.

Raman spectra for the other oxidized materials are presented in Fig. 5.35. Both the D-band and the G-band are present in all the spectra. The G-band of the 900 °C air oxidized sample has increased after subsequent heat treatment at 900 °C in argon (CC900Ar-Air). The samples which are chemically treated with H_2O_2 (CCH2O2) and HNO_3 (CCHNO3) show similar D-band/G-band ratios. However, the spectra of the HNO_3 sample has an additional peak close to the D-band. The effect of heat treating the functional carbon cones at 900 °C in argon (CC900-Func) seems to have little effect on the Raman spectra compared to the sample without heat treatment (CC-Func). Any possible shoulder peak for these samples are overshadowed by the width of the G-band.

The untreated low grade carbon cones sample (LGCC) has D-band and G-band of similar intensity. The heat treated low grade sample (LGCC2700) has a much larger G-band peak compared to its D-band peak. A shoulder peak is also present in this particular spectrum. Raman spectra are also obtained for the low grade carbon cones and the basic grade carbon cones treated with microwave radiation. Microwave radiation in neither air nor argon seem to significantly influence the Raman spectrum.

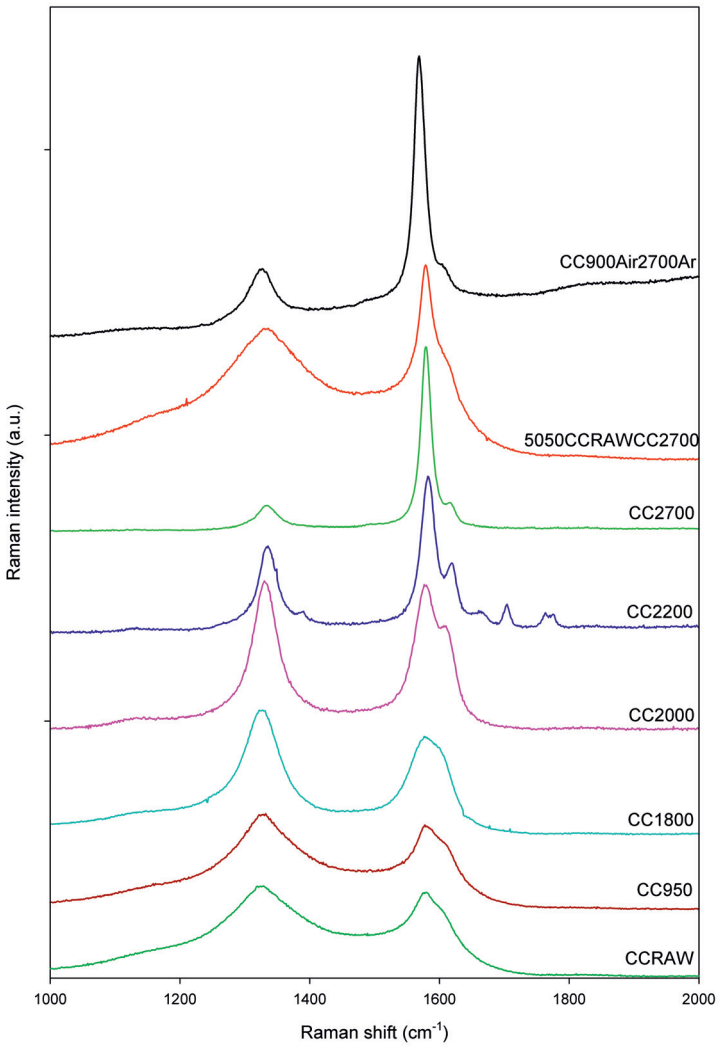

Figure 5.33: Raman spectra of the heat treated carbon cone electrodes and the sample oxidized in air at 900 °C followed by heat treatment in Ar atmosphere at 2700 °C (CC900Air2700Ar).

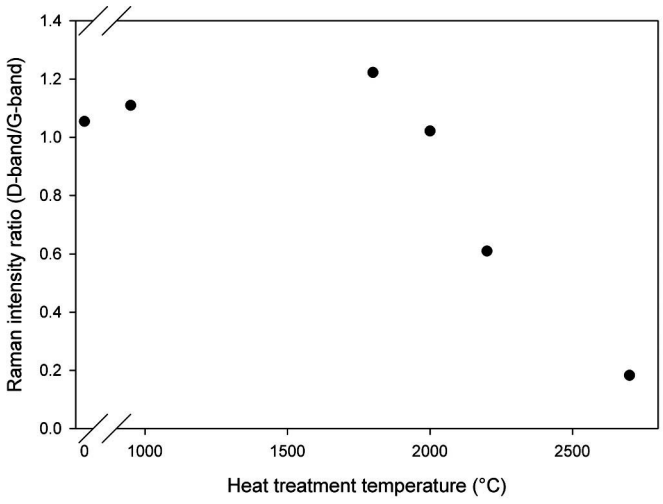

Figure 5.34: Raman intensity ratios of the D-band and G-band as a function of heat treatment temperature

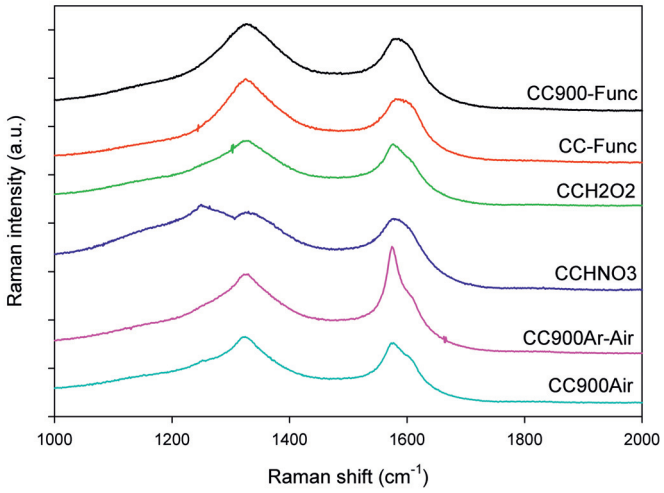

Figure 5.35: Raman spectra of the different oxidized carbon cones electrodes.

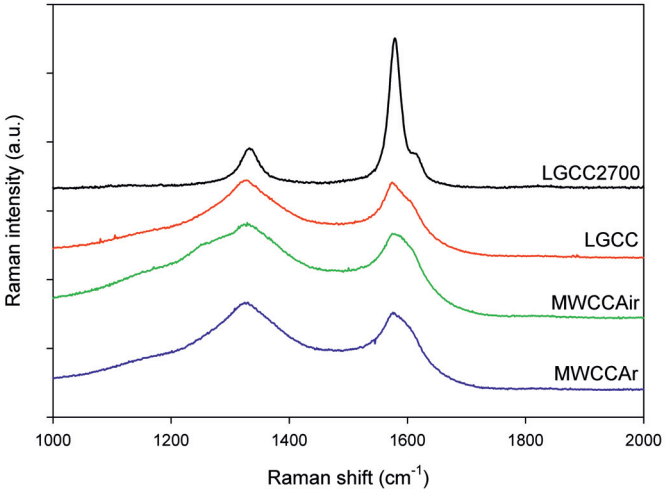

Figure 5.36: Raman spectra of the microwave treated and the low grade carbon cones electrodes.

5.3.5 Nitrogen Adsorption Measurements (BET)

The BET (Brunauer, Emmett, and Teller) specific surface area (m^2/g) has been measured for heat treated basic grade carbon cones samples. Specific surface area decreases from approximately 20 m^2/g for non heat treated carbon cones to 14.5 m^2/g for 2700 °C treated samples, see Fig. 5.37. The reported uncertainties are calculated from the corresponding adsorption isotherms given by the measurements. Table 5.2 shows the specific surface area of selected materials.

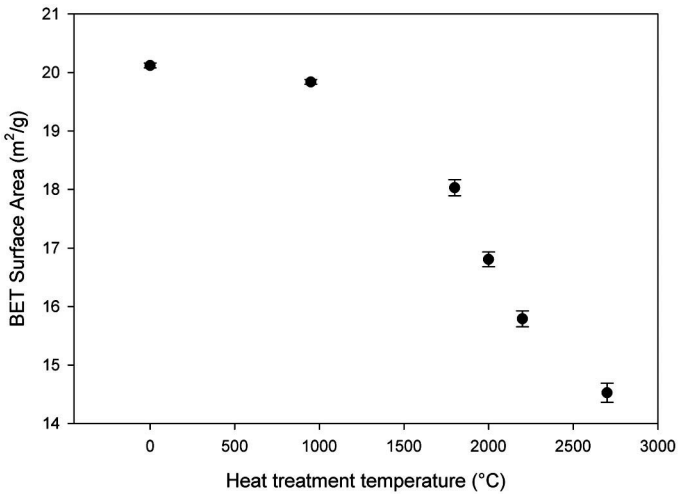

Figure 5.37: The BET specific surface area (m^2/g) as a function of the heat treatment temperature.

Table 5.2: Specific surface area of selected carbon materials.

Carbon type	**BET surface (m^2/g)**
CC900Air	89.16 ± 0.92
MWCCAr	20.08 ± 0.04
MWCCAir	21.64 ± 0.03
LGCC	12.41 ± 0.03
LGCC2700	10.94 ± 0.09

5.3.6 Bulk Density Measurements of Carbon Powder

The density of several carbon materials were tested with the intention to further characterize the material and find a relation between density and battery performance. The bulk densities were measured with a modified Scott Volumeter. The results are given in Table 5.3. The densities for the commercial graphite are compared to the values given by the manufacturer.

Table 5.3: Table of apparent density of different carbon powders.

Carbon powder	**Measured density (g/cm^3)**	**Density from manufacturer (g/cm^3)**
CCRAW	0.04	–
CC2700	0.07	–
SLP30	0.39	0.32 [138]
SLP50	0.49	0.40 [138]

5.4 Carbon/Lithium Half-Cells

5.4.1 Charge/Discharge Measurements

All the cell were assembled as described in Section 4.3.4 prior to testing. The initial discharge and charge were performed at a slow rate of 10 mA/g (C/37.2), in order to ensure complete formation of the SEI in the first cycle. The cells were discharged from open circuit potential down to 5 mV before charging to 1.5 V. Subsequent cycles, between 1.5 V and 5 mV, were performed at C/20, C/10, C/5, C/2, and C, unless otherwise stated. Some cells were cycled with a low current rate at the end of the testing procedure to confirm regained capacity after fast cycles. All cycles were performed galvanostatically during both discharge and charge and the cell was allowed to rest at open circuit voltage for 1 min between each cycle. All cells were tested at room temperature. Several parallels were made to ensure reproducibility. The standard deviations are calculated from the duplicates and represented as error bars. The error bars are presented in the cyclic figures and its corresponding value is given in Table 5.4 and 5.5.

Basic Grade Carbon Cones

Untreated (CCRAW) As produced carbon cones samples were tested as anodes in carbon/lithium half-cells. The results of a typical half-cell are shown in Fig. 5.38. The first discharge capacity is 632 mAh/g when discharging at 10 mA/g. The irreversible capacity for the first cycle is 253 mAh/g or 40 % of the initial discharge capacity. The first discharge curve has a kink starting at 0.85 V. The other curves generally have a steep slope with no apparent intercalation plateau. Average charge and discharge capacities from several parallels are plotted against the cycle number as shown in Fig. 5.39. There is a big gap between the discharge and charge capacity of the first cycle. The other charge/discharge pairs follow each other more closely. A capacity decrease is observed as the current density increases. The error bars do not change significantly during cycling at different current rates.

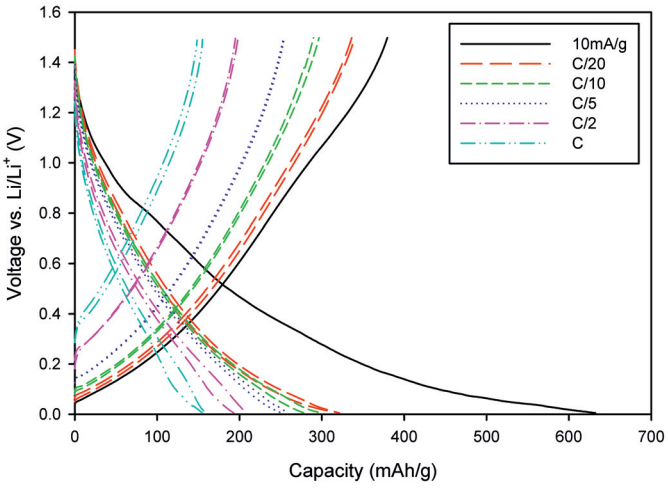

Figure 5.38: Charge/discharge measurements of a typical basic grade carbon cones half-cell at different rates (CCRAW), where the initially cycle is performed at 10 mA/g.

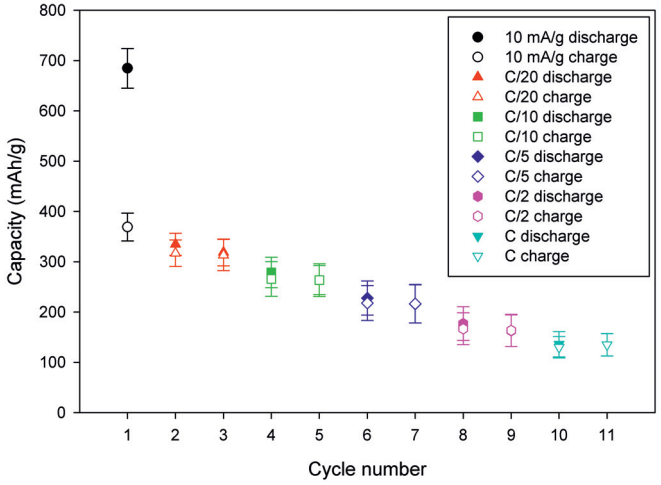

Figure 5.39: Cycling of a carbon/lithium half-cell based on untreated basic grade carbon cones (CCRAW).

Electrode Thickness Comparison Charge/discharge responses of three different tape cast thicknesses of the untreated basic grade carbon cones were measured. The doctor blade was set to 100 µm, 200 µm, and 300 µm, corresponding to a total electrode thickness after solvent evaporation of 35 µm, 77 µm, and 118 µm, respectively. A difference in capacity can be observed in Fig. 5.40. The thinnest electrode material shows the highest discharge capacity. The 11th cycle is discarded due to faults in the testing procedures.

Regained Capacity Cells cycled at higher current rate shows typically a decrease in capacity. If the current rate is again decreased, the capacity is regained as seen in Fig. 5.41. The regained capacity at C/20 rate is plotted with a yellow stippled line at the end of the testing procedure. Its capacity profile is almost identical to the prior C/20 rate cycles.

Heat Treatment As described earlier, basic grade carbon cones samples were heat treated to different temperatures to investigate the effect on cell performance. Various temperatures were chosen to pinpoint a change in the charge/discharge behavior. The temperatures were also based on electron microscope and X-ray diffraction observations of the carbon cones' morphological and structural change. The lowest heat treatment temperature was 950 °C. The maximum temperature available was 2700 °C. All samples were held at the desired temperature for 3 h in an argon atmosphere.

Heat Treated at 950 °C (CC950) A typical result for the basic grade carbon cones heat treated at 950 °C can be seen in Fig. 5.42. A small plateau at 0.8 V can be observed for the first discharge. The first discharge reaches a capacity of 549 mAh/g while the first charge reaches 367 mAh/g giving a irreversible capacity of 33 %. The capacities at different rates are plotted against the cycle number in Fig. 5.43. The error bars for the first discharge capacity are to a certain extent larger compared to the error bars for the successive cycles.

Heat Treated at 1800 °C (CC1800) Fig. 5.44 shows the charge/discharge results from the carbon electrode heat treated at 1800 °C. A plateau occurring between 0.8 V and 0.9 V is clearly visible for the first discharge. Compared to the raw material and the carbon cones heat treated at 950 °C this plateau is more apparent. The first discharge capacity is 381 mAh/g and the first charge capacity is 246 mAh/g. The capacity plotted against cycle number is given in

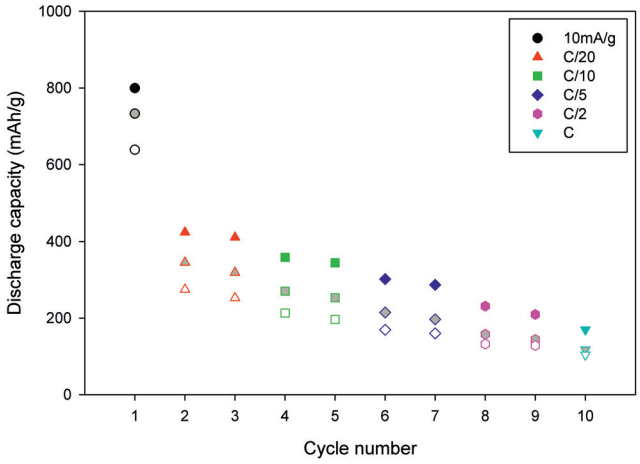

Figure 5.40: Comparison of discharge capacity for batteries prepared from different electrode thickness (CCRAW) cycled at various C-rates. The solid symbols are the 100 µm electrode, while the gray and hollow points are the 200 µm and 300 µm electrodes, respectively

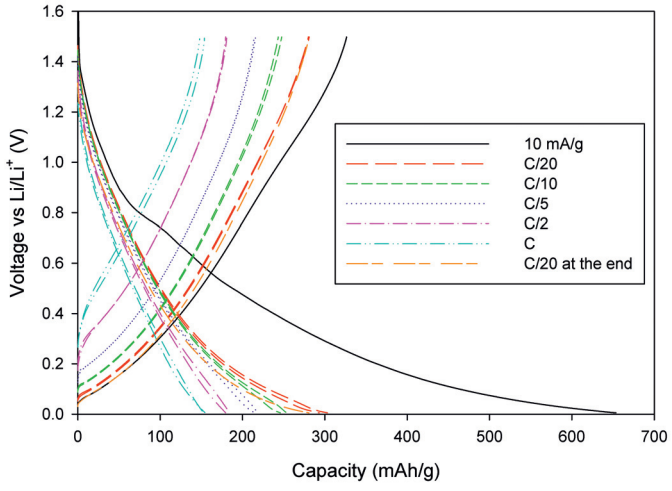

Figure 5.41: Comparison of cycling at different rates with recovered capacity. The last cycle has a lower current to determine if the capacity is regained after fast charge/discharge (CCRAW).

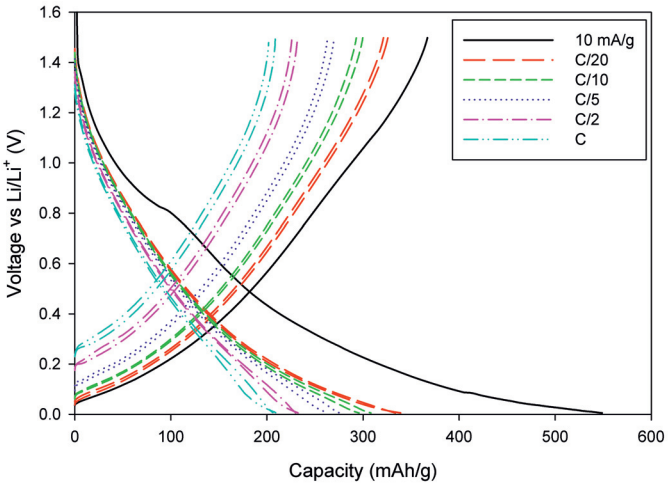

Figure 5.42: Charge/discharge measurements of basic grade carbon cones heat treated at 950 °C (CC950). The cell was cycled at different rates.

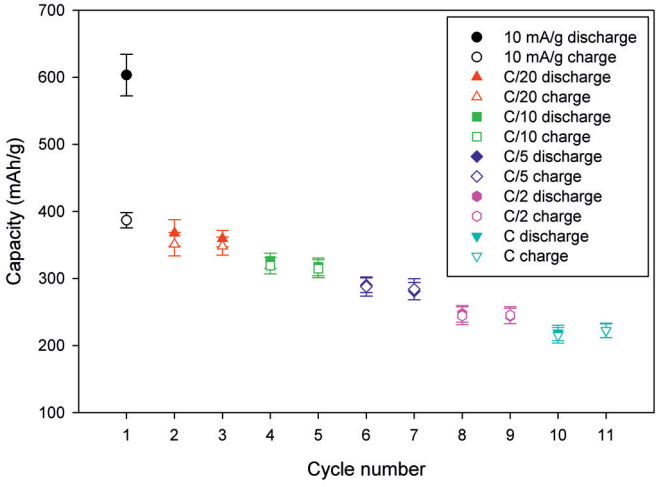

Figure 5.43: Cycling of carbon/lithium half-cells based on basic grade carbon cones heat treated at 950 °C (CC950).

Fig. 5.45. The largest uncertainty contribution is again from the initial discharge.

Heat Treated at 2000 °C (CC2000) Basic grade carbon cones samples were heat treated at 2000 °C. The corresponding galvanostatic results are shown in Fig. 5.46. A plateau can be seen at 0.8 V on the first discharge curve. The initial discharge capacity is 323 mAh/g, while the charge capacity for the 10 mA/g cycle is 212 mAh/g. The different cycles are also plotted versus cycle number in Fig. 5.47. Error bars show the variation in the samples. Here, the successive cycles have the largest deviation.

Heat Treated at 2200 °C (CC2200) Galvanostatic profiles of CC2200 electrodes are presented in Fig. 5.48. The bend on the first discharge cycle associated with the SEI film generation occurs at 0.8 V. Initial discharge and charge capacity is 335 mAh/g and 198 mAh/g, respectively. Fig. 5.49 shows the average cyclic performance for several cells. The error bars indicate a good consistency for all current rates.

Heat Treated at 2700 °C (CC2700) Basic grade carbon cones were heated treated in Ar to the highest available temperature (2700 °C). The charge/discharge results are shown in Fig. 5.50. The initial discharge capacity is 368 mAh/g, while the first charge capacity is measured to be 270 mAh/g. A small sharp plateau at 0.8 V, similar to what is previously observed, is also seen here. Moreover, the charge/discharge profiles have now changed considerably compared to the samples heat treated at lower temperatures. There is a wider and very distinct plateau at 0.1 V, which has not been observed previously. Also the initial discharge capacity is somewhat reduced compared to the as-produced material and the material heat treated at 950 °C. At the same time the irreversible capacity loss from the first to the second cycle is considerably smaller. The different cycles are also plotted versus cycle number in Fig. 5.51. The error bar for the initial discharge is considerably larger compared to the subsequent cycles.

Basic Grade Carbon Cones (50 wt%) and Carbon Cones Heat Treated at 2700 °C (50 wt%) (5050CCRAWCC2700) Charge/discharge measurements were also performed using electrodes made from a mixture of two different carbon cone samples. Untreated basic grade carbon cones and carbon

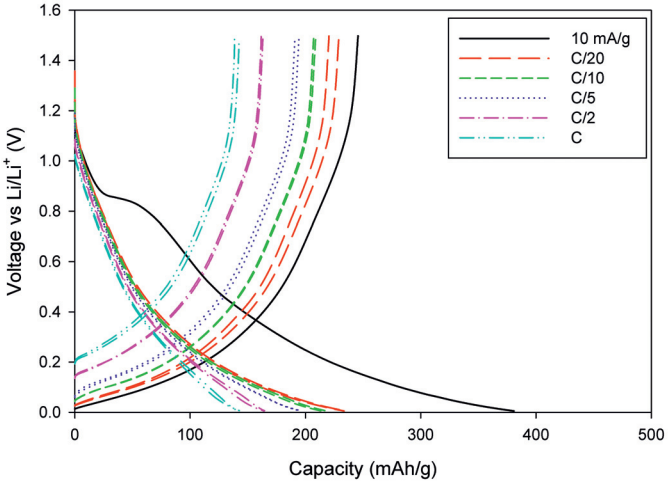

Figure 5.44: Charge/discharge measurements of basic grade carbon cones heat treated at 1800 °C (CC1800). The cell was cycled at different rates.

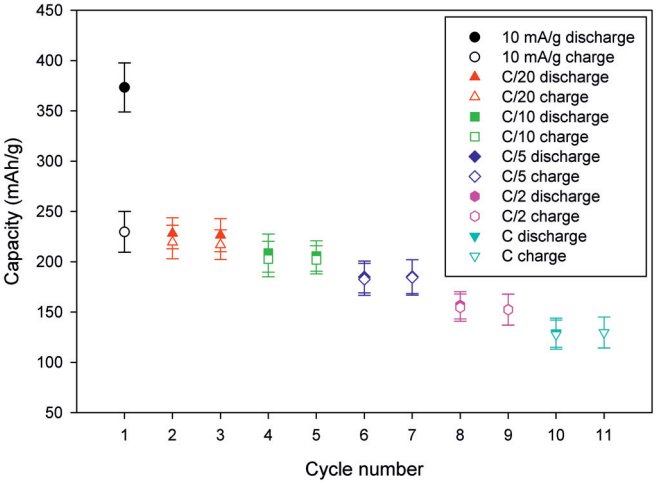

Figure 5.45: Cycle performance at different rates for the basic grade carbon cones heat treated at 1800 °C (CC1800).

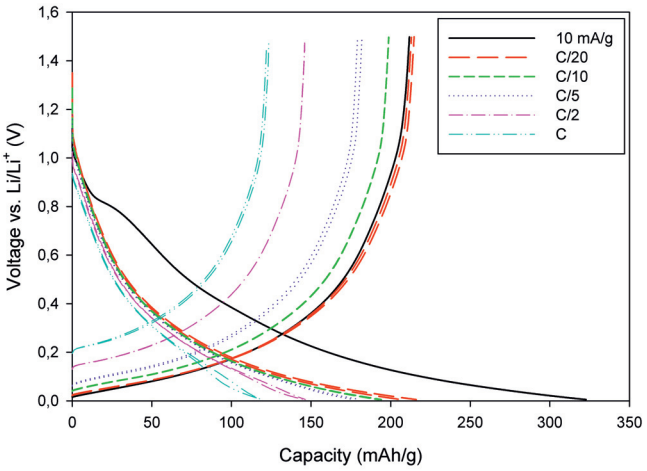

Figure 5.46: Charge/discharge measurements of basic grade carbon cones heat treated at 2000 °C. The cell was cycled at different charge rates (CC2000).

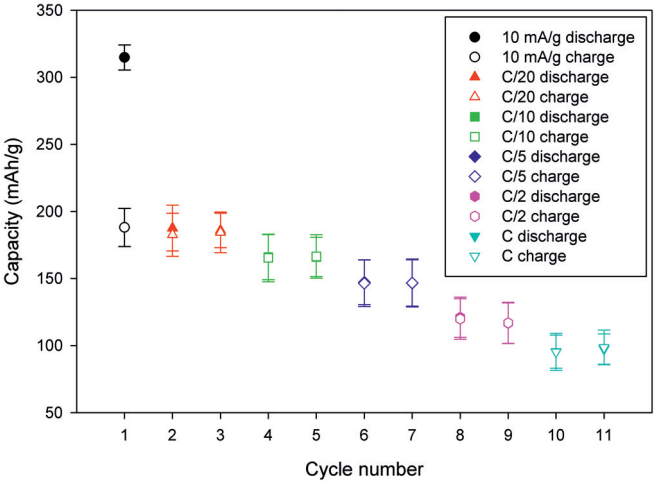

Figure 5.47: Galvanostatic cycling at various currents for basic grade carbon cones heat treated at 2000 °C (CC2000).

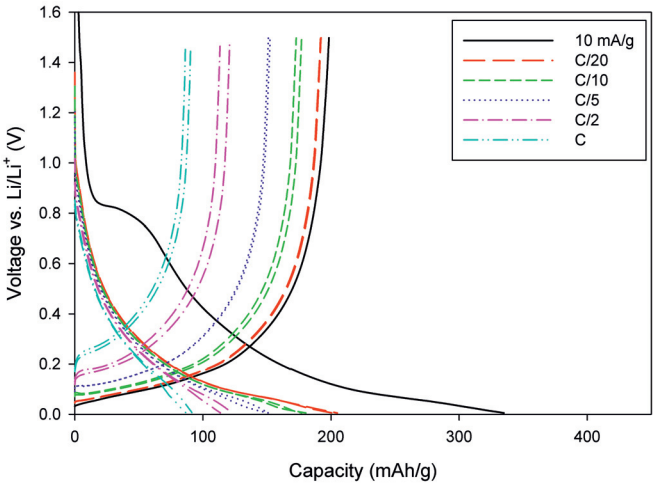

Figure 5.48: Charge/discharge measurements of basic grade carbon cones heat treated at 2200 °C. The cell was cycled at different charge rates (CC2200).

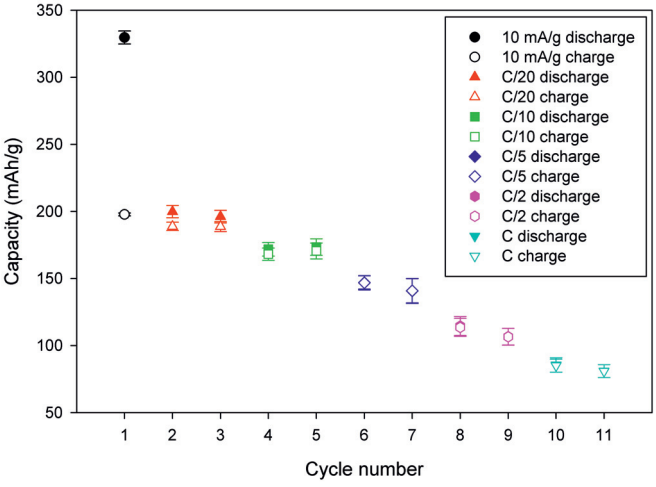

Figure 5.49: Charge/discharge capacity of basic grade carbon cones heat treated at 2200 °C versus the cycle number at different rates (CC2200).

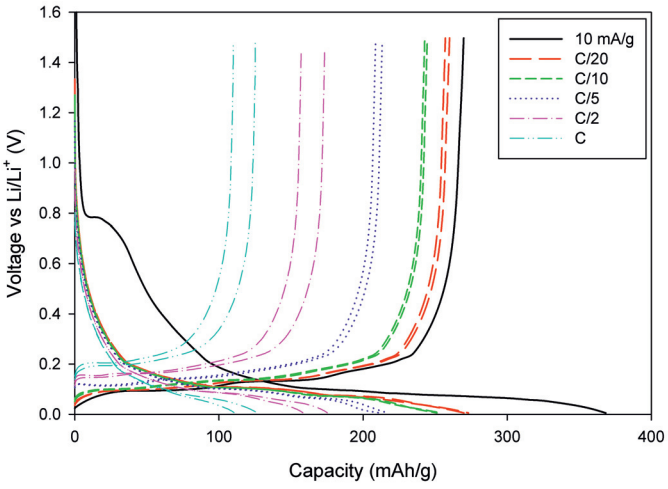

Figure 5.50: Charge/discharge measurements of basic grade carbon cones heat treated at 2700 °C. The cell was cycled at different rates (CC2700).

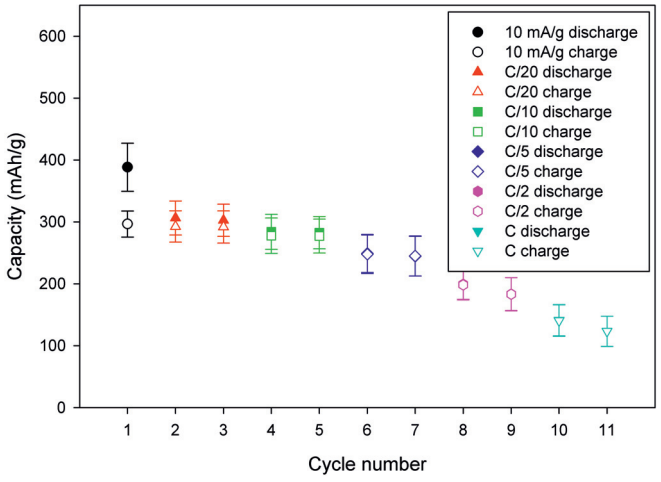

Figure 5.51: Cycling response of basic grade carbon cones heat treated at 2700 °C (CC2700).

cones heat treated at 2700 °C were mixed at equal mass ratios to obtain electrochemical features from both materials. The charge/discharge profile in Fig. 5.52 have the characteristics of both materials. At 0.85 V, the first discharge profile show a clear bend. The initial discharge capacity is measured to 584 mAh/g, while the first charge capacity is 354 mAh/g. The charge/discharge data is also plotted against the cycle number in Fig. 5.53. This type of electrode shows a trend of the decreasing error bars. The CCRAW/CC2700 combination is not represented in the test tree for carbon cones, Fig. 5.27.

Oxidation As described previously, the basic grade carbon cones material was oxidized with the intention to alter the cell performance. Two principal techniques have been used, namely wet chemical oxidation and heat treatment in an oxygen containing atmosphere. The results are given below.

Heat Treated in Air at 900 °C (CC900Air) Basic grade carbon cones were heat treated in air at 900 °C for 1 h with the intention to facilitate for SEI formation. A large percentage of the material decomposed and oxidized to gaseous CO_2 or CO. The remaining material was used for electrochemical characterizations. The corresponding charge/discharge measurement is given in Fig. 5.54. The first discharge capacity is measured to be 864 mAh/g and the first charge capacity is 441 mAh/g showing an extremely high irreversible capacity loss of 49 %. The curve otherwise looks similar to the non-oxidized cells with for instance the small kink on the first discharge profile at 0.8 V. Cyclic performance is given in Fig. 5.55. Some deviations occur in the error bars. The electrode material shows a good consistency at the start and end of the cycle program.

Heat Treatment at 900 °C in Air Followed by 900 °C in Argon (CC900Ar-Air) Basic grade carbon cones were initially heat treated at 900 °C in synthetic air before it was heated in argon at the same temperature with the intention to remove residual oxygen and act as a comparison to CC900Air. The results from the carbon/lithium half-cells are given in Fig. 5.56 and Fig. 5.57. The first discharge capacity is 802 mAh/g and the first charge capacity is 437 mAh/g. The charge/discharge curves are similar to the measurements for the untreated basic carbon cones, with a bend at 0.8 V. The irreversible capacity loss is almost 50 %. Error bars from the cyclic response does not show large variation for the different current rates. Nonetheless, a small deviation increase can be seen for the mid-cycles.

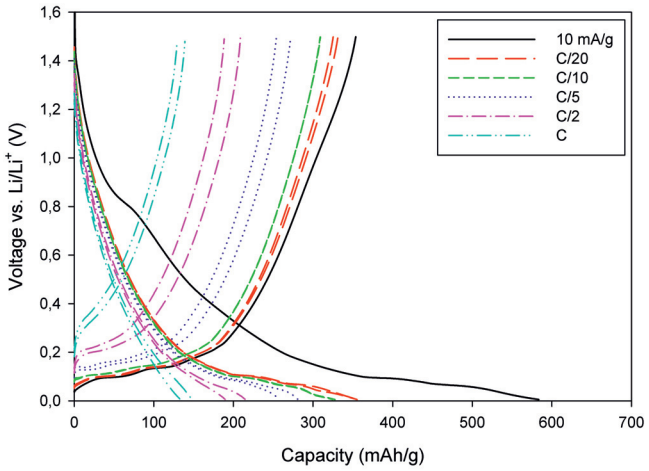

Figure 5.52: Charge/discharge measurements of untreated carbon cones (50 wt%) and carbon cones heat treated at 2700 °C (50 wt%). The cell was cycled at different rates (5050CCRAWCC2700).

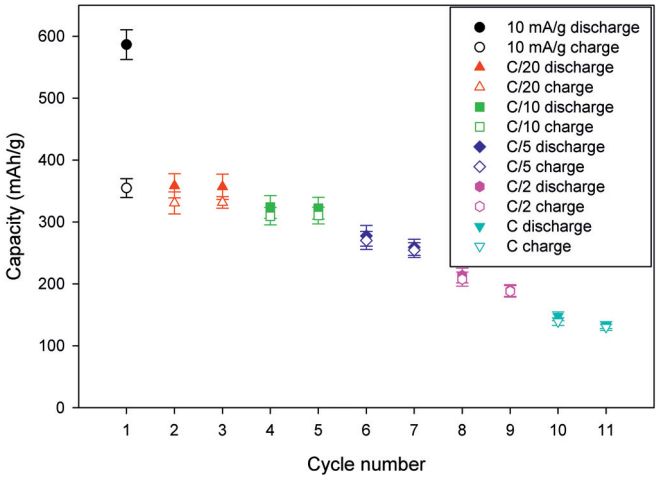

Figure 5.53: Cycling response at various rates of untreated carbon cones (50 wt%) and carbon cones heat treated at 2700 °C (50 wt%) (5050CCRAWCC2700).

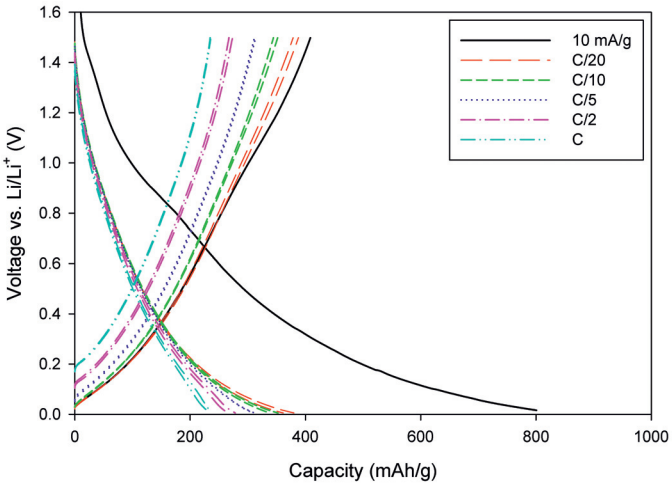

Figure 5.54: Charge/discharge measurements of basic grade carbon cones heat treated at 900 °C in an air atmosphere. The cell was cycled at different rates (CC900Air).

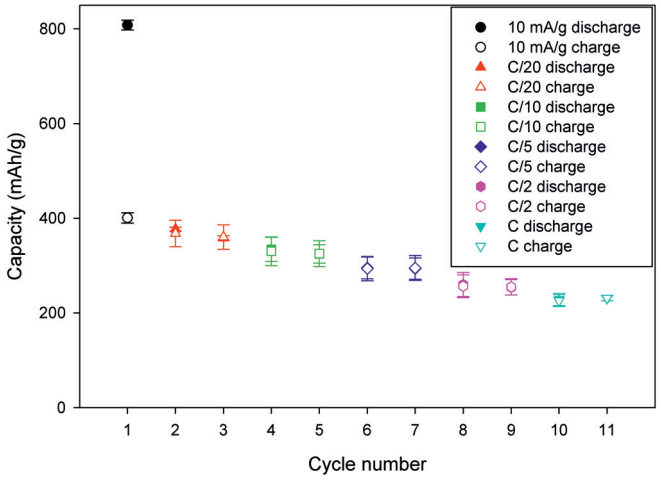

Figure 5.55: Specific charge/discharge capacity versus cycle number of basic grade carbon cones heat treated at 900 °C in an air atmosphere (CC900Air).

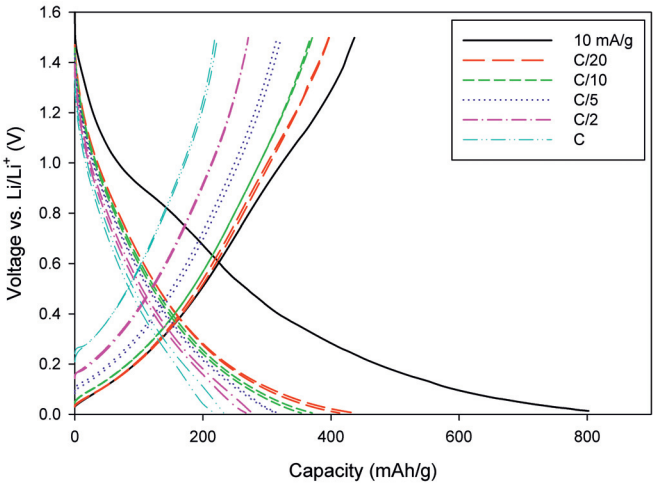

Figure 5.56: Charge/discharge measurements of basic grade carbon cones heat treated at 900 °C in air followed by 900 °C in argon. The cell was cycled at different rates (CC900Ar-Air).

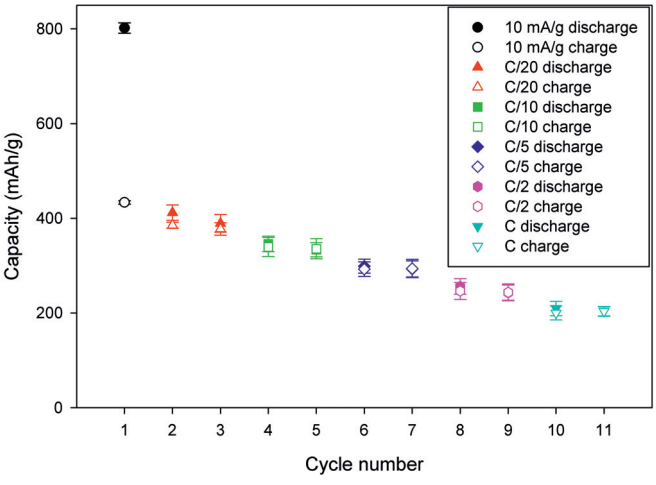

Figure 5.57: Cycling of a carbon/lithium half-cell based on the basic grade carbon cones heat treated at 900 °C in air followed by 900 °C in argon (CC900Ar-Air).

Heat Treated at 2700 °C Followed by Heat Treatment in Air at 900 °C (CC900Air2700) Basic grade carbon cones was initially heat treated to 2700 °C in argon. The material was then heat treated at 900 °C for 1 h in synthetic air to oxidize the carbon. Some material was lost to gaseous CO_2 and CO due to the oxidation of carbon. However, the mass loss was significantly lower compared to the basic grade carbon cones sample which was oxidized at 900 °C. The charge/discharge measurements can be seen in Fig. 5.58. The initial discharge capacity is 553 mAh/g and the equivalent charge capacity is 376 mAh/g. The charge/discharge curves are similar to the ones obtained for the samples heat treated at 2700 °C. Nevertheless, the plateau (0.8 V) is slightly less distinct. Each charge and discharge capacity is also plotted against cycle number in Fig. 5.59. The standard deviation represented as error bars for these cycles are large compared to the other electrode materials tested in this study.

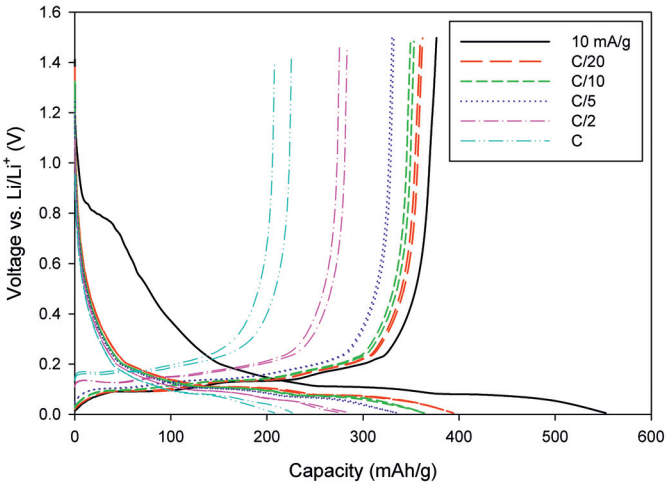

Figure 5.58: Charge/discharge measurements of basic grade carbon cones heat treated at 2700 °C in argon and then oxidized at 900 °C. The cell was cycled at different rates (CC900Air2700).

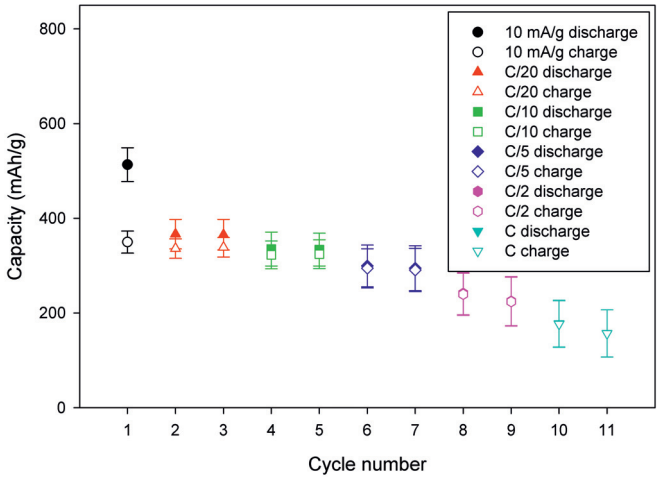

Figure 5.59: Cycle performance at different rates for basic grade carbon cones heat treated at 2700 °C in argon and subsequently heat treated in air at 900 °C at various rates (CC900Air2700).

Hydrogen Peroxide (H_2O_2) Treatment (CCH2O2) Basic grade carbon cones were treated with H_2O_2 in water solution. Mild oxidation with H_2O_2 can have a positive effect on the SEI generation. The cleaned and dried material was tested as electrodes in carbon/lithium half-cells. The charge/discharge profiles are given in Fig. 5.60. The first discharge capacity is 562 mAh/g, while the first charge capacity is 393 mAh/g. The charge/discharge curves are very similar to the untreated basic grade carbon cones. A small bend appears at 0.9 V for the first discharge profile. The capacities are also plotted against the cycle number in Fig. 5.61. Here, the largest error bar arises from the first discharge. The successive standard deviations are almost negligible.

Nitric Acid (HNO_3) Treatment (CCHNO3) A similar process with nitric acid was used to modify the basic grade carbon cones. Again, the oxidation will facilitate for the SEI layer and it can have a positive effect on the irreversible capacity. HNO_3 was used as a comparison to H_2O_2. The cleansed and dried material was used to make electrodes which were tested with charge/discharge measurements. The results of a typical cell can be seen in Fig. 5.62, where first discharge and charge capacities are 604 mAh/g and 384 mAh/g, respectively. The charge/discharge curves are also very similar to the untreated basic grade carbon cones. The SEI formation kink is also present for this material, though its signal is very weak. Moreover, the nitric acid treatment yields a slightly higher irreversible capacity loss compared to the hydrogen peroxide treatment. The corresponding results where the capacities are plotted against the cycle number are shown in Fig. 5.63. The error bars are minimal for all the cycles except for the initial discharge.

Functionalized Carbon Cones (CC-Func) Carbon cones functionalized with oxygen was tested as electrode material. This material differs from the oxidized material as oxygen is functionalized on to the carbon with the intention to cover the surface instead of changing the materials outer chemistry. The results can be seen in Fig. 5.64. The initial discharge capacity is extremely high with a value of 901 mAh/g at 0.09 V. The measurement was stopped at this voltage due to time limitation in the testing procedure. If the initial discharge profile is extrapolated to 5 mV, which was the lower discharge limit, a capacity of almost 1100 mAh/g could have been reached. During the first discharge, the cell gained capacity as a plateau evolves at high voltages (above 1.6 V). The first charge capacity is 312 mAh/g yielding a huge irreversible capacity for the first cycle. Subsequent curves are similar to the curves for untreated basic grade

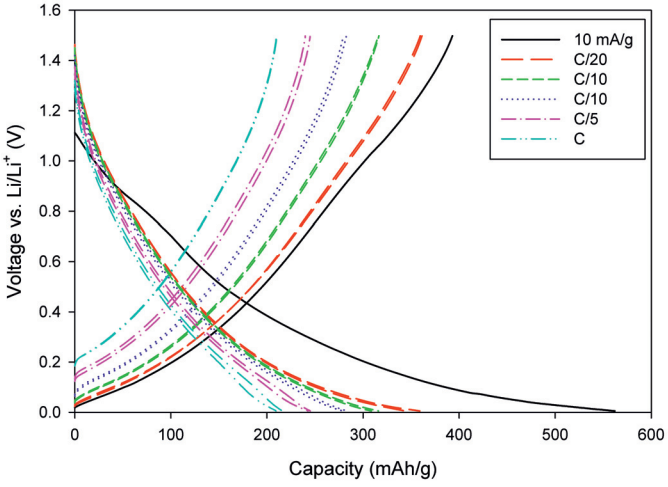

Figure 5.60: Charge/discharge measurements of basic grade carbon cones treated in hydrogen peroxide. The cell was cycled at different rates (CCH2O2).

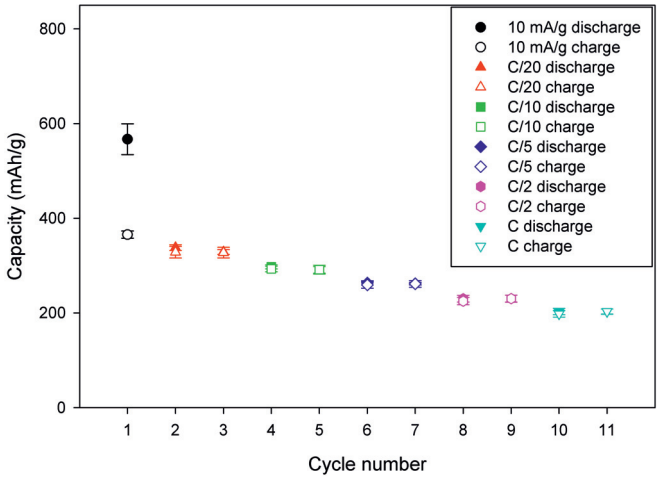

Figure 5.61: Cycling response of basic grade carbon cones treated in hydrogen peroxide versus the cycle number at different rates (CCH2O2).

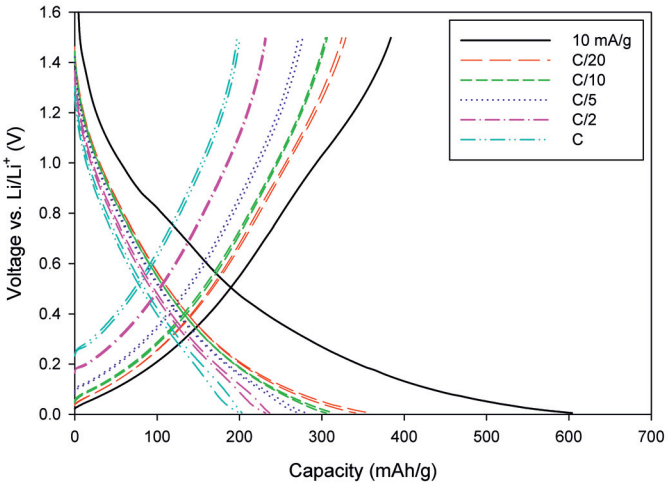

Figure 5.62: Charge/discharge measurements of basic grade carbon cones treated in nitric acid. The cell was cycled at different rates (CCHNO3).

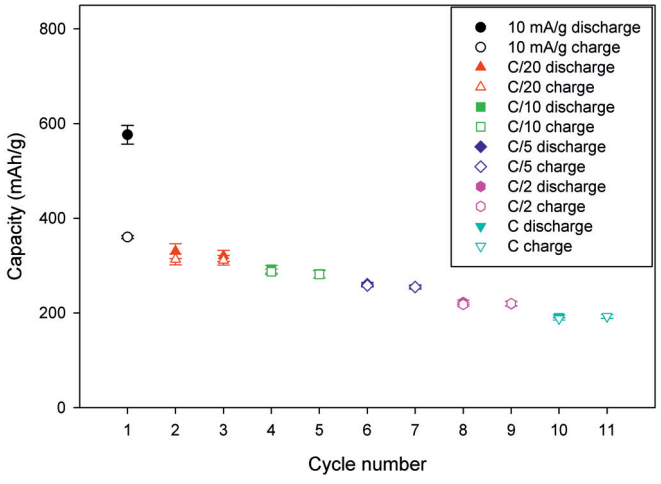

Figure 5.63: Cycling response at various rates of basic grade carbon cones treated in nitric acid (CCHNO3).

carbon cones. Only one cell with this composition was assembled, hence no error bars in Fig. 5.65.

Functionalized Carbon Cones Heat Treated at 900 °C in Argon (CC900-Func) The functionalized carbon cones provided by n-Tec were heat treated at 900 °C in argon atmosphere to remove the functionalized oxygen groups present on the carbon surface. The final material was prepared as electrode material. The charge/discharge results are given in Fig. 5.66. A bend appears at 0.9 V for the first discharge curve. The initial discharge capacity is 677 mAh/g while the initial charge capacity is 405 mAh/g. Corresponding cycling data based on several cells are plotted in Fig. 5.67. For the first cycle the standard deviation is almost negligible. However, the standard deviation increases for the subsequent cycles.

Effect of Microwave Radiation on Carbon Cones and Subsequent Cell Performance Samples of carbon cones were irradiated with microwaves in a conventional kitchen microwave oven. The aim was to radically change the crystal structure and surface of the carbon material. Untreated basic grade carbon cones samples were microwave treated in an argon or air atmosphere.

Microwave Irradiated in Argon (MWCCAr) Basic grade carbon cones were irradiated with microwaves in an argon atmosphere. The powder was transferred to an air tight Teflon container in an argon filled glove box. No reaction was observed during treatment. Although, smoke developed as the container was disassembled in air. The 50 bar safety valves did not ventilate, hence indicating that no great pressure increase occurred. The typical charge/discharge result for a such an electrode is given in Fig. 5.68. A kink can be seen at 0.9 V for the first discharge profile. The initial discharge capacity is 708 mAh/g, while the initial charge capacity is 370 mAh/g, which means an irreversible loss of 48 %. As for many other charge/dischage profiles it is possible to see the SEI formation starting at 0.8 V. The cyclic behavior for this material is given in Fig. 5.69. The stardard deviation is generally small for the first half of the total cycles (cycle: 1 - 5), while it increases to a certain extent for the second half (cycle: 6 - 11).

Microwave Irradiated in Air (MWCCAir) Basic grade carbon cones material was also treated with microwaves in an air atmosphere. The carbon

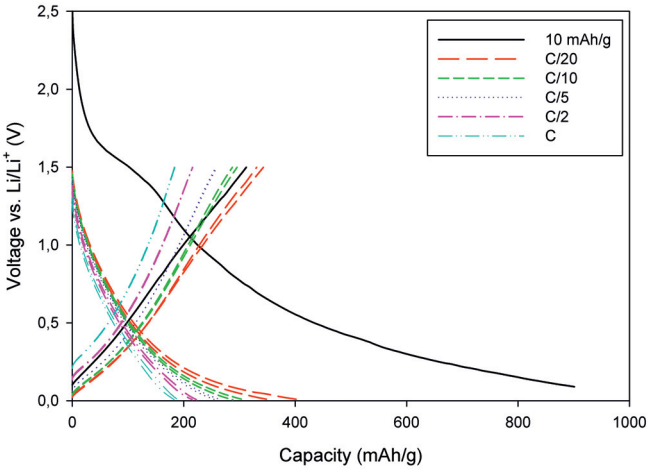

Figure 5.64: Charge/discharge measurements of functionalized carbon cones . The cell was cycled at different rates (CC-Func).

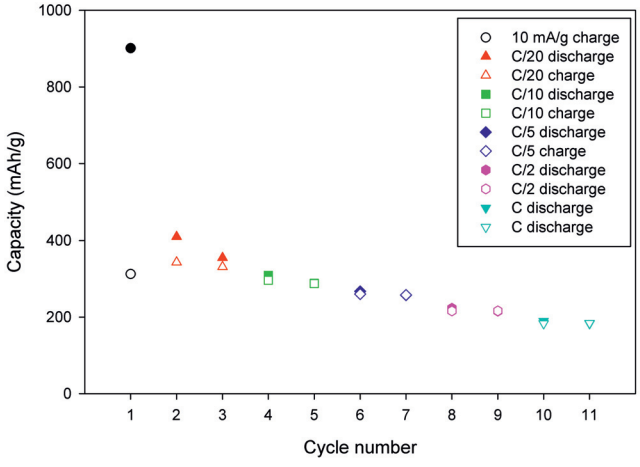

Figure 5.65: Specific charge/discharge capacity of functionalized carbon cones versus the cycle number at various currents (CC-Func).

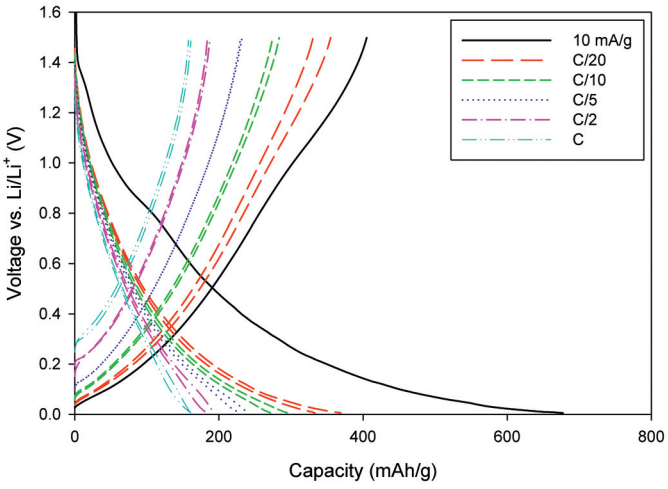

Figure 5.66: Charge/discharge measurements of functionalized carbon cones heat treated at 900 °C in argon. The cell was cycled at different rates (CC900-Func).

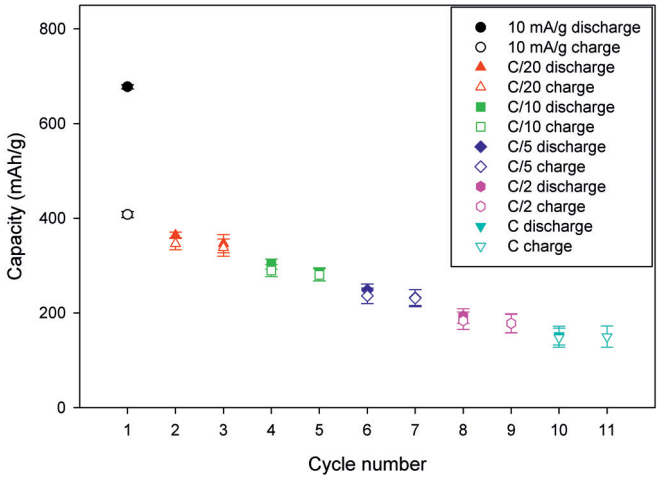

Figure 5.67: Cycling performance at different rates for functionalized carbon cones heat treated at 900 °C in argon versus the cycle number at different rates (CC900-Func).

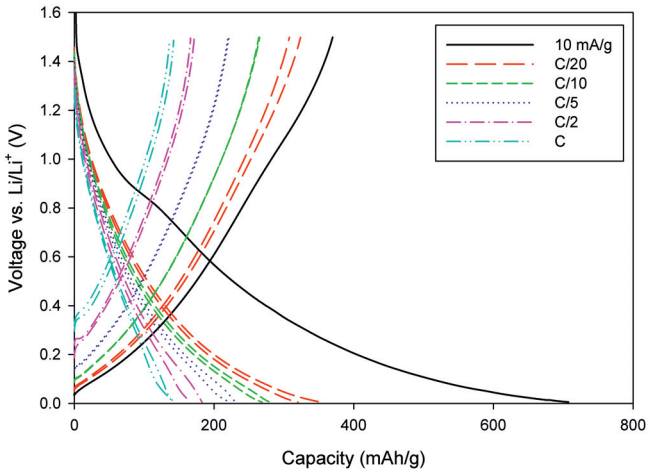

Figure 5.68: Charge/discharge measurements of microwave irradiated carbon cones in argon. The cell was cycled at different rates (MWCCAr).

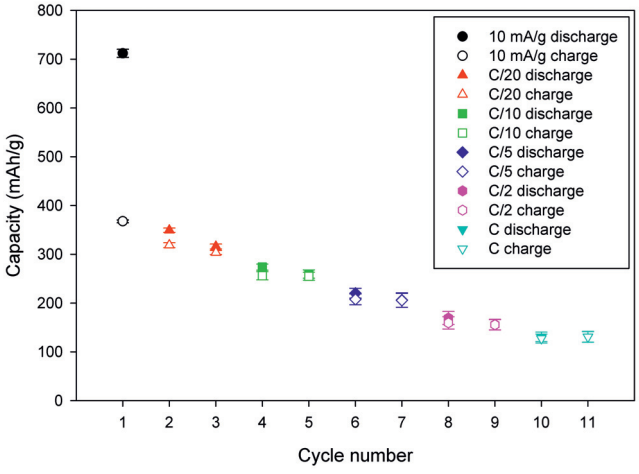

Figure 5.69: Cycling response at various rates of microwave irradiated carbon cones in argon (MWCCAr).

powder started glowing almost immediately as the irradiation started. The red/yellow glow was distinctly different from the sparks produced by microwave irradiation of sharp metal objects. Specific charge and discharge capacity was measured for electrodes produced from this material. The results are shown in Fig. 5.70. Again, a small bend appears at 0.8 V for the first discharge curve. Specific discharge capacity is measured to be 643 mAh/g while corresponding charge capacity is 381 mAh/g. This yields a capacity loss of 41 wt%. Cyclic performance was tested at various rates, see Fig. 5.71. The first discharge shows a large standard deviation compared to the successive measurements.

Low Grade Carbon Cones

A second batch of carbon cones material, referred to as low grade carbon cones, was also produced in the Kværner carbon black and hydrogen process. The material has been tested as electrode material. The low grade carbon cones have also been heat treated to observe potential effects on cell performance.

Untreated (LGCC) As-produced low grade carbon cones were prepared as electrode material. The samples were tested and the charge/discharge results are shown in Fig. 5.72. The initial discharge and charge capacity is 788 mAh/g and 432 mAh/g, respectively. Corresponding charge/discharge profiles lack plateaus and the descending initial discharge curve is not as smooth compared to the former measurements. The charge/discharge capacities are plotted against the cycle number in Fig. 5.73. The errors bars vary to a certain extent with the different cycle numbers.

Heat Treated at 2700 °C (LGCC2700) The low grade carbon cones material was also heat treated to 2700 °C before it was tested as electrodes. The results are shown in Fig. 5.74. LGCC2700 has a similar bend to CC2700 at 0.9 V. The first discharge capacity is measured to be 496 mAh/g, while the first charge capacity is 341 mAh/g. Fig. 5.75 depicts the cycle response at different succeeding rates. The deviations represented as error bars are relatively similar to each other, with the exception of the first and middle cycles.

Commercial graphite

Commercially available graphites from Timcal have been tested. The graphite functions as a benchmark material for comparison to the various carbon cones

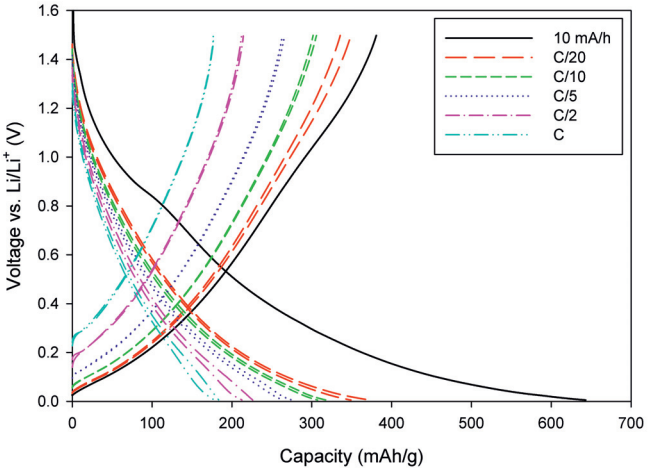

Figure 5.70: Charge/discharge measurements of microwave irradiated carbon cones in air. The cell was cycled at different rates (MWCCAir).

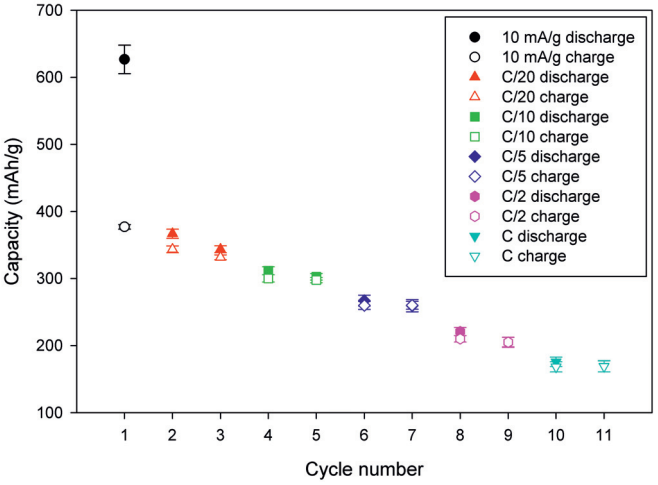

Figure 5.71: Charge/discharge capacity of microwave irradiated carbon cones in air versus the cycle number at different rates (MWCCAir).

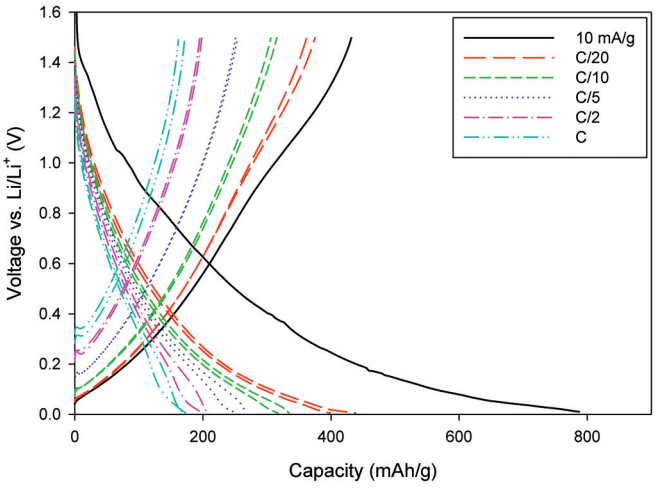

Figure 5.72: Charge/discharge measurements of as-produced low grade carbon cones. The cell was cycled at different rates (LGCC).

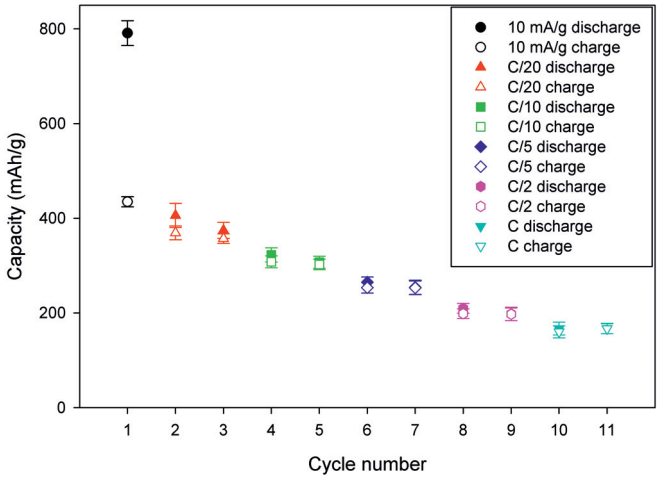

Figure 5.73: Specific charge/discharge capacity of as-produced low grade carbon cones versus the cycle number at different rates (LGCC).

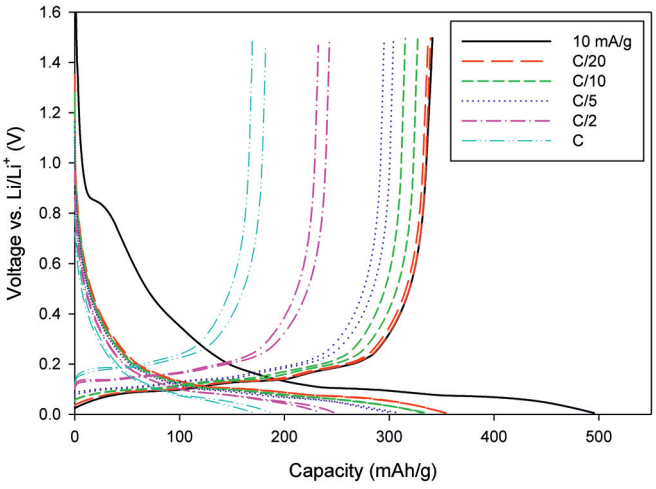

Figure 5.74: Charge/discharge measurements of low grade carbon cones heat treated at 2700 °C in argon. The cell was cycled at different rates (LGCC2700).

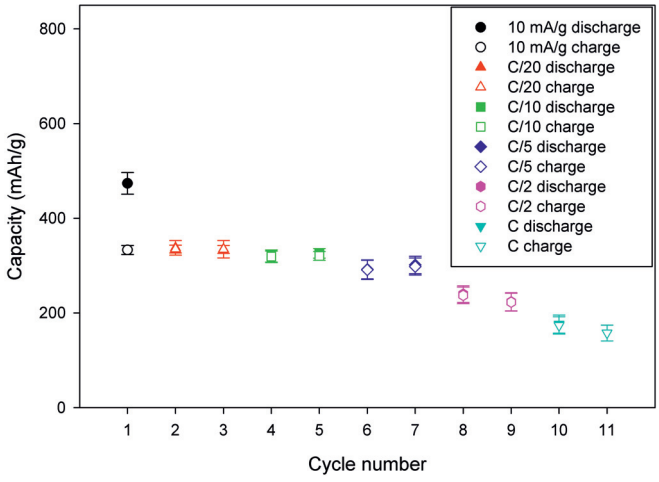

Figure 5.75: Cycling response of low grade carbon cones heat treated at 2700 °C in argon versus the cycle number at different rates (LGCC2700).

materials. Specifications for the two slightly different carbon samples can be found elsewhere [138]. SLP50 was chosen as the principal material over the SLP30, since SLP50 was developed as a continuation of SLP30.

TIMREX® SLP30 Samples with the graphite TIMREX® SLP30 were used to make electrodes. The results from the charge/discharge measurements are given in Fig. 5.76. The first discharge capacity is measured to be 553 mAh/g, while the first charge capacity is 480 mAh/g. The curves have an initial plateau at 0.2 V and at least two plateaus around 0.1 V for all the cycles. The irreversible capacity loss is very low compared to the carbon cones samples. Similarly, the capacities have been plotted against the cycle number in Fig. 5.77. The results given in Fig. 5.76 and 5.77 are representative for the electrode material. The standard deviation is not calculated for this material, as the electrode only functions as a comparison for the carbon cones.

TIMREX® SLP50 TIMREX® SLP50 graphite was tested as electrode material. The SLP50 material has a slightly larger particle size and bulk density than the SLP30 graphite. The charge/discharge curves resemble the curves from the SLP30 sample regarding shape (plateaus) and irreversible capacity. Representative charge/discharge profiles are shown in Fig. 5.78. The initial discharge and charge capacity is 521 mAh/g and 434 mAh/g, respectively. Charge/discharge capacities have been plotted against the cycle number in Fig. 5.79. Error bars are not calculated for this electrode material for the same reasons as for the SLP30 material.

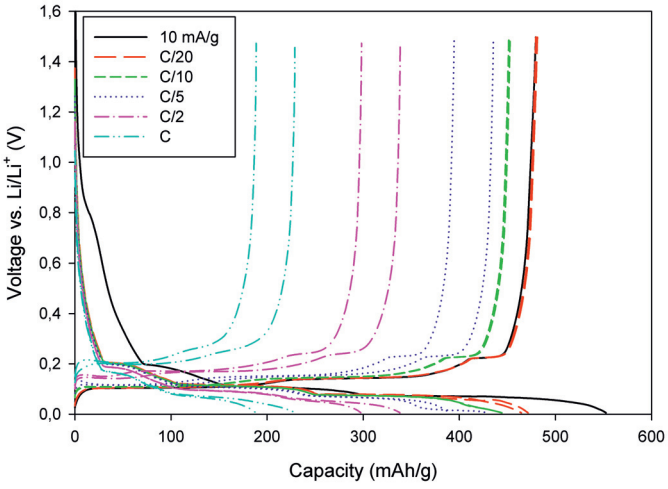

Figure 5.76: Charge/discharge measurements of commercially available graphite TIMREX® SLP30. The cell was cycled at different rates.

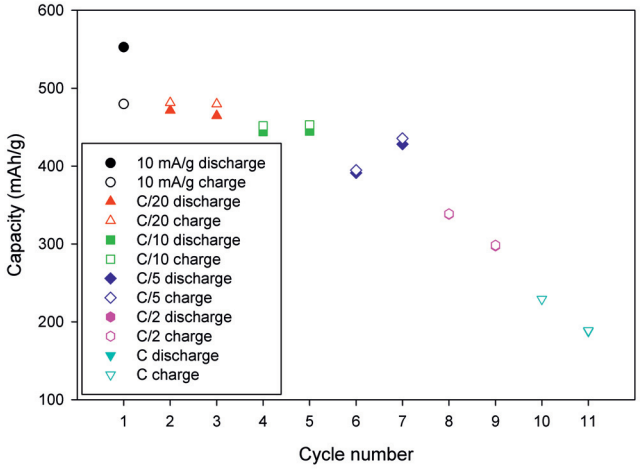

Figure 5.77: Charge/discharge capacity of commercially available graphite TIMREX® SLP30 versus the cycle number at different rates.

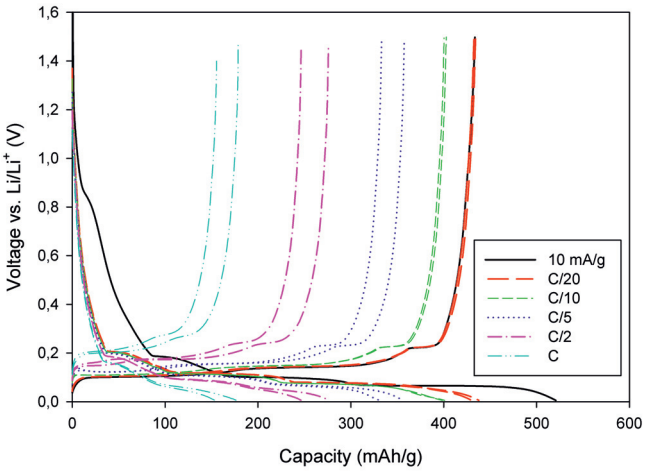

Figure 5.78: Charge/discharge measurements of commercially available graphite TIMREX® SLP50. The cell was cycled at different rates.

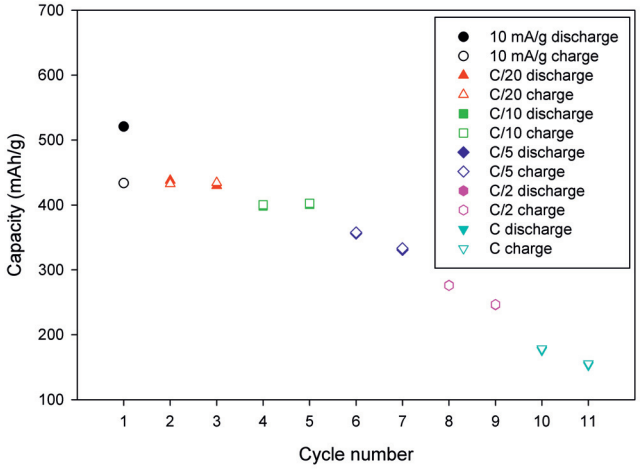

Figure 5.79: Charge/discharge capacity of commercially available graphite TIMREX® SLP50 versus the cycle number at different rates.

Long-term Testing of Half-cells

Three different electrode materials were selected for extended testing to investigate long-term stability. Carbon/lithium half-cells with untreated basic grade carbon cones, basic grade carbon cones heat treated at 2700 °C, and commercial graphite (TIMREX® SLP50) were cycled 100 times at C/4 after an initial cycle at 10 mA/g. Both the discharge and charge capacity are plotted, however it may be difficult to differentiate the plots as the coulombic efficiency is high. The discharge capacities are represented as solid triangles, while the hollow triangles are the charge capacities. The capacity from the first cycle is omitted from the results as its value is significantly larger compared to the successive cycles.

Untreated Basic Grade Carbon Cones (CCRAW) The results from the prolonged cycling experiments of untreated basic grade carbon cones are given in Fig 5.80. The initial discharge capacity is 699 mAh/g, while the corresponding charge capacity 356 mAh/g. Both capacities reaches a low point at cycle 9, before they increase and and stabilize at around 200 mAh/g for C/4.

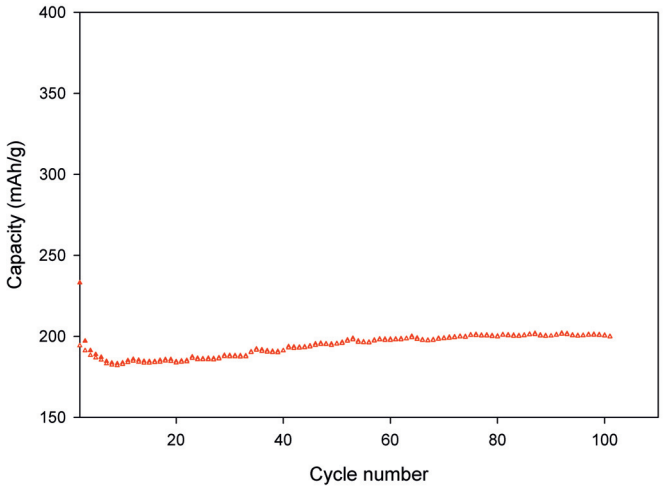

Figure 5.80: Extended cycling of coin cells constructed with basic grade carbon cones electrode (CCRAW). The first cycle is omitted from the figure.

Basic Grade Carbon Cones Heat Treated at 2700 °C (CC2700) The extended capacity for heat treated basic grade carbon cones is given in Fig. 5.81. An initial discharge and charge capacity is measured to be 453 mAh/g and 325 mAh/g for a rate of 10 mA/g, respectively. The capacities reach their lowest point at cycle 3. Subsequent cycles show steadily increasing capacity before it stabilizes at approximately 310 mAh/g for C/4.

Commercial Graphite (TIMREX® SLP50) Commercially available graphite is tested and its long-term cycling response is given in Fig. 5.82. The initial discharge capacity is 497 mAh/g and the corresponding charge capacity is 418 mAh/g. At cycle 8, the capacity is at its lowest. Subsequent cycles shows an increasing trend, however the capacities are much more scattered compared to CCRAW and CC2700. The capacity averages around 300 mAh/g for C/4-rate.

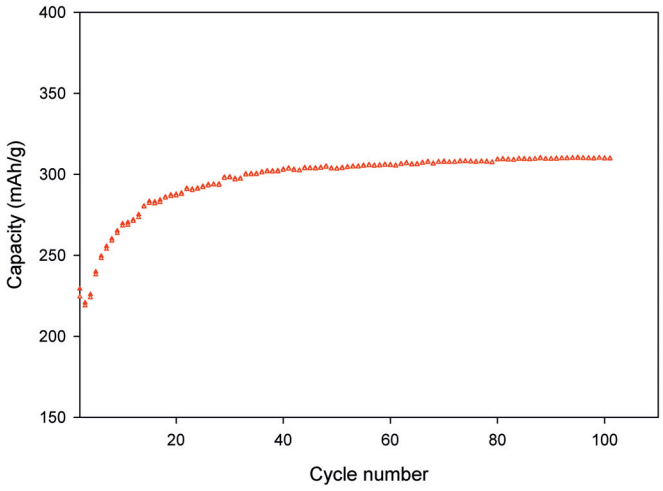

Figure 5.81: Cycling stability of basic grade carbon cones heat treated at 2700 °C (CC2700) The first cycle is omitted from the figure.

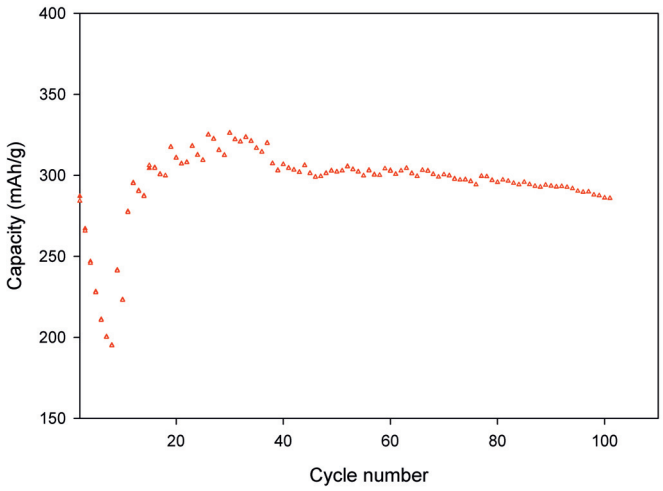

Figure 5.82: Capacity retention of commercially available graphite (SLP50). The first cycle is omitted from the figure.

Cell performance summary

A summary of the discharge and charge capacities are given in Table 5.4 and 5.5, respectively. The tables provide an overview of the different carbon materials. The given values are taken from the average capacities of at least 3 individual cells. Each value is the capacity during the first cycle at that corresponding rate. A low current rate yields higher capacities compared to higher current rates. The uncertainties are calculated by standard deviation. They vary from a low 1 mAh/g to a staggering 49 mAh/g. Table 5.6 shows important capacity parameters associated with the charge/discharge data.

Table 5.4: Summary of discharge (lithiation) capacity performance at different current rates. All values are given in mAh/g.

Carbon type	**10 mA/g**	**C/20**	**C/10**	**C/5**	**C/2**	**C**
CCRAW	685 ± 39	335 ± 22	279 ± 30	228 ± 34	117 ± 33	136 ± 25
CC950	603 ± 31	368 ± 20	326 ± 11	290 ± 11	247 ± 13	219 ± 11
CC1800	373 ± 24	228 ± 15	209 ± 19	185 ± 16	157 ± 14	129 ± 15
CC2000	315 ± 9	188 ± 17	166 ± 17	147 ± 17	121 ± 15	96 ± 12
CC2200	330 ± 5	200 ± 5	172 ± 5	147 ± 5	115 ± 7	86 ± 5
CC2700	388 ± 37	306 ± 17	284 ± 19	249 ± 23	199 ± 19	141 ± 23
5050CCRAWCC2700	586 ± 24	358 ± 20	324 ± 18	278 ± 17	213 ± 12	148 ± 7
CC900Air	808 ± 10	377 ± 4	334 ± 26	295 ± 23	260 ± 25	228 ± 13
CC900Ar-Air	802 ± 11	412 ± 7	346 ± 7	299 ± 10	256 ± 10	210 ± 6
CC900Air2700	513 ± 36	367 ± 31	335 ± 36	299 ± 44	242 ± 45	178 ± 49
CCH2O2	567 ± 13	338 ± 6	297 ± 4	263 ± 3	230 ± 7	203 ± 7
CCHNO3	576 ± 20	330 ± 16	292 ± 8	261 ± 4	222 ± 4	193 ± 3
CC900-Func	678 ± 4	364 ± 7	303 ± 11	248 ± 13	194 ± 15	152 ± 20
MWCCAr	712 ± 8	349 ± 5	274 ± 6	220 ± 10	169 ± 13	131 ± 10
MWCCAir	627 ± 21	367 ± 7	312 ± 5	267 ± 8	221 ± 6	176 ± 7
LGCC	791 ± 26	406 ± 25	323 ± 15	265 ± 11	210 ± 10	167 ± 13
LGCC2700	474 ± 23	338 ± 15	320 ± 13	292 ± 20	240 ± 18	176 ± 19

Table 5.5: Summary of charge (delithiation) capacity performance at different current rates. All values are given in mAh/g.

Carbon type	**10 mA/g**	**C/20**	**C/10**	**C/5**	**C/2**	**C**
CCRAW	369 ± 28	317 ± 26	266 ± 34	218 ± 35	167 ± 32	130 ± 21
CC950	387 ± 12	351 ± 17	319 ± 12	288 ± 14	244 ± 13	215 ± 12
CC1800	229 ± 20	220 ± 17	203 ± 18	182 ± 16	154 ± 14	128 ± 14
CC2000	188 ± 14	183 ± 16	165 ± 18	146 ± 17	120 ± 15	95 ± 14
CC2200	198 ± 1	189 ± 3	168 ± 5	147 ± 5	114 ± 7	85 ± 5
CC2700	297 ± 12	293 ± 14	278 ± 18	248 ± 22	198 ± 18	141 ± 23
5050CCRAWCC2700	355 ± 15	331 ± 18	309 ± 14	270 ± 15	208 ± 11	139 ± 6
CC900Air	401 ± 11	368 ± 28	330 ± 30	294 ± 26	256 ± 24	226 ± 12
CC900Ar-Air	434 ± 4	385 ± 2	339 ± 6	293 ± 7	247 ± 10	200 ± 6
CC900Air2700	350 ± 23	336 ± 21	323 ± 29	294 ± 41	240 ± 44	177 ± 49
CCH2O2	365 ± 6	329 ± 7	293 ± 4	259 ± 6	225 ± 8	198 ± 7
CCHNO3	360 ± 19	313 ± 12	287 ± 6	258 ± 3	218 ± 4	188 ± 3
CC900-Func	408 ± 6	346 ± 13	290 ± 13	236 ± 16	184 ± 18	148 ± 20
MWCCAr	368 ± 3	319 ± 5	256 ± 8	208 ± 11	159 ± 12	127 ± 9
MWCCAir	377 ± 3	344 ± 5	300 ± 5	260 ± 6	210 ± 5	168 ± 8
LGCC	435 ± 11	369 ± 15	308 ± 13	253 ± 11	198 ± 10	160 ± 13
LGCC2700	333 ± 10	335 ± 8	319 ± 11	291 ± 20	237 ± 18	174 ± 18

Table 5.6: Various capacity parameters and electrode loading

Electrode material	$\mathbf{C_{init}}$ [a]	$\mathbf{C_{irr}}$ [b c]	$\mathbf{C_{irr}(\%)}$ [c]	**Loading** [d]
CCRAW	632	253	40	1.4
CC950	549	182	33	1.7
CC1800	381	135	35	1.2
CC2000	323	111	34	1.2
CC2200	335	137	41	0.7
CC2700	368	98	27	0.9
5050CCRAWCC2700	584	230	39	1.3
CC900Air	864	423	49	1.3
CC900Ar-Air	802	365	46	1.8
CC900Air2700	553	177	32	1.2
CCH2O2	562	169	30	1.7
CCHNO3	604	220	36	2.1
CC-Func	901	589	66	1.1
CC900-Func	677	272	40	2.1
MWCCAr	708	338	48	2.2
MWCCAir	643	262	41	1.5
LGCC	788	356	45	1.8
LGCC2700	496	155	31	0.9
SLP30	553	73	15	3.1
SLP50	521	87	17	2.0

[a] Initial discharge capacity (mAh/g) [b] Irreversible capacity (mAh/g)
[c] Capacity loss for the first cycle [d] Mass of electrode material per area (mg/cm^2)

5.4.2 Electrochemical Impedance Spectroscopy

Electrochemical impedance spectroscopy (EIS) was employed to investigate the electrochemical behavior of lithium-ion insertion into the carbon cones material. EIS has been measured using a test cell (HS-3E) provided by Hohsen Corp. Lithium metal was used as both reference and counter electrode. Efforts to make identical cells were made, such that the only variable would be the studied electrode. The impedance was measured on CCRAW and CC2700 electrodes and compared to electrodes prepared from commercially available graphite (SLP50) at potentials of OCV, 0.5 V, 0.2 V, and 0.005 V. The intercepts on the horizontal axis at the high frequencies are 3.3 Ω, 2.6 Ω, and 2.3 Ω for the CCRAW, CC2700 and SLP50 respectively.

The impedance spectra of CCRAW contains one dominating semicircle in

the high and middle range frequency area. At lower frequencies the impedance curls towards the center before it inclines as it reaches the lowest frequencies. The dominating semicircle decrease with decreasing potential, see Fig. 5.83.

The Nyquist plots of the heat treated basic grade carbon cones (CC2700) have two distinguishable semicircles in the high and middle range frequency area for all the potentials except for the OCV which shows only one visible semicircle. An incline is shown at low frequencies, see Fig. 5.84. The first semicircle decreases with decreasing potential, but the results obtained at OCV show again a somewhat different behavior.

Fig. 5.85 shows the impedance spectra of the SLP50 electrode. One dominating semicircle is present at the high and low frequencies. Again, the impedance curls inwards to the center at low frequencies. The OCV slopes upwards at low frequencies. The semicircles decrease with decreasing potential.

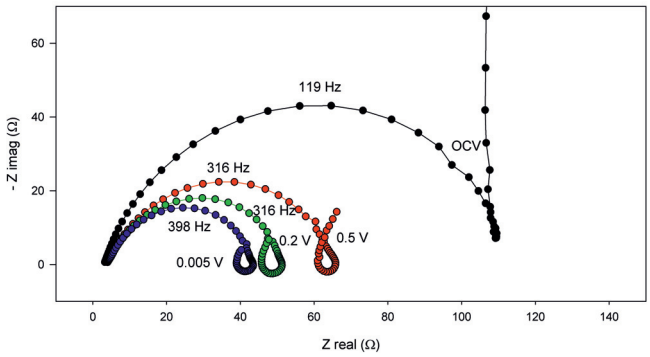

Figure 5.83: Nyquist plot of the CCRAW electrode. 119 Hz, 316 Hz, 316 Hz, and 398 Hz is the characteristic frequencies at the top of each semicircle for OCV, 0.5 V, 0.2 V, and 0.005 V, respectively.

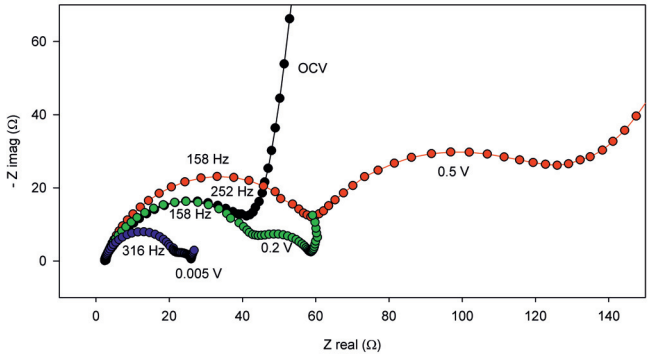

Figure 5.84: Nyquist plot of the CC2700 electrode. 158 Hz, 252 Hz, 158 Hz, and 316 Hz is the characteristic frequencies at the top of each semicircle for OCV, 0.5 V, 0.2 V, and 0.005 V, respectively.

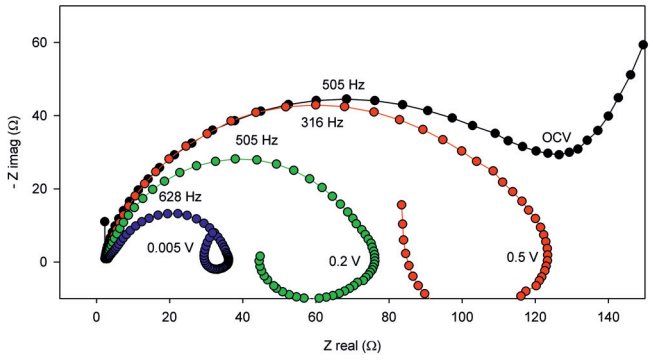

Figure 5.85: Nyquist plot of the SLP50 electrode. 505 Hz, 316 Hz, 505 Hz, and 628 Hz is the characteristic frequencies at the top of each semicircle for OCV, 0.5 V, 0.2 V, and 0.005 V, respectively.

5.4.3 Cyclic Voltammetry

Electrodes were characterized using cyclic voltammetry (CV) to achieve a better understanding of the charge/discharge process and to identify the intercalation/deintercalation potentials for lithium in the material. A test cell (HS-3E) provided by Hohsen Corp. was used for the measurements. Lithium metal acted as both reference and counter electrodes.

Fig. 5.86 shows an untreated basic grade carbon cones (CCRAW) electrode which was scanned from OCV down to 0.40 V at a scan rate of 50 μV/s. A minute current response is induced almost immediately as the scan starts from OVC (omitted from the figure). A small reduction peak is observed at 0.77 V. The scan rate is changed to 15 μV/s below 0.40 V. The current steadily increases as the voltage reaches 0.005 V. When the voltage is reversed, the current responds immediately. An oxidation peak is observed around 0.05 V before the current decreases towards the voltage turnaround. For the second cycle, the current follows the initial scan. However, the current response is lower for the discharge part.

A CV scan of a heat treated basic grade carbon cones electrode (CC2700) can be seen in Fig. 5.87. A scan rate of 50 μV/s was employed from OCV to 0.40 V. A reduction peak can be seen at 0.71 V. At 0.40 V, the scan rate is changed to 15 μV/s. There is a sudden increase in the current slope at 0.20 V

and 0.09 V. The reduction reaches its pinnacle at 0.03 V. Two oxidation peaks are found at 0.12 V and 0.14 V. For the second discharge, the current slope increases at 0.20 V, 0.15 V, and 0.10 V. Three distinguishable reduction peaks can be observed at 0.08 V, 0.06 V, and 0.04 V. As for the charging process, two oxidation peaks are present at 0.11 V and 0.13 V.

Cyclic voltammetry was not performed on any commercial graphite due to the known electrochemical characteristics provided by the manufacturer.

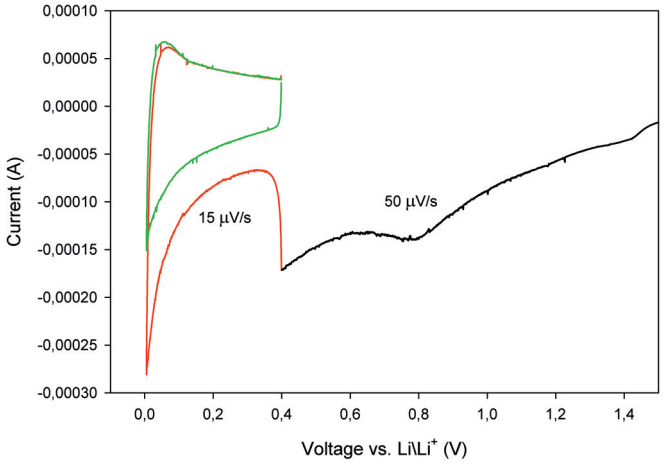

Figure 5.86: Cyclic voltammetry scans of the CCRAW electrode. The scan is initially performed at 50 μV/s from OCV down to 0.40 V. Following this the cell is cycled twice between 0.40 V and 0.005 V at a scan rate of 15 μV/s.

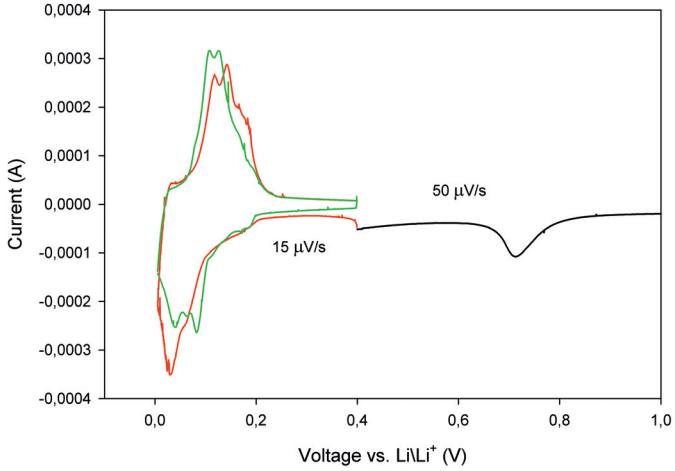

Figure 5.87: Cyclic voltammetry scans of the CC2700 electrode. The scan is initially performed at 50 μV/s from OCV down to 0.40 V. Following this the cell is cycled twice between 0.40 V and 0.005 V at a scan rate of 15 μV/s.

5.5 Thermal Studies

Two types of thermal analysis methods have been employed in this study. The first method is differential scanning calorimetry (DSC), which has been used to determine the exothermic reactions occurring in the tested electrodes. The second method is an in-house method for measuring thermal conductivity for different electrode materials. The carbon cones material has again been compared to commercially available graphite. The results are presented in the following sections. These studies are performed in order to gain a better understanding of thermal runaway processes and to identity the main contribution to this detrimental behavior.

5.5.1 Differential Scanning Calorimetry

A test matrix for the differential scanning calorimetry (DSC) was drawn up before initial testing. The same electrolyte was used in all three carbon samples. The following electrode samples were tested with the DSC, see Table. 5.7.

Table 5.7: Test matrix used for DSC measurements.

Carbon material	**Lithiated**	**Delithiated**
CCRAW	✓	✓
CC2700	✓	✓
SLP50	✓	✓

The differential scanning calorimetry curves are presented in Fig. 5.88 - 5.93. The results are plotted as heat flow (exothermic peak up) versus temperature. Samples from both lithiated and delithiated carbon are tested. Commercially available graphite has been compared to untreated carbon cones (CCRAW) and carbon cones heat treated at 2700 °C (CC2700). Three parallel samples were cut out from each cycled cell. The DSC results for three samples taken from a single anode are plotted in the same figure. The results from 30 °C and 60 °C are omitted due to startup transitions of the DSC apparatus. Exothermic reactions are set as upward peaks in the figures. Small sharp peaks are believed to be artifacts or noise from the measurement or base line.

Delithiated CCRAW shows several peaks, see Fig. 5.88. As the temperature is increasing the first exothermic peaks are located at 115 °C. The same curve also has a peak centered at 145 °C. The second curve has its heat responses at

130 °C and 200 °C, before it has a large peak at 300 °C. The third signal shows one exothermic peak at 160 °C.

The DSC measurements of lithiated untreated basic grade carbon cones is shown in Fig. 5.89. The first curve shows exothermic peaks at 130 °C and 240 °C. It may also have a small broad heat signal at 175 °C. The two other curves have a fairly similar heat evolution trend, both with exothermic peaks around 170 °C.

Heat treated basic grade carbon cones (CC2700) which are delithiated show almost identical responses for all parallels, see Fig. 5.90. Very little heat flows before the temperature reaches 200 °C. The heat response is endothermic for the three samples at higher temperatures.

The lithiated CC2700 results are shown in Fig. 5.91. The trend shows little or no endothermic responses from 60 °C. As the temperature increases, the endothermic response becomes stronger. The curve which goes outside of the figure, shows the same trends as the two others.

For the delithiated commercially available graphite (SLP50) it is possible to see an exothermic peak between 116 °C and 122 °C for all three samples, see Fig. 5.92. The curves continue towards higher temperatures and show exothermic heat responses above 250 °C.

The three parallels of lithiated SLP50 show similar features with an exothermic peak located between 127 °C and 149 °C. Each curve has at least one more peak at higher temperatures.

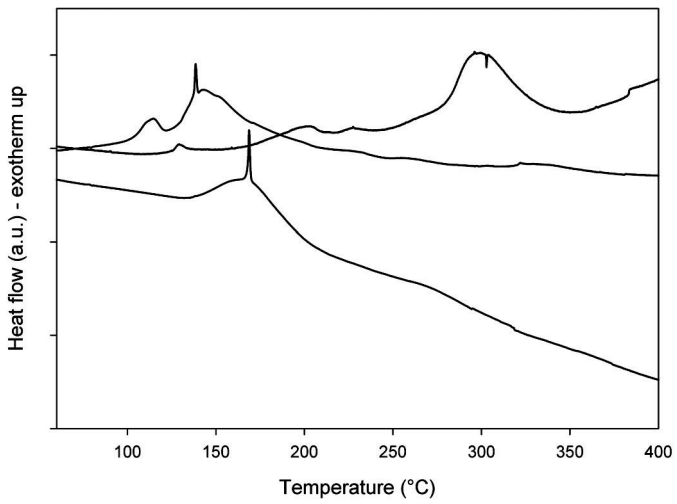

Figure 5.88: DSC measurement of delithiated untreated basic grade carbon cones (CCRAW).

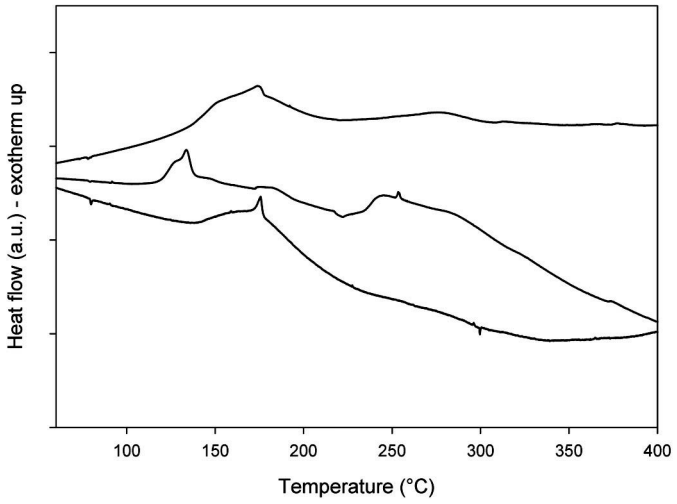

Figure 5.89: DSC measurement of lithiated untreated basic grade carbon cones (CCRAW).

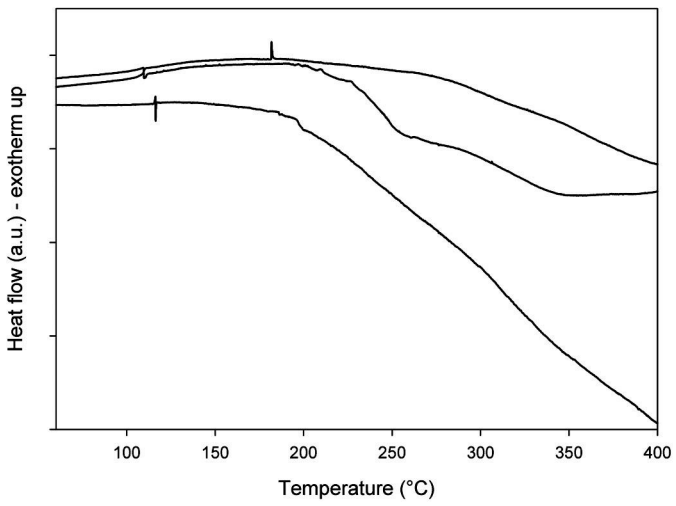

Figure 5.90: DSC measurement of delithiated basic grade carbon cones heat treated at 2700 °C (CC2700).

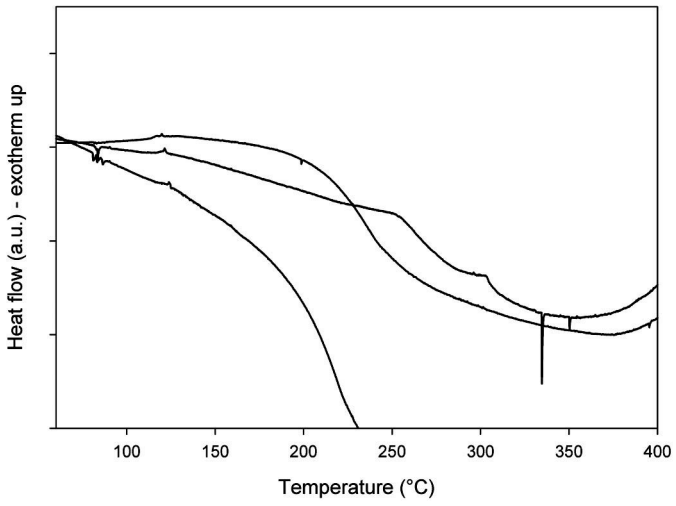

Figure 5.91: DSC measurement of lithiated basic grade carbon cones heat treated at 2700 °C (CC2700).

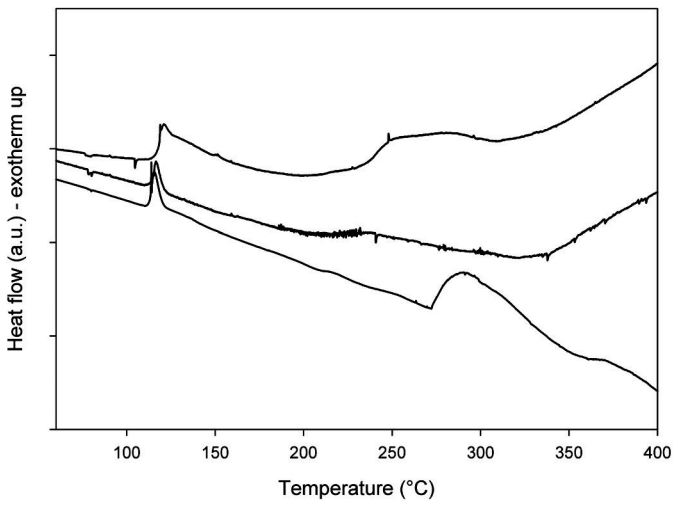

Figure 5.92: DSC measurement of delithiated commercially available graphite (SLP50).

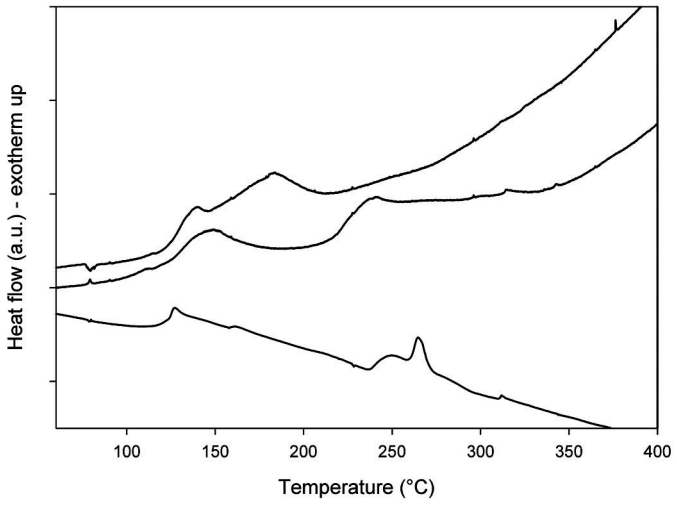

Figure 5.93: DSC measurement of lithiated commercially available graphite (SLP50).

5.5.2 Thermal Conductivity of Electrode Materials

Thermal conductivity is an important property with respect to heat dissipation. A material with low thermal conductivity would be much more likely to cause thermal runaway in a battery compared to a material with higher thermal conductivity. The thermal resistance of dry and soaked electrodes are plotted versus sample thickness in Fig. 5.94 and 5.95. The error bars for the thermal resistance follow from the apparatus calibration and has an accuracy limitation of 5 %, while the error bars for the thickness are estimated to be 5 µm. The thermal conductivities (inverse slope of plots in Fig. 5.94 and 5.95) with uncertainty from regression analysis are summarized in Table 5.8. For the dry specimens, untreated basic grade carbon cones (CCRAW) has the lowest thermal conductivity of all samples. However, its value exceeds the commercial materials (SLP50 and $LiCoO_2$) upon heat treatment (CC2700). The commercially available graphite (SLP50) and $LiCoO_2$ have similar dry thermal conductivities.

The soaked materials show a larger thermal conductivity. The thermal conductivity succession for the soaked samples are identical for the dry samples.

The improvement factor column in Table 5.8 is the ratio between soaked sample and dry sample. It expresses the enhancement in thermal conductivity for the wet electrode compared to the dry one. The factors are very similar for SLP50, CC2700 and $LiCoO_2$, while it is higher for CCRAW.

Table 5.8: Summary of thermal conductivity k measurements

Electrode material	**Dry** $(\mathbf{WK^{-1}m^{-1}})$	**Soaked** $(\mathbf{WK^{-1}m^{-1}})$	**Improvement factor**
SLP50	0.30 ± 0.01	0.89 ± 0.04	2.97
CCRAW	0.07 ± 0.01	0.36 ± 0.01	5.14
CC2700	0.41 ± 0.02	1.26 ± 0.07	3.07
$LiCoO_2$	0.36 ± 0.03	1.10 ± 0.06	3.06

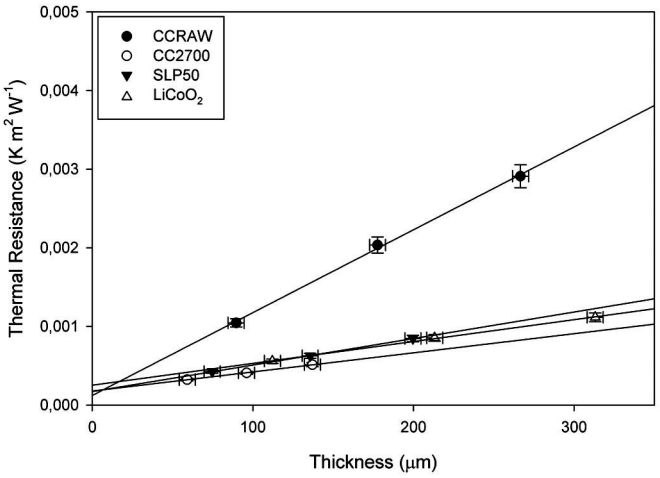

Figure 5.94: Thermal resistance of dry electrode samples as function of thickness

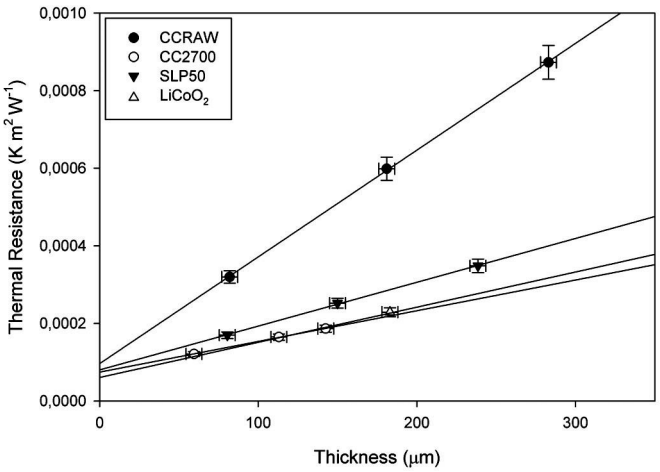

Figure 5.95: Thermal resistance of soaked electrode samples as function of thickness

Chapter 6

Discussion

6.1 Carbon Cones

Carbon cones have a unique conical structure which is attributed to defects in the graphene sheet. The defects are pentagon ring configurations which induce a curvature in the honeycomb layer. The number of defects determine the apex angle of the cone. One defect will yield the most open cone, while five defects will yield the most closed cone, i.e. smallest apex angle. The carbon layer will be flat if no pentagon rings are present. Six pentagon defects will not create a cone, but will rather form the end cap of a carbon tube. Further addition of defects in the same layer will produce closed structures, as stated in 3.8.

The cones produced in the Kværner carbon black and hydrogen process are to some extent different than the cones described above. The as-produced carbon cones consist of two parts, namely, ordered and disordered carbon, where the core is highly crystalline, while the outer shell is disordered. However, the apex angles are consistent with the angles described in the literature, indicating a good correlation between theory and produced material. It should be emphasized thoroughly that the main quantity of carbon in the produced sample consists of flat carbon disks, i.e. no pentagon defects are present in the hexagonal layers. Some smaller agglomerates of disordered carbon are also present in the samples. Both the cones and the disks are found to vary in size, see Fig. 5.1 and Fig. 5.8 for the basic grade and low grade carbon cones, respectively.

There are at least two special characteristics with the carbon cone. Firstly, the local size variation for a single cone is large. In other words, the cone has a

base diameter of several micrometers, while the diameter at the apex approaches zero. The vast size variations mean that size-dependent properties change along the length of the cones. The cone might have unique properties at nanoscale, but still have "normal" properties at macroscopic scale, particularly related to the decreasing curvature which may affect the hybridization of electron orbitals. Secondly, the other special feature where the cone shape is a consequence, is the assumed growth mechanism. It is natural to assume that the cone growth started at the apex. This assumption will be discussed later. If the cone started growing at the pinnacle, this means that the amount of pentagon rings dictates the final shape of the cone. After the initial growth, the shape of the cone is then set and the rest of the carbon is added on to the structure growing outwards to the expected cone base, which will eventually determine the diameter at the base and the height of the cone. Tens of carbon atoms will literally decide the shape of a cone consisting of billions of atoms.

The formation process of the cones is obviously still unknown, since the reproduction attempts have not been successful. However, it is still possible to elaborate on the mechanism for the formation process. The nucleation process most likely starts at the tip of the cone, determining the symmetry and the shape of the cones. This is the most logical starting point due to the structure and the nature of crystal growth. It is hard to predict how pentagons can act as a nuclei, although modeling and data simulations may give a hint. Energy considerations of the cone structures will also be a good pointer. Another fact to consider is that the amount of disks is about four times larger than the amount of cones. This agrees with the Jahn-Teller effect [139] that states:

> If the ground electronic configuration of a nonlinear complex is orbitally degenerate, the complex will distort so as to remove the degeneracy and achieve a lower energy.

It is challenging to determine the reason why the cone growth is terminated. However, it will most likely be connected to the dwell time during the formation. When the cone growth ceases, the cones are no longer in a part of the reactor where the growth variables are optimal. This termination can be compared with controlling the length of carbon nanotubes [140]. It is also difficult to predict why some defects occur in the graphene sheet, while other areas are defect free. This will be elaborated on in Section 6.1.1.

The particle size distribution from the basic grade carbon cones batch can give information about the conditions inside the reactor. The majority of the cones are of nearly the same size, while the disks can be larger or the same size

as the cones. The relatively even size of the cones means that the cones are created either during a short period of time or at a very specific set of reaction conditions. The cone and disk distribution indicates also a high nucleation rate. A nonuniform size distribution would have indicated otherwise. It is important to remember that the carbon cones material was produced during a test run of several hours. The desired cones could have been produced only in a limited period of time during the complete test run, while the disks could have been produced in the remaining period.

Some observed carbon cones do not have the predicted apex angles. This is due to the cones orientation relative to the projection plane. A narrow cone can appear to have a wide apex angle if it is viewed with the tip pointing towards or away from the observer. Another possibility is that the cones are growing like a spiral [141]. As indicated in reference [7] the wide distribution in apex angles is controlled by entropy. This hypothesis will predict that it will always be difficult to produce a single type of cone structure with this specific production method.

As explained earlier, the original purpose of the Kværner carbon black and hydrogen process was in fact to produce carbon black and hydrogen. However, cones were produced instead. It is worth noticing that the cones were only produced when a coke deposit was blocking the gas flow which means that gas and carbon material flow had to find a new pathway through the reactor. Similarly, cones were not produced when the deposited coke was removed from the reactor. The deposit may have played a crucial role in the production, which most likely resulted in changed pathways, ideal dwell time, and in ideal heating conditions. Reactor temperature and pressure would also be affected. This agrees with the requirement of specific reaction conditions.

Many of the observations done in this study have also been made previously [52].

6.1.1 Thoughts on the Carbon Cones First Stage Formation Mechanism

As stated earlier, the cone consists of an inner core and an outer shell. The two parts indicate a two-stage formation process.In the following sections, several different mechanisms for cone formation are suggested. These reflections are based on observations of the carbon cones material and the driving force behind dangling bonds saturation. There are many factors to consider, including the reaction rates of the different formation mechanisms which are important as they control the availability of reactants in the reactor chamber. For instance, a

limited supply of reactive hydrogen atoms will yield more pure carbon material and not hydrocarbons.

It is possible to speculate on the importance of a plasma in the presence of the cone formation. It is well-known that carbon nanostructures are manufactured in such environments as in the arc discharge or plasma enhanced chemical vapor deposition method [142,143]. A plasma gas is created by the ionization of neutral atoms. The plasma is in a quasineutral state with charged electrons and ions. Positive ions may bombard the hydrocarbons and provide the energy needed for carbon formation. The plasma may contribute in making highly reactive free radicals. It is natural to ask if the free radicals can provide a starting point for pentagon defects and therefore conical structures. The cone/disk ratio may be explained by the fact that the cones have formed in the presence of the free radicals and the disk have been produced in a purely hot region. A plasma can also be used to force growth in certain direction.

Ge *et al.* successfully produced single layer cones by vapor condensation [6]. These cones all had the smallest possible apex angle of approximately 19° associated with five pentagon defects. The growth of these cones may be initiated by fullerene-type nucleation seeds with different numbers of pentagon defects. They also suggested a lower probability of forming cones with between 2, 3, or 4 pentagon defects due to large strains in the structure. Their mechanism agrees very well with the formation of the five-pentagon cone, however, it does not does explain the findings of different cones in this and other studies [7,53]. The single layered cone growth can be terminated by closure of the dangling bonds at the carbon edge, finally forming a fullerene structure. The cones studied here are all open. The sheer size and the outer disordered layer may have prevented the closed cones to form.

Defect Migration Mechanism

After the initial evaporation and atomization, the carbon atoms travel towards a colder section of the reactor. The atoms collide and start forming solid carbon in the thermodynamically most stable formation which is in this stage a small graphene sheet. Carbon atoms will continue to add to the edge on the dangling bonds of the minuscule layer. At an early stage of the formation, a single defect is introduced to the edge of the hexagonal layer. The defect can for instance be induced by a foreign atom such as sulfur, see Fig. 6.1a. As the defect (pentagon ring) is settled in the structure, the rest of the small hexagonal layers bend in order to accommodate for the introduced pentagon. The growth can continue

from this configuration. This initial structure acts as a seed to further cone growth. At this stage, the cone seed can develop differently. If no more defects are introduced to the structure, the shape and apex angle of the cone are settled. The cone seed with the most open structure then flow further into the reactor. However, since there are cones with five different apex angles, more defects can be introduced to the structure. At an early stage of the cones formation, more defects can find its way to the edge of the hexagonal layer. More defects will create higher curvature. It is very unlikely that two defect will form at the same time, but due to the cone shape it is known that the defects have to be located close together. This can be explained by defect migration. For instance, if two defects are in the same curved hexagonal layer at some distance apart, the defect can migrate together by the means of the defect migration mechanism [144]. In a graphene sheet, a single defect migration will have an arbitrary direction until the defect reaches the edge of the plane and vanishes as the atoms around the defect bond to a potential surplus of atoms outside of the sheet. This can explain the large amount of disks in the sample. In the case where more than one defect is present, the defects will move relative to each other. They can move away from each other and the defects will disappear or the defects can gather, forming cones of a more closed structure. As an example, imagine two defects at some distance apart in a curve layer. Due to the induced curvature, the two defects can only move away from each other or towards each other. If it is assumed that the first defect is stationary, the other defect can travel towards the first defect directly until they coalesce, see Fig. 6.1b for illustration. After the cone angle (and amount of defects) is set, the cone can continue to grow at the base of the cone. If a defect is introduced at a late stage in the cone seed formation, it might not be able to travel towards the other defects, which might lead to cones with two areas with defects. Anomalous cones with two peaks have been observed by the author, see Fig 5.9 - 5.12. Even though the non-symmetric cones are present, their occurrence is rare. Pentagon ring defects formed late in the cone growth might also be canceled out by heptagon rings of seven carbon atoms. Another reason for finding few cones with multiple defect sites is that the defect "initiator" (i.e. sulfur atoms) has already reacted with hydrogen to form hydrogen sulfide gas. In the mind of the author, the abnormal cones may just as well be an affirmation that the cone growth starts at the apex. It is difficult to imagine a cone formation originating from a large cone wall or graphene layer.

Defects can migrate in a hexagonal layer, but to rearrange the carbon atom requires large quantities of energy. The average bond enthalpy of a covalent

carbon-carbon bond in benzene is 507 kJ/mol [66]. This means in principle that high temperatures are needed to induce defect transportation.

A drawback with this mechanism is that it does not explain the reason why there are more cones with the 60° angle compared to other cones [141]. Somehow the process favors the 60° cone. Another fact to consider is that the largest share of particles in the carbon cones sample from the Kværner carbon black and hydrogen process consists of carbon disks. They are similar to the cones with respect to a crystalline inner core and a disordered outer shell, and they have been through the same stages as the cones, but they are completely flat. The disks are regarded as cones with a 180° apex angle. It is fair to draw the conclusion that flat disks are the most favorable structure and it would be natural to assume that the 112.9° cone is the most common cone structure, due to the low strain and high defect probability in the structure. However, it is not known why the 60° cone is the most frequently observed cone.

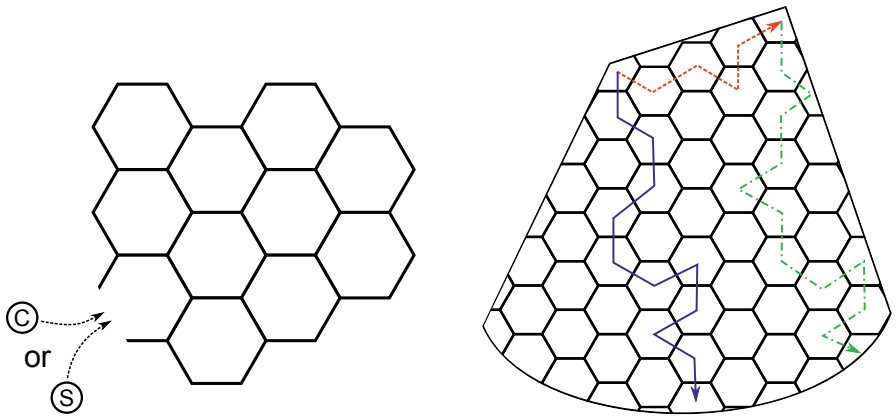

Figure 6.1: A schematic representation of the defect migration mechanism. a) The initiation of a pentagon defect in the hexagonal layer. b) The transport of a pentagon defect. The defect goes towards another defect and create a more closed cone structure (red dotted line). The defect(s) can also travel out of the structure, producing a more open cone (blue solid line) or disk (blue solid line and green solid-dotted line).

Edge Fusion Mechanism

Another feasible mechanism for the cone formation is controlled by the fusion of the graphene edges. As a very small hexagonal layer is formed, it will bend due to attractive forces between the dangling bonds, see Fig. 6.2a for illustration. The edges will fuse together, but this can only occur when a complete sector (60°, 120°, 180°, 240°, or 300°) of a graphene is missing from the graphene sheet. This will create the five different cones. The initial shape of the small graphene can be of a certain nature, yielding a cone which is not initially closed at the tip. Single atoms or rings of carbon might react with the dangling bonds the tip and fill the empty space quickly. If the graphene does not fuse with itself, but with other graphene layers, the familiar disks are formed. This can contribute to the explanation for why large amounts of disks are present in the sample. If there is a large amount of small graphene sheets available, the probability of combining with another sheet is high. The further growth of additional layers might hinder the first inner sheets from fusing with themselves.

Collapsed Graphene Mechanism

This mechanism is very similar to the edge fusion mechanism. Here, the graphene sheet will also fuse to itself, but the carbon atom will start to combine at the defect or apex of the resulting cone. This method will not create an opening at the cone tip, but the cone will rather be closed initially from the pinnacle. The cone will continue to self-merge (similar to a zipper) and grow outwards. New layers of graphene sheets will add to the existing cone core in the second stage of the cone formation. This mechanism might favor the formation of some cone morphologies, but it is difficult to predict which atomic arrangement is most favorable. For instance, if a collapse at a straight zig-zag edge of a graphene sheet occurs, a cone with the 60° apex angle will be created. This cone will correspond to the 180° disclination.

6.1.2 Thoughts on the Carbon Cones Second Stage Formation Mechanism

All the suggested mechanism above, only treat the initial cone formation. Studies show that the cones clearly consist of a graphitic inner core and a disordered outer layer [53]. This is also supported by the heat treatment results done in this work. The two phases of crystalline structures suggest a two stage formation of the carbon cones from the Kværner carbon black and hydrogen process. The

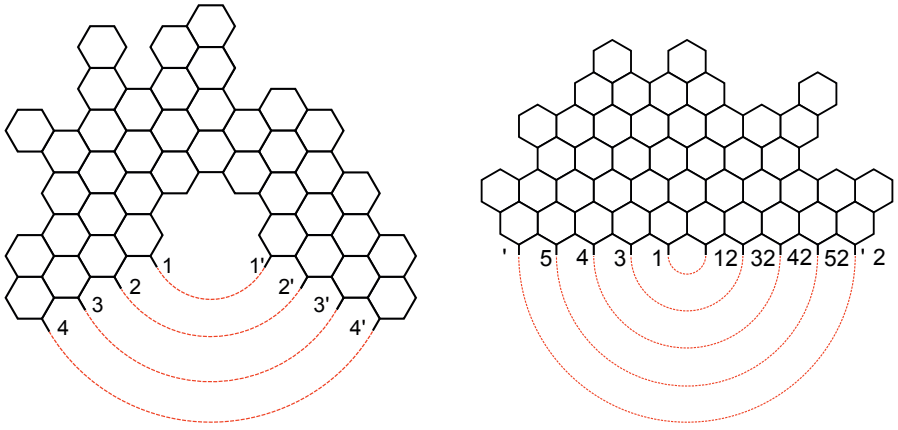

Figure 6.2: A schematic representation of a) the edge fusing mechanism and b) the collapsed graphene mechanism.

second layer is added to the core at a later stage in the process. As the cone seed continues to add carbon atoms to its edge, sheets of graphene can also add to the surface of the cone seed. If the addition occurs in the high temperature region, the external sheets will also be crystalline, and the wall thickness of the cone core will grow. When the cone has reached a colder region in the reactor, the additional layers of carbon will be disordered. A gradual transformation from crystalline to disordered is expected. However, this is difficult to verify. The disordering might be due to a typical island growth of the small graphite crystals and the low temperature prevents the further graphitization.

Transmission Electron Microscope Studies

All the five different cone types are presented in transmission electron microscope (TEM) images in Fig. 5.2 to Fig. 5.6. The wall thickness is uniform from the base to the tip for all the cones. This might indicate that they have grown during a short period of time, which indicates that the cones have either flown rapidly through the reactor chamber or the conditions for growth have only been ideal for a few moments. Due to the fact that they are also single particles shows that the cones have not had enough time to grow larger, as opposed to the carbon cigars in Fig. 5.15.

Fig. 5.7 shows the tip of the cone in Fig. 5.6. It is difficult, but possible, to see single atomic layers, because of the overlap of the different layers. The outermost layers are the most distinguishable as they are not covered by many layers. It is possible to see some minuscule graphitic structures within the cone, which align relatively parallel to the cone wall. It is not possible to distinguish the core structure in this micrograph.

6.2 New Carbon Cones Production Attempts

Several attempts to reproduce carbon cones have been made. Between September 14, 2007 and September 3, 2009, 29 test runs were performed in the carbon reactor at SINTEF's locations. During this period, there has been a major progress in the development, but there are still many challenges left to overcome. The progress can be verified from studying the field emission gun electron microscope images taken from the various batches. From the first batches, it is only possible to observe turbostatic carbon, while from the latest production it is possible to see conical structures in the samples.

Although the latest production attempts yielded structures that more closely resembled the original carbon cones, it can be concluded that the reactor conditions did not match the conditions in the Hofors reactor since no large amount of cones were produced. It is difficult to point out which factors have been the main reasons for the failed reactor runs, but some necessary requirements have been established. The presence of conical structures may indicate that the temperature and dwell time were within the correct range for the latest attempts. The temperature in the Hofors reactor was uncertain, because of a broken thermocouple. However, it is predicted that the temperature had to be sufficiently high to achieve the high energies needed to produce graphitization and the potential defect diffusion. The dwell time during the reaction may also not have been optimal. It is assumed that the dwell time has to be long enough for the cones to grow. A seed or several pentagons are most likely needed to induce growth.

At Hofors, the reactor product was collected in relatively large batches in downstream filters and cyclones. Since the basic grade carbon cones product contains a mixture of various carbon products, it is natural to assume that the cones were produced with a distinct set of variables as the conditions in the reactor were changing during test trials. At a later stage, the constituents can have been mixed during for instance handling or transportation. In the SINTEF reactor, the number of unknown variables were reduced by taking out samples

continuously during the test runs. In general, for each reactor trial a new set of variables were tested to verify the importance of the parameters. Details are omitted due to proprietary right belonging to n-Tec.

The oil derivate used to produce carbon cones was composed of mainly heavy hydrocarbons. As the oil was pumped through the reactor nozzle, it was sprayed as droplets into the reactor chamber. At this stage it is difficult to know what happens next. One alternative is that the droplets vaporize in the reactor chamber due to the heat from the plasma. The gas molecules are further torn apart and atomized into single carbon and hydrogen atoms, or small hydrocarbons. As the atoms/molecules flow further into the reactor, the temperature falls and the atoms are in a thermodynamically unfavorable state. Carbon atoms condense to form solid carbon, while hydrogen atoms combine and form H_2-gas. The hydrogen gas formation were confirmed by the pressure build-up inside the reactor. Excess hydrogen gas was either used as plasma gas or was purged out through an outlet.

A sulfur component as a reaction product is expected since the production reactant is a crude oil derivate containing sulfur. Hydrogen sulfide is easily detectable because it smells like rotten eggs. The hydrogen sulfide is produced as a result of the reaction between the abundant hydrogen and the small amount of sulfur present in the oil derivate.

The polyaromatic hydrocarbon naphthalene also has a very pungent smell and its presence was easily detectable. Naphthalene would be expected as a reactor product since it consists of two fused benzene rings bonded together. Polycyclic aromatic hydrocarbons are most likely very important in the production of more complex carbon structures such as carbon black, cones, and disks.

6.2.1 Electron Microscope Studies

Both the FEGSEM and TEM provide excellent images of the different carbon samples.

Field Emission Gun Scanning Electron Microscope

The images provided in Section 5.2 show the unsuccessful carbon cones production attempts. The main product of these trial runs consisted of agglomerates of spherical carbon particles, with a diameter of approximately 1 µm, while the

agglomerates can be several tens of micrometers across. In Fig. 5.14 it is possible to see the spheres up close. The spherical shape suggests a turbostatic structure, and the irregular surface indicates merging of small graphite crystals and the fact that the particles are covered with amorphous carbon. The temperature used in the reactor at the time of production was most likely not sufficiently high.

Some of the material found inside the reactor is presented in Fig. 5.16. A large percentage of the material consisted of carbon scrolls. The scrolls have a diameter of approximately 2 µm and length of 10 µm. The scroll shape indicates a helical growth. It is believed that the scrolls are anchored to a solid surface and the growth occurs at the disengaged side. The studied material was scraped off the inner linings of the reactor, which indicates that the scrolls were exposed to high temperatures for periods of a few hours.

The large size variation of the produced material is seen in Fig. 5.17. The smallest particles seem to be more agglomerated than the large particles. The largest spheres have a diameter up to ten times higher than the smallest particles.

Fig. 5.18 provides a close up of a typical large particle and it can be seen that the spheres consist of smaller sheets of carbon.

The overview image, see Fig. 5.19, shows the high amount of carbon stacks, while normally have a constant diameter along the length of the stack. However, some stacks have a diameter which varies along the length.

Three separate carbon stacks can be seen in Fig. 5.15. It is difficult to explain the reason for the directional growth. It is also uncertain why the stacks stop growing in a radial direction. Some stacks are shaped as a cigar, meaning the diameter is smaller at the two ends. This might have a connection with the temperature in the reactor chamber. In the beginning of each trial run, the decant oil was injected at temperatures around 2200 °C. The temperature increased steadily during the injection until the trial run was terminated. When the process was finished, the reactor was shut down and the oil injection stopped. As temperature decreased, there were still hydrocarbons present inside the reactor as the exhaust gases were recycled. The stacks could have continued to grow during the whole period, such that the small diameter of the stacks is due to lower temperature during growth.

Fig. 5.20 shows a structured carbon stack with an uniform diameter. The stack has the distinct conical structure similar to the carbon cones found in the Kværner carbon black and hydrogen process. The tip of the stack shows the facets which can also be observed in the carbon cones heat treated at 2700 °C.

The samples were collected from the inner reactor wall with a scraper. As the material was collected, several types of carbon could have been mixed together. The stack indicate an ideal condition for highly crystalline conical structures. These results confirm the importance of the high temperature during production.

Fig. 5.21 and 5.22 show two cases of exfoliated stacks. The closed layer on the stack in the middle of Fig. 5.21 is folded and unattached from the rest of the stack. Fig. 5.22 clearly shows many layers of carbon on top of each other. This stack does not have the amorphous layer covering the stack. The image indicate a growth mechanism where each layer has been added and grown separately.

Fig. 5.23 and 5.24 show nanofibers found in the bag filters of the reactor. Only small amounts were observed. The formation of nanofibers can originate from the discharge arc of the plasma process [5]. As the electrical arc discharges between the electrodes, a large amount of energy is released at a single point. This energy has the potential of producing carbon nanotubes. The reactor was disassembled after each trial run, and the electrodes inspected. The electrodes were replaced if they were heavily worn. This indicates that some of the carbon material produced, originated from the electrodes.

Transmission Electron Microscope

TEM images of the carbon material produced in the SINTEF plasma reactor is the clearest evidence of conical formation in the most recent trial runs. The structures are shown in Fig. 5.25 and 5.26. These cone shapes have probably one single pentagon defect in the apex due to the broad angle. The cone in Fig. 5.25 seems to have an almost perfect conical structure. As these structures were found on the inner linings of the reactor, it is believed that the growth started on the reactor wall surface. The conical orientation of the carbon atoms must have been formed in a late stage of the process as many layers have grown on top of each other. This contradicts the general assumption that the cone initiation starts at the apex and in a free flowing condition. However, these findings confirm the need for high temperature and long residence times. Fig. 5.26 shows what looks like a stack of cones. If the growth started at the concave side to the right of the image, the cones seem to be closer together when going to the left. It is unclear why the inter-cone distance decreases, but higher temperature towards the center in the reactor may lead to a higher degree of graphitization. The disordered coverage of the stack could have been introduced at a later stage in the process.

6.3 Characterization and Modification of Carbon Cones

6.3.1 X-Ray Diffraction

Powder X-Ray diffraction (XRD) was used to determine the degree of graphitization and the structural features of the carbon cones. The diffractograms are presented in Section 5.3.3. The diffraction lines appearing at 2θ-values of 26°, 42°, and 54°correspond to the (002), (100), and (004) planes of graphite, respectively [145]. Since the (002)-plane is the most dominant plane in the graphite structure, its contribution will be far greater compared to the other lattice planes.

Untreated basic grade carbon cones (CCRAW) have only one significant peak at 26°. The (002) reflection peak is asymmetrical as it is a superposition of at least two other components, one of which corresponds to an interlayer spacing of 0.34 nm. This signal arises from relatively ordered graphite crystals. The other component relates to a larger interlayer distance which is typically found in turbostatic graphite crystals [146]. For CCRAW, this can be interpreted as the XRD signals from the crystalline core and the disordered outer layer, which was observed by Garberg *et al.* [53]. The disordered carbon black component in the carbon cones material will also contribute to the signal from the larger interlayer distance crystals.

For the heat treated materials, the 26° peak is very sharp, indicating a high crystallinity in both a-axis and c-axis direction. An increase in crystallinity is connect to the increasing temperature. With XRD, the whole carbon bulk is measured and the signals are not limited to the surface. As the trend of high crystallinity is also show in the Raman spectroscopy, it is believe that the heat treatment holding time of 3 h is sufficient to induce graphitization of the entire sample. The alignment of the small crystallites takes place in bulk and at surface. The crystallite growth is also conformed by the observation of facets in FEGSEM images, see Fig. 5.28 and 5.29. It is believe that the heat treatment temperature of 950 °C is not sufficient to alter the structure of the carbon cones material. It should be noted, that the position of the 26° peak does not change with annealing.

The other non-heat treaded samples does not have a prominent effect on the X-Ray diffraction signals.

6.3.2 Raman Spectroscopy

Raman spectroscopy was employed to find supplementary information to the XRD study above. The technique is highly sensitive to covalent bonds with little or no dipole moment. As carbon-carbon bonds fulfill this criteria, Raman spectroscopy is an especially useful technique for studying carbon materials, and can provide valuable information regarding the surface regions.

Every band in the Raman spectrum corresponds to a vibrational frequency of a chemical bond within the carbon structure. The vibrational frequency (position of the Raman peak) is sensitive to the bond orientation and the weight of the atoms in each end of the bond. The Raman spectra exhibit typical features for graphite and similar materials, which are recognizable peaks at around 1340 cm^{-1} and 1590 cm^{-1}, called the D-band and G-band, respectively. Overtones are also present, such as the D'-band (1620 cm^{-1}) [147]. The G-band signal arises from the vibrational movement as the sp^2 carbon atoms move/vibrates in the graphene plane, while the D-band can be observed at non-symmetric regions, such as edge planes or lattice defects like edge dislocations, lattice vacancies, and interstitial carbon atoms between the basal planes of graphite [35, 148]. The ratio between the G-band and D-band is often used as a measure for graphitization, and the bond sharpness tells that the bond is uniform in nature. Since the typical particle size of the carbon cones is smaller than the measured area (diameter of the laser beam), Raman spectroscopy will yield information covering the over-all mix of structures.

The heat treated material shows an increase in the G-band intensity compared to the D-band, see Fig. 5.33 and 5.34, which indicates a graphitization of the carbon cones as the temperature reaches 2700 °C, as also confirmed by FEGSEM and XRD. The full width at half maximum (FWHM) value of the G-band decreases which indicates an increase of the crystallite size in the surface region [149]. As the graphitization occurs, the number of edge locations will be negligible compared to the number of interior carbon atoms, and hence gives a stronger G-peak than D-peak.

A small shoulder peak is distinguishable in the heat treated spectra, which originates from the D'-band [150] and indicates disorder. The D'-band appears in carbons with a low disorder such as microcrystalline carbon. However, it can not be observed as the wide G-band of the untreated carbon cones overshadows any potential D'-signal from the carbon black present in the samples. The carbon black alone may give rise to distinct D'-bands. Even though the carbon black also undergoes graphitization upon heat treatment, the crystallite size is much smaller compared to the cones and disks which explains the D'-band

present in heat treated carbon cones.

The mixture sample (5050CCRAWCC2700) of untreated and heat treated carbon cones has a Raman response similar to the superposition of the CCRAW and CC2700 spectra, which would be expected by a sample containing both carbon materials. CC2200 has a visible peak at 1704 cm^{-1}, which is not present in any other measurements and is therefore disregarded.

A shift in the G-band can be attributed to structural changes on the graphite surface as the sample is oxidized, as seen for CC900Air2700Ar compared to CC2700 (Fig. 5.33). Upon heat treatment, the disordered carbon covering the crystalline core of cones becomes graphitized. However, some microcrystallites on the surface might not be able to completely merge together with other microcrystallites due to the limited amount of carbon at a surface [1]. These small crystallites are burned off during subsequent oxidation in air, while the larger crystallines remain more or less unchanged. As a consequence, when performing Raman spectroscopy, the signal obtained from the carbon surface originates mainly from larger crystallites which are no longer covered by microcrystallites [149].

Raman spectra for treated carbon cones which are similar to the CCRAW spectrum indicate that the corresponding treatment is not an efficient method in altering the carbon structure at the surface, or that the Raman spectroscopy method is not adequate for studying these samples. For instance, the functional groups of CC-Func might not be Raman active. This is true for several of the oxidized carbon samples, see Fig. 5.35. The CC900Air-spectra is almost identical to the response from the untreated basic grade carbon cones (CCRAW). Carbon black will oxidize at 900 °C in air [151]. However, CCRAW-spectra did not change as it was oxidized, which means that the disordered carbon covering the crystalline core is more stable than typical carbon black. FEGSEM images of the CC900Air show the presence of carbon black structures. It is important to remember that the term carbon black covers a vast range of different types. These Raman studies show that the carbon black present in the carbon cones material has different properties compared to the carbon black studied by Snow *et al.* [151].

CC900Ar-Air shows similar features to the CC900Air except from a clearly sharper G-band. The reason for this is unclear as the temperature is too low to provide a sufficient graphitization. Nevertheless, it is possible to speculate that some curing of the carbon surface occurs at 900 °C.

[1] Atoms on the surface have fewer neighbor atoms compared to atom in the bulk.

The material treated with nitric acid (CCHNO3) shows a new wide peak at 1250 cm^{-1}. The origin of this peak is also unknown to the author, however it is possible that some Raman active functional groups are present on the surface after nitric acid treatment.

The three top spectra in Fig. 5.35, namely CCH2O2, CC-Func, and CC900-Func does not differ from CCRAW. It is therefore reasonable to conclude that the respective treatment does not alter the surface structure of the Raman active components of the carbon cones material.

Fig. 5.36 depicts the Raman signal from the microwave treated and low grade carbon cones. LGCC, MWCCAir, MWCCAr are similar to the CCRAW, demonstrating these methods to be ineffective with respect to surface alteration of Raman active species. The surface of the low grade carbon cones is believed to be similar to the surface of basic grade carbon cones, since the two materials show much of the same properties. This is not surprising since the materials were produced in the same reactor process, although at different times. The low grade carbon cones heat treated at 2700 °C (LGCC2700) have a strong G-band compared to LGCC. This indicates a successful graphitization of the the low grade carbon cones, as also confirmed by X-ray diffraction data and FEGSEM images.

Gruber *et al.* claim wide bands are owed to microcrystallites of various sizes [152]. In this respect, the band width in the Raman spectroscopy provides information on the size distribution of microcrystallites. Nevertheless, it is difficult to use the band width as a quantitative method for determining the size distribution of graphitic structures. In general, it is intrinsically difficult to evaluate Raman shift (cm^{-1}) data from disordered carbon due to the wide peaks as opposed to the peaks from the crystalline graphite.

Raman spectroscopy studies of graphite material is usually performed as a matrix scan to obtain the average information from the whole system. This was not necessary for the carbon cones material due to a wide laser diameter relative to the small particle size. A single Raman scan should therefore be sufficient for a good overall picture of the surface conditions. Particle sizes for commercial graphite materials are normally larger than 10 µm, while the carbon cones are an order of magnitude smaller.

As a small digression, it is worth mentioning the radial breathing mode (RBM) of single-wall carbon nanotubes (SWCNT), which appear between 150 cm^{-1} and 250 cm^{-1} depending on the laser excitation energy and tube diameter. The band corresponds to the contraction and expansion of the tube [153]. For single sheeted cones, such as the ones produced and observed by Ge *et al.* [6], a similar

RBM-bond can be anticipated. However, this band will be more of an elevation (plateau) rather than a peak as the diameter of the cone varies along its axis.

6.3.3 Nitrogen Adsorption Measurements (BET)

The specific surface area of heat treated carbon cones decreases with increasing temperature, see Fig. 5.37. This is expected since the high temperature leads to graphitization of the carbon material, which is confirmed by XRD (Fig. 5.30) and Raman spectroscopy (Fig. 5.33). High crystallinity is achieved by the fusing of microcrystallites. As this process proceeds, the surface area is minimized when the edge plane and microporosity concentration decreases. It is believed that the dangling bonds of the edge planes in the graphite sheets forms closed loops, hence reducing surface area similar to the findings of Lim *et al.* [154]. Such concentric loops have been proposed to be formed through the folding of carbon sheets at their edges [155]. The formation is based on the regularity of the structure within the carbon material. The bonding is stabilized at the looped edges, even though the induced curvature create strains. In relation to lithium-ion batteries, closed loops can hinder the lithium ion to penetrate between the graphene layers. Fortunately, lithium ions can intrude into the bulk carbon through the defects in the closed-edge structures [155], resulting in high capacity.

Novák *et al.* state that an increase in the structural order hinders the formation of the passivation layer (SEI-layer) as the active surface area decreases [156]. The active surface area has some correlation with BET surface area for non-microporous solids of the same family, which have a comparable density of active sites [157]. The latter publication ([157]) shows a clear relation between the SEI formation and the BET surface area on the carbon cones material. However, the BET surface determines only the external surface of the carbon. As graphitized carbon is anisotropic, it has both edge and basal planes. At the edge planes, reactions like co-intercalation of solvated lithium ions and self-discharge of intercalated lithium can contribute to the irreversible loss usually attributed to the SEI-formation. The BET-technique can therefore not alone determine the charge loss. Additional information regarding the surface plane ratios is needed [158].

The heat treatment in air at 900 °C (CC900Air) appears to be a very efficient method for increasing the specific surface area as it is almost 5 times higher compared to the untreated basic grade carbon cones. This could be attributed to oxygen reacting with the carbon at the defect sites, since the carbon atoms

at the graphite edge planes are not saturated in bonding valance, hence creating more pores [159]. For lithium-ion batteries, a mild oxidation of the carbon can create carbonyl, carboxyl, and hydroxyl surface groups etc. [160]. These oxides become a part of the SEI-layer and inhibit the decomposition of the electrolytes by decreasing the activity of the edge planes [161]. However, over-oxidation can have a negative effect on the irreversible loss if carbon has a high concentration of active sites.

The microwave radiation of the basic grade carbon cones in argon (MWCCAr) did not significantly change the surface area. The aim of this treatment was to rapidly release volatile compounds within the carbon cones. The anticipated gas release should expand and open the carbon structure leading to a higher surface area. However, this was not accomplished. The results are confirmed by FEGSEM and Raman spectroscopy. The short treatment time of 20 s in an inert atmosphere may have contributed to the negative results, but the lack of a sudden depressurization is believed to be the main cause. Dr. Theodore Steriotis from the Institute of Physical Chemistry at NCSR Demokritos obtained expanded carbon cones when he experienced a release of a 50 bar safety value when performing identical experiments. In air microwave treated carbon cones (MWCCAir) had a small increase in the surface area compared to the MWCCAr. MWCCAir was believed to be oxidized over a short period of 20 s. During the 20 s, the carbon started glowing which indicated high temperatures. A larger increase in surface area is expected if the treatment time was increased.

Low grade carbon cones (LGCC) show a lower surface area compared to the basic grade carbon cones. This can be explain by the fact that LGCC particles are thicker and therefore larger then the CCRAW particles. The surface area is inversely proportional to the particle size. The BET surface area for (LGCC2700) is lower than the surface area of LGCC due to the same reasons as for the CCRAW/CC2700 occurrence.

6.3.4 Bulk Density Measurements of Carbon Powder

The as-produced untreated carbon cones (CCRAW) have the lowest apparent bulk density of the measured carbon materials. The carbon cones material heat treated to 2700 °C (CC2700) is almost twice as dense as the untreated material. During heat treatment the powder is pressed into a crucible. After the heat treatment, the powder was filtered through several sieves. The large density difference between the carbon cones materials may be caused by the

compression prior to the heat treatment and higher particle packing. A minor part of the bulk density differences can be attributed to the graphitization of the carbon cones.

Both of the commercial carbon materials have a density about one order of magnitude higher than the untreated carbon cones. TIMREX® SLP50 has a higher density than the TIMREX® SLP30. The particle sizes (d_{90})[2] for SLP30 and SLP50 are 32 µm and 45 µm, respectively. A different particle size distribution correlates well with the different bulk densities.

The density values given by the manufacturer are some what different from the values measured here. The Scott Volumeter method is apparatus and operator dependent, however, the results show the same trend as the values given by TIMCAL. Therefore, the variations could merely be a result of different measuring techniques.

The bulk density difference between the carbon cones and the commercial graphite is most likely caused by the physical shape and morphology of the carbon particles. Bulk density gives an indication of the voids between the particles. The carbon cones material consists of mainly cones and disks with a wide global size distribution, as discussed in Section 5.1.1. The particles are oriented randomly with respect to each other, but the disks and cones will cause some alignment, similar to a fallen house of cards. The commercial graphite particles are approximately spherical, relatively uniform in size, and typically one order of magnitude larger than the carbon cones particles.

In this study, the tape casted electrodes are not calendered during manufacturing. The bulk density of the carbon will thus have a significant effect on the mass loading (mg/cm^2) of electrodes with similar thickness, where a high density material will yield a higher loading. This will consequently give a higher volumetric capacity of the cell [162]. The anode density of the studied graphite may have a significant effect on the cell performance as it alters the SEI-formation and cyclability [163]. Density differences can also change the performance due to increased conductivity within the electrode. Smaller voids improve the contact between particles, reducing the electrical and thermal resistance of the electrode. Small voids help the binder properties and give a mechanically stronger electrode. A reduction in the anode porosity will reduce the electrode surface area and hence the irreversible capacity loss [164] due to SEI formation.

[2] d_{90} describes the average particle diameter where 90 % of the distribution has a smaller particle size and 10 % has a larger particle size than stated.

6.4 Carbon/Lithium Half-Cells

The current section treats the issues regarding the electrochemical cells tested in this work.

Some parameters that could affect the cell properties, such as storage of carbon and/or electrode have not been accounted for. The treatment and subsequent testing were performed at different locations. In addition, due to limited charge/discharge testing capacity, this made the effect of storage difficult to control/measure. In order to avoid contributions from newly treated carbons, all samples were stored at least a few days in air and at room temperature before cell manufacturing.

6.4.1 Charge/Discharge Measurements

The charge/discharge measurements will be addressed according to the different features rather than for each individual electrode material. The features will be discussed loosely in the order of occurrence.

Initial Open Circuit Voltage

Almost all cells show an initial open circuit voltage (OCV) at approximately 3 V which is higher than the voltage window used in the charge/discharge testing (0.005 V - 1.5 V). The OCV varies some between the different parallel cells and electrode material. Voltage variations can be expected as the initial high voltage is attributed to the electrochemical potential differences between the surface atoms on the carbon electrode and the lithium [165]. Different electrode materials have different surface properties and this can therefore alter the OCV. Various carbon treatments performed in this study will also effect the surface. Another important factor for the OCV is the assembly process. During coin cell manufacturing it is easy to short circuit the cell unless precautions are taken. The internal resistance of the cell will also contribute to the OCV. Regardless of these variations, the OCV might not be the most important parameter for carbon/lithium half-cell characterization. Due to the rapid decline in the initial discharge profile (only a small charge goes through the cell), the OCV does not significantly affect the carbon capacity. For instance, the initial discharge profile of the CCH2O2 electrode (Fig. 5.60) starts at a voltage of 1.1 V which is within the potential window of the testing. This cell still reaches the high capacity which is typical for the first discharge. The voltage response of

CC-Func (Fig. 5.64) is a bit different compared to the other charge/discharge measurements, where the cell gains capacity at a higher voltage (≈1.5 V). Oxygen functionalization on the carbon surface could cause a reaction with the lithium ions in an early stage of the discharge process contributing to a massive irreversible loss. CC900-Func also shows the same feature, however it is not as prominent compared to the CC-Func electrode.

Solid Electrolyte Interphase (SEI) Formation

At voltages around 0.8 V, a plateau is forming on almost all initial discharge curves except for the LGCC (Fig. 5.72). The plateau is formed as a consequence of the SEI formation as explain in Section 3.2.11. Lithium ions are consumed and the current through the cell is spent on the decomposition of the electrolyte. The plateau becomes more apparent with increasing heat treatment temperatures. The decomposition of the electrolyte occurs at a specific potential for a specific environment. It is known that the SEI formation on carbon depends on the surface structure [111, 112]. SEI reaction continues until a complete coverage of the carbon surface is archived. As the carbon becomes graphitized, the basic building block units rearrange creating larger crystals. Due to the hollow or flat shape of the carbon cones and disks, a large portion of the exposed carbon is the basal plane. This creates a distinct potential for the SEI formation. The more amorphous carbon possesses a disordered surface with active sites at different chemical potentials. The small particles of the carbon cones material have a large specific surface area, resulting in a large SEI contribution and a large irreversible capacity loss. Furthermore, the SEI signal is not as strong for the larger particles for the two commercial alternatives (Fig. 5.76 and 5.78). SEI formation is the main reason for the high initial discharge capacity and irreversible loss. It can therefore be desirable with particles larger than the carbon cones. On the other hand, smaller particles facilitate faster lithium insertion and removal. By reducing the characterizing dimensions of the active material, the cycling rates are improved as the time constant for diffusion is proportional to the square of the diffusion length [166]. There is a trade-off between rate performance of a cell and its capacity. For all other samples, it is difficult to distinguish between the SEI profile curvature. On the other hand, it is possible to differentiate the voltage with respect to the capacity or time to obtain a clearer picture on the potential changes. However, this was not calculated here.

It is worth mentioning a few words regarding the exfoliation phenomena. The curvature in the charge/discharge profiles associated with the SEI formation

increases with heat treatment temperature of the basic grade carbon cones. As the heat treatment temperature increases, the surface area of the carbon becomes smaller, as seen in Fig. 5.37. This should lead to a reduction in the charge consumed by the SEI. A second mechanism might be the reason for the lack of change in the charge consumption, namely the exfoliation. Graphitized carbon cones are not cover by a disordered layer which contains many cross-linking carbon bonds. The edge planes are not protected and co-intercalation can occur at the cone base or disk rim. Exfoliation causes the carbon layers to separate and new fresh surfaces are exposed to the electrolyte resulting in further SEI formation.

Further Slope Development

As the initial discharge proceeds past the SEI formation, the profile flattens out at the lower potentials. For disordered samples, the discharge continues smoothly and without any perturbations. For the commercial graphite and the high temperature heat treated carbon cones, the discharge reaches stages or plateaus at low voltages. It is well know that this process is attributed to the intercalation of lithium ions in between the graphite layers as explained in Section 3.2.6. The intercalation is also supported by the cyclic voltammetry measurement of Section 5.4.3. It appears the SLP30 and SLP50 electrodes have at least three different plateaus, the first occurring at 0.2 V. These plateaus correspond to the different stages in the carbon lithium stoichiometry. The voltage is leveled during the shift from one stoichiometry to another. The SLP30/SLP50 charge/discharge curves smoothen out at higher current rates. This is the result of kinetic limitations. Lithium ions do not have time to diffuse through the carbon and complete each intercalation stage before the next is started. This is also observed by Henry *et al.* [167].

CC2700 and LGCC2700 does not seem to have the similar discharge development as the commercial graphite. They typically start to flatten out at 0.2 V, but it is not possible to distinguish the different intercalation steps, which may again be assigned to the small particle size and heterogeneity of the sample. Intercalation of the graphitized carbon cones material occurs at different potentials as the cone surface has different chemical potentials for the lithium intercalation. Lithium ions which penetrates the structural defects in the closed loop curvature will have a different activation energy compared to the lithium which accesses the carbon in between the closed loops. The mixed sample (5050CCRAWCC2700) seems to have features from both the corresponding electrodes.

The initial discharge capacity at 5 mV varies immensely. There are two main reasons for this. Firstly, the previously discussed SEI formation consumes a large amount of charge and therefore contribute to the initial discharge capacity. Due to the larger specific surface area of the carbon cones, more electrolyte is decomposed. The cones therefore have generally a larger initial discharge capacity compared to the commercial alternatives. The second reason for the variations, is the measured mass of the active material. Since capacity is measured in mAh/g, any errors in the electrode weight will cause changes in the capacity. The carbon cones are extra sensitive to weighing errors due to its low loading (mg/cm^2) on the current collector. The electrode mass was determined as explained in Section 4.3.4, with a current collector mass of typically one order of magnitude larger than the carbon weight. The electrode weighing was performed inside a glove box. Since the pressure inside the glove box can vary slightly during operations, this could cause instabilities at such a low mass. Even though the weighing was done with extreme caution, it is not possible to exclude this error from the results. Nevertheless, there are two ways of avoiding this error. Electrodes can be cut out and weighed out in a more stable environment, even though this may lead to some practical experimental implications. Secondly, pouch cells can be employed as the specific capacity is not as sensitive to the mass errors due to larger electrodes. Values for absolute specific capacity reported from coin cells should therefore be treated with care. Such errors in the mass will naturally affect the successive cycle capacities. The low loading is supported by the use of large amounts of NMP (1-methyl-2-pyrrolidinone) for the electrode production for the carbon cones compared to the commercial material. Low loading and excessive use of NMP resulted in a high porosity which may also help to explain the thermal conductivity measurements discussed later.

As the voltage changes polarization, the charge profiles proceed in a similar manner as for the discharge curves. All the electrodes are reversible when disregarding the capacity loss from the SEI formation. The commercial graphite shows analogous staging as the lithium deintercalates from the carbon, while the carbon cones material has the typical smooth charge profile of disordered carbon. The parabolic-like curve is typical for capacitive charge and discharge. As the charging continues, the potential increase almost exponentially towards 1.5 V, which was chosen as the cut off voltage as no further capacity is gained at this point.

A hysteresis effect can be seen in the charge/discharge plots as there is a voltage difference between lithium insertion and lithium extraction. The hysteresis can be assigned to the large charge transfer resistance and the slow diffusion of

lithium during delithiation of lithiated carbon. The large charge transfer can in the case of intercalated carbon be interpreted as a mechanical alteration of the carbon structure [168].

Cycle Performance

All cells have been cycled at least 11 times with increasing current rate of 10 mAh/g, C/20, C/10, C/5, C/2, and C. Each current rate was repeated twice to ensure rate reproducibility. It can be clearly seen that the initial discharge capacity is significantly larger than the other capacities, again ascribed to the SEI formation. At increased current rate, the capacity decreases. This effect can be attributed to slow lithium diffusion within the carbon particle, transport rate for lithium across the SEI film [81]. As the rate increases from the 10 mAh/g to C/20, the current density almost doubles, without significantly altering the capacity. The lithium diffusion at C/20 is sufficient to achieve maximum lithium storage. As the current doubles to C/10, a capacity decrease is seen in all cells except for the CC2700, CC900Air2700, and LGCC2700 cells within reasonable values of the error bars. Due to the high graphitic nature of these materials, lithium ions can easily diffuse between the graphene layers. The small particles also contribute to a lower diffusion time constant. Together, these properties allow for improved rate capabilities. Especially the LGCC2700 electrode shows excellent performance at even higher rates compared to the disordered carbon cells. It is difficult to determine if the rate capabilities for the LGCC2700 are better than the CC2700 and CC900Air2700 due to the measurement errors.

The error bars for the first discharge capacity is often significant when compared to the subsequent cycles. The main reason for this trend is the variations of the initial open circuit voltage (OCV) and SEI formation. It can be challenging to assemble identical cell with respect to the internal resistance and the OCV due to among others the heterogeneity of the sample surface. Minor leak currents can also occur, which result in lower voltage. If the error bar sizes decrease with consecutive cycles, the cell charge and discharge capacities have stabilized. However, if the error bars increase, the capacity development is destabilized. Large deviations from the average capacities for all cycles can be assigned to the weighing errors of the electrodes in the glove box.

Long-term Testing of Half-Cells

Three different electrode materials (CCRAW, CC2700 and SLP50) were tested for extended cycling. An initial cycle of 10 mA/g was performed before the cell

was cycled 100 times at C/4 rate. It was not desirable to perform more cycles, due to risk of lithium dendrite formation and short circuiting of the cell. All the cells show the initial drop associated with SEI formation, though the initial cycle is excluded from the graphs, see Fig. 5.80 to 5.82. The CCRAW electrode shows a somewhat lower capacities compared to the other samples. This is in accordance with the standard cycling performed in this study. The basic grade carbon cones CCRAW shows a remarkable stability during the first cycles (3-20) compared to the heat treated carbon cones (CC2700) and commercial SLP50 electrode. The latter samples exhibit a capacity drop in the early stages of the cycling, before they experience stable capacities for the subsequent cycles. The origin of the drop is uncertain, but it is possible to speculate in the instabilities of the SEI formation of the first cycles. The fact that the drop does not occur for CCRAW may indicate a more stable SEI for the raw cones which again may be attributed to the particle size and disordered structure. It is very likely that a similar capacity drop have occurred for the cycling at different rates, hence resulting in a perturbation of the high current capacities. The high rate capacities can therefore be slightly higher than first thought if measured at stable conditions.

The majority of the basic grade carbon cones material consist of flat disks. Due to the shape of the disks, most of them will have a parallel orientation to the current collector after tape casting. For the CC2700, the orientation can have a negative effect on the cyclability of the cell since during intercalation the carbon tends to expand perpendicular to the current collector surface. The process is associated with the loss of contact between the active material and the current collector.

The Coulombic efficiency of the cells are adequate for long-term cycling,[3] indicating a low degree of parasitic side-reactions. It is difficult to predict further development due to the unavoidable dendrite formation. For a reasonable prediction of the long-term properties of an electrode material it is important to use a complete cell with an adequate cathode material. Prolonged experimental measurements can be avoided by thought-through cell predictions and the utilization of a highly accurate battery tester [169].

[3]The statement "long-term cycling" as is perceived differently between the researchers and the industry. Here, 100 cycles are sufficient. However, the car industry for instance, are interested in cells exceeding 3000 cycles and above.

Electrode Thickness Comparison

The CCRAW material was tape casted with three different thicknesses to study the effect of electrode thickness. A doctor blade gap of 100 µm, 200 µm, and 300 µm was chosen as practical thicknesses to work with. The dry final thickness was approximately half of the coated wet film. The thinest electrode shows the highest specific capacity, while the thickest electrode has the lowest lithium storage capacity. This can easily be explained if the lithium storage mechanism for raw carbon cones is understood correctly. Both the charge/discharge measurements and the cyclic voltammetry show a capacitive charging behavior for as-produced basic grade carbon cones. The lithium is stored on the carbon surface exposed to the electrolyte. If the electrolyte is not able to penetrate deep within the carbon electrode, the same amount of lithium will be stored on the surface regardless of the electrode thickness. Due to the higher mass of a thick electrode, the specific capacity will be lower.

Another reason for the different capacities can be assigned to the ohmic resistance across the electrode. Since the cells were cycled between 1.5 V and 5 mV regardless of the electrode thickness, the thicker electrodes would have a higher resistance due to the longer resistive path. A larger ohmic overpotential is therefore needed as the current is held constant. With the same cut-off potential for all electrodes, the capacity of the thin electrode will be higher compared to the thicker electrodes. The same observations were obtained by Shu *et al.* [170]. This behavior emphasize the importance of an uniform thickness profile for the electrode. Calendering would significantly improve the capacity variations due to different electrode thicknesses.

In order to find an ideal electrode thickness, other aspects should also be taken into account. A too thin electrode will lead to experimental problems of the tape casting procedure. It is for instance difficult to obtain a thin smooth surface due to relatively larger particle sizes. A high weight of the current collector compared to the active material will contribute to a low specific capacity of a complete battery. Too thick electrodes can crack and cause delamination from the current collector.

In a similar study by Zheng *et al.*, several different carbon materials were tested with regard to capacity, rate capability, cycle life and electrode thickness [171]. Most of the carbon materials did not change their reversible capacity and first cycle efficiency with electrode thickness. However, the capacity at high rates were very sensitive to the thickness of the electrode. The tested carbons were of a graphitic nature, allowing for intercalation as opposed to the carbon cones. The graphite structure would explain the features mentioned above.

The effect of loading (mg/cm^2), i.e. the amount of carbon on the current collector has not been prioritized in this study. The process of producing slurries with an adequate viscosity for each carbon material lead to the use of the different NMP solvent amounts. This clearly affects the electrode porosity which again influences the irreversible capacity [107]. The lack of a working calendering machine resulted in a wide spread in carbon loading, see Table 5.6.

Regained Capacity

After the standard cycling procedure with increasing current rate, some cells were exposed to low current densities (C/20). The regained capacity proved to be very similar to the first two C/20 measurements. This shows the importance of current rates for the cell capacity. Infinitesimal traces of parasitic reactions occurred between the two stages of C/20 cycles since the capacity was not significantly changed.

Oxidation

Two main approaches can be made for carbon oxidation, namely gaseous or wet chemical oxidation. Oxidation is often incorporated in the commercial carbon production as it has a significant effect on the cell characteristics. It is utilized to reduce the reactivity of carbon atoms at the edges planes, hence increasing the first cycle efficiency by inhibiting the decomposition of the electrolyte [161]. Treatment with solution oxidants like H_2O_2 [172] and HNO_3 [173] have the advantage of producing uniform surfaces which improve reproducibility on a large scale production compared to oxidation by gaseous oxidants. This is achieved as the reaction takes place at the interphase between the solution oxidants and the carbon, as the graphitic particles are immersed and stirred in the oxidant solution [161].

Three different samples were exposed to air at elevated temperature (gaseous oxidation), namely CC900Air, CC900Ar-Air, and CC900Air2700, and two samples were treated with wet chemical oxidation, CCH2O2 and CCHNO3. None of the oxidized samples show any reduction in the irreversible capacity loss. On the contrary, some of these samples have the highest losses of all the electrodes. The initial discharge capacity is exceptionally high for especially CC900Air and CC900Ar-Air. For CC900Air, the oxygen must have reacted with the disordered carbon, creating more active surface sites for SEI formation. The corresponding BET surface supports this observation. It is also believed that oxygen containing functional groups are present on the carbon surface facilitating film formation.

The air oxidized sample was later heat treated in argon (CC900Ar-Air) as an attempt remove the functional groups. The small decline in the irreversible capacity (from 49 % to 46 %) can be attributed to the removal of the functional groups and the termination of surface atoms. CC900Air2700 shows to a certain degree higher irreversible capacity than the CC2700 electrode (from 32 % to 27 %). The CC2700 sample is not as sensitive to oxidation compared to CCRAW due to its high crystallinity and lower reactivity. Nevertheless, the oxidation leads to a somewhat increased irreversible loss which validates the effect of oxygen groups on the carbon surface.

Wet chemical oxidation using H_2O_2 and HNO_3 has lead to a decrease in the irreversible capacity compared to the basic grade carbon cones, as seen in Table 5.6. Results indicate that the use of H_2O_2 and HNO_3 have lead to a functionalization of the carbon surface. The mild oxidation reduces the reactivity of the edge plane carbon atoms by forming oxides [161]. This type of oxidation can also produce well-defined voids in the basal planes of graphite as local defects. The induced nanochannels are too small for penetration of solvated lithium ions (co-intercalation), but allow for lithium ion transport and intercalation [174]. Nanochannels will result in an improved rate capability, which is also the case for the mild oxidation electrodes in this study.

Functionalized Carbon Cones

Little information on functionalized carbon cones have been given due to proprietary rights of n-Tec. n-Tec reported an oxygen content of 12 wt%. CC-Func was later analyzed with an oxygen analyzer and an oxygen content of 17 wt% was obtained. However, the oxygen analyzer was calibrated for lower concentrations. The result is therefore not reliable.

As mentioned earlier, the charge/discharge profile of CC-Func is somewhat different compare to the other measurements. The initial discharge does not reach the set cut-off voltage of 0.005 V. This can be explained by the high amount of oxygen reacting with the electrolyte leading to a large consumption of charge. The testing conditions for the initial discharge was set to last shorter than the actual time necessary to reach 0.005 V. The discharge stopped therefore before complete lithiation.

The heated functionalized carbon cones sample (CC900-Func) was subjected to the same testing regime as the CC-Func. It shows similar characteristics to the CCRAW sample. This indicates that the heat treatment at 900 °C in argon reversed the functionalization process with respect to the charge/discharge

measurements. It is likely that the surface oxygen reacted, forming gaseous O_2, CO, and CO_2.

Microwave Irradiation

Carbons are in general a good microwave absorbent. In other words, most carbon materials can easily be heated by microwave radiation. This property allows for carbon modifications giving rise to new structures. The π-electrons, which are free to move in a defined region of the carbon structure, can generate a current induced by the electromagnetic field. Energy (heat) is dissipated as the π-electrons cannot couple with the electric field phase changes [175].

Carbon nanohorns were successfully oxidized with a radiation of 150 Wmin (9 kJ) in a study by Yoshida *et al.* [176]. Basic grade carbon cones were therefore irradiated with almost 400 Wmin (24 kJ) to ensure a certain structural transformation. As-produced carbon cones contain volatile compounds which will evaporate during heating. A rapid increase in temperature provided by the microwaves can lead to a sudden release of these compounds, creating pores and cracks in the outer carbon shell. Performed in an argon atmosphere, the gas release should alter the structure. Additionally, when performed in air, the carbon should also oxidize due to the presence of oxygen and high temperatures.

The microwave treatment in both argon and oxygen did not seem to have an effect on the charge/discharge performance. This is in agreement with other results performed in this study. The charge/discharge profiles for MWCCAr and MWCCAir are almost identical to CCRAW with respect to shape and capacity. The capacity deceases as an effect of increasing current also progresses in a similar fashion. MWCCAr has a larger irreversible capacity as opposed to CCRAW and MWCCAir. However, this can not be explained by surface area as it does not significantly change during microwave radiation in argon.

6.4.2 Electrochemical Impedance Spectroscopy

Electrochemical Impedance Spectroscopy (EIS) is a very versatile method for characterizing batteries. It can be applied in different manners to extract a vast range of electrochemical data. For a carbon/lithium half-cell, the impedance consists of the resistance from the electrode, electrolyte, and the solid electrolyte interphase. EIS measurements were performed during the initial discharge (lithiation) of three different carbon materials, specifically the untreated basic grade carbon cones (CCRAW), heat treated carbon cones (CC2700) and commercially

available graphite (SLP50). Fig. 5.83 to 5.85 show the corresponding EIS results.

Despite the large variations in carbon materials, the electrochemical behavior and EIS spectra of lithiated carbon exhibit certain common features. At least three different time constants are present for a carbon/lithium half-cell system [177]. Kamishah *et al.* claims the first semicircle in the high frequency range is generally assigned to lithium ion migration in the solid electrolyte interphase, that is the hindered mass transport through the surface films of the electrode [118]. In the same frequency range, semicircles can be ascribed to the contact resistance between each particle of active material [178]. Chang *et al.* claim the first semicircle is attributed to the contact resistance between the current collector and the electrode [179]. Wang *et al.* conclude that the first depressed arc at high frequency range results from the passivation film while it is also influenced by the electrode contact resistance [180]. Any potential second semicircle in the mid-range frequency area is ascribed to the lithium ion transfer across the interphase between film and carbon surface, in other words charge transfer resistance across the electrode/electrolyte interphase [179]. At the low frequency range of the spectra, a linear incline is usually assigned to the slow diffusion of intercalated lithium in the carbon matrix [178].

The impedance spectra show intercepts with the real axis at the high frequency area. This intercept results from three sources, namely the electrolyte resistance between the working (WE) and reference electrode (RE), the wire resistance of the system, and the contact resistance between the electrodes and electrolyte. The first source is significantly larger than the other two and the intercept can therefore be used as a measure of the solvent resistance as long as the distance between WE and RE is constant [181]. As all the impedance measurements were performed with the same electrolyte and electrode setup, the intercept should give similar resistance measurements independent of electrode material. The measured electrolyte resistance of the three cells is almost identical. The small variation may be attributed to the ageing of the electrolyte as the solvent resistance experiences a minor increase with storage time. During storage and use, the diethyl carbonate (DEC) component of the solvent can evaporate, which results in a higher electrolyte viscosity and ionic resistance.

The EIS spectra obtained for CCRAW, CC2700, and SLP50 show characteristics which are to some extent different from the ones found in the literature. It is therefore difficult to interpret the results accordingly without a more thorough analysis. This study has been an attempt to obtain quantitative data without the complications of equivalent circuits.

There are at least two general trends in the obtained spectra. Firstly, a single large arc dominates in the first quadrant, except for the graphite electrode (SLP50) where two semicircles are present. The dominant arcs can be assigned to the contribution explained above. A depressed single semicircle can in fact overshadow individual impedance contributions if the individual time constants are similar. Secondly, it can be seen from the results that lower potentials yield lower impedances. The decreasing semicircles are caused by the lithiation of the carbon which lowers the cell impedance. The OVC impedance graph continues outside of the figures for the low frequency values. At these frequencies, the incline is nearly 90° to the horizontal axis. This is typical for a blocking electrode which exhibits a very high impedance as the frequency approaches zero. This indicates a reasonable amount of lithium ions which are not intercalated at this potential [182]. The 0.2 V and 0.005 V measurements of CC2700 in Fig. 5.84 show an inclined line at low frequencies which is associated with diffusion of lithium ions within the carbon host. The steep slope indicates a capacitive component which is closely connected to a charge saturation and finite diffusion. This behavior can be attributed to the small particle size of the carbon cones materials. It is not detectable for the SLP50 sample. Similar observations were done by Funabiki *et al.* [182]. Cyclic voltammetry indicates that the main lithium storage mechanism for CCRAW is not intercalation. The behavior explained above can therefore not be used on CCRAW electrodes.

A loop at lower frequencies can be seen in Fig. 5.83 and 5.85. The source of this impedance element remains unclear and is therefore difficult to explain. However, Song *et al.* claim that similar behavior originates from an adsorption/desorption process at the carbon/electrolyte interphase [181]. The loop only exists at potentials of 0.5 V, 0.2 V, and 0.005 V. Charge/discharge measurements confirm the occurrence of lithiation of carbon at these voltages where the lithium ions are free to flow through the forming SEI film. For the SLP50 spectra, the loops decrease with decreasing potential. This may indicate a lower activation energy for lithium intercalation at lower voltages. The loop size is more or less constant for the CCRAW electrode. This might imply that the activation energy for the capacitive lithiation does not change. Unfortunately, the adsorption/desorption explanation does not clarify the lack of loops in the CC2700 sample. Another plausible explanation for the loop is given by Gnanaraj *et al.* [183]. They claim the loop is caused by induction which is induced when an electromotive force is generated due to lithium ion concentration differences. As the carbon/lithium half-cell is discharged (lithiation), the SEI will form as islands on the surface of carbon due to heterogeneous conditions. The surface

film islands lead to isolation of carbon regions with different lithium concentrations. Different states of lithiation result in a local $Li_{1-x}C_6/C_6$ concentration cell between Li-rich and Li-deficient carbon particles. The $Li_{1-x}C_6/C_6$ concentration cell result in a current flow that opposes the main lithiation reaction. Current will leak until the lithium concentration is equalized. The inductive loop (IL) disappears as a stable SEI film has been established. The lack of ILs in the CC2700 spectrum indicate a uniform charge distribution between the different regions. A highly graphitized surface can create an even SEI growth (not island formation).

For the CC2700 electrodes, the semicircles are smaller compared to the CCRAW electrodes. Heat treatment has an evident effect on the system impedance. The arcs become smaller with a higher degree of graphitization. These findings are in accordance with the work done by Takami *et al.* [177].

Due to the physical form of the carbon cones materials, the carbon disks tend to orient parallel to the current collector surface. Graphitic carbons have a higher electronic resistivity perpendicular to the basal planes and therefore the graphite orientation leads to higher internal ohmic impedance in the cell. This factor is crucial for high rate charge/discharge as the diffusion paths can be elongated [71].

Obtaining EIS spectra can be time consuming, often several hours if low frequencies are used. The system must be in steady state throughout the measurements to avoid artifacts, which can be difficult to achieve. All cells were therefore held at the desired voltage for 4 h prior to testing. Varying impedance results were obtained for identical cells, proving the difficulties of obtaining accurate results. The spectra shown in Section 5.4.2 are representative of the corresponding half-cells. Minor changes in the cell can cause large variations within the Nyquist plot. There are numerous changes which can occur within a cell. The resistance of an ionic electrolyte depends on the salt concentration, types of ions, and temperature. Another important factor is the geometry of the electrodes [184]. The reference electrode (RE) is placed between the working (WE) and counter electrode (CE), but shifted from the central axis of WE and CE. Due to the shift, the assembled WE and CE will not be parallel to each other. This results in a nonuniform impedance distribution across the electrodes. Errors related to the cell geometry could be improved by better cell design. Two alternatives are shown in paper [181] and [185].

Ivanishchev *et al.* have shown that all experimental impedance spectra can be adequately modeled with equivalent circuits [178]. Calculated data of high precision can be achieved, but the method is not without drawbacks. When

establishing a corresponding equivalent circuit, compromises must be made. On one hand, sufficient amount of circuits must be introduced to provide a good agreement between experimental and calculated data. On the other hand, the interpretation of circuit element parameters can be somewhat unclear when too many elements are introduced. Nevertheless, it's important that the elements in an equivalent circuit can be related to a physical phenomenon in the cell.

During the initial lithiation of carbon, several reactions occur at the same time which lead to complex impedance spectra. Combined with the complexity of the carbon electrode, similar time constants and experimental errors, a good analysis of the spectra can prove to be difficult. The impedance results are to some extent highly informative. Nevertheless, their interpretations are ambiguous. A more thorough investigation as to why the semicircles appear as they do is required.

6.4.3 Cyclic Voltammetry

Cyclic voltammetry (CV) is normally used to study a redox-reaction in the proximity of the electrode by recording the current response as the potential is changed. It is possible to extract information about the controlling processes in the system, such as diffusion, chemical reaction, and electron transfer. It is also possible to obtain information on the reversibility of the electrochemical reaction [120]. CV is a suitable technique to study the LiC_6 intercalation and lithium-carbon adsorption process. Two cycles are normally sufficient to show trends within reproducibility. More cycles are needed to predict the cycle development.

The first discharge of CCRAW in Fig. 5.86 shows a larger capacity compared to that of the second discharge. This is clear even though the scan rate was changed at 0.4 V and the continuity of the graph was interrupted. During the initial discharge, a peak is observed at 0.78 V which is attributed to the build-up of the SEI layer. These findings are in accordance with the charge/discharge curves and the results obtained by Gnanaraj *et al.* [87]. As the voltage continues to decrease, the current steadily increases until the scan rate is changed at 0.40 V. At the lowest potentials there are no indications of any cathodic peaks. The current decreases to zero as the potential decrease ceases. As the potential is reversed and starts to increase, an anodic peak can be seen which is assigned to lithium deinsertion (not deintercalation) [87]. The lack of cathodic peaks during the two cycle scans indicate that no intercalation is present and can be attributed to the wide lithium adsorption site energy distribution of dis-

ordered carbon. Similar CV curves were measured on amorphous carbon by Kim *et al.* [186]. Such behavior is attributed to a pseudocapacitive process of slowly increasing and decreasing current during discharge and charge, respectively [87]. The lack of CV peaks agrees with the findings of Garberg *et al.* [53] and the corresponding charge/discharge curves of CCRAW, see Fig. 5.38. CV is therefore an inadequate method to determine if the lithium ions reach the center graphitic layers of the carbon cones material as the core is covered in a disordered carbon shell. XRD and Raman spectroscopy measurements also confirm the presence of disordered carbon. The purely capacitive discharging and charging mechanism of the carbon/lithium half-cell is not fully understood, but several mechanism have been proposed. Dahn *et al.* suggest different mechanisms for the reversible insertion of lithium depending on the carbon type [187]. They claim the lithium bonds in the vicinity of hydrogen-terminated carbon atoms as the inserted lithium is proportional to the hydrogen content in the carbon material. Another mechanism applies to carbon materials containing predominately single sheets of carbon. Here, lithium can bond to both sides of the layers and hence increase the theoretical capacity [87].

The insertion mechanism for CC2700 is completely different compared to the capacitive discharging and charging of CCRAW, see Fig. 5.87. Intercalation peaks can be clearly seen for the heat treated material. As the potential decreases from OCV, a peak appears at 0.71 V due to the formation of the SEI. This response can be seen as a plateau for similar cells in Fig. 5.50. Further on, the large reduction peak appears to consist of at least two contributions as both intercalation and formation of the SEI occurs. The reversible deintercalation process shows two distinct peaks which each represent changes in the solid-state stages. Levi *et al.* have presented similar features for a graphitic material with another electrolyte system [121]. The dominating peaks are located within the same vicinity. This can be interpreted as overlapping phase transformations. In other words, several phases occur at the same time as the phase change mechanism take place at the same potential or at different rates. This will explain the less prominent plateaus on charge/discharge curves of the CC2700 (Fig. 5.50) compared to the SLP50 graphite (Fig. 5.78). For the second cycle, three reduction peaks are distinguishable as they are no longer overshadowed by irreversible SEI formation. There is a separation or hysteresis effect between the reduction and oxidation peaks. Such behavior is explained by Levi *et al.* [121] as the slow conversion rate between the transformation phases for the lithium carbon intercalation compounds. Yazami *et al.* [188] conclude in their work that the intercalation process proceeds more easily as higher cathodic cur-

rent densities can be obtained. The same can not be said in this study, as it is difficult to decide which of the current responses (cathodic or anodic) are the most dominant.

The difference in the SEI-layer buildup between the CCRAW and CC2700 should be addressed more carefully. The reduction peak at 0.71 V in Fig. 5.87 for CC2700 is more distinct compared to the corresponding peak for CCRAW. This can be partially explained by the continuous SEI-formation over a broader potential range which is again related to the smaller crystallites of the untreated basic grade carbon cones. Another occurrence is the exfoliation process of carbon. As highly structured carbon layers are separated, fresh carbon surface is exposed to the electrolyte leading to further SEI-layer buildup. CC2700 is more graphitic than CCRAW, and is therefore more prone to exfoliation. The cross-bindings in CCRAW will prevent any carbon separation. The exfoliation will also be suppressed if the SEI formation occurs first [156].

6.5 Thermal Studies

6.5.1 Differential Scanning Calorimetry

For differential scanning calorimetry (DSC), the thermally active components in the samples are the carbon material in a lithiated or delithiated state, as well as traces of electrolyte and the SEI. Interactions between these constituents result in thermal responses which can be studied with DSC. All DSC profiles were obtained by subtracting a baseline, determined by an earlier heating procedure of an empty sample holder. The samples were prepared and the electrodes were cycled as described in Section 4.3.9.

The DSC results are given in Fig. 5.88 - 5.93. At first glance, it might be difficult to see the features of the heat responses due to large variation within the same electrode. However, some trends can be distinguished in the DSC profiles. The results will be discussed in the following order: delithiated CCRAW, lithiated CCRAW, delithiated CC2700, lithiated CC2700, delithiated SLP50, and finally lithiated SLP50.

Fig. 5.88 shows the thermal response of delithiated untreated basic grade carbon cones (CCRAW). All parallels have their first peak between 115 °C and 160 °C. These peaks can be assigned to the SEI-layer decomposition. The onset temperature differs, even though the samples measured are from the same electrode. One curve shows two peaks below 150 °C, maybe indicating a SEI decomposition in two steps. The second curve shows a large peak at 160 °C, which

is typically associated with the reaction between the electrolyte and intercalated lithium. However, this sample was at a delithiated state.

The thermal responses for the lithiated state of the untreated basic grade carbon cones (CCRAW) are presented in Fig. 5.89. The peaks assigned to the SEI decomposition is located between 130 °C and 175 °C. Some positive responses at temperatures above 225 °C can be distinguished which is explained by the reaction of the surface lithium and electrolyte solvent.

It is difficult to distinguish between the thermal responses between the lithiated and delithiated state of basic grade carbon cones. Both states have a clear exothermic peak for the decomposition of the passivation layer. However, the delithiated material has one DSC profile with a peak at high temperatures. The peak is normally associated with lithiated carbons. Some residue intercalated lithium might be left in the sample after delithiation which can explain this peak. Local differences on the electrode can explain the large variation in the sample heat signatures.

The three parallels of the delithiated heat treated basic grade carbon cones (CC2700) show a relatively similar heat response, see Fig. 5.90. No peaks can be observed for the SEI decomposition. This could indicate a minimal SEI formation, but the charge/discharge measurements of the same electrode material clearly shows an irreversible capacity loss attributed to the passivating layer, see Fig. 5.50. The lack of heat response can be assigned to a highly stable SEI-layer. Another explanation for this phenomenon can be the occurrence of co-intercalation. Electrolyte within the carbon layer might need higher temperature to decompose and yielding exothermic peaks, as opposed to the surface SEI.

A mild cooling evolution starts after the temperature reaches 200 °C. It is believed that at least the steepest slope indicates leaking sample holder as the pressure release is an endothermic process.

Some exothermic responses can be seen for the lithiated heat treated carbon cones samples (CC2700). Two of the curves follow each other until one of them show thermal responses at 253 °C and 303 °C associated with the reaction between the intercalated lithium and electrolyte. Heat responses between 200 °C and 300 °C can also be assigned to electrolyte decomposition [189]. Again, the negative slopes are associated with leaking sample holders.

It is also difficult to decipher the lithiated from the delithiated state of the heat treated carbon cones (CC2700). The lack of clear exothermic peaks for delithiated electrodes makes it suitable as anode material because of the thermal stability. Several cells were made of the same composition and they all showed

the missing endothermic peaks. Other cells, where only the carbon electrode was substituted, all showed exothermic peaks for the SEI decomposition.

Commercially available graphite (SLP50) in a delitihiated state has its thermal response given in Fig. 5.92. The first peaks lay close together between 116 °C and 122 °C. This response is again assigned to the SEI decomposition. Further on, the second thermal response can be seen at temperatures above 250 °C. Since these samples are delithiated, the most likely reason for the high temperature thermal response is the electrolyte decomposition.

The lithiated state of SLP50 is shown in Fig. 5.93. Each curve has at least two exothermic peaks. The first peak is located between 127 °C and 149 °C and represents the SEI decomposition. The positions of the second peaks are spread from 183 °C to 255 °C. The second heat responses are originated from the reaction of the intercalated lithium and electrolyte.

The consistency of the lithiated and delithiated state of the commercially available graphite was also poor. The onset temperatures and generated heat of the first peaks are very similar for each case. This indicates a homogeneous SEI layer on the parallel samples. The temperature variation of the second peak can be attributed to differences in the amount of intercalated lithium.

These results must be regarded with some reservations due to several error sources. Assembled lithium-ion cells contain large amount of electrolyte carbonates. In this study, the DEC component of the electrolyte has evaporated before the DSC sample holder is sealed. Also, the amount of solvent present in the sample holder may differ and influence the heat response [129]. Better reproducibility between the sample parallels could be achieved if the DEC was allowed to evaporate for the same amount of time. Alternatively, the samples could have been rinsed with the appropriate alkyl carbonate to reduce the variations. In general, the poor reproducibility can be assigned to the heterogeneity of the samples even though measures were taken to produce identical samples from each cell or electrode.

Large temperature variations for the peaks can also be assigned to different affinity between the SEI and carbon surface. SEI formation can be more closely bonded to certain carbon surfaces (edge/basal-plane) and functional groups. Stronger bonds needs higher temperatures for the SEI to decompose and it is already verified that the carbon cones material has a heterogeneous surface, hence the different temperature peaks.

The peaks associated with the reaction between intercalated lithium and electrolyte are sometimes present in the deintercalated samples. The reason for this might be the presence of some residual lithium. The cells were cycled at C/5

and this rate might be too high for complete delithiation. Thermal reactions occurring at around 250 °C and above, may also involve the polyvinylidene diflouride binder (PVDF) [93]. All samples contain the PVDF and it is therefore likely that the binder contributes to the thermal response. This hypothesis can be verified by omitting the PVDF binder in similar experiments.

Abrupt changes in the curves or sharp peaks are regarded as noise. These artifacts can be induced by sample pan distortion, electrical effects, and/or power spikes. In this study, many problems were associated with the baseline as the background measurement had a tendency to not stay consistent. In order to minimize this effect, the baseline and sample were measured immediately after each other.

All samples were hermetically sealed. Nevertheless, several DSC profiles show an endothermic trend at high temperatures as the sample pans start leaking. The leakage was confirmed by weighing the assembled sample holder before and after each DSC scan, combined with separate thermogravimetric analysis. Endothermic heat evolutions were also observed by Joho *et al.* [129]. The leakage is caused by poor sealing of the cell, a high internal pressure due to the evaporation of electrolyte, or a combination of the two.

There is some correlation between the SEI properties and thermal stability. CC2700 shows low irreversible capacity meaning a minor SEI generation. This corresponds well to the lack or minute exothermic DSC signal for the same electrode material. However, it contradicts with the DSC peaks present in the SLP50 samples which has even lower irreversible capacity. It was found that low surface area (active surface area), and smooth particle surface created a stable SEI-layer and hence thermally stable properties [190]. Park *et al.* studied the influence of particle size on the thermal stability of lithiated carbon electrodes. The heat generation associated with the SEI decomposition increases with decreasing particle size. The onset temperature for exothermic responses were also lower for smaller particles. The change in thermal stability was attributed to a thermally induced delithiation process which was facilitated by small particles [190]. This indicates that the smaller carbon cones particles are less suitable for lithium-ion battery purposes compared to the larger commercially available graphite.

6.5.2 Thermal Conductivity of Electrode Materials

Thermal conductivity of four different electrode materials were tested, which included one cathode sample of commercial $LiCoO_2$. The four electrodes were

subjected to heat fluxes in a dry and solvent soaked state. Under dry conditions CCRAW has a significantly lower thermal conductivity compared to the other materials. Small or few contact points between particles contribute to this. The large carbon black particles of the carbon cones material will not contribute in increasing the contact points. However, both the SLP50 and $LiCoO_2$ have large amounts of small carbon black particles in between the spherical particles, leading to many/large contact points where heat can be transferred by conduction. As for the CC2700 sample, it shows the highest thermal conductivity of all the dry electrodes, even though it has the same particle distribution as CCRAW. This can be explained by CC2700's graphitic nature. Graphite is an extremely good thermal conductor parallel its honeycomb lattice. It seems that the effect of graphitization is more important than the sheer number of contact points between the particles. For the carbon materials, thermal resistance should show some correlation with electrical resistance, as seen in the EIS results for CCRAW and CC2700.

The number of contact points between the carbon particles are closely related to the porosity of electrodes. Large amounts of NMP was necessary when making slurries with CCRAW and CC2700, compared to SLP50. As the NMP evaporates, it leaves behind air-filled voids. The amount of NMP used in the slurry will therefore have a significant influence on the thermal conductivity.

Thermal conductivity increases with a factor of three for soaked CC2700, SLP50, and $LiCoO_2$. The CCRAW sample increase with a factor of five. The values of the thermal conductivity are in the same consecutive order as for the dry electrodes. When dry, the particles are separated by air which does not conduct heat well. As the electrode is soaked, solvent will penetrate the voids. Liquids have in general a better thermal conductivity than gases. If the voids are not completely filled, it is believed that the solvent will additionally wet the contact points creating larger areas where heat can be transfered. The consequences of electrodes drying out during use due to a leakage can be tremendous. As the thermal conductivity decreases, heat dissipation will be dramatically reduced, potentially resulting in thermal runaway.

Chapter 7

Conclusion

7.1 Carbon Cones

The conical carbon structure is a unique arrangement of carbon atoms. Between one to five pentagonal defects in the honeycomb lattice dictate the global shape of the cone. The height is determined by the size of the surrounding graphene sheet which is further determined by the residence time and growth conditions. A cone exhibits characteristics including the buckminsterfullerene, carbon nanotube, and graphene.

Kværner carbon black and hydrogen process is the only reported large quantity production of carbon cones known to the author. The material was accidentally produced with the original intention to manufacture carbon black. The quite remarkable results also consisted of flat disks and spherical particles of carbon. Due to the high amount of disks and difficulties of separating the individual particles, it is believed that the disks are responsible for the primary properties of the bulk material. Even though the carbon disks are the main constituent, the special structure of the cones has lead to a research interest in the material. The trial runs carried out in the hot plasma-torch reactor at SINTEF's locations, produced carbon material in 25 out of 29 attempts. No cones or disks similar to the original material were produced. Nevertheless, conical structures were found on the inner linings of the reactor walls. The deposited material was found in close proximity to the hot plasma after an extended period of production time. The new structures are believed to be a condensation product due to the heat loss to the wall. To avoid condensation and obtain free

cones, a long growth time in the gas phase is essential. Reactor volume and insulation are therefore important. The original reactor for the Kværner carbon black and hydrogen process was considerably larger than the hot plasma-torch reactor at SINTEF's locations. It is not likely that further progress could have been achieved with the constraints given by the present reactor. These findings indicate that the essential parameters for producing conical structures are high temperatures and sufficient holding times. A systematical set of trial runs with very many possible variables have been performed. The right conditions for forming and growing cones solely in a gas phase still need to be clarified. The other reactor conditions are at this point under proprietary rights of n-Tec.

7.2 Carbon Cones as Electrode Material

The carbon cones material from Kværner carbon black and hydrogen process were investigated as negative electrodes for lithium-ion batteries. A vast range of methods have been employed to characterize different classes of carbon cones. The various categories of cones were produced with a distinctive set of treatments. The cones underwent heat treatment up to temperatures of 2700 °C. As-produced material was also exposed to an oxidizing environment. Microwave radiation was also utilized as a treatment method. In addition, batches of so-called low grade and functionalized cones were a part of the total test matrix.

Morphology was studied with FEGSEM. Non-destructive analytical techniques such as XRD and Raman spectroscopy were used to characterize bulk and surface properties, respectively. Density and surface area measurements were performed to yield additional material information. Thermal properties were identified with DSC and thermal conductivity measurements. Electrochemical characterization was predominantly studied by galvanostatic charge/discharge measurements and electrochemical impedance spectroscopy.

The heat treatment has clearly a significant effect on the cones and corresponding battery performance. The biggest effect is seen when comparing CCRAW and CC2700. CCRAW was recognized by a capacitive-like lithium storage mechanism, as opposed to CC2700 which has a clear indication of lithium intercalation. The intermediate heat treatment temperatures show a consecutive change from the as-produced material to the high temperature heat treated material. However, a discontinuity is seen between the CC2200 to CC2700 sample. In hindsight, it would be interesting to further heat treat the basic grade carbon cones to temperatures between 2200 °C and 2700 °C to completely determine the capacitive/plateau threshold behavior. Even though the experimental

Raman spectroscopy and XRD characterization show high crystallinity of the CC2200 sample, the sample does not display the anticipated plateaus in the charge/discharge profiles.

Two main directions were chosen for carbon oxidization. Firstly, gaseous oxidation (CC900Air, CC900Ar-Air and CC900Air2700) at high temperatures in an air atmosphere created a new surface morphology as the carbon atoms react with oxygen. This treatment method resulted in a slightly higher irreversible capacity loss compared to CCRAW. Secondly, wet chemical oxidation (CCH2O2 and CCHN03) lead to a decrease in irreversible capacity. The functionalized material (CC-Func) was not suitable for electrode purposes due to the high consumption of electrolyte. On the other hand, heated functionalized carbon cones (CC900-Func) have characteristics very similar to CCRAW. Furthermore, microwave radiation did not remarkably change the charge/discharge response except for an increase in irreversible loss. The low grade carbon cones (LGCC) and the heat treated counterpart (LGCC2700) show similar attributes to their corresponding basic grade material, beside the somewhat larger irreversible capacity loss.

The error bars in the cycle plots should not be underestimated. They are taken from the standard deviation for several parallels. The spread in data makes it difficult to conclude regarding the optimal approach when applying carbon cones as electrode material for lithium-ion batteries. A major contribution to the errors arise from uncertainties of the small electrode masses. Larger cells should be employed to determine the absolute capacities.

The discharge process of the carbon/lithium half-cell was studied with electrochemical impedance spectroscopy (EIS). The large amount of simultaneously occurring processes and similar time constants complicated the quantitative analysis. The attempt of finding equivalent circuits was discarded and a more qualitative analysis was performed.

It is clear that electrochemical performance is only one piece of the puzzle. Good initial galvanostatic performance is obviously not sufficient to tell if a material is suitable for lithium-ion battery purposes. A time consuming method to achieve accurate results, is to test materials in real applications. However, as this might be troublesome, it is a good idea to include a large variety of testing methods when characterizing cells.

DSC is one measurement method worth testing as it yields information regarding safety issues. The thermal stability of the carbon electrodes depends on the lithiated state and on the active lithium host material, in other words, the carbon material. Thermally active components such as electrolyte and SEI

layer will also contribute to the heat response. The DSC performed in this work shows large variation in the exothermic signals for apparently identical samples. The large variations are attributed to local differences on the electrode surface. Peaks representing SEI-layer decomposition and reactions between electrolyte and lithiated carbon are present in the majority of the measurements. By merely studying the DSC data, it is possible to conclude that the CC2700 at either a lithiated or delithiated state is the safest alternative due to its lack of thermal response upon heating.

Another approach for obtaining thermal data of the electrode material, is the measurement of thermal conductivity. Dry CCRAW proves to be the material with the lowest thermal conductivity as opposed to wet CC2700 which has the best heat transport properties. A commercial material was also studied, and the thermal conductivity was between the extremities of dry CCRAW and wet CC2700. In general, it is reported that the thermal conductivity is increased by a factor of three when going from dry to wet. Unfavorably large temperature gradients inside a cell can occur when the thermal resistance is high. It is therefore advised that thermal conductivity is reported along with other properties of the lithium-ion cell electrode materials.

This thesis is an attempt to give the reader a good understanding of the carbon cones and its characteristics as anode material in lithium-ion batteries. The study provides a disclosure whether or not the carbon cones are suitable for lithium-ion battery purposes. Working carbon/lithium half-cells with a range of different carbon cones materials have been successfully manufactured. The material's distinct feature is the smooth charge/discharge curve without intercalation plateaus. Stages only occur for the SEI formation and the cones heat treated at 2700 °C. Another characteristic is the high irreversible capacity assigned to the SEI formation on the relatively large surface area. Furthermore, the biggest drawback with anodic carbon cones is the undisputed fact that there are only a limited amount of carbon cones available. Carbon cones cannot compete with other commercially available carbons as long as there are no carbon cones production method available. There are too many disadvantages with carbon cones to recommended a resumption of the trial run experiments with the sole purpose of making anode materials for lithium-ion batteries. However, the possibility of potentially tailoring large quantities of carbon materials with specific properties designed for lithium-ion batteries will have a great future potential.

Chapter 8

Future

8.1 Carbon Cones

The single walled carbon cones structure will surely continue to intrigue researchers in the future. Its unique features may possess unexpected and interesting properties. The author finds the changes in dimensions along the cone length fascinating. At the apex, the cone can resemble a zero-dimensional cluster similar to the C_{60} buckyballs. As the cone's gradually open, it exhibits a more one-dimensional tube structure. At the cones base, the noticeable structure is the two-dimensional graphene layer. Due to these changes, the charge transport properties vary from insulating at the pinnacle to metallic at the cone base [6]. Cones may have a bright future in nanosized devices.

The forthcoming future of the carbon cones from the Kværner carbon black and hydrogen process is at the moment uncertain. The lack of success in reproducing the cones made it clear that this was not a trivial task. Large investments are necessary for a successful production. It is certainly possible to manufacture these cones again, as they have been already made once. The plasma technology is still interesting in many aspects, for instance the CO_2-emission free combustion of natural gas. Furthermore, some research communities have established contact with the patent holders and the "know-howers" of the Kværner carbon black and hydrogen process. The technology behind the carbon cones material has enormous potential if large amounts of designed carbon nanostructures can be produced with ease. The author hopes that the successful production of carbon cones in a large scale will some day be realized.

8.2 Batteries

Today, it is impossible to live a "normal" life without using some sort of battery to get through the day. Mankind's dependence on portable energy will only increase. Battery researchers will therefore have to continue on their quest of improving batteries. Since the performance of batteries are essentially determined by the chemical potential of elements in various environments, there are only a limited amount of cell combinations possible. Truth is, that there is not likely going to be a revolutionary new battery system in the near future. Nevertheless, there are always exceptions and it's impossible to predict the future. The effect of miniaturization has failed to come into force for several years, but the trend is going towards nanosized materials also in battery technology. For instance, Zhang *et al.* have developed a nanostructured cathode which allows for extremely fast charging and discharging. They claim rates up to 400C for lithium-ion batteries, meaning a full charge in 9 s(!) [166]. Apparently these cathodes does not sacrifice capacity for the fast charge resulting in the best of both worlds, namely capacitor-like power and battery-like energy [166]. New possibilities will arise as nanotechnology in batteries will mature. The trends within the technology are clear. We are going slowly towards safer, cheaper and higher capacity batteries.

8.2.1 Future Research in Lithium-Ion Battery Technology

Simultaneous research on performance, life, cost and abuse have to be addressed in order to improve the current lithium-ion technology. These issues are the critical challenges in the future. The choice of application is crucial to decide which problems that need to be solved. The use of lithium-ion batteries in electric vehicles can be said to be some sort of benchmark for battery requirements as it is very difficult to meet these demands. To resolve current issues improved structural design can yield a better cycling stability. Nanostructures may give better control of unwanted side reactions. Another idea is to use protective coatings on electrode surfaces to suppress such reactions. For anodes, composite materials such as Si/C nanofibers are already showing promising results [191].

At the moment of writing, the American company Envia systems has claimed to breached the 400 Wh/kg barrier in large format lithium-ion pouch cells. They are also saying that the price of these cells will be drastically reduced. However, the commercializations are not yet realized and their cell performance is based in laboratory testing. The Achilles heel for traditional lithium-ion cells are in

many aspects the cathode. Envia uses a manganese based cathode to reach the high power density together with a silicon/carbon composite anode. Their exact cell composition is a well protected secret. In the field of batteries, secretiveness has too often meant that the concept has been a pipe dream. Let's hope this is not the case here, as this may be the pivotal moment for the success of the battery electric vehicle.

Another exciting company utilizing nanotechnology is Prieto Battery which has developed a non-toxic and non-flammable cell type. Their goal is to redesign the battery by utilizing a three-dimensional solid-state battery architecture. The cell's cathode and anode are intertwined instead of having the standard parallel electrodes. This is achieve by electrodeposited Cu_2Sb and other cell constituents on to copper foam (nanowires). This allows for a high surface area and reduces the lithium ion diffusion paths. The solid-state electrolyte eliminates the hazards associated with liquid electrolytes [192]. Envia and Prieto Battery are just two examples of the promising technology developers nowadays.

8.2.2 Future Battery Alternatives

By combining lithium with oxygen, lithium-air batteries may lead to the next big leap in battery technology. The cell capacity performance can be improved with a up to a tenfold since the battery's energy density is increased. The cell can be made significantly lighter by extracting oxygen directly from ambient air. The weigh loss is attributed to the loss of the heavy transition metal oxides and replacing them with a lightweight high-surface carbon structure. The carbon structure will act as the catalytic air cathode. However, there are still some technological hurdles to overcome before the batteries can be commercialized. Some of the challenges include creation of a suitable catalyst and a stable electrolyte. Efficient stabilization of the lithium metal is also crucial [193, 194].

An exciting alternative to the lithium-ion technology is the magnesium-sulfur battery. It offers a unique combination of high capacity and low volume giving an energy density more than twice that of a lithium-ion battery. A sulfur cathode will be ideal for a magnesium anode with the corresponding current carrying Mg^{2+}-ion. Researchers have found an electrolyte which is stable in both electrode environments. There are at least two major challenges still to overcome. Firstly, researchers have to find a way to avoid sulfur dissolution during discharge. Secondly, the capabilities of the fast charge/discharge needs to be improved [195]. Toyota is leading the work in this field, but they are at

the moment very secretive regarding their technology.

A completely different method to store energy is by using a capacitor. The energy is stored with a static charge over a large surface area. An improved type of capacitor, namely the ultracapacitor has extreme properties. It has a higher power output and a cycle life that will surpass any battery. Ultra capacitors can be charged within minutes at a vast range of temperatures. However, capacitors can not store much energy. By improving the endurance of ultracapacitors, researchers are able to retain the power and longevity advantages and at the same time storing about as much energy as modern batteries [196] [197]

A continuation of the ultracapacitors, and still only an idea, is the concept of digital quantum batteries. Nanovacuum tubes do not lose its stored charge because the electric breakdown can be suppressed with quantization phenomena. The nanovacuum tubes therefore possess a large capacitance over small gap sizes. It is claimed that the energy density and power density in nanovacuum tubes can be large compared to lithium-ion batteries. Large arrays of nanovacuum tubes can be connected together to meet the desired criteria. The digital quantum batteries can be fabricated using photolithographic techniques [198]. A successful development of this type of device will mark a paradigm shift in the energy storage technology.

A more far-fetched idea is that of an alternative energy storage device. By applying extremely high pressures to XeF_2, Kim *et al.* have recently managed to store energy in the most condensed form disregarding nuclear energy [199]. By compressing the material to pressures up to 70 GPa it is possible to store mechanical energy into chemical energy as the as the compression is stored within the molecular bonds. How to harvest these energies should be a challenge for future researchers. Creative thinking like this might result in new possibilities in the energy storage technology.

List of Abbreviations

Acronym	Explanation
AFM	Atomic Force Microscope
BET	Brunauer-Emmett-Teller (specific surface area technique)
CC	Carbon Cones
CE	Counter Electrode
C_{init}	Initial Discharge Capacity
C_{irr}	Irreversible capacity
CNT	Carbon Nanotube
CV	Cyclic Voltammetry
DEC	Diethylene Carbonate
DSC	Differential Scanning Calorimetry
EC	Ethylene Carbonate
EV	Electric Vehicle
EIS	Electrochemical Impedance Spectroscopy
FTIR	Fourier Transform Infrared Spectroscopy
FWHM	Full Width at Half Maximum
GIC	Graphite Intercalation Compound
IL	Induction Loop
LIB	Lithium-Ion Battery
MCMB	Mesocarbon Microbead
MWNT	Multi-Wall Carbon Nanotubes
NMP	1-Methyl-2-Pyrrolidinone
NTNU	Norges Teknisk-Naturvitenskapelige Universitet (Norwegian University of Science and Technology)
OCV	Open Circuit Voltage
PVDF	Polyvinylidene Fluoride
RBM	Radial Breathing Mode
RE	Reference Electrode
SEI	Solid Electrolyte Interphase
SEM	Scanning Electron Microscope
SLP	Collective term of commercially graphite from Timcal
SOC	State Of Charge
SST	Stainless Steel
SWNT	Single-Wall Carbon Nanotubes
TGA	Thermo Gravimetric Analysis

TEM	Transmission Electron Microscope
WE	Working Electrode
XRD	X-Ray Diffraction

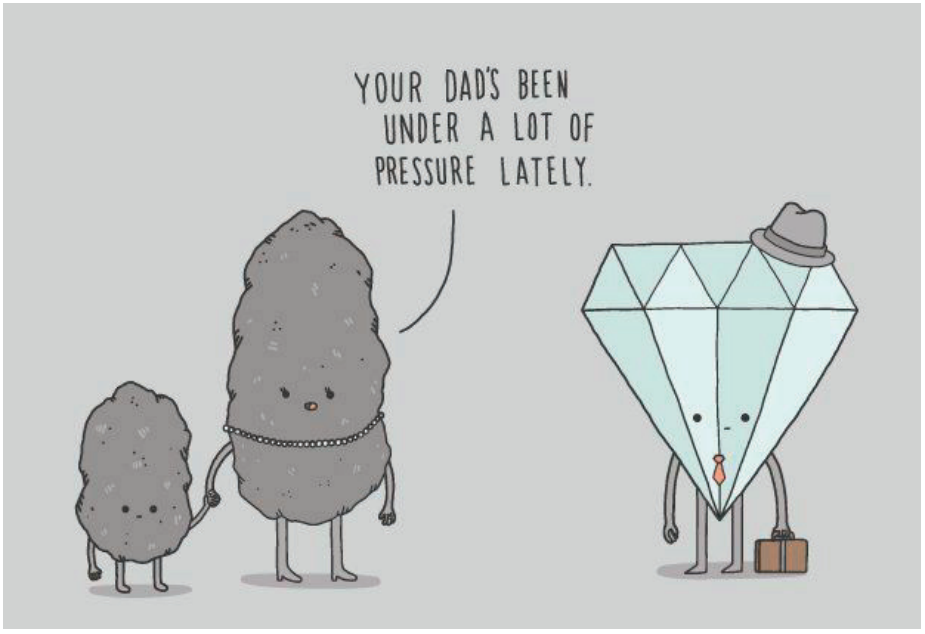

Figure 8.1: The Carbon family (Artwork: Jaco Haasbroek©)

Bibliography

[1] P. Ege. Final report of carbon cones reproduction test work. Technical report, Reactech Process Development Inc., 2011.

[2] H. Marsh, E. A. Heintz, and F. R. Reinoso. *Introduction to Carbon Technologies*. Universidad de Alicante, 1997.

[3] H. Marsh and F. R. Reinoso. *Sciences of Carbon Materials*. Universidad de Alicante, 2000.

[4] H. W. Kroto, J. R. Heath, S. C. O'Brien, R. F. Curl, and R. E. Smalley. C60: Buckminsterfullerene. *Nature*, 318(6042):162–163, 1985.

[5] S. Iijima. Helical microtubules of graphitic carbon. *Nature*, 354(6348):56–58, 1991.

[6] M. Ge and K. Sattler. Observation of fullerene cones. *Chemical Physics Letters*, 220(3-5):192–196, 1994.

[7] A. Krishnan, E. Dujardin, M. M. J. Treacy, J. Hugdahl, S. Lynum, and T. W. Ebbesen. Graphitic cones and the nucleation of curved carbon surfaces. *Nature*, 388(6641):451–454, 1997.

[8] T. Ohtani, T. Nishikawa, K. Harada, K. Ikeda, and N. Takayama. Novel nanocarbons with a mushroom shape found in glassy carbon powder. *Journal of Alloys and Compounds*, 483(1-2):491–494, 2009.

[9] H. Kiehne. *History*. Battery Technology Handbook. CRC Press, 2003.

[10] B. Franklin, Personal Communication, Letter, P. Collinson, 1749.

[11] L. Galvani. De viribus electricitatis in motu musculari commentarius ("commentary on the force of electricity on muscular motion"). *De Bononiensi Scientiarum et Artium Instituto atque Academia Commentarii*, 7:363–415, 1791.

[12] M. Pera. *The Ambiguous Frog: The Galvani-Volta Controversy on Animal Electricity.* Princeton Univ Press; First Edition, 1992.

[13] A. Volta. On the electricity excited by the mere contact of conducting substances of different kinds. *Philosophical Transactions of the Royal Society of London*, 90:403–431, 1800.

[14] J. W. Ritter. *Beyträge zur nähern Kenntniss des Galvanismus und der Resultate seiner Untersuchung*, volume Volume 2. Friedrich Frommann, Jena, 1802.

[15] J. F. Daniell. On voltaic combinations. *Philosophical Transactions of the Royal Society of London*, 126:107–124, 1836.

[16] R. G. Planté. Note sur la polarisation voltaique. *Comptes rendus hebdomadaires des séances de l'Académie des sciences*, 49:402–405, 1859.

[17] G. Leclanché. Battery, 71,865, 1866.

[18] C. Gassner. Galvanic battery, 37,758, 1886.

[19] Gates and E. Products. *Rechargeable batteries applications handbook / technical marketing staff of Gates Energy Products, Inc.* Butterworth-Heinemann, Boston, 1998.

[20] T. A. Edison. Nickel-iron battery, 678.722/1901, 1903.

[21] L. Urry. Dry cell, 2960558, 1957.

[22] J. D. Dunlop and J. F. Stockel. Nickel-hydrogen battery technology - development and status. *COMSAT Tech. Rev.*, 10:281–297, 1982.

[23] K. Beccu. Negative electrode of titanium-nickel alloy hydride phases, 3824131, 1972.

[24] M. S. Whittingham. Electrical energy storage and intercalation chemistry. *Science*, 192(4244):1126–1127, 1976.

[25] K. Mizushima, P. C. Jones, P. J. Wiseman, and J. B. Goodenough. LixCoO2 (0<x<1): A new cathode material for batteries of high energy density. *Materials Research Bulletin*, 15(6):783–789, 1980.

[26] K. Ozawa. Lithium-ion rechargeable batteries with LiCoO2 and carbon electrodes: the LiCoO2/C system. *Solid State Ionics*, 69(3-4):212–221, 1994.

[27] D. Linden and T. Reddy. *Handbook of Batteries*. McGraw-Hill Professional Publishing, New York, NY, USA, 2001.

[28] E. Fitzer, K. H. Kochling, H. P. Boehm, and H. Marsh. Recommended terminology for the description of carbon as a solid - (IUPAC recommendations 1995). *Pure and Applied Chemistry*, 67(3):473–506, 1995.

[29] P. J. F. Harris. New perspectives on the structure of graphitic carbons. *Critical Reviews in Solid State and Materials Sciences*, 30(4):235–253, 2005.

[30] A. R. Ubbelohde and F. A. Lewis. *Graphite and its crystal compounds*. Clarendon Press, Oxford, 1960.

[31] A. T. Balaban, D. J. Klein, and X. Liu. Graphitic cones. *Carbon*, 32(2):357–359, 1994.

[32] F. P. Bundy, W. A. Bassett, M. S. Weathers, R. J. Hemley, H. U. Mao, and A. F. Goncharov. The pressure-temperature phase and transformation diagram for carbon; updated through 1994. *Carbon*, 34(2):141–153, 1996.

[33] R. Yazami. From rome to como: 20 years of active research on carbon-based electrodes for lithium batteries at INP-grenoble. *Journal of Power Sources*, 97-8:33–38, 2001.

[34] Wikipedia. http://en.wikipedia.org/wiki/carbon, 2012.

[35] M. J. Allen, V. C. Tung, and R. B. Kaner. Honeycomb carbon: A review of graphene. *Chemical Reviews*, 110(1):132–145, 2009.

[36] M. Meyyappan. *Carbon nanotubes: science and applications*. CRC Press, Boca Raton, FL, 2005.

[37] T. Placke, V. Siozios, R. Schmitz, S. F. Lux, P. Bieker, C. Colle, H. W. Meyer, S. Passerini, and M. Winter. Influence of graphite surface modifications on the ratio of basal plane to "non-basal plane" surface area and on the anode performance in lithium ion batteries. *Journal of Power Sources*, 200(0):83–91, 2012.

[38] D. Bar-Tow, E. Peled, and L. Burstein. A study of highly oriented pyrolytic graphite as a model for the graphite anode in li-ion batteries. *Journal of The Electrochemical Society*, 146(3):824–832, 1999.

[39] K. E. Spear and J. P. Dismukes. *Synthetic Diamond: Emerging CVD Science and Technology*. John Wiley and Sons. Inc., New York, 1994.

[40] R. Khare and S. Bose. Carbon nanotube based composites - a review. *Journal of Minerals and Materials Characterization and Engineering*, 4(No.1):pp 31–46, 2005.

[41] P. J. F. Harris. *Carbon nanotube science: synthesis, properties and applications*. Cambridge University Press, Cambridge, UK, 2009.

[42] G. A. Ozin and A. C. Arsenault. *Nanochemistry: a chemical approach to nanomaterials*. RSC Publ., Cambridge, 2005.

[43] T. W. Ebbesen and T. Takada. Topological and sp3 defect structures in nanotubes. *Carbon*, 33(7):973–978, 1995.

[44] K. Kinoshita. *Carbon: electrochemical and physicochemical properties*. Wiley, New York, 1988.

[45] L. Fransson, T. Eriksson, K. Edström, T. Gustafsson, and J. O. Thomas. Influence of carbon black and binder on Li-ion batteries. *Journal of Power Sources*, 101(1):1–9, 2001.

[46] R. D. Heidenreich, W. M. Hess, and L. L. Ban. A test object and criteria for high resolutionelectron microscopy. *Journal of Applied Crystallography*, 1:1–19, 1968.

[47] J.-B. Donnet, R. C. Bansal, and M.-J. Wang. *Carbon Black Second Edition, Revised and Expanded*. Marcel Dekker, Inc., 1993.

[48] A. T. Balaban, C. C. Rentia, and E. Ciupitu. Chemical graphs .6. estimation of relative stability of several planar and tridimensional lattices for elementary carbon. *Revue Roumaine De Chimie*, 13(2):231–, 1968.

[49] H. Heiberg-Andersen, K. K. G. Helgesen, J. P. Pinheiro, E. Svaasand, and A. T. Skjeltorp. Nanocones - a different form of carbon with unique properties. *Materials Research Society Symposium Proceedings*, 901E:0901–Ra16–34–Rb16–34.1 – 0901–Ra16–34–Rb16–34.8, 2006.

[50] D. Baowan and J. M. Hill. Equilibrium locations for nested carbon nanocones. *Journal of Mathematical Chemistry*, 43(4):1489–1504, 2008.

[51] K. R. Bates and G. E. Scuseria. Energetic analysis of pentagon road intermediates of C60-buckminsterfullerene formation. *The Journal of Physical Chemistry A*, 101(16):3038–3041, 1997.

[52] T. W. Ebbesen. Cones and tubes: Geometry in the chemistry of carbon. *Accounts of Chemical Research*, 31(9):558–566, 1998.

[53] T. Garberg, S. N. Naess, G. Helgesen, K. D. Knudsen, G. Kopstad, and A. Elgsaeter. A transmission electron microscope and electron diffraction study of carbon nanodisks. *Carbon*, 46(12):1535–1543, 2008.

[54] J. Muller, A. T. Skjeltorp, G. Helgesen, K. D. Knudsen, and H. Heiberg-Andersen. *Carbon Discs and Carbon Cones - New High Risk Materials for Nano-Sensors With Low Detection Limit and Fast Kinetics Silicon Versus Carbon*. NATO Science for Peace and Security Series B: Physics and Biophysics. Springer Netherlands, 2009.

[55] A. Westermoen. *Modelling of dynamic arc behaviour in a plasma reactor*. PhD thesis, 2007. Avhandling (ph.d.) - Norges teknisk-naturvitenskapelige universitet, Trondheim, 2007.

[56] P. Ege, Personal Communication, E-mail, N. Myklebust, 2007.

[57] J. M. Romo-Herrera, D. A. Cullen, E. Cruz-Silva, D. Ramirez, B. G. Sumpter, V. Meunier, H. Terrones, D. J. Smith, and M. Terrones. The role of sulfur in the synthesis of novel carbon morphologies: From covalent y-junctions to sea-urchin-like structures. *Advanced Functional Materials*, 19(8):1193–1199, 2009.

[58] K. Zahlsen. Carbon cones - measurements of volatile and semivolatile organic compounds in gas samples from reactor experiments with gas chromatography - mass spectromentry. Technical report, SINTEF, 2009.

[59] S. Ahmed, A. Aitani, F. Rahman, A. Al-Dawood, and F. Al-Muhaish. Decomposition of hydrocarbons to hydrogen and carbon. *Applied Catalysis a-General*, 359(1-2):1–24, 2009.

[60] N. Probst, E. Grivei, F. Fabry, L. Fulcheri, G. Flamant, X. Bourrat, and A. Schroder. Quality and performance of carbon blacks from plasma process. *Rubber Chemistry and Technology*, 75(5):891–905, 2002.

[61] S. Lynum, J. Hugdahl, K. Hox, R. Hildrum, and M. Nordvik. For production of micro domain particles by use of a plasma process, pct/no98/00093., 2000.

[62] M. Inagaki and T. Noda. Changes of the lattice constants and crystallite sizes of various types of carbons with heat treatment. *Bulletin of the Chemical Society of Japan*, 35(10):1652–1657, 1962.

[63] H. Marsh and F. R. Reinoso. *Activated Carbon*. Elsevier Science Ltd, 2006.

[64] M. Winter, J. O. Besenhard, M. E. Spahr, and P. Novák. Insertion electrode materials for rechargeable lithium batteries. *Advanced Materials*, 10(10):725–763, 1998.

[65] D. Berndt. *Electrochemical Energy Storage*. Battery Technology Handbook. CRC Press, 2003.

[66] G. H. Aylward and T. J. V. Findlay. *SI Chemical Data*. John Wiley and Sons Ltd, 5th edition edition, 2001.

[67] M. W. Chase. *NIST-JANAF thermochemical tables*, volume no. 9 of *Journal of physical and chemical reference data, Monograph*. American Chemical Society and the American Institute of Physics for the National Institute of Standards and Technology, Washington, D.C., 1998.

[68] J. R. Dahn and R. R. Haering. Entropy measurements on LixTiS2. *Canadian Journal of Physics*, 61(7):1093–1098, 1983.

[69] A. J. Bard and L. R. Faulkner. *Electrochemical methods: fundamentals and applications*. Wiley, New York, 2001.

[70] K. Xu. Nonaqueous liquid electrolytes for lithium-based rechargeable batteries. *Chemical Reviews*, 104(10):4303–4417, 2004.

[71] T. Takamura and R. J. Brodd. *CARBONACEOUS MATERIALS FOR BATTERIES New Carbon Based Materials for Electrochemical Energy Storage Systems: Batteries, Supercapacitors and Fuel Cells*, volume 229 of *NATO Science Series*. Springer Netherlands, 2006.

[72] F. Cao, I. V. Barsukov, H. J. Bang, P. Zaleski, and J. Prakash. Evaluation of graphite materials as anodes for lithium-ion batteries. *Journal of The Electrochemical Society*, 147(10):3579–3583, 2000.

[73] B. Simon, S. Flandrois, K. Guerin, A. Fevrier-Bouvier, I. Teulat, and P. Biensan. On the choice of graphite for lithium ion batteries. *Journal of Power Sources*, 81:312–316, 1999.

[74] J. Graetz, C. C. Ahn, R. Yazami, and B. Fultz. Highly reversible lithium storage in nanostructured silicon. *Electrochemical and Solid-State Letters*, 6(9):A194–A197, 2003.

[75] A. Manthiram and T. Muraliganth. *Lithium Intercalation Cathode Materials for Lithium-Ion Batteries*. Wiley-VCH Verlag GmbH & Co. KGaA, 2011.

[76] G.-A. Nazri and G. Pistoia. *Lithium batteries: science and technology*. Springer, New York, N.Y., 2003.

[77] W. C. Forsman, T. Dziemianowicz, K. Leong, and D. Carl. Graphite intercalation chemistry: An interpretive review. *Synthetic Metals*, 5(2):77–100, 1983.

[78] F. Lévy. *Intercalated layered materials*. D. Reidel Pub., Dordrecht, 1979.

[79] D. Billaud, E. McRae, and A. Hérold. Synthesis and electrical resistivity of lithium-pyrographite intercalation compounds (stages i, ii and iii). *Materials Research Bulletin*, 14(7):857–864, 1979.

[80] T. Ohzuku, Y. Iwakoshi, and K. Sawai. Formation of lithium-graphite intercalation compounds in nonaqueous electrolytes and their application as a negative electrode for a lithium ion (shuttlecock) cell. *Journal of The Electrochemical Society*, 140(9):2490–2498, 1993.

[81] A. Herstedt, L. Fransson, and K. Edstrom. Rate capability of natural swedish graphite as anode material in li-ion batteries. *Journal of Power Sources*, 124(1):191–196, 2003.

[82] J. R. Dahn. Phase-diagram of LixC6. *Physical Review B*, 44(17):9170–9177, 1991.

[83] N. Daumas and A. Herold. Relations between phase concept and reaction mechanics in graphite insertion compounds. *Comptes Rendus Hebdomadaires Des Seances De L Academie Des Sciences Serie C*, 268(5):373–375, 1969.

[84] Y. F. Reynier, R. Yazami, and B. Fultz. Thermodynamics of lithium intercalation into graphites and disordered carbons. *Journal of The Electrochemical Society*, 151(3):A422–A426, 2004.

[85] M. S. Dresselhaus and G. Dresselhaus. Intercalation compounds of graphite. *ChemInform*, 33(51):228–228, 2002.

[86] E. Buiel and J. R. Dahn. Li-insertion in hard carbon anode materials for Li-ion batteries. *Electrochimica Acta*, 45(1-2):121–130, 1999.

[87] J. S. Gnanaraj, M. D. Levi, E. Levi, G. Salitra, D. Aurbach, J. E. Fischer, and A. Claye. Comparison between the electrochemical behavior of disordered carbons and graphite electrodes in connection with their structure. *Journal of The Electrochemical Society*, 148(6):A525–A536, 2001.

[88] A. Van der Ven, M. K. Aydinol, G. Ceder, G. Kresse, and J. Hafner. First-principles investigation of phase stability in Li(x)CoO(2). *Physical Review B*, 58(6):2975–2987, 1998.

[89] Z. Chen and J. R. Dahn. Methods to obtain excellent capacity retention in LiCoO2 cycled to 4.5 v. *Electrochimica Acta*, 49(7):1079–1090, 2004.

[90] H. Zhou, M.-A. Einarsrud, and F. Vullum-Bruer. Pva-assisted combustion synthesis and characterization of porous nanocomposite Li2FeSiO4/C. *Solid State Ionics*, 2012.

[91] K. Momma and F. Izumi. Vesta 3 for three-dimensional visualization of crystal, volumetric and morphology data. *Journal of Applied Crystallography*, 44(6):1272–1276, 2011.

[92] B. Lestriez. Functions of polymers in composite electrodes of lithium ion batteries. *Comptes Rendus Chimie*, 13(11):1341–1350, 2010.

[93] P. Biensan, B. Simon, J. P. Pérès, A. de Guibert, M. Broussely, J. M. Bodet, and F. Perton. On safety of lithium-ion cells. *Journal of Power Sources*, 81-82(0):906–912, 1999.

[94] A. Bottino, G. Capannelli, S. Munari, and A. Turturro. Solubility parameters of poly(vinylidene fluoride). *Journal of Polymer Science Part B: Polymer Physics*, 26(4):785–794, 1988.

[95] S.-T. Myung, Y. Hitoshi, and Y.-K. Sun. Electrochemical behavior and passivation of current collectors in lithium-ion batteries. *Journal of Materials Chemistry*, 21(27):9891–9911, 2011.

[96] J. B. Goodenough and Y. Kim. Challenges for rechargeable li batteries. *Chemistry of Materials*, 22(3):587–603, 2010.

[97] H. J. Gores, J. Barthel, S. Zugmann, D. Moosbauer, M. Amereller, R. Hartl, and A. Maurer. *Liquid Nonaqueous Electrolytes*. Wiley-VCH Verlag GmbH & Co. KGaA, 2011.

[98] M. Winter. The solid electrolyte interphase - the most important and the least understood solid electrolyte in rechargeable li batteries. *Zeitschrift für Physikalische Chemie*, 223(10-11):1395–1406, 2009.

[99] R. Fong, U. Vonsacken, and J. R. Dahn. Studies of lithium intercalation into carbons using nonaqueous electrochemical-cells. *Journal of The Electrochemical Society*, 137(7):2009–2013, 1990.

[100] M. Egashira, H. Takahashi, S. Okada, and J. Yamaki. Measurement of the electrochemical oxidation of organic electrolytes used in lithium batteries by microelectrode. *Journal of Power Sources*, 92(1-2):267–271, 2001.

[101] X. R. Zhang, R. Kostecki, T. J. Richardson, J. K. Pugh, and P. N. Ross. Electrochemical and infrared studies of the reduction of organic carbonates. *Journal of The Electrochemical Society*, 148(12):A1341–A1345, 2001.

[102] L. O. Valoen and J. N. Reimers. Transport properties of lipf6-based li-ion battery electrolytes. *Journal of The Electrochemical Society*, 152(5):A882–A891, 2005.

[103] P. Arora and Z. M. Zhang. Battery separators. *Chemical Reviews*, 104(10):4419–4462, 2004.

[104] A. J. Smith, J. C. Burns, X. M. Zhao, D. J. Xiong, and J. R. Dahn. A high precision coulometry study of the sei growth in Li/graphite cells. *Journal of The Electrochemical Society*, 158(5):A447–A452, 2011.

[105] P. Verma, P. Maire, and P. Novák. A review of the features and analyses of the solid electrolyte interphase in Li-ion batteries. *Electrochimica Acta*, 55(22):6332–6341, 2010.

[106] J. O. Besenhard, M. Winter, J. Yang, and W. Biberacher. Filming mechanism of lithium-carbon anodes in organic and inorganic electrolytes. *Journal of Power Sources*, 54(2):228–231, 1995.

[107] S. H. Ng, C. Vix-Guterl, P. Bernardo, N. Tran, J. Ufheil, H. Buqa, J. Dentzer, R. Gadiou, M. E. Spahr, D. Goers, and P. Novák. Correlations between surface properties of graphite and the first cycle specific charge loss in lithium-ion batteries. *Carbon*, 47(3):705–712, 2009.

[108] Y. Wang and P. B. Balbuena. *Lithium-ion batteries: solid-electrolyte interphase*. Imperial College Press, London, 2004.

[109] K. Edström, M. Herstedt, and D. P. Abraham. A new look at the solid electrolyte interphase on graphite anodes in Li-ion batteries. *Journal of Power Sources*, 153(2):380–384, 2006.

[110] D. Aurbach. Review of selected electrode - solution interactions which determine the performance of Li and Li ion batteries. *Journal of Power Sources*, 89(2):206–218, 2000.

[111] H. J. Santner, K. C. Möller, W. Kohs, C. Veit, E. Lanzer, A. Trifonova, M. R. Wagner, P. Raimann, C. Korepp, J. O. Besenhard, and M. Winter. *ANODE-ELECTROLYTE REACTIONS IN Li BATTERIES: THE DIFFERENCES BETWEEN GRAPHITIC AND METALLIC ANODES New Carbon Based Materials for Electrochemical Energy Storage Systems: Batteries, Supercapacitors and Fuel Cells*, volume 229 of *NATO Science Series*. Springer Netherlands, 2006.

[112] J. P. Olivier and M. Winter. Determination of the absolute and relative extents of basal plane surface area and "non-basal plane surface" area of graphites and their impact on anode performance in lithium ion batteries. *Journal of Power Sources*, 97-98(0):151–155, 2001.

[113] P. G. Balakrishnan, R. Ramesh, and T. Prem Kumar. Safety mechanisms in lithium-ion batteries. *Journal of Power Sources*, 155(2):401–414, 2006.

[114] J. M. Chen, C. Y. Yao, S. P. Sheu, Y. C. Chiou, and H. C. Shih. The study of carbon half-cell voltage in lithium-ion secondary batteries. *Journal of Power Sources*, 68(2):242–244, 1997.

[115] S. Tobishima. *SECONDARY BATTERIES - LITHIUM RECHARGEABLE SYSTEMS - LITHIUM-ION - Thermal Runaway*. Elsevier, Amsterdam, 2009.

[116] Application note from gamry instruments - basics of electrochemical impedance spectroscopy.

[117] B. Y. Liaw, G. Nagasubramanian, R. G. Jungst, and D. H. Doughty. Modeling of lithium ion cells - a simple equivalent-circuit model approach. *Solid State Ionics*, 175(1-4):835–839, 2004.

[118] M. Kamisah, H. Siti Munirah, and M. Mansor. Electrochemical impedance study of lithium-ion insertion into rice husk carbon. *Ionics*, 13(4):223–225, 2007.

[119] C. H. Hamann, A. Hamnett, and W. Vielstich. *Electrochemistry*. Wiley-VCH, Weinheim, 1998.

[120] D. K. Gosser. *Cyclic voltammetry: simulation and analysis of reaction mechanisms*. VCH, New York, 1993.

[121] M. D. Levi and D. Aurbach. The mechanism of lithium intercalation in graphite film electrodes in aprotic media .1. high resolution slow scan rate cyclic voltammetric studies and modeling. *Journal of Electroanalytical Chemistry*, 421(1-2):79–88, 1997.

[122] P. J. Haines and G. R. Heal. *Principles of thermal analysis and calorimetry*. Royal Society of Chemistry, Cambridge, 2002.

[123] E. L. Charsley and S. B. Warrington. *Thermal analysis: techniques and applications*, volume 117. The Royal Society of Chemistry, London, 1992.

[124] G. W. H. Höhne, W. Hemminger, and H. J. Flammersheim. *Differential scanning calorimetry*. Springer, Berlin, 2003.

[125] H. Maleki, G. P. Deng, A. Anani, and J. Howard. Thermal stability studies of Li-ion cells and components. *Journal of The Electrochemical Society*, 146(9):3224–3229, 1999.

[126] H. Yang, H. Bang, K. Amine, and J. Prakash. Investigations of the exothermic reactions of natural graphite anode for Li-ion batteries during thermal runaway. *Journal of The Electrochemical Society*, 152(1):A73–A79, 2005.

[127] J. Yan, C. Zhu, X. Guoqing, Q. Huihuan, and X. Yangsheng. Fuzzy control for battery equalization based on state of charge. In *Vehicular Technology Conference Fall (VTC 2010-Fall), 2010 IEEE 72nd*, pages 1–7.

[128] Z. Zhang, D. Fouchard, and J. R. Rea. Differential scanning calorimetry material studies: implications for the safety of lithium-ion cells. *Journal of Power Sources*, 70(1):16–20, 1998.

[129] F. Joho, P. Novák, and M. E. Spahr. Safety aspects of graphite negative electrode materials for lithium-ion batteries. *Journal of The Electrochemical Society*, 149(8):A1020–A1024, 2002.

[130] B. Kennedy, D. Patterson, and S. Camilleri. Use of lithium-ion batteries in electric vehicles. *Journal of Power Sources*, 90(2):156–162, 2000.

[131] X. W. Zhang. Thermal analysis of a cylindrical lithium-ion battery. *Electrochimica Acta*, 56(3):1246–1255, 2011.

[132] N. Sato. Thermal behavior analysis of lithium-ion batteries for electric and hybrid vehicles. *Journal of Power Sources*, 99(1-2):70–77, 2001.

[133] J. P. Holman. *Heat transfer*. McGraw-Hill, Singapore, 1989.

[134] F. P. Incropera and D. P. DeWitt. *Introduction to heat transfer*. Wiley, New York, 1985.

[135] J. B. J. Fourier. *The analytical theory of heat*. Dover, New York, 1955.

[136] O. Burheim, P. J. S. Vie, J. G. Pharoah, and S. Kjelstrup. Ex situ measurements of through-plane thermal conductivities in a polymer electrolyte fuel cell. *Journal of Power Sources*, 195(1):249–256, 2010.

[137] http://www.n-tec.no, 2012.

[138] TIMCAL. http://www.timcal.com/scopi/group/timcal/timcal.nsf/pagesref/scmm-7evdst?opendocumen&lang=en, 2012.

[139] D. F. Shriver and P. W. Atkins. *Inorganic chemistry*. Oxford University Press, Oxford, 1999.

[140] C. Bréchignac, P. Houdy, and M. Lahmani. *Nanomaterials and nanochemistry*. Springer, Berlin, 2007.

[141] H. Heiberg-Andersen, G. Walker, A. Skjeltorp, and S. Naess. *Graphene Cones*. Handbook of Nanophysics. CRC Press, 2010.

[142] E. G. Gamaly and T. W. Ebbesen. Mechanism of carbon nanotube formation in the arc discharge. *Physical Review B*, 52(3):2083–2089, 1995.

[143] M. Meyyappan, L. Delzeit, A. Cassell, and D. Hash. Carbon nanotube growth by pecvd: a review. *Plasma Sources Science and Technology*, 12(2):205–216, 2003.

[144] R. Andrews, D. Jacques, D. Qian, and E. C. Dickey. Purification and structural annealing of multiwalled carbon nanotubes at graphitization temperatures. *Carbon*, 39(11):1681–1687, 2001.

[145] Z. Q. Li, C. J. Lu, Z. P. Xia, Y. Zhou, and Z. Luo. X-ray diffraction patterns of graphite and turbostratic carbon. *Carbon*, 45(8):1686–1695, 2007.

[146] J. B. Aladekomo and R. H. Bragg. Structural transformations induced in graphite by grinding: Analysis of 002 X-ray diffraction line profiles. *Carbon*, 28(6):897–906, 1990.

[147] M. A. Pimenta, G. Dresselhaus, M. S. Dresselhaus, L. G. Cancado, A. Jorio, and R. Saito. Studying disorder in graphite-based systems by raman spectroscopy. *Physical Chemistry Chemical Physics*, 9(11):1276–1291, 2007.

[148] T. D. Shen, W. Q. Ge, K. Y. Wang, M. X. Quan, J. T. Wang, W. D. Wei, and C. C. Koch. Structural disorder and phase transformation in graphite produced by ball milling. *Nanostructured Materials*, 7(4):393–399, 1996.

[149] D. Goers, H. Buqa, L. Hardwick, A. Würsig, and P. Novák. Raman spectroscopic and structural studies of heat-treated graphites for lithium-ion batteries. *Ionics*, 9(3):258–265, 2003.

[150] S. Kurita, A. Yoshimura, H. Kawamoto, T. Uchida, K. Kojima, M. Tachibana, P. Molina-Morales, and H. Nakai. Raman spectra of carbon nanowalls grown by plasma-enhanced chemical vapor deposition. *Journal of Applied Physics*, 97(10):104320–104320–5, 2005.

[151] C. W. Snow, D. R. Wallace, and A. E. Daniell. 116. the carbon black-oxygen reaction: oxidation promotors. *Carbon*, 6(2):224, 1968.

[152] T. Gruber, T. W. Zerda, and M. Gerspacher. Raman studies of heat-treated carbon blacks. *Carbon*, 32(7):1377–1382, 1994.

[153] A. Jorio, R. Saito, J. H. Hafner, C. M. Lieber, M. Hunter, T. McClure, G. Dresselhaus, and M. S. Dresselhaus. Structural (n, m) determination of isolated single-wall carbon nanotubes by resonant raman scattering. *Physical Review Letters*, 86(6):1118–1121, 2001.

[154] S. Lim, S. H. Yoon, I. Mochida, and J. H. Chi. Surface modification of carbon nanofiber with high degree of graphitization. *Journal of Physical Chemistry B*, 108(5):1533–1536, 2004.

[155] K. Moriguchi, S. Munetoh, M. Abe, M. Yonemura, K. Kamei, A. Shintani, Y. Maehara, A. Omaru, and M. Nagamine. Nano-tube-like surface structure in graphite particles and its formation mechanism: A role in anodes of lithium-ion secondary batteries. *Journal of Applied Physics*, 88(11):6369–6377, 2000.

[156] P. Novák, J. Ufheil, H. Buqa, F. Krumeich, M. E. Spahr, D. Goers, H. Wilhelm, J. Dentzer, R. Gadiou, and C. Vix-Guterl. The importance of the active surface area of graphite materials in the first lithium intercalation. *Journal of Power Sources*, 174(2):1082–1085, 2007.

[157] M. Winter, P. Novák, and A. Monnier. Graphites for lithium-ion cells: The correlation of the first-cycle charge loss with the brunauer-emmett-teller surface area. *Journal of The Electrochemical Society*, 145(2):428–436, 1998.

[158] F. Béguin, F. Chevallier, M. Letellier, C. Vix, C. Clinard, J. N. Rouzaud, and E. Frackowiak. *MECHANISMS OF REVERSIBLE AND IRREVERSIBLE INSERTION IN NANOSTRUCTURED CARBONS USED FOR Li-ION BATTERIES New Carbon Based Materials for Electrochemical Energy Storage Systems: Batteries, Supercapacitors and Fuel Cells*, volume 229 of *NATO Science Series*. Springer Netherlands, 2006.

[159] K. Zaghib, X. Song, and K. Kinoshita. Thermal analysis of the oxidation of natural graphite: isothermal kinetic studies. *Thermochimica Acta*, 371(1-2):57–64, 2001.

[160] Y. Ein-Eli and V. R. Koch. Chemical oxidation: A route to enhanced capacity in Li-ion graphite anodes. *Journal of The Electrochemical Society*, 144(9):2968–2973, 1997.

[161] L. J. Fu, H. Liu, C. Li, Y. P. Wu, E. Rahm, R. Holze, and H. Q. Wu. Surface modifications of electrode materials for lithium ion batteries. *Solid State Sciences*, 8(2):113–128, 2006.

[162] O. J. Kwon, Y. S. Jung, J. H. Kim, and S. M. Oh. A simple preparation method for spherical carbons and their anodic performance in lithium secondary batteries. *Journal of Power Sources*, 125(2):221–227, 2004.

[163] K. A. Striebel, A. Sierra, J. Shim, C. W. Wang, and A. M. Sastry. The effect of compression on natural graphite anode performance and matrix conductivity. *Journal of Power Sources*, 134(2):241–251, 2004.

[164] J. Shim and K. A. Striebel. The dependence of natural graphite anode performance on electrode density. *Journal of Power Sources*, 130(1-2):247–253, 2004.

[165] F. Béguin and E. b. Frackowiak. *Carbons for electrochemical energy storage and conversionsystems*. CRC Press, Boca Raton, 2010.

[166] H. G. Zhang, X. D. Yu, and P. V. Braun. Three-dimensional bicontinuous ultrafast-charge and -discharge bulk battery electrodes. *Nature Nanotechnology*, 6(5):277–281, 2011.

[167] F.-X. Henry, I. V. Barsukov, J. E. Doninger, S. Anderson, P. R. Booth, P. L. Zaleski, R. J. Girkant, D. J. Derwin, M. A. Gallego, T. Huerta, and G. Uribe. *NEW DEVELOPMENTS IN THE ADVANCED GRAPHITE FOR LITHIUM-ION BATTERIES New Carbon Based Materials for Electrochemical Energy Storage Systems: Batteries, Supercapacitors and Fuel Cells*, volume 229 of *NATO Science Series*. Springer Netherlands, 2006.

[168] N. Takami, A. Satoh, T. Ohsaki, and M. Kanda. Large hysteresis during lithium insertion into and extraction from high-capacity disordered carbons. *Journal of The Electrochemical Society*, 145(2):478–482, 1998.

[169] A. J. Smith, J. C. Burns, S. Trussler, and J. R. Dahn. Precision measurements of the coulombic efficiency of lithium-ion batteries and of electrode materials for lithium-ion batteries. *Journal of The Electrochemical Society*, 157(2):A196–A202, 2010.

[170] Z. X. Shu, R. S. McMillan, and J. J. Murray. Electrochemical intercalation of lithium into graphite. *Journal of The Electrochemical Society*, 140(4):922–927, 1993.

[171] H. Zheng, P. Ridgway, X. Song, S. Xun, J. Chong, G. Liu, and V. Battaglia. Comparison of cycling performance of lithium ion cell anode graphites. *ECS Transactions*, 33(29):91–100, 2011.

[172] Y. P. Wu, C. Jiang, C. Wan, and R. Holze. Mild preparation of anode materials by a salt-free green method. *Electrochemistry Communications*, 4(6):483–487, 2002.

[173] Y. P. Wu, C. Jiang, C. Wan, and R. Holze. Modified natural graphite as anode material for lithium ion batteries. *Journal of Power Sources*, 111(2):329–334, 2002.

[174] E. Peled, C. Menachem, D. Bar-Tow, and A. Melman. Improved graphite anode for lithium-ion batteries - chemically bonded solid electrolyte interface and nanochannel formation. *Journal of The Electrochemical Society*, 143(1):L4–L7, 1996.

[175] J. A. Menendez, A. Arenillas, B. Fidalgo, Y. Fernandez, L. Zubizarreta, E. G. Calvo, and J. M. Bermudez. Microwave heating processes involving carbon materials. *Fuel Processing Technology*, 91(1):1–8, 2010.

[176] S. Yoshida and M. Sano. Microwave-assisted chemical modification of carbon nanohorns: Oxidation and pt deposition. *Chemical Physics Letters*, 433(1-3):97–100, 2006.

[177] N. Takami, A. Satoh, M. Hara, and I. Ohsaki. Structural and kinetic characterization of lithium intercalation into carbon anodes for secondary lithium batteries. *Journal of The Electrochemical Society*, 142(2):371–379, 1995.

[178] A. Ivanishchev, A. Churikov, I. Ivanishcheva, K. Zapsis, and I. Gamayunova. Impedance spectroscopy of lithium-carbon electrodes. *Russian Journal of Electrochemistry*, 44(5):510–524, 2008.

[179] Y. C. Chang and H. J. Sohn. Electrochemical impedance analysis for lithium ion intercalation into graphitized carbons. *Journal of The Electrochemical Society*, 147(1):50–58, 2000.

[180] C. Wang, A. J. Appleby, and F. E. Little. Electrochemical impedance study of initial lithium ion intercalation into graphite powders. *Electrochimica Acta*, 46(12):1793–1813, 2001.

[181] J. Y. Song, H. H. Lee, Y. Y. Wang, and C. C. Wan. Two- and three-electrode impedance spectroscopy of lithium-ion batteries. *Journal of Power Sources*, 111(2):255–267, 2002.

[182] A. Funabiki, M. Inaba, Z. Ogumi, S.-i. Yuasa, J. Otsuji, and A. Tasaka. Impedance study on the electrochemical lithium intercalation into natural graphite powder. *Journal of The Electrochemical Society*, 145(1):172–178, 1998.

[183] J. S. Gnanaraj, R. W. Thompson, S. N. Iaconatti, J. F. DiCarlo, and K. M. Abraham. Formation and growth of surface films on graphitic anode materials for li-ion batteries. *Electrochemical and Solid State Letters*, 8(2):A128–A132, 2005.

[184] M. Cimenti, A. C. Co, V. I. Birss, and J. M. Hill. Distortions in electrochemical impedance spectroscopy measurements using 3-electrode methods in SOFC. i-effect of cell geometry. *Fuel Cells*, 7(5):364–376, 2007.

[185] F. La Mantia, J. Vetter, and P. Novák. Impedance spectroscopy on porous materials: A general model and application to graphite electrodes of lithium-ion batteries. *Electrochimica Acta*, 53(12):4109–4121, 2008.

[186] J. S. Kim, J. U. Kim, C. H. Sung, and H. B. Gu. *The electrical and electrochemical properties of poly(p-phenylene)-based carbon for lithium rechargeable batteries.* Proceedings of the 5th International Conference on Properties and Applications of Dielectric Materials, Vols 1 and 2. IEEE, New York, 1997.

[187] J. R. Dahn, T. Zheng, Y. H. Liu, and J. S. Xue. Mechanisms for lithium insertion in carbonaceous materials. *Science*, 270(5236):590–593, 1995.

[188] R. Yazami and P. Touzain. A reversible graphite lithium negative electrode for electrochemical generators. *Journal of Power Sources*, 9(3-4):365–371, 1983.

[189] E. P. Roth, D. H. Doughty, and J. Franklin. DSC investigation of exothermic reactions occurring at elevated temperatures in lithium-ion anodes containing pvdf-based binders. *Journal of Power Sources*, 134(2):222–234, 2004.

[190] Y. S. Park and S. M. Lee. Effects of particle size on the thermal stability of lithiated graphite anode. *Electrochimica Acta*, 54(12):3339–3343, 2009.

[191] A. Magasinski, P. Dixon, B. Hertzberg, A. Kvit, J. Ayala, and G. Yushin. High-performance lithium-ion anodes using a hierarchical bottom-up approach. *Nat Mater*, 9(4):353–358, 2010.

[192] J. M. Mosby and A. L. Prieto. Direct electrodeposition of cu2sb for lithium-ion battery anodes. *Journal of the American Chemical Society*, 130(32):10656–10661, 2008.

[193] J. Christensen, P. Albertus, R. S. Sanchez-Carrera, T. Lohmann, B. Kozinsky, R. Liedtke, J. Ahmed, and A. Kojic. A critical review of Li/air batteries. *Journal of The Electrochemical Society*, 159(2):R1–R30, 2012.

[194] M. K. Song, S. Park, F. M. Alamgir, J. Cho, and M. L. Liu. Nanostructured electrodes for lithium-ion and lithium-air batteries: the latest developments, challenges, and perspectives. *Materials Science and Engineering R-Reports*, 72(11):203–252, 2011.

[195] H. S. Kim, T. S. Arthur, G. D. Allred, J. Zajicek, J. G. Newman, A. E. Rodnyansky, A. G. Oliver, W. C. Boggess, and J. Muldoon. Structure and compatibility of a magnesium electrolyte with a sulphur cathode. *Nat Commun*, 2:427, 2011.

[196] R. Kötz and M. Carlen. Principles and applications of electrochemical capacitors. *Electrochimica Acta*, 45(15-16):2483–2498, 2000.

[197] A. F. Burke. Batteries and ultracapacitors for electric, hybrid, and fuel cell vehicles. *Proceedings of the Ieee*, 95(4):806–820, 2007.

[198] A. W. Hübler and O. Osuagwu. Digital quantum batteries: Energy and information storage in nanovacuum tube arrays. *Complexity*, 15(5):48–55, 2010.

[199] M. Kim, M. Debessai, and C.-S. Yoo. Two- and three-dimensional extended solids and metallization of compressed XeF2. *Nat Chem*, 2(9):784–788, 2010.